

Western  Graduate&PostdoctoralStudies

Western University  
Scholarship@Western

---

Electronic Thesis and Dissertation Repository

---

4-26-2012 12:00 AM

## Enhancement of Local Buckling Behaviour of Steel Structures Retrofitted Through Bonding GFRP Plates

Mohammad Al Amin Siddique  
*The University of Western Ontario*

Supervisor

Dr. Ashraf El Damatty  
*The University of Western Ontario*

Graduate Program in Civil and Environmental Engineering

A thesis submitted in partial fulfillment of the requirements for the degree in Doctor of  
Philosophy

© Mohammad Al Amin Siddique 2012

Follow this and additional works at: <https://ir.lib.uwo.ca/etd>



Part of the [Civil Engineering Commons](#), and the [Structural Engineering Commons](#)

---

### Recommended Citation

Siddique, Mohammad Al Amin, "Enhancement of Local Buckling Behaviour of Steel Structures Retrofitted Through Bonding GFRP Plates" (2012). *Electronic Thesis and Dissertation Repository*. 487.

<https://ir.lib.uwo.ca/etd/487>

This Dissertation/Thesis is brought to you for free and open access by Scholarship@Western. It has been accepted for inclusion in Electronic Thesis and Dissertation Repository by an authorized administrator of Scholarship@Western. For more information, please contact [wlsadmin@uwo.ca](mailto:wlsadmin@uwo.ca).

**ENHANCEMENT OF LOCAL BUCKLING BEHAVIOUR OF STEEL  
STRUCTURES RETROFITTED THROUGH BONDING GFRP PLATES**

(Spine Title: Enhancement of Local Buckling Behaviour of Steel Structures)

(Thesis Format: Integrated-Article)

By

**Mohammad Al Amin Siddique**

Graduate Program in Engineering Science  
Department of Civil and Environmental Engineering

A thesis submitted in partial fulfilment  
of the requirements for the degree of  
Doctor of Philosophy

School of Graduate and Postdoctoral Studies  
The University of Western Ontario  
London, Ontario, Canada  
April, 2012

© **Mohammad Al Amin Siddique 2012**

THE UNIVERSITY OF WESTERN ONTARIO  
SCHOOL OF GRADUATE AND POSTDOCTORAL STUDIES

**CERTIFICATE OF EXAMINATION**

Supervisor

\_\_\_\_\_  
Dr. Ashraf A. El Damatty

Examiners

\_\_\_\_\_  
Dr. Michael Tait

\_\_\_\_\_  
Dr. Jon Southen

\_\_\_\_\_  
Dr. Samuel Asokanthan

\_\_\_\_\_  
Dr. Magdi Mohareb

The thesis by

**Mohammad Al Amin Siddique**

entitled:

**Enhancement of Local Buckling Behaviour of Steel Structures through bonding  
GFRP plates**

is accepted in partial fulfilment of the  
requirements for the degree of  
Doctor of Philosophy

Date \_\_\_\_\_

\_\_\_\_\_  
Chair of the Thesis Examination Board

## ABSTRACT

An effective technique involving the use of glass fiber reinforced polymer (GFRP) plates to enhance the local buckling behaviour of steel plates, beams, and moment resisting frames is presented in this Thesis. The enhancement in buckling capacity is achieved by bonding GFRP plates to the steel sections. These steel/GFRP joints have the advantages of ease of application, low cost, high strength-to-weight ratio, and resistance to corrosion. An interface element that simulates the behaviour of the adhesive bonding the steel and GFRP elements is developed and is implemented into an in-house developed finite element model to represent steel/GFRP joints. The model is based on a powerful nonlinear shell element that is capable of simulating both thin and thick-walled structures. The strength and stiffness of both the GFRP and the adhesive used in the model are based on values obtained from previously conducted tests.

The enhancement in buckling capacity of retrofitted steel/GFRP plates is studied by bonding GFRP plates to steel plates having different aspect and slenderness ratios. The study also considers the effect of initial geometric imperfections on both the elastic and inelastic buckling capacities of retrofitted plates. Better improvement in load capacity is predicted for slender steel plates. The strength of the adhesive is shown to play an important role in defining the mode of failure and in determining the capacity of the retrofitted plates.

The improvement in buckling behaviour of retrofitted steel/GFRP beams is then studied considering various thicknesses of GFRP plates. The conducted analysis covers a range of slenderness ratios of steel beams and assesses the effect of plastic modulus of steel,

initial geometric imperfection, and residual stresses of the steel section on the load-deflection behaviour of steel beams.

The lateral behaviour of moment resisting steel frames retrofitted with GFRP plates is studied to assess their capacity improvement in seismic regions. Nonlinear static pushover analyses are carried out for frames retrofitted at their beams' flanges with different thickness of GFRP plates. The global capacity curves for the retrofitted frames are compared with their corresponding original frames to assess the improvement in seismic performance of the frames.

Finally, an experimental investigation is carried out to assess the strength and stiffness properties of adhesively bonded steel/GFRP joints under cyclic loading. A number of shear lap tests are conducted and the obtained results are used to determine the characteristics of spring systems that simulate the shear and peel behaviour of the adhesive. Comparison is made between the stiffness and strength capacity under cyclic loading to the corresponding values under monotonic loading.

**KEYWORDS:** Steel Structures, Glass Fiber Reinforced Polymer (GFRP) Plates, Adhesive, Local Buckling, Failure Modes, Slenderness Ratio, Geometric Imperfections, Spring Constants, Cyclic Loading.

## **CO-AUTHORSHIP**

This thesis has been prepared in accordance with the regulations for an Integrated-Article format thesis stipulated by the School of Graduate and Postdoctoral Studies at the University of Western Ontario and has been co-authored as:

### **Chapter 2: Enhancement of Buckling Capacity of Steel Plates Strengthened with GFRP Plates**

Numerical modeling work was conducted by M. A. A. Siddique under close supervision of Dr. A. A. El Damatty. Drafts of Chapter 2 were written by M. A. A. Siddique and modifications were done under supervision of Dr. A. A. El Damatty. A version of this work co-authored by M. A. A. Siddique and A. A. El Damatty was submitted to the *Journal of Thin-Walled Structures*.

### **Chapter 3: Improvement of Local Buckling Behaviour of Steel Beams through bonding GFRP Plates**

All the numerical works were conducted by M. A. A. Siddique under close supervision of Dr. A. A. El Damatty. Drafts of Chapter 3 were written by M. A. A. Siddique and modifications were done under supervision of Dr. A. A. El Damatty. A version of this work co-authored by M. A. A. Siddique and A. A. El Damatty was submitted to the *Journal of Composite Structures*.

#### **Chapter 4: Seismic Performance of Moment Resisting Steel Frames Retrofitted at Beams' Flanges with GFRP Plates**

All the numerical works were conducted by M. A. A. Siddique under close supervision of Dr. A. A. El Damatty. Drafts of Chapter 4 were written by M. A. A. Siddique and modifications were done under supervision of Dr. A. A. El Damatty. A version of this work co-authored by M. A. A. Siddique and A. A. El Damatty will be submitted to the *Canadian Journal of Civil Engineering*.

#### **Chapter 5: Testing and Prediction of Shear and Peeling Behaviour of Bonded Steel/GFRP Joints under Cyclic Loading**

All the testing preparation and setup were undertaken by M. A. A. Siddique under supervision of Dr. A. A. El Damatty. Numerical studies were conducted by M. A. A. Siddique under supervision of Dr. A. A. El Damatty. Drafts of Chapter 5 were written by M. A. A. Siddique and modifications were done under supervision of Dr. A. A. El Damatty. A version of this work co-authored by M. A. A. Siddique and A. A. El Damatty will be submitted to the *International Journal of Adhesion and Adhesives*.

## **DEDICATION**

To my daughter Alveena

To my beloved parents

To my beloved wife

To my beloved uncle and aunt



## **ACKNOWLEDGEMENT**

The author would like to express his appreciation and sincere gratitude to his supervisor, Dr. Ashraf A. El Damatty for his advice, support, valuable guidance, and encouragement throughout the course of this research work. It has been a privilege to work under his supervision. It has also been such a great opportunity to gain from his engineering knowledge.

The author would like to acknowledge his colleagues for their help in the structures laboratory. A special thank to Mr. Wilbert Logan for his great help in conducting the experiments. The author would like also to acknowledge University Machine Services for their help in preparing the GFRP plate specimens and the test setup. Also, the author deeply appreciates the SHARCNET supercomputer facility, Canada.

The author wishes to express his sincere gratitude to his family and family-in-law for their continuous support and encouragement.

Finally, the author would like to dedicate this thesis to his daughter, parents and wonderful patient wife for their love, encouragement, great sacrifices, and fruitful care during the period of this study.

## TABLE OF CONTENTS

<b>CERTIFICATE OF EXAMINATION</b> .....	ii
<b>ABSTRACT</b> .....	iii
<b>CO-AUTHORSHIP</b> .....	v
<b>ACKNOWLEDGEMENT</b> .....	viii
<b>TABLE OF CONTENTS</b> .....	ix
<b>LIST OF TABLES</b> .....	xv
<b>LIST OF FIGURES</b> .....	xvi
<b>LIST OF APPENDICES</b> .....	xxiii
<b>LIST OF SYMBOLS</b> .....	xxv
<b>CHAPTER 1</b> .....	1
<b>INTRODUCTION</b> .....	1
1.1 General.....	1
1.2 Application of FRP in Steel Structures.....	3
1.3 Bonded Steel/FRP Joints in Retrofitting of Structures.....	5
1.4 Strength of Adhesively Bonded Steel/GFRP Joints under Cyclic Loading.....	7
1.5 Objectives of the Study.....	8
1.6 Scope of the Thesis.....	9
1.6.1 Enhancement of Buckling Capacity of Steel Plates Strengthened with GFRP Plates.....	9
1.6.2 Improvement of Local Buckling Behaviour of Steel Beams through Bonding GFRP Plates.....	10
1.6.3 Seismic Performance of Moment Resisting Steel Frames Retrofitted at Beams' Flanges with GFRP Plates.....	10
1.6.4 Testing and Prediction of Shear and Peeling Behaviour of Bonded Steel/GFRP Joints under Cyclic Loading.....	11
1.7 References.....	12

<b>CHAPTER 2</b> .....	17
<b>ENHANCEMENT OF BUCKLING CAPACITY OF STEEL PLATES STRENGTHENED WITH GFRP PLATES</b> .....	17
2.1 Introduction.....	17
2.2 Finite Element Model and Bond Behaviour.....	20
2.2.1 Adhesive Bond Model.....	21
2.2.2 Boundary Conditions and Assumed Geometric Imperfection Shape.....	24
2.2.3 Validation of Finite Element Model.....	26
2.2.3.1 Analysis of Type I Plates.....	27
2.2.3.2 Analysis of Type II Plates.....	29
2.3 Effect of Addition of GFRP Plates on the Buckling Capacity of Retrofitted Steel Plates.....	30
2.3.1 Material Properties used in the Analyses.....	32
2.3.1.1 GFRP Plate Properties.....	32
2.3.1.2 Adhesive Properties.....	32
2.3.2 Description of Analyses of Retrofitted Plates.....	33
2.3.3 Failure Modes of Retrofitted Plates.....	36
2.3.4 Results of Elastic Buckling Analyses.....	37
2.3.4.1 (i) AI-E-C and (ii) AI-E-NC.....	37
2.3.4.2 (iii) BII-E-C and (iv) BII-E-NC.....	38
2.3.4.3 (v) CI-E-C and (vi) CI-E-NC.....	40
2.3.4.4 (vii) DII-E-C and (viii) DII-E-NC.....	41
2.3.4.5 (ix) EI-E-C.....	42
2.3.4.6 (x) EI-E-NC.....	46
2.3.4.7 (xi) FII-E-C and (xii) FII-E-NC.....	46
2.3.5 Results of Inelastic Buckling Analyses.....	47
2.3.5.1 (i) AI-IE-C and (ii) AI-IE-NC.....	47
2.3.5.2 (iii) BII-IE-C and (iv) BII-IE-NC.....	48
2.3.5.3 (v) CI-IE-C and (vi) CI-IE-NC.....	49
2.3.5.4 (vii) DII-IE-C and (viii) DII-IE-NC.....	51
2.3.5.5 (ix) EI-IE-C.....	51

2.3.5.6 (x) EI-IE-NC.....	53
2.3.5.7 (xi) FII-IE-C.....	53
2.3.5.8 (xii) FII-IE-NC.....	54
2.4 Conclusions.....	54
2.5 References.....	58
<b>CHAPTER 3.....</b>	<b>61</b>
<b>IMPROVEMENT OF LOCAL BUCKLING BEHAVIOUR OF STEEL BEAMS THROUGH BONDING GFRP PLATES.....</b>	<b>61</b>
3.1 Introduction.....	61
3.2 Finite Element Model.....	65
3.2.1 Interface Element Model.....	66
3.2.2 Assumed Initial Geometric Imperfection Shape of Beam.....	68
3.2.3 Assumed Residual Stresses Distribution of Section of Beams.....	70
3.2.4 Validation of Finite Element Model.....	71
3.3 Description of Analysis of Retrofitted Beams.....	74
3.3.1 Geometric Properties of Beams.....	74
3.3.2 GFRP and Adhesive Properties.....	76
3.3.3 Mesh Sensitivity Analysis of Beams.....	76
3.4 Effect of GFRP Plate Thickness on the Buckling Improvement Factors.....	77
3.4.1 Cantilever Beams with Free-end Loading (CF1).....	77
3.4.2 Simply Supported Beams with Center Point Loading (SS1).....	80
3.4.3 Simply Supported Beams with Two-Point Loading (SS2).....	80
3.5 Influence of Strain Hardening Behaviour of Steel on the Capacities of the Retrofitted Beams.....	82
3.5.1 CF1 Beams.....	83
3.5.2 SS1 Beams.....	84
3.5.3 SS2 Beams.....	84
3.6 Influence of Geometric Imperfections on the Capacities of Retrofitted Beams.....	85
3.6.1 CF1 Beams.....	86
3.6.2 SS2 Beams.....	88

3.7	Influence of Residual Stresses in Steel Section on the Capacities of Retrofitted Beams.....	89
3.8	Effect of Span Length of the Beams on the Improvement Factors.....	90
3.8.1	CF1 Beams.....	91
3.8.2	SS2 Beams.....	92
3.9	Conclusions.....	94
3.10	References.....	96
<b>CHAPTER 4.....</b>		<b>100</b>
<b>SEISMIC PERFORMANCE OF MOMENT RESISTING STEEL FRAMES RETROFITTED AT BEAMS' FLANGES WITH GFRP PLATES.....</b>		<b>100</b>
4.1	Introduction.....	100
4.2	Description of Steel Frames Used in the Study.....	103
4.2.1	Original Steel Frames.....	103
4.2.2	Generic 3-story Steel Frames.....	105
4.2.3	Retrofitted Steel Frames with GFRP Plates.....	106
4.2.3.1	3-story Frames.....	106
4.2.3.2	9-story Frames.....	107
4.2.3.3	Generic 3-story Frames.....	107
4.3	Moment-Rotation Relationships for Beams of the Frame.....	108
4.3.1	Finite Element Model.....	108
4.3.2	Determination of Moment (M)-Rotation ( $\theta$ ) Relationships of Beams.....	111
4.3.3	Idealization of Moment (M)-Rotation ( $\theta$ ) Relationships of Beams.....	113
4.3.4	Original 3-story and 9-story Frames.....	115
4.3.5	Generic 3-story Frames with Beams of $b/t = 25$ .....	117
4.3.6	Generic 3-story Frames with Beams of $b/t = 30$ .....	118
4.4	Nonlinear Static Pushover Analysis of Frames.....	119
4.4.1	Ground Motions.....	119
4.4.2	Distribution of Seismic Forces along the Height of the Frame.....	120
4.4.3	Effective Fundamental Period.....	122
4.4.4	Target Displacement.....	123

4.4.5	Parameters for Seismic Performance Assessment of Frames.....	124
4.4.6	Steps for NSP Analysis of Frames.....	126
4.5	Results of NSP Analysis of Original Frames.....	127
4.5.1	Results of NSP Analysis of Retrofitted 3-story Frames.....	131
4.5.2	Results of NSP Analysis of Retrofitted 9-story Frames.....	133
4.6	Results of NSP Analysis of Generic 3-Story Frames.....	134
4.6.1	Results of NSP Analysis of Retrofitted Generic Frames with $b/t = 25$ .....	135
4.6.2	Results of NSP Analysis of Retrofitted Generic Frames with $b/t = 30$ .....	137
4.7	Conclusions.....	138
4.8	References.....	140
<b>CHAPTER 5.....</b>		<b>145</b>
<b>TESTING AND PREDICTION OF SHEAR AND PEELING BEHAVIOUR OF BONDED STEEL/GFRP JOINTS UNDER CYCLIC LOADING.....</b>		<b>145</b>
5.1	Introduction.....	145
5.2	Experimental Program.....	147
5.2.1	Test Specimens.....	147
5.2.2	Specimen Preparation.....	149
5.2.3	Loading Procedure and Displacement Measurement.....	151
5.2.4	Classification of Failure Modes of Adhesives in a Bonded Joint.....	155
5.3	Results of Phase I Tests.....	155
5.4	Results of Phase II Tests.....	157
5.5	Effect of Bond Size on the Capacity of Steel/GFRP Joints.....	160
5.6	Analytical Prediction of the Shear Stiffness of the Adhesive.....	161
5.6.1	Prediction of Shear Stiffness of the Adhesive under Monotonic Loading...161	
5.6.2	Prediction of Shear Stiffness of the Adhesive under Cyclic Loading.....	165
5.7	Numerical Prediction of Peeling Stiffness of the Adhesive.....	170
5.8	Summary and Conclusions.....	177
5.9	References.....	179
<b>CHAPTER 6.....</b>		<b>182</b>

<b>CONCLUSIONS</b> .....	182
6.1 General .....	182
6.2 Summary and Conclusions.....	182
6.3 Recommendations for Future Research.....	184
<b>APPENDIX I</b> .....	186
<b>CURRICULUM VITAE</b> .....	202

## LIST OF TABLES

Table 2.1	Comparison of obtained elastic buckling capacities of steel plates with numerical values predicted by Bakker et al.[19].....	29
Table 2.2	Comparison of predicted values of critical buckling stress of steel plates with analytical values [18].....	30
Table 3.1	Comparison of predicted and observed values of maximum load capacity.....	72
Table 3.2	Properties of wide flange built-up sections used in the parametric studies.....	75
Table 4.1	Distribution of story level shear force for NSP analyses.....	121
Table 4.2	Parameters and coefficients used in the estimation of roof displacements of the frames.....	124
Table 5.1	Test results of bonded steel/GFRP shear lap joints.....	159
Table 5.2	Summary of test results and processing of shear lap monotonic tests.....	164
Table 5.3	Prediction of peeling stiffness of adhesive under monotonic loadings.....	176



## LIST OF FIGURES

Figure 2.1	Shell element coordinate system and nodal degrees of freedom [13].....	21
Figure 2.2	Linear spring system simulating the adhesive .....	22
Figure 2.3	Contact elements between steel and GFRP plates.....	23
Figure 2.4	Boundary conditions for the steel plates under compressive stress (a) Type I and (b) Type II.....	25
Figure 2.5	Comparison of obtained buckling capacities of steel plates with theoretical values for different aspect ratios.....	28
Figure 2.6	Comparison of obtained buckling capacities of steel plates with theoretical values for different slenderness ratios.....	28
Figure 2.7	A typical finite elements mesh for both the steel and GFRP plates.....	31
Figure 2.8	Variation of elastic buckling magnification factors of type I plates with aspect ratio.....	37
Figure 2.9	Variation of elastic buckling magnification factors of type II plates with aspect ratio.....	39
Figure 2.10	Variation of elastic buckling magnification factors of type I plates with slenderness ratio.....	40
Figure 2.11	Variation of elastic buckling magnification factors of type II plates with slenderness ratio.....	42
Figure 2.12	Elastic responses of type I imperfect C-plates retrofitted with 12.5	

	mm GFRP plate.....	43
Figure 2.13	Elastic responses of type I imperfect NC-plates retrofitted with 12.5 mm GFRP plate.....	43
Figure 2.14	Effect of geometric imperfection on type I plates retrofitted with 9.5 mm GFRP plate.....	45
Figure 2.15	Effect of geometric imperfection on type I plates retrofitted with 19.0 mm GFRP plate.....	45
Figure 2.16	Effect of geometric imperfection on type II plates retrofitted with 19.0 mm GFRP plate.....	47
Figure 2.17	Variation of inelastic buckling magnification factors of type I plates with aspect ratio.....	48
Figure 2.18	Variation of inelastic buckling magnification factors of type II plates with aspect ratio.....	49
Figure 2.19	Variation of inelastic buckling magnification factors of type I plates with slenderness ratio.....	50
Figure 2.20	Variation of inelastic buckling magnification factors of type II plates with slenderness ratio.....	50
Figure 2.21	Inelastic load-deflection responses of type I C-plates retrofitted with 9.5 mm GFRP for different imperfection amplitudes.....	52
Figure 2.22	Effect of geometric imperfection on type I C-plates.....	52
Figure 2.23	Effect of geometric imperfection on type II C-plates.....	54
Figure 3.1	Shell element coordinate system and nodal degrees of freedom [21]...	66
Figure 3.2	Interface elements between steel and GFRP plates used in the	

	model.....	68
Figure 3.3	Initial geometric imperfection shape of the beam used in the model....	69
Figure 3.4	Boundary conditions of the steel beam used in the model.....	69
Figure 3.5	Assumed residual stresses pattern of steel section used in the model...	70
Figure 3.6	Comparison of load-deflection responses of the bare steel beams.....	71
Figure 3.7	Comparison of predicted and measured load-deflection responses of the bare and retrofitted steel beams with GFRP.....	73
Figure 3.8	Load-deflection responses of cantilever retrofitted beam B1 ( $b_f/2t_f =$ 10).....	79
Figure 3.9	Load-deflection responses of cantilever retrofitted beam B25 ( $b_f/2t_f =$ 30).....	79
Figure 3.10	Load-deflection responses of simply supported retrofitted beam B1 with two-point loading.....	81
Figure 3.11	Load-deflection responses of simply supported retrofitted beam B25 with two-point loading.....	82
Figure 3.12	Variation of capacities of retrofitted CF1 beams with and without strain hardening of steel (a) load and (b) deflection.....	84
Figure 3.13	Variation of capacities of retrofitted SS2 beams with and without strain hardening of steel (a) load and (b) deflection.....	85
Figure 3.14	Influence of geometric imperfection on the capacities of CF1 beams B1 (a) load and (b) deflection.....	87
Figure 3.15	Influence of geometric imperfection on the capacities of CF1 beams B25 (a) load and (b) deflection.....	88

Figure 3.16	Influence of geometric imperfection on the capacities of SS2 beams B1 (a) load and (b) deflection.....	88
Figure 3.17	Influence of geometric imperfection on the capacities of SS2 beams B25 (a) load and (b) deflection.....	89
Figure 3.18	Influence of residual stresses of steel on the capacities of beams B25 (a) load and (b) deflection.....	90
Figure 3.19	Effect of span length on the Improvement factors of CF1 beams B1 (a) load and (b) deflection.....	91
Figure 3.20	Effect of span length on the Improvement factors of CF1 beams B25 (a) load and (b) deflection.....	92
Figure 3.21	Effect of span length on the Improvement factors of SS2 beams B1 (a) load and (b) deflection.....	93
Figure 3.22	Effect of span length on the Improvement factors of SS2 beams B25 (a) load and (b) deflection.....	94
Figure 4.1	Elevation of the original frames considered in the present study.....	105
Figure 4.2	Retrofitting schemes for the 3-story frame.....	106
Figure 4.3	A typical finite element mesh for a W-shaped cantilever beam.....	110
Figure 4.4	Derivation of the rotation capacity at the end of a girder of a frame....	112
Figure 4.5	Typical (a) P- $\Delta$ and (b) M- $\theta$ relationships of a beam.....	112
Figure 4.6	Generalized moment-rotation (M- $\theta$ ) relationship of steel elements.....	113
Figure 4.7	Actual and idealized moment-rotation (M- $\theta$ ) relationships of steel beams.....	115
Figure 4.8	Moment-rotation relationships of the top floor beams of the 3-story	

	frame retrofitted with GFRP plates.....	116
Figure 4.9	Moment-rotation relationships of the top floor beams of the generic 3-story frame having $b/t = 25$ .....	117
Figure 4.10	Moment-rotation relationships of the top floor beams of the generic 3-story frame having $b/t = 30$ .....	118
Figure 4.11	Elastic spectra corresponding to the set of ground motions under consideration [30] .....	120
Figure 4.12	Calculation of effective stiffness, $K_e$ [32].....	122
Figure 4.13	Description of overstrength and ductility factors for a structural response.....	126
Figure 4.14	Pushover curves for the 3- and 9-story original steel frames.....	128
Figure 4.15	Interstory drift indexes for the original steel frames (a) 3-story (b) 9-story.....	129
Figure 4.16	Capacity and idealized curves of original steel frames for the evaluation of seismic performance parameters (a) 3-story and (b) 9-story.....	130
Figure 4.17	Capacity curves for the 3-story retrofitted frames.....	131
Figure 4.18	Capacity improvement for the F3-B3-C frame retrofitted with 19.0 mm GFRP plates.....	132
Figure 4.19	Interstory drift indexes for the F3-B3-C frame with 19.0 mm GFRP plates.....	133
Figure 4.20	Capacity curves for the retrofitted 9-story frames.....	134
Figure 4.21	Capacity curves for the GF3-B3-C retrofitted frames with $b/t = 25$ .....	136

Figure 4.22	Interstory drift indexes for the GF3-B3-C frames with $b/t = 25$ .....	136
Figure 4.23	Capacity curves for the GF3-B3-C retrofitted frames with $b/t = 30$ .....	137
Figure 4.24	Interstory drift indexes for the GF3-B3-C frames with $b/t = 30$ .....	138
Figure 5.1	A photo of prepared test specimens (bonded size = 50 x 25 mm).....	150
Figure 5.2	Schematic of a shear lap test setup.....	152
Figure 5.3	A photo of the shear lap test setup.....	153
Figure 5.4	Loading protocol used in the cyclic tests.....	154
Figure 5.5	A photo of a mode of failure of the adhesive.....	156
Figure 5.6	Strength comparisons between the bonded joints with the adhesives of MA300 and AO420 in Phase I tests.....	157
Figure 5.7	Typical load-deflection response of a monotonic shear lap test.....	158
Figure 5.8	Typical load-deflection response of a cyclic shear lap test.....	160
Figure 5.9	A free body diagram of GFRP plate that bonded to steel elements.....	162
Figure 5.10	Distribution of axial displacements along the height of GFRP plate (C25-1).....	165
Figure 5.11	Variation of the shear stiffness of the adhesive under cyclic loading (bond size =76x51mm) (a) upward loading and (b) downward loading	166
Figure 5.12	Variation of the shear stiffness of the adhesive under cyclic loading (bond size =50x25mm) (a) upward loading and (b) downward loading	167
Figure 5.13	Effect of the amplitudes of cyclic loading on the shear stiffness of the adhesive (a) upward loading and (b) downward loading.....	169
Figure 5.14	Variation of average shear stress developed in the adhesive with different amplitudes of cyclic loading.....	169

Figure 5.15	Geometry and boundary conditions for the joint of a bonded shear lap test.....	171
Figure 5.16	Comparison of mid-surface axial displacements of GFRP plate along the height of the plate (a) 76 x 51 mm and (b) 50 x 25 mm.....	173
Figure 5.17	Typical load vs. out-of-plane displacement diagrams measured by tests and predicted by the model (C51-1).....	175
Figure 5.18	Effect of cyclic loading on the variation of peeling stiffness of the adhesive (a) upward loading and (b) downward loading.....	177

## LIST OF APPENDICES

<b>Appendix I</b> .....	186
Table 3.1 Predicted values of load and deflection of the retrofitted cantilever beams ( $b_f = 150$ mm and $t_f = 7.5$ mm) with free end loading.....	187
Table 3.2 Predicted values of load and deflection of the retrofitted cantilever beams ( $b_f = 150$ mm and $t_f = 5.0$ mm) with free end loading.....	188
Table 3.3 Predicted values of load and deflection of the retrofitted cantilever beams ( $b_f = 150$ mm and $t_f = 3.0$ mm) with free end loading.....	189
Table 3.4 Predicted values of load and deflection of the retrofitted cantilever beams ( $b_f = 300$ mm and $t_f = 7.5$ mm) with free end loading.....	190
Table 3.5 Predicted values of load and deflection of the retrofitted cantilever beams ( $b_f = 300$ mm and $t_f = 5.0$ mm) with free end loading.....	191
Table 3.6 Predicted values of load and deflection of the retrofitted simply supported beams ( $b_f = 150$ mm and $t_f = 7.5$ mm) with center point loading.....	192
Table 3.7 Predicted values of load and deflection of the retrofitted simply supported beams ( $b_f = 150$ mm and $t_f = 5.0$ mm) with center point loading.....	193
Table 3.8 Predicted values of load and deflection of the retrofitted simply supported beams ( $b_f = 150$ mm and $t_f = 3.0$ mm) with center point loading.....	194
Table 3.9 Predicted values of load and deflection of the retrofitted simply	



	supported beams ( $b_f = 300$ mm and $t_f = 7.5$ mm) with center point loading.....	195
Table 3.10	Predicted values of load and deflection of the retrofitted simply supported beams ( $b_f = 300$ mm and $t_f = 5.0$ mm) with center point loading.....	196
Table 3.11	Predicted values of load and deflection of the retrofitted simply supported beams ( $b_f = 150$ mm and $t_f = 7.5$ mm) with two-point loading..	197
Table 3.12	Predicted values of load and deflection of the retrofitted simply supported beams ( $b_f = 150$ mm and $t_f = 5.0$ mm) with two-point loading..	198
Table 3.13	Predicted values of load and deflection of the retrofitted simply supported beams ( $b_f = 150$ mm and $t_f = 3.0$ mm) with two-point loading..	199
Table 3.14	Predicted values of load and deflection of the retrofitted simply supported beams ( $b_f = 300$ mm and $t_f = 7.5$ mm) with two-point loading..	200
Table 3.15	Predicted values of load and deflection of the retrofitted simply supported beams ( $b_f = 300$ mm and $t_f = 5.0$ mm) with two-point loading..	201

## LIST OF SYMBOLS

<b>Symbol</b>	<b>Description</b>
$i, j$	Nodal points of a two noded spring
$r, s, t$	Curvilinear coordinates
$u, v, w$	Displacements along global $x, y, z$
$u_s, v_s, w_s$	Displacements of a steel element along global $x, y, z$
$u_f, v_f, w_f$	Displacements of a GFRP element along global $x, y, z$
$x, y, z$	Global Cartesian coordinates
$x', y', z'$	Local Cartesian coordinates
$a$	Length of a plate
$b$	Width of a plate
$b_f$	Flange width
$h$	Depth of beam
$t$	Thickness
$t_f$	Flange thickness
$w$	Thickness of the web of a beam
$w_0$	Initial geometric imperfection
$A$	Amplitude of geometric imperfection
$A_e$	Contact adhesive area
$C_{vi}$	Lateral load distribution factor
$E_s$	Modulus of elasticity of steel
$E_f$	Modulus of elasticity of GFRP

$F_{cr}$	Critical buckling load
$F_i$	Lateral force at any floor level $i$
$F_y$	Yield strength of steel
$K_e$	Effective stiffness
$K_i$	Initial stiffness
$K_p$	Peel stiffness of adhesive
$K_s$	Shear stiffness of adhesive
$N$	Number of cycles
$P_b$	Buckling capacity of a bare plate
$P_{imp}$	Load capacity of an imperfect beam
$P_{res}$	Load capacity of a beam with residual stresses
$P_{Ret}$	Buckling capacity of a retrofitted plate
$P_s$	Load acting in one sheet of GFRP
$P_0$	Load capacity of a perfect beam
$R$	Response modification factor
$S_a$	Spectral acceleration
$T_e$	Effective time period
$T_1$	Fundamental time period
$V_d$	Design base shear
$V_e$	Elastic base shear
$V_t$	Shear capacity at the target displacement
$V_y$	Shear capacity at the yield strength
$U$	Strain energy of the contact element

$\sigma_{cr}$	Critical buckling stress
$\sigma_{crp}$	Predicted buckling stress
$\sigma_p$	Peeling stress
$\sigma_s$	Shear stress
$\xi_b$	A buckling magnification factor
$\xi_{be}$	Elastic buckling magnification factor
$\xi_{bine}$	Inelastic buckling magnification factor
$\lambda$	A parameter
$\lambda_L$	Load amplitude ratio
$\nu_s$	Poisson's ratio of steel
$\nu_f$	Poisson's ratio of GFRP plate
$\mu$	Ductility factor
$\mu_L$	A load improvement factor
$\mu_\Delta$	A deflection improvement factor
$\Delta_0$	Deflection capacity of a perfect beam
$\Delta_{imp}$	Deflection capacity of an imperfect beam
$\Delta_{res}$	Deflection capacity of a beam with residual stresses
$\Delta_u$	Ultimate displacement
$\Delta_m$	Displacement at the maximum load
$\Delta_y$	Yield displacement
$\delta_t$	Target displacement
$\Omega_d$	Overstrength factor

## **CHAPTER 1**

### **INTRODUCTION**

#### **1.1 General**

Moment resisting steel frames are widely used in civil engineering infrastructure, especially in seismic regions. In practice, they are normally designed based on the strong-column/weak-beam concept. After the Northridge earthquake in 1994, more than 150 steel buildings were severely damaged, including hospitals and other healthcare facilities, government, civic and private offices, cultural and educational facilities, residential structures, as well as commercial and industrial buildings. Damage was found in new as well as in old steel buildings, and in both high-rise and low-rise structures [1]. The most common type of damage occurred at welded beam-column connections. Local buckling and yielding of the top and bottom flanges of the girders and buckling of the columns of the frames were also reported in some steel buildings [2]. More severe damage was observed in the Hyogoken-Nanbu (Kobe) earthquake in 1995, with 6,000 people confirmed dead, 26,000 people reported injured, and more than 108,000 buildings and homes damages beyond repair causing 300,000 people to be homeless immediately after the earthquake [3]. Out of a total of 3,406 damaged buildings, 1247 steel framed structures were reported to have some level of damage due to failures of beams, columns, beam-to-column connections, and column bases. A large number of steel moment resisting frames with failures at different locations were reported [4]. The failures shown in steel frames during this earthquake were somewhat different from the Northridge failures. Most of the fractures of the frames were shown in the lower flange of the beams,

and the beams exhibited clear signs of yielding as well as local buckling in many cases. New guidelines and modifications were implemented in the seismic design codes around the world after the Northridge and the Kobe earthquakes. These guidelines can reduce the possibility of damage of newly constructed structures. However, the instability caused by local buckling of the slender flange of steel beams is still a concern for existing built structures. Premature local buckling of the flange of a steel beam is a concern for the ductility and overall stability of a rigid frame. Tremblay et al. [4] pointed out the large vulnerability of old structures located in high seismic regions in Canada designed according to low level seismic provisions specified in old codes. Therefore, the beams of existing structures, which lack an adequate flange slenderness ratio, are prone to local buckling and require retrofitting. Structures which have been overstressed due to a significant increase in load demand can also benefit from retrofitting to improve the behaviour at service level.

The common practice for rehabilitation and/or strengthening of steel structures includes welding or bolting steel cover plates to existing members. However, these techniques involve the addition of bulky and heavy steel plates, which are difficult to apply and can be susceptible to corrosion and fatigue damages. Fiber reinforced polymer (FRP) composites have many advantages such as ease of application, high strength-to-weight ratio, and resistance to corrosion and environmental degradation. Therefore, FRP can be an effective option to rehabilitate damaged members and/or to strengthen existing steel members. The use of adhesively bonded glass FRP (GFRP) plates to retrofit steel plates can serve to control the local buckling in the members of steel frames. This may be achieved despite the low modulus of elasticity of GFRP compared to steel. GFRP plates

have relatively large thicknesses. As the buckling capacity of the plate is proportional to the square of its thickness, GFRP plates are expected to increase the buckling capacity of the steel sections without significantly increasing their strength capacity.

Review of research studies previously conducted on the use of FRP in steel structures is first provided in this chapter. A brief review of the application of heavy-duty adhesive in steel/FRP joints is then presented. Finally, the objectives and scope of the Thesis with a brief description of various chapters are illustrated.

## **1.2 Application of FRP in Steel Structures**

Fiber reinforced polymer (FRP) composites are widely used in rehabilitation and strengthening techniques in civil, aerospace, and marine structures. The scope of the application of advanced polymer composites in infrastructures is reported in the state-of-the-art review by Bakis et al. [5]. FRP has been extensively used in concrete structures to enhance the flexural and shear capacities of members [6-9]. In recent years, the use of FRP composites for strengthening metallic structures has become an attractive option. A state-of-the-art review on steel structures strengthened by FRP has been conducted by Zhao and Zhang [10]. They discussed the bond behaviour between steel surfaces and FRP, and possible failure modes in a carbon FRP (CFRP) bonded steel system. They also provided information about the retrofitting of tubular steel structures and the repair of cracked steel members with FRP composites. A number of studies have been conducted to enhance and/or repair flexural steel members with CFRP composites. Research studies are available in the literature on the use of CFRP in steel beams, steel-concrete composite

girder, and corrosion-damaged steel-concrete composite beams [11-15]. The enhancement in the load and deflection capacities of members is obtained due to the high strength and high elastic modulus of CFRP composites. The retrofitting is accomplished in such a way that the bonded CFRP and steel sections are subjected to tension and bending. Since CFRP composites have high strength and high modulus values, the addition of CFRP results in an enhancement in the load carrying capacity of the retrofitted members.

Although much work has been done on the application of CFRP composites on steel structures, glass FRP (GFRP) plates, which have a lower modulus and a larger thickness, are less utilized in strengthening applications. El Damatty et al. [16] studied the effectiveness of using GFRP plates bonded to steel beams to assess the increase in the flexural capacity of the beams. They conducted an experimental investigation on I-shaped steel beams strengthened with GFRP plates under a two-point simply supported loading system. A significant enhancement in the flexural capacity of the beams was observed in this application. They also performed a numerical study on a steel-concrete composite bridge rehabilitated with GFRP plates bonded to the bottom flange of its girder to assess the increase in the bridge capacity. They achieved a 25% increase in the truck weight-carrying capacity of the girder for such a GFRP retrofitted scheme without premature failure in the GFRP, adhesive or concrete [17].

FRP composites have been used in recent years to enhance the stability of steel members. High modulus CFRP was utilized to improve the buckling and post-buckling behaviour of steel members [18-21]. A pilot experimental study was conducted by Harries et al. [18] on both long and stub WT steel sections strengthened with CFRP to investigate the



enhancement in torsional buckling and web local buckling of the members. Both the axial load carrying capacity and bifurcation loads were shown to increase in such applications. High modulus CFRP composites have been shown to enhance the axial capacity of slender as well as thin steel hollow structural square and lipped channel columns [19-21]. Accord and Earls [22] conducted finite element analyses to study the effectiveness of using GFRP strips bonded to the compression flange of I-shaped steel cantilever members. Their study focused on the enhancement of the moment and rotation capacities of the steel beams through the addition of GFRP strips. They found that the addition of longitudinally oriented GFRP strips to the compression flange of I-shaped members increases the structural ductility of the members.

### **1.3 Bonded Steel/FRP Joints in Retrofitting of Structures**

The use of adhesive bonded joints has increased in recent years in the FRP retrofitting applications of structures. Bonding steel and FRP elements using a heavy-duty adhesive is preferable over conventional assembly methods such as bolting or welding [23-24]. The main advantages of the bonded joints include less sources of stress concentration and efficient load transfer in a large area of bonding compared to discrete bolted or welded joints. El Damatty and Abushagur [25] conducted an experimental investigation to determine the type of adhesive that can achieve the highest bond strength between a GFRP plate and a steel element. They found from the test results that a methacrylate MA420 achieved the highest load resistance with a superior performance. This type of adhesive has been also used by Chakrabarti and Mosallam [26] to assess the improvement in the beam-to-column joint of steel frames retrofitted with advanced polymer

composites.

Miller et al. [27] performed experimental and analytical studies on the use of adhesively bonded CFRP plates for the rehabilitation of steel bridge girders. Increases in stiffness of 10-37% were achieved using CFRP plates applied on the tension flange of corrosion-damaged bridge girders. They also applied tension to six 914-mm long steel specimens, reinforced with CFRP cover plates on both sides of the specimen to determine the rate of force transfer between the steel substrate and the CFRP plate. The middle 457 mm steel plate was bonded with 37 mm wide and 5.25 mm thick CFRP plates. They revealed that approximately 98% of the total force transfer occurs within the first 100 mm of the end of the cover plate. Therefore, the development length for the considered configuration of the CFRP plates was in the order of 100 mm. An experimental study was also conducted by Lenwari et al. [28] on steel beams strengthened with CFRP strips to evaluate the bond behaviour of the retrofitting system. A total of seven W100 x 17.2 steel beams of a span length of 1800 mm were strengthened with three different CFRP lengths and tested under four-point bending loading. The lengths of the considered plates were 500 mm, 650 mm, and 1200 mm, respectively. Their test results have shown that the debonding of the CFRP plate occurred for the beams with the shorter plate lengths of 500 mm and 650 mm. CFRP rupture was observed at the failure of the strengthened beams for the addition of 1200 mm plate.

Analytical studies were conducted on bonded joints to predict the strength and the distribution of stresses in the adhesive layer [29-32]. Due to the complex nature of the stresses, researchers have conducted finite element analyses to predict the bond stresses along the length and through the thickness of the adhesive layer. The major challenge

involved in the modeling is the appropriate representation of bonded adhesive medium between the steel and the GFRP plates. El Damatty and Abushagur [25] conducted an analytical study to quantify the shear and peeling stiffnesses of the adhesive as a continuous linear spring system. They incorporated the results of shear lap tests conducted on steel/GFRP joints into the analytical model to estimate the characteristics of the continuous spring system simulating both the shear and peeling stiffnesses of the adhesive.

#### **1.4 Strength of Adhesively Bonded Steel/GFRP Joints under Cyclic Loading**

Research has been conducted to assess the shear lap behaviour of bonded steel/FRP joints under monotonic loading. da Silva et al. [33] provided an extensive literature review on various types of analytical models for both single and double lap joints. From their literature review, it is shown that almost all the analytical models for adhesively bonded lap joints are two-dimensional. A detailed comparative study for various types of analytical models for bonded lap joints are also reported by da Silva et al. [34]. Pandey and Narasimhan [35] used a three-dimensional finite element analysis of bonded single lap joints considering material and geometric nonlinearities. They modeled the adhesive layer using 20 noded solid elements to predict the peel and shear stresses in the adhesive layer. Three-dimensional numerical studies were also conducted by Diaz et al. [36] on a single CFRP bonded lap joint for the evaluation of stresses and strains in the adhesive layer under monotonic loading. They also performed a comparative study on the computational cost of different types of elements and mesh sizes used to simulate the adhesive layer. They concluded that the use of shell elements in the adherends resulted in

a smaller computational cost without affecting the precision of the results.

Although many research studies have been conducted on FRP bonded steel lap joints under monotonic loading, the bond behaviour under cyclic loading has not been studied. Bonded joints can fail in cyclic debonding in which progressive separations of bonded elements can occur by the failure of the adhesive. The adhesive may be more prone to damage when the joints of structures are subjected to loading and reverse loading conditions. Hence, an accurate prediction of strength and stiffness of the bonded joints are needed in order to determine the stress distribution within the adhesive for the worst combination of load which may act on the structure. The reversing of load usually occurs when the structures are subjected to a seismic excitation. Therefore, the strength and stiffness of adhesively bonded joints need to be predicted accurately under cyclic loading to assess the actual performance of the retrofitted bonded steel/GFRP joints used in seismic prone areas.

### **1.5 Objectives of the Study**

The main objectives of the current research are summarized in the following points:

1. Develop an interface finite element between the steel and GFRP layers simulating the shear and peel behaviour of the adhesive and incorporate this element into an in-house developed finite element model.
2. Assess the enhancement of the buckling capacity of retrofitted steel plates using GFRP plates based on the actual stiffness properties of the adhesive obtained from previously conducted experiments.

3. Asses the improvement of the buckling capacity of retrofitted steel beams using different thicknesses of GFRP plates and study the effect of different slenderness ratios, plastic modulus, initial geometric imperfection, and residual stresses of steel sections on the improved behaviour of the retrofitted beams.
4. Assess the improvement in the overall capacity of moment resisting steel frames retrofitted at their beams' flanges with different thickness of GFRP plates.
5. Study experimentally the strength capacity of adhesively bonded steel/GFRP joints under cyclic loading and predict the shear and peel stiffness properties of the adhesive under such a loading.

## **1.6 Scope of the Thesis**

This thesis has been prepared in “Integrated-Article” format. In the present chapter, a review of the studies related to the application of FRP in retrofitting steel sections is presented. The objectives of the study are then provided. The following four chapters address the thesis objectives. Chapter 6 presents relevant conclusions of the study together with suggestions for further research work.

### **1.6.1 Enhancement of Buckling Capacity of Steel Plates Strengthened with GFRP Plates**

In Chapter 2, an interface element capable of simulating the shear and peel behaviour of the bonded adhesive medium between the steel and GFRP components is developed. This element is then incorporated into a previously developed in-house finite element model. In this numerical model, consistent shell elements are used to simulate the steel as well as

the GFRP plates. The failure modes in the adhesive and the GFRP plates, based on real strength values, as well as the instability of the entire system are considered. A buckling magnification factor relating the capacity of the retrofitted system to the capacity of the corresponding bare steel plate is evaluated. The study considers two types of boundary conditions as well as two types of in-plane compatibility between the steel and GFRP plates. The effect of geometric imperfection is also studied. Both elastic and inelastic stability analyses are considered in this investigation.

### **1.6.2 Improvement of Local Buckling Behaviour of Steel Beams through Bonding GFRP Plates**

In Chapter 3, the numerical model developed in Chapter 2 is extended to assess the load and deflection improvements of retrofitted steel beams using GFRP plates. The numerical model is validated using test results and numerical predictions available in the literature. Various failure modes, including GFRP rupture, adhesive failure, and local buckling of the flanges of beams are included in the model. The effects of geometric imperfections and residual stresses are also included. The model is then used to conduct a parametric study to assess the effect of bonding GFRP plates on enhancing the local buckling behaviour of wide flange steel beams.

### **1.6.3 Seismic Performance of Moment Resisting Steel Frames Retrofitted at Beams' Flanges with GFRP Plates**

In Chapter 4, an investigation is conducted to assess the effectiveness of using GFRP plates to improve the seismic performance of moment resisting steel frames. The flexural

stiffness of steel beams retrofitted by GFRP plates is first determined using a nonlinear finite element model developed in-house. The moment-rotation characteristics of the retrofitted beams are then implemented into a frame model in order to carry out nonlinear static (pushover) analyses. A lateral load pattern based on the first mode shape of the frame is increased gradually till the failure of the frames occurs. The global pushover curves that represent base shear versus roof displacement for each frame is obtained from the analyses. The interstory drift index of the frame is calculated at the target displacement of each frame and is compared with FEMA regulations. The seismic performance level (overstrength and ductility factors) of the retrofitted frames is then compared with that of the bare frames.

#### **1.6.4 Testing and Prediction of Shear and Peeling Behaviour of Bonded Steel/GFRP Joints under Cyclic Loading**

The main objective of Chapter 5 is to assess the strength and stiffness properties of bonded joints under cyclic loading. An experimental investigation is carried out on bonded steel/GFRP joints under both monotonic and cyclic loadings. The strength of the bonded joints under cyclic loading is studied in comparison to that under monotonic loading. The stiffness properties of the adhesive are predicted using analytical and numerical studies. The variations of the shear and peeling stiffness of the adhesive are assessed under different load amplitudes of cyclic loading. The stiffness values are also compared with those under monotonic loading.

## 1.7 References

- [1] Mahin, S. A., Lessons from damage to steel buildings during the Northridge earthquake, *Engineering Structures* 1998; 20(4-6): 261-270.
- [2] Youssef, N. F. G., Bonowitz, D., and Gross, J. L., A survey of steel moment-resisting frame buildings affected by the 1994 Northridge earthquake, Building and Fire Research Laboratory, National Institute of Standards and Technology, Report No. NISTIR 5625, 1995, Gaithersburg, MD.
- [3] Nakashima, M, Inoue, K, and Tada, M., Classification of damage to steel buildings observed in the 1995 Hyogoken-Nanbu earthquake, *Engineering Structures* 1998; 20(4-6): 271-278.
- [4] Tremblay, R., Bruneau, M., Nakashima, M., Prion, H. G. L., Filiatrault, A., and DeVall, R., Seismic design of steel buildings: lessons from the 1995 Hyogo-ken Nanbu earthquake, *Canadian Journal of Civil Engineering* 1996; 23: 727-756.
- [5] Bakis, C. E., Bank, L. C., Brown, V. L., Cosenza, E., Davalos, J. F., Lesko, J. J., Machida, A., Rizkalla, S. H., and Triantafillou, T. C., Fiber-Reinforced polymer composites for construction- State-of-the-Art review, *Journal of Composites for Construction*, ASCE 2002; 6(2): 73-87.
- [6] Saadatmanesh, H. and Ehsani, M. R., RC beams strengthened with GFRP plates. I: Experimental Study, *Journal of Structural Engineering*, ASCE 1991; 117(11): 3417-3433.
- [7] Saadatmanesh, H., Extending service life of concrete and masonry structures with fiber composites, *Construction and Building Materials* 1997; 11(5-6): 327-335.
- [8] Sheikh, S. A., DeRose, D., and Mardukhi, J., Retrofitting of concrete structures for



- shear and flexure with fiber-reinforced polymers, *ACI Structural Journal* 2002; 99(4): 451-459.
- [9] Tan, K. H. and Zhou, Y., Performance of FRP-strengthened beams subjected to elevated temperatures, *Journal of Composites for Construction*, ASCE 2011; 15(3): 304-311.
- [10] Zhao, X-L. and Zhang, L., State-of-the-art review on FRP strengthened steel structures, *Engineering Structures* 2007; 29(8): 1808-1823.
- [11] Sen, R., Liby, L., and Mullins, G., Strengthening steel bridge sections using CFRP laminates, *Composites Part B: Engineering* 2001; 32(4): 309-322.
- [12] Tavakkolizadeh, M. and Saadatmanesh, H., Strengthening of steel-concrete composite girders using carbon fiber reinforced polymer sheets, *Journal of Structural Engineering*, ASCE 2003; 129(1): 30-40.
- [13] Al-Saidy, H., Klaiber, F. W., and Wipf, T. J., Repair of steel composite beams with carbon fiber-reinforced polymer plates, *Journal of Composites for Construction*, ASCE 2004; 8(2):163-171.
- [14] Colombi, P. and Poggi, C., Strengthening of tensile steel members and bolted joints using adhesively bonded CFRP plates, *Construction and Building Materials* 2006; 20(1-2): 22-33.
- [15] Fam, A., MacDougall, C., and Shaat, A., Upgrading steel-concrete composite girders and repair of damaged steel beams using bonded CFRP laminates, *Journal of Thin-Walled Structures* 2009; 47(10): 1122-1135.
- [16] El Damatty, A., Abushagur, M., and Youssef, M. A., Experimental and analytical investigation of steel beams rehabilitated using GFRP sheets, *Steel and Composite*

- Structures 2003; 3(6): 421-438.
- [17] El Damatty, A., Abushagur, M., and Youssef, M. A., Rehabilitation of composite steel bridges using GFRP plates, *Applied Composite Materials* 2005; 12: 309-325.
- [18] Harries, K. A., Peck, A. J., and Abraham, E. J., Enhancing stability of structural steel sections using FRP, *Journal of Thin-Walled Structures* 2009; 47(10): 1092-1101.
- [19] Silverstre, N., Young, B., and Camotim, D., Non-linear behaviour and load-carrying capacity of CFRP-strengthened lipped channel steel columns, *Engineering Structures* 2008; 30(10): 2613-2630.
- [20] Shaat, A. and Fam, A., Slender steel columns strengthened using high-modulus CFRP plates for buckling control, *Journal of Composites for Construction, ASCE* 2009; 13(1): 2-12.
- [21] Bambach, M. R., Jama, H. H., and Elchalakani, M., Axial capacity and design of thin-walled SHS strengthened with CFRP, *Journal of Thin-Walled Structures* 2009; 47(10): 112-1121.
- [22] Accord, N. B. and Earls, C. J., Use of fiber-reinforced polymer composite elements to enhance structural steel member ductility, *Journal of Composites for Construction, ASCE* 2006; 10(4): 337-344.
- [23] Hentinen, M., Hilderbrand, M., and Visuri, M., Adhesively bonded joints between FRP sandwich and metal, *Research Notes 1862, VIT Manufacturing technology, Espoo, Finland* 1997.
- [24] Clifford, S. M., Manger, C. I. C., and Clyne, T. W., Characterisation of a glass-fibre reinforced vinylester to steel joint for use between a naval GRP superstructure and a

- steel hull, *Composite Structures* 2002; 57(1-4): 59-66.
- [25] El Damatty, A. and Abushagur, M., Testing and modeling of shear and peel behavior for bonded steel/FRP connections, *Journal of Thin-Walled Structures* 2003; 41(11): 987-1003.
- [26] Chakrabarti, P. R. and Mosallam, A. S., Performance of welded steel beam-to-column joints seismically retrofitted with polymer composites & steel stiffeners, *Fiber Composites in Infrastructure Conference, Tuscan, Arizona, USA ICCI-1998*, pp. 160 – 174.
- [27] Miller, T. C., Chajes, M. J., Mertz, D. R., and Hastings, J. N., Strengthening of a steel bridge girder using CFRP plates, *Journal of Bridge Engineering, ASCE* 2001; 6(6): 514-522.
- [28] Lenwari, A., Thepchatri, T., and Albrecht, P., Debonding strength of steel beams strengthened with CFRP plates, *Journal of Composites for Construction, ASCE* 2006; 10(1): 69-78.
- [29] Tong, L., Strength of adhesively bonded single-lap and lap-shear joints, *International Journal of Solids and Structures* 1998; 35(20): 2601-2616.
- [30] Her, S-C., Stress analysis of adhesively-bonded lap joints, *Composite Structures* 1999; 47: 673-678.
- [31] Luo, Q. and Tong, L., Linear and higher order displacement theories for adhesively bonded lap joints, *International Journal of Solids and Structures* 2004; 41: 6351-6381.
- [32] Luo, Q. and Tong, L., Analytical solutions for nonlinear analysis of composite single-lap adhesive joints, *International Journal of Adhesion and Adhesives* 2009;

29: 144-154.

- [33] da Silva, L. F. M., das Neves, P. J., Adams, R. D., and Spelt, J. K., Analytical models of adhesively bonded joints-Part I: Literature survey, *International Journal of Adhesion and Adhesives* 2009; 29(3): 319-330.
- [34] da Silva, L. F. M., das Neves, P. J., Adams, R. D., Wang, A., and Spelt, J. K., Analytical models of adhesively bonded joints-Part II: Comparative study, *International Journal of Adhesion and Adhesives* 2009; 29(3): 331-341.
- [35] Pandey, P. C. and Narasimhan, S., Three-dimensional nonlinear analysis of adhesively bonded joints considering viscoplasticity in adhesives, *Computers and Structures* 2001; 79: 769-783.
- [36] Diaz, J., Romera, L., Hernandez, S., and Baldomir, A., Benchmarking of three-dimensional finite element models of CFRP single-lap bonded joints, *International Journal of Adhesion and Adhesives* 2010; 30(3): 178-189.

**CHAPTER 2**  
**ENHANCEMENT OF BUCKLING CAPACITY OF STEEL PLATES**  
**STRENGTHENED WITH GFRP PLATES\***

**2.1 Introduction**

The use of fiber reinforced polymer (FRP) composite to repair and strengthening concrete and steel structures is continuously increasing. FRP composites are often applied on the top, bottom, and sides of concrete members for retrofitting and rehabilitation of deteriorated members [1-9]. Metallic structures may become structurally inadequate for different reasons such as deterioration of material or variation of the loads acting on the structures. The load carrying capacity might also be reduced due to fatigue and corrosion damage. The standard techniques of rehabilitation and/or strengthening of steel structures include welding or bolting steel cover plates to existing members. However, these techniques involve addition of bulky and heavy steel plates, which are difficult to apply and are susceptible to corrosion and fatigue. On the other hand, FRP composites have many advantages such as ease of application, high strength-to-weight ratio, and resistance to environmental degradation. Therefore, FRP can be an effective option to improve the behaviour of damaged steel members. Few research studies have been conducted on the application of FRP on metallic structures. Most of those studies have focused on the improvement of the flexural capacity of steel members. In most cases, carbon FRP (CFRP) sheets were applied on the tension flange of steel members to improve their capacities. A notable increase in the flexural capacity was observed due to addition of

---

\*A version of this chapter is prepared for publication in the *Journal of Thin-Walled Structures*.

CFRP sheets. Al-Saidy et al. [10] investigated the application of CFRP on corrosion damaged steel beams. In their study, steel beams were damaged intentionally on the tension face of the beams for corrosion simulation and were then repaired with CFRP plates. They observed a full recovery for the flexural strength of the original undamaged members with the application of the CFRP plates. Shaat and Fam [11] studied the behaviour of axially loaded short and long steel columns strengthened with CFRP sheets. They tested five slender hollow structural square (HSS) steel column specimens of a constant slenderness ratio of 68. Four of five specimens were strengthened by unidirectional CFRP sheets. The improvement of axial strength of the columns wrapped with both longitudinally and transversely oriented CFRP sheets varied between 13% and 23% and failure occurred due to overall buckling. The test results showed that transverse CFRP can help restrain outward directed local buckling of the HSS sections. However, for long columns, the failure was governed by initial imperfections and lateral torsional buckling, in which CFRP sheets had no contribution. Accord and Earls [12] performed a finite element study of I-shaped flexural members strengthened with glass fiber reinforced polymer (GFRP) sheets under non uniform moment applied along the span length. GFRP strips were applied longitudinally to the compression flange of cantilever beams, which were subjected to a concentrated vertical end load. The concentrated force was applied at the free end of the cantilever at the lower flange-web junction. The primary interest of that study was to assess the local buckling capacity in the plastic hinge region of the beam and the use of GFRP to prevent this buckling mode. The results obtained from the study indicated that the addition of longitudinally oriented GFRP strips to the compression face of I-shaped cantilever beams increased the local buckling

capacity during plastic hinge formations; thereby improving ultimate strength and structural ductility. The strengthened beams were observed to buckle under a lateral torsional buckling mode instead of a local buckling mode. In this study, the strength of the adhesive was assumed to be one-fourth that of the GFRP strips.

There are four possible failure modes in a GFRP bonded steel plate subjected to compressive forces. These are: (i) shear failure of adhesive, (ii) peeling failure of adhesive, (iii) GFRP rupture, and (iv) steel yielding and plastification. The actual improvement in the behaviour of retrofitted plates can only be obtained when real strengths of both the adhesive and GFRP are considered.

A major issue in the design of thin-walled steel structures is local instability due to buckling. The current study assesses the buckling capacity of steel plates retrofitted using GFRP plates. The modulus of elasticity of GFRP plates is approximately one order of magnitude smaller than that of steel. However, GFRP plates have relatively large thicknesses. As the buckling capacity of the plate is proportional to the square of its thickness, the GFRP plates are expected to increase the buckling capacity of the steel plates. The current study is conducted numerically using a finite element model developed in-house that considers the real strength of the adhesive medium between steel and GFRP plates as well as the material and geometric non-linear effects. A special two dimensional element simulating the shear and peeling behaviour of the adhesive and compatible with a previously developed shell element is formulated in this study. The improvement in elastic and inelastic buckling capacities of steel plates strengthened with GFRP is assessed for different aspect ratios and different slenderness ratios of the steel plates. The effect of geometric imperfection is also included in the study. The analyses

are carried out for plates with two different end conditions related to the compatibility of displacements between the steel and GFRP plates.

## **2.2 Finite Element Model and Bond Behaviour**

A finite element model developed in-house is used to study the enhancement of the buckling capacity of thin steel plates bonded with GFRP plates. The numerical model is based on a consistent degenerated triangular subparametric shell element that was developed by Koziey and Mirza [13] and was then extended by El Damatty et al. [14] to include the effects of geometric and material nonlinearities. The nonlinear material model has the flexibility to incorporate either elastic perfectly plastic or bilinear strain hardening behavior for steel. The plastic model is based on the von Mises yield criterion and its associated flow rule. The mid-surfaces of both the steel and GFRP plates are modelled using an assembly of consistent shell elements. This shell element is free from the shear-locking phenomenon observed in many isoparametric degenerated shell elements when used to model thin shell structures. This was achieved through employing a consistent formulation that involves a cubic interpolation for displacements and a quadratic interpolation for rotations. This triangular element consists of 13 nodes, as shown in Figure 2.1, of which 10 nodes are used to interpolate the displacements  $u$ ,  $v$ , and  $w$ , that act along the global axes  $x$ ,  $y$  and  $z$ , respectively. The rotational degrees of freedom  $\alpha$ ,  $\beta$ ,  $\phi$ , and  $\psi$  are associated with the corner and mid-side nodes, where rotations  $\alpha$  and  $\phi$  are about the local  $y'$  axis and rotations  $\beta$  and  $\psi$  are about the local  $x'$  axis, where  $y'$  and  $x'$  are located in a plane tangent to the mid-surface. The rotations  $\alpha$  and  $\beta$  provide a linear variation of displacements through the thickness simulating bending deformations, while



$\varphi$  and  $\psi$  lead to a cubic variation of the through thickness displacements, simulating shear deformations.

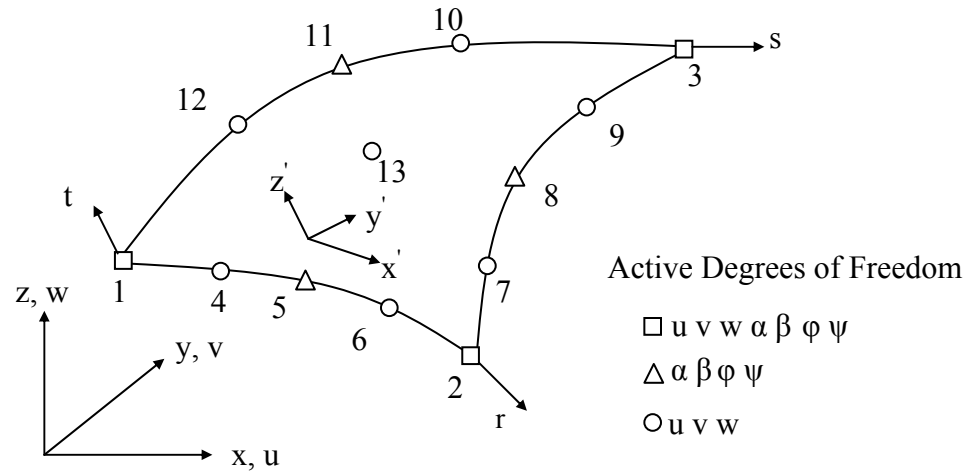


**Figure 2.1** Shell element coordinate system and nodal degrees of freedom [13].

### 2.2.1 Adhesive Bond Model

The major challenge in the proposed retrofitting technique relies in the connection between the steel and GFRP plates. In this application, the use of a heavy-duty adhesive to bond the two materials would be preferred compared to the option of using bolts and clamps. This is because the use of adhesive does not result in stress concentrations. Among various heavy-duty adhesives, El Damatty and Abushagur [15] have shown that the best level of bond between steel and GFRP sheets can be achieved using a methacrylate adhesive system (MA420). Sen et al. [16] performed analytical studies to assess the adequacy of epoxy adhesive in bonding CFRP laminates to steel girders. The obtained results indicated that high peeling stresses could cause the failure of the epoxy at the end of the CFRP laminate. Miller et al. [17] also performed experimental and

analytical studies to quantify the transfer force between the steel/CFRP adherents and the epoxy adhesives. The study concluded that the length and termination position of the CFRP plate determine the transfer forces. Epoxy failure at the end of the CFRP laminate was also observed due to high peeling stresses. A large number of shear lap tests were conducted on GFRP bonded with steel by El Damatty and Abushagur [15]. Failure loads, displacements, and strains were recorded. In the same study, the shear and peel rigidity of the adhesive were simulated using continuous linear springs. The average values for those spring constants were determined in the study. A schematic presentation of the spring system is presented in Figure 2.2.

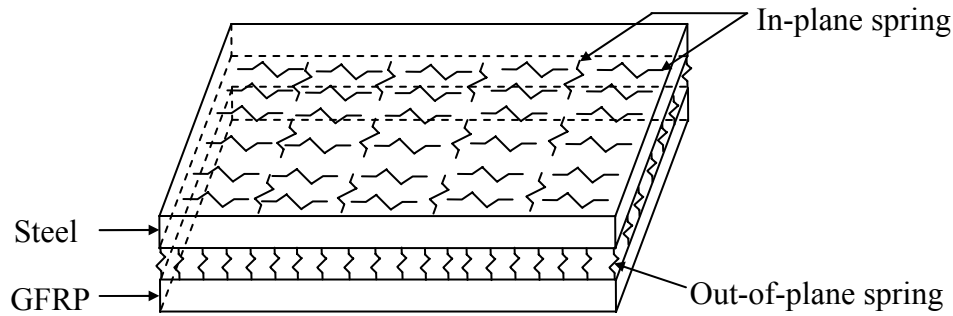


**Figure 2.2** Linear spring system simulating the adhesive.

A special 26-node contact element is derived in the present study to model the continuous springs simulating the shear and peeling behaviour of the adhesive. A sketch of the element is shown in Figure 2.3. The two-dimensional horizontal springs represent the shear behaviour, while the springs along the transverse direction represent the peeling behaviour. This element is compatible with the 13-node consistent shell element used to model the steel and GFRP plates.

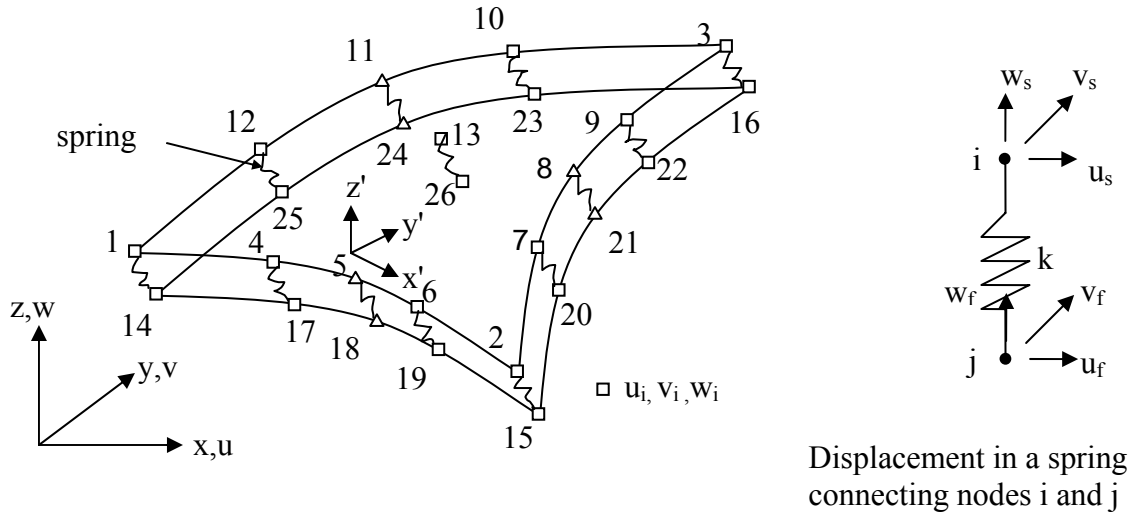


**Figure 2.3** Contact elements between steel and GFRP plates.

A linear elastic behaviour is considered for the springs. The strain energy,  $U$ , stored in the contact element that bond two layers of shell elements simulating steel and GFRP plates is given as:

$$U = \frac{1}{2} K_s \int_{A_e} (u_s - u_f)^2 dA_e + \frac{1}{2} K_s \int_{A_e} (v_s - v_f)^2 dA_e + \frac{1}{2} K_p \int_{A_e} (w_s - w_f)^2 dA_e \quad (2.1)$$

where,

$U$  = strain energy of the contact element between the steel and GFRP plates,

$K_s$  = stiffness of the shear spring per unit area,

$u_s, v_s$  = horizontal (in-plane) displacement components of the steel element in two perpendicular directions,

$u_f, v_f$  = horizontal (in-plane) displacement components of the GFRP element in two perpendicular directions,

$K_p$  = stiffness of the peeling spring per unit area,

$w_s$  = transverse displacement component of the steel element,

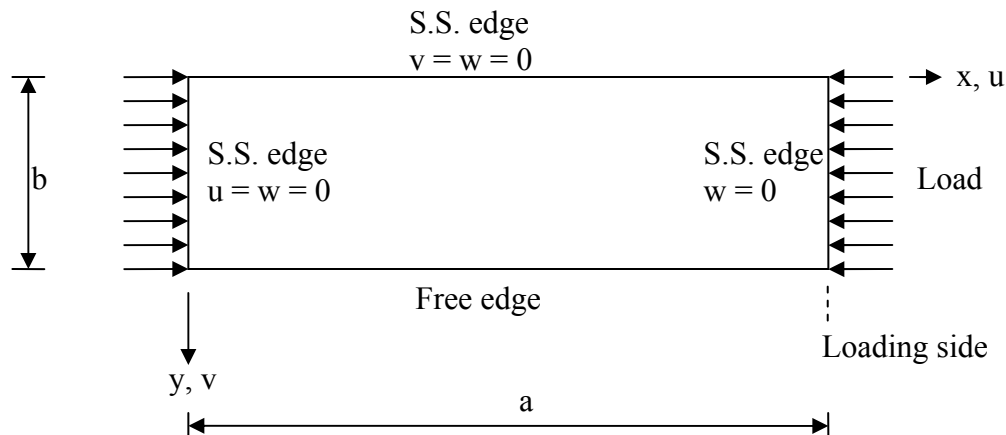
$w_f$  = transverse displacement component of the GFRP element,

$A_e$  = bonded area of the contact element.

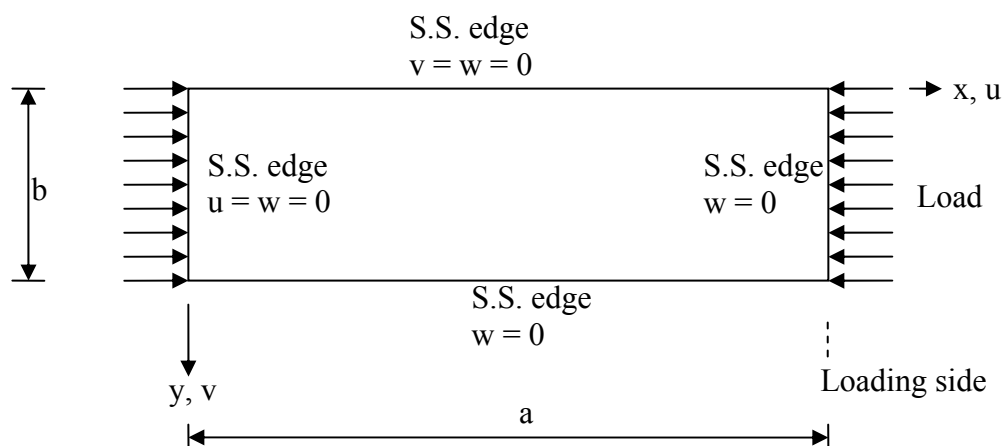
Accordingly, the contact element has 78 degrees of freedom; 39 coinciding with the steel shell element ( $u, v, w$  for each 13 nodes) and 39 coinciding with the GFRP shell element ( $u, v, w$  for each 13 nodes). The cubic shape function of the consistent shell element used to interpolate  $u_s, u_f, v_s, v_f, w_s$  and  $w_f$  are then substituted into Equation 2.1. The stiffness matrix of the contact element is obtained by differentiating “U” twice with respect to the element’s degrees of freedom.

### **2.2.2 Boundary Conditions and Assumed Geometric Imperfection Shape**

Two types of boundary conditions, as shown in Figure 2.4, are considered to assess the enhancement of buckling capacity of steel/GFRP bonded plates. Figure 2.4a shows the boundary conditions of Type I plate having three sides as simply supported and one side free. The displacement components  $u, v,$  and  $w$  are along the global  $x, y,$  and  $z$ -axes, respectively. This plate can represent one of those cases: leg of an angle, plate girder stiffener, and flanges of I, T or C-sections. Figure 2.4b shows Type II plate having simply supported boundary conditions along its four sides. Such a plate can simulate one of the following cases: flange of a rectangular hollow section, flange of a box section, flange of a cover plate, and a diaphragm plate. The restrained side boundary conditions of the GFRP plate in the retrofitted system are also the same as the steel plate as shown in the Figure 2.4. Loads are applied only on the steel plate of the retrofitted system.



(a) Plate simply supported at three sides and free at one side



(b) Plate simply supported at all sides.

Note: S.S.- Simply supported.  $u$ ,  $v$  and  $w$  denote the displacement in  $x$ ,  $y$ , and  $z$  axes, respectively

**Figure 2.4** Boundary conditions for the steel plates under compressive stress (a) Type I and (b) Type II

Geometric imperfections play a vital role in determining the buckling capacity of thin-walled steel structures. As such, the buckling capacity of steel/GFRP bonded plates is assessed in the study taking into account the effect of geometric imperfections. The

assumed imperfection shapes are selected to match the first buckling mode of the perfect plates.

For Type I and Type II plates, the assumed imperfection shapes are described by Equations (2.2) and (2.3), respectively [18].

$$w_0(x, y) = A \frac{y}{b} \sin \frac{\pi x}{a} \quad (2.2)$$

$$w_0(x, y) = A \sin \frac{\pi y}{b} \sin \frac{\pi x}{a} \quad (2.3)$$

where, A is the amplitude of initial geometric imperfection, a and b are the length and width of the plate, respectively, and  $w_0$  is the initial imperfection perpendicular to the plane of the plate.

It should be noted that the above imperfection shapes are compatible with the boundary conditions of the two plates' type.

### 2.2.3 Validation of Finite Element Model

Various examples involving buckling analysis of bare steel plates are considered in order to validate the finite element model. Both plates, Type I and Type II, described above, are considered in these examples. Also, the validation examples consider both thin and thick plates as well as elastic and inelastic buckling analyses. In all examples, the modulus of elasticity,  $E_s$ , is assumed as  $2 \times 10^5$  MPa, the yield strength is assumed to be 350 MPa and the Poisson's ratio is 0.3. For elastic buckling analyses, a high fictitious value of yield strength is assumed in order to eliminate the possibility of yielding of steel. A mesh sensitivity analysis is first performed. It is observed that a mesh with a total number of

288 elements having 36 rectangular divisions along the x-axis and 4 rectangular divisions along the y-axis provides an accurate prediction for the capacity of the plates. The uniaxial compressive force is applied on one of the short sides of the plates.

### **2.2.3.1 Analysis of Type I Plates**

Rectangular plates with aspect ratios ( $a/b$ ) of 3, 5, 10, and 20 are considered. For the four considered aspect ratios, the width ( $b$ ) and thickness ( $t$ ) are kept constant with values of 76 mm and 6.6 mm, respectively. The predicted buckling capacities of the plates obtained from the analyses are compared with the corresponding analytical values. The elastic and inelastic buckling capacities of the four considered plates are shown in Figure 2.5 together with the corresponding analytical solutions provided by Bulson [18]. As shown in the figure, the inelastic analysis considers both the case of zero strain hardening and the case of strain hardening with a tangent modulus of 1000 MPa. The figure shows an excellent agreement between the numerical and analytical solutions.

The validation proceeds by considering plates with a length,  $a = 1520$  mm and a thickness,  $t = 6.6$  mm. The widths of the plate,  $b$ , are varied between values 76 mm to 760 mm resulting in slenderness ratios,  $b/t$ , ranging between 11.5 to 115.2. These analyses cover the cases of thin plates where buckling is anticipated to occur elastically. The elastic buckling loads obtained from these analyses are plotted in Figure 2.6 together with the corresponding analytical prediction. An excellent agreement between the two sets of results is shown in this figure.

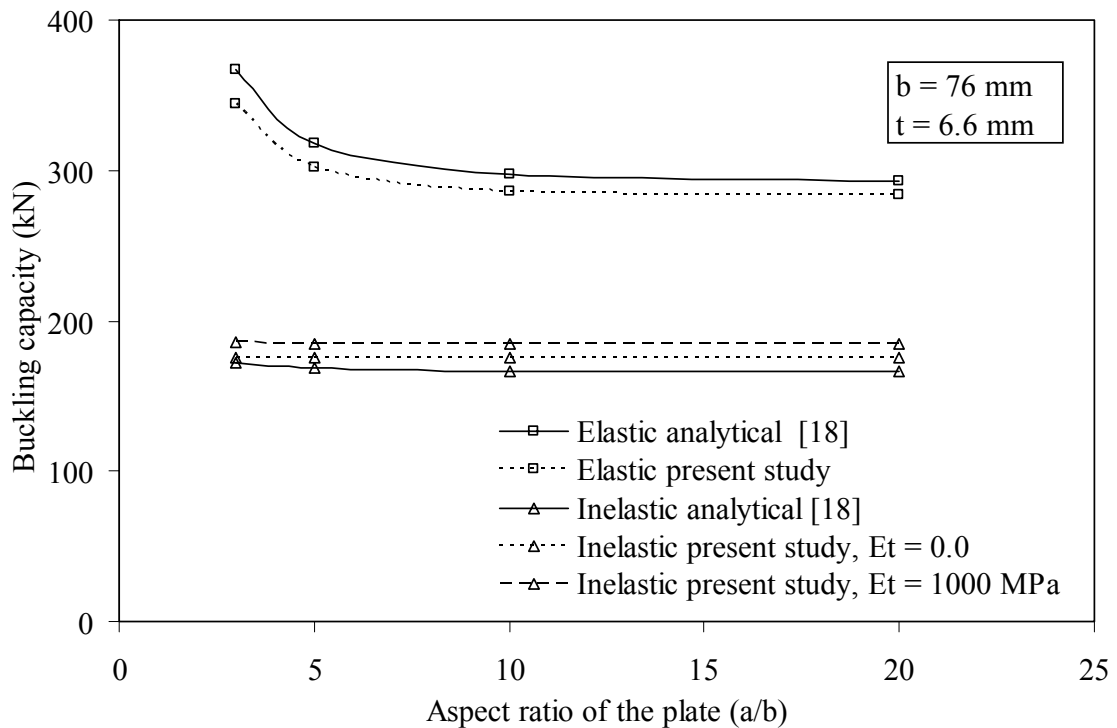


**Figure 2.5** Comparison of obtained buckling capacities of steel plates with theoretical values for different aspect ratios.

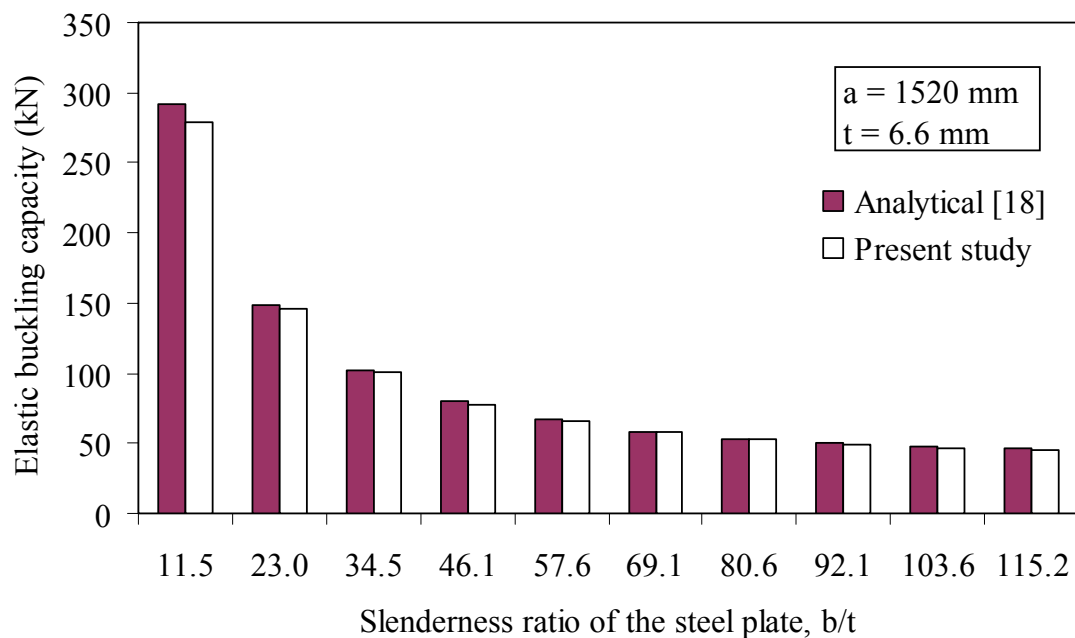


**Figure 2.6** Comparison of obtained buckling capacities of steel plates with theoretical values for different slenderness ratios.



### 2.2.3.2 Analysis of Type II Plates

Various square plates, with Type II boundary conditions and a thickness,  $t = 0.7$  mm, are considered for buckling analyses. The widths of the plate are varied from 35.2 mm to 99.6 mm resulting in slenderness ratios,  $b/t$ , varying 50.3 to 142.3. Buckling analyses of the same plates were conducted numerically by Bakker et al. [19]. A comparison between the elastic buckling loads predicted by the two sets of analyses is provided in Table 2.1. An excellent agreement is shown between the two sets of results.

**Table 2.1** Comparison of obtained elastic buckling capacities of steel plates with numerical values predicted by Bakker et al. [19]

b (mm)	b/t	$F_{cr}$ [19] (N)	$F_{cr}$ [Present study] (N)	$F_{cr}$ [Present study]/ $F_{cr}$ [19]
35.2	50.3	7392	7296	0.987
40.7	58.1	6410	6336	0.988
49.8	71.1	5229	5184	0.991
61.0	87.1	4270	4256	0.997
70.4	100.6	3696	3680	0.996
86.3	123.3	3020	3008	0.996
99.6	142.3	2614	2624	1.004

Buckling analyses are also done for Type II plates having moderate thickness values. The thickness of the plates considered in these analyses is 6.6 mm. The width of the plate is varied between 76 mm to 600 mm, resulting in slenderness ratios,  $b/t$ , that varies between 11.5 and 90.9. The critical buckling strength of the plate,  $\sigma_{cr}$ , is obtained analytically using the solution provided by Bulson [18]. Limit load of the steel plates at the onset of buckling is obtained from the finite element analyses. The critical buckling stress,  $\sigma_{crp}$  (= limit load/area), is calculated for each plate and is compared with an analytical solution

[18] as presented in Table 2.2. A good agreement between the results is shown in the table.

**Table 2.2** Comparison of predicted values of critical buckling stress of steel plates with analytical values [18]

Plate width, b (= a) (mm)	b/t	Analytical stress, $\sigma_{cr}$ (MPa) [18]	Predicted stress, $\sigma_{crp}$ (MPa)	$\sigma_{crp}/\sigma_{cr}$
76	11.5	5453	4881	0.89
150	22.7	1400	1346	0.96
225	34.1	622	610	0.98
300	45.4	350	346	0.99
375	56.8	224	223	1.00
450	68.2	155.5	154.6	1.00
600	90.9	87.5	87.4	1.00

### 2.3 Effect of Addition of GFRP Plates on the Buckling Capacity of Retrofitted Steel Plates

The geometric and material properties of a GFRP plate and adhesive system previously used in the experimental study conducted by El Damatty et al. [20] are employed in the current study. By considering the stiffness and strength properties of GFRP and adhesive that have been previously tested, the results of the numerical study presented in this investigation become more realistic.

The enhancement in the buckling capacity due to addition of GFRP plates is expressed using a buckling magnification factor,  $\xi_b = P_{Ret}/P_b$ ; where  $P_{Ret}$  is the buckling capacity of the retrofitted plate and  $P_b$  is the buckling capacity of the corresponding bare steel plate. The analyses are repeated considering four different values for the thickness of the GFRP

plate,  $t_{\text{GFRP}} = 9.5, 12.5, 15.5, \text{ and } 19.0 \text{ mm}$ , respectively. It is also assumed that the GFRP plate covers the entire area of the steel plate. Both elastic and inelastic buckling analyses are considered. For elastic and inelastic analyses, the buckling magnification parameters are denoted as  $\xi_{\text{be}}$  and  $\xi_{\text{bine}}$ , respectively. The results of analyses are used to assess the variations of  $\xi_{\text{be}}$  and  $\xi_{\text{bine}}$  with the following parameters:

- (a) aspect ratio of the steel plate,  $a/b$
- (b) slenderness ratio of the steel plate,  $b/t$
- and (c) amplitude of initial geometric imperfection,  $w_0$ .

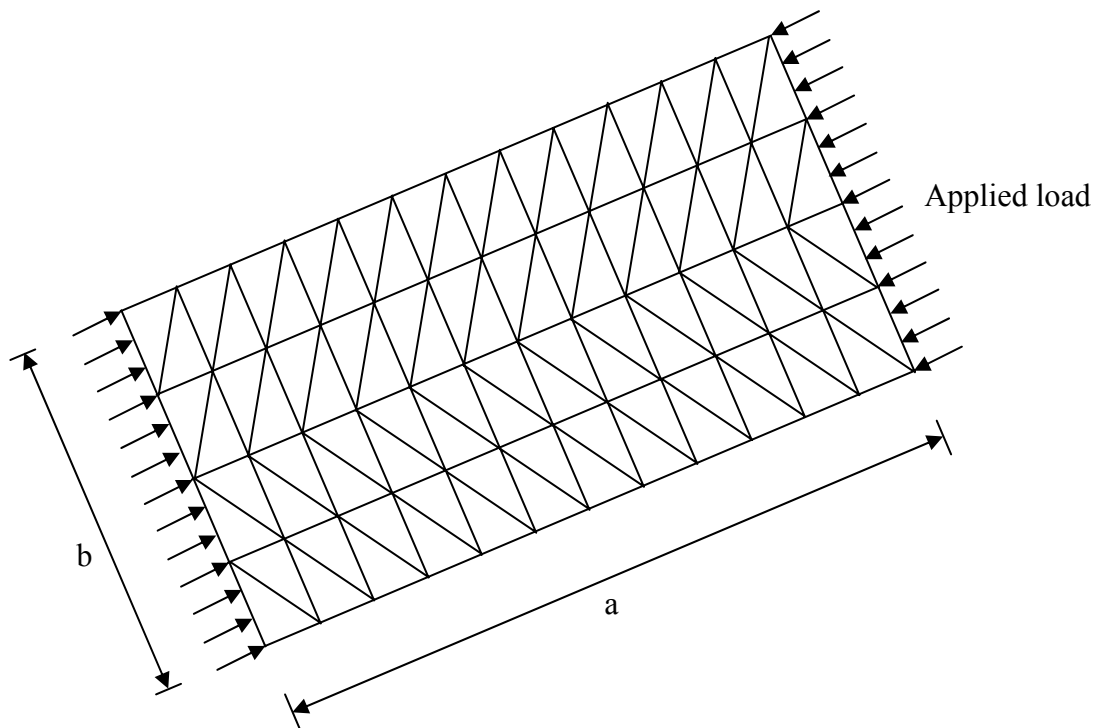


**Figure 2.7** A typical finite elements mesh for both the steel and GFRP plates.

A mesh sensitivity analysis is first conducted in order to determine the proper mesh that can capture accurately the buckling capacity of the retrofitted plates. The sensitivity

analysis predicts that a mesh with a total number of 576 elements provides an accurate prediction for the buckling capacity of the steel/GFRP plates. In this mesh, 288 elements are used to model each of the steel and GFRP plates. Each plate is meshed with 4 rectangular divisions perpendicular to the direction of loading and 36 rectangular divisions along to the axis of loading. A horizontal projection of a typical mesh showing the symbols used to present the dimensions of the plate together with the direction of application of loading is shown in Figure 2.7.

### **2.3.1 Material Properties used in the Analyses**

#### **2.3.1.1 GFRP Plate Properties**

The considered GFRP plates are manufactured using the pultrusion process and consist of uni-directional layers. They have the following mechanical properties; as provided by the manufacturer.

(i) Flexural stress = 206.8 MPa

(ii) Flexural modulus = 13,800 MPa

(iii) Poisson's ratio = 0.31

The GFRP plates behave linearly up to their ultimate strength. The fibers of the uni-directional layer are parallel to the direction of loading.

#### **2.3.1.2 Adhesive Properties**

A methacrylate adhesive is used with a thickness of 0.79 mm. Based on the tests conducted by El Damatty and Abushagur [15], the average values for the spring constants simulating the shear and peeling stiffness of the adhesive are 21.79 N/mm<sup>3</sup> and 2.26

$\text{N/mm}^3$ , respectively. The allowable shear strength and peel strength of this adhesive are 15.5 MPa and 4.0 N/mm, respectively, based on the information provided by the manufacturer and confirmed through tests [15].

### **2.3.2 Description of Analyses of Retrofitted Plates**

Both Type I and Type II boundary conditions, as shown in Figure 2.4, are considered in this study. Two types of compatibility between the steel and GFRP plates at the loading edge are assumed. In the first case, full compatibility in axial displacement between the steel and GFRP plates at the loading edge is assumed. It is defined as “C” bonded plates. This type of compatibility may arise through clamping the bonded steel/GFRP plates at their edges. For the second case, no compatibility in axial displacement is assumed at the loading edges between the steel and GFRP plates. It is defined as “NC” bonded plates.

Elastic and inelastic buckling analyses are conducted considering various values for the aspect ratio ( $a/b$ ), slenderness ratio ( $b/t$ ), and initial geometric imperfection on both the C and NC bonded plates with different thickness of GFRP plates. The material properties of the GFRP plates and the adhesive used in all the analyses are provided in Section 2.3.1.

The modulus of elasticity,  $E_s$  and Poisson’s ratio,  $\nu_s$ , of the steel plate are  $2 \times 10^5$  MPa and 0.3, respectively. The GFRP plates are assumed to cover the entire area of the steel plates.

In each set of analysis, four different values of the thickness of the GFRP plate,  $t_{\text{GFRP}} = 9.5, 12.5, 15.5, \text{ and } 19.0$  mm, are considered.

Description of various sets of analysis conducted in the current study is provided below:

#### **(i) AI-E-C**

Elastic analysis is conducted on Type I plates with C-type end condition to assess the

variation of  $\xi_{be}$  with the aspect ratio,  $a/b$ . In this set, the width,  $b$  and thickness,  $t$ , of the steel plate are assumed fixed value of 76 mm and 6.6 mm, respectively. The length is varied between 228 mm and 1520 mm, resulting in a variation of the aspect ratio,  $a/b$ , between 3 and 20.

(ii) AI-E-NC

Same as AI-E-C with the NC-type of end condition.

(iii) BII-E-C

Same as AI-E-C but applied on Type II plates.

(iv) BII-E-NC

Same as AI-E-NC but applied on Type II plates.

(v) CI-E-C

This set involves elastic analyses conducted on Type I plates with C-type end condition to assess the variation of  $\xi_{be}$  with the slenderness ratio,  $b/t$ . In this set, the length of the plate,  $a = 1500$  mm and width,  $b = 150$  mm are kept constant, giving an aspect ratio,  $a/b = 10$ . The thickness of the steel plate,  $t$ , is varied between 3 mm to 15 mm, resulting in a variation of  $b/t$  between 10 and 50.

(vi) CI-E-NC

Same as CI-E-C with NC-type of end conditions.

(vii) DII-E-C

This set involves elastic analyses conducted on Type II plates with C-type end condition to assess the variation of  $\xi_{be}$  with the slenderness ratio,  $b/t$ . In this set, the length of the square plate is assumed 300 mm. The thickness of the steel plate,  $t$ , is varied between 3 mm to 15 mm, resulting in a variation of  $b/t$  between 20 and 100.

(viii) DII-E-NC

Same as DII-E-C with NC-type of end conditions.

(ix) EI-E-C

This set of analysis is conducted to assess the variation of the buckling magnification factor with the amplitude of geometric imperfection “A”. The values of “A” are taken as ratio of the thickness of the steel plate “t” and the following ratios are considered: 0.01t, 0.1t, 0.25t, 0.5t, 1.0t, 1.5t, and 2.0t. This set of analysis is applied on Type I plates with C-type end conditions. The plates have the following dimensions: a = 1520 mm, b = 76 mm, and t = 6.6 mm, giving an aspect ratio  $a/b = 20$ . The imperfection shape, expressed by Equation (2.2), is applied to both the steel and GFRP plates.

(x) EI-E-NC

Same as EI-E-C with NC-type of end conditions.

(xi) FII-E-C

This set is similar to EI-E-C but applied to type II-plates. Square plates with  $a = b = 300$  mm and a thickness,  $t = 6.6$  mm, resulting in a slenderness ratio,  $b/t = 45.4$ , are considered in this set. The imperfection shape, expressed by Equation (2.3), is applied to both the steel and GFRP plates.

(xii) FII-E-NC

Same as FII-E-C but with NC-type of end conditions.

Inelastic analyses:

The above 12-sets of elastic analyses are repeated by considering inelastic buckling. The same labeling used to describe the elastic analyses is employed with the exception of

replacing the middle label “E” with “IE” denoting inelastic analyses. The yield strength of steel,  $\sigma_y$ , is assumed to be 350 MPa in all these analyses.

### **2.3.3 Failure Modes of Retrofitted Plates**

The following four failure modes are considered in the buckling analyses:

#### - Buckling of the system

This is associated with a state of elastic or inelastic instability depending on the type of analysis. Since the analyses are conducted in a load controlled manner, a state of numerical divergence is observed when the buckling load (limit load) is reached.

#### - Shear failure of the adhesive

The shear stress,  $\sigma_s$ , at a certain location in the adhesive is calculated by multiplying the spring constant,  $K_s$ , by the relative displacement between the steel and the GFRP plates at this location, i.e.  $\sigma_s = K_s (u_s - u_f)$ . An adhesive failure is considered when the shear stress,  $\sigma_s$ , at any location of the adhesive reaches its ultimate value of 15.5 MPa.

#### - Peeling failure of the adhesive

The peeling stress,  $\sigma_p$ , at a certain location in the adhesive is calculated by multiplying the spring constant,  $K_p$ , by the relative displacement between the steel and the GFRP plate at this location, i.e.  $\sigma_p = K_p (w_s - w_f)$ . The peeling stresses are then integrated along the length of the plate and the resultant value is compared to the ultimate strength which is equal to 4.0 N/mm.

#### - GFRP failure

The axial stresses in the GFRP plates are calculated at each load increment. Those are



compared to the ultimate strength of the GFRP, which is equal to 206.8 MPa. Failure is assumed when the axial stress at any location of the GFRP plate exceeds this strength value.

### 2.3.4 Results of Elastic Buckling Analyses

#### 2.3.4.1 (i) AI-E-C and (ii) AI-E-NC

The variation of the buckling magnification factor,  $\xi_{be}$ , with the aspect ratio of the steel plate is presented in Figure 2.8. In view of the analyses and the plotted results, the following observation can be stated:

- No premature failure, either in the GFRP or the adhesive, is observed in any of the analyzed cases. Failure is shown to be governed by elastic buckling of the system in all cases.

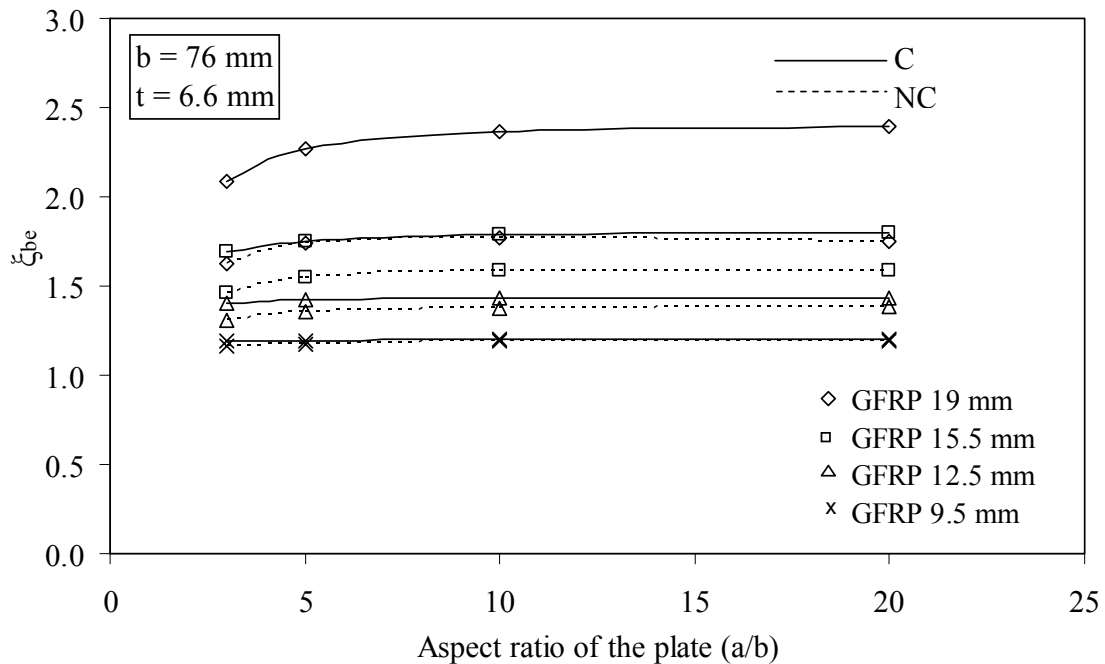


**Figure 2.8** Variation of elastic buckling magnification factors of type I plates with aspect ratio.

- The variation of the buckling magnification factor,  $\xi_{be}$ , with the aspect ratio,  $a/b$ , is very small. It appears only for the cases of small  $a/b$  values and 19.0 mm GFRP plate.
- The maximum buckling magnification factor reaches a value of 2.4 for  $a/b = 20$ , GFRP = 19.0 mm, and type C-end condition.
- The maximum value for the shear stresses that develop in the adhesive occurs for the case of  $a/b = 3$  and NC-end condition. These values are 6.6 MPa and 12.1 MPa for the 9.5 mm and 19.0 mm thick GFRP plates, respectively.
- Typically, the C-type end conditions lead to higher values of  $\xi_{be}$  compared to the NC-type end conditions. The thicker the GFRP plate, the larger is the difference between the C and NC cases. This is interpreted by the fact that in case of using thick GFRP plate, more stresses are transferred to the GFRP plate through the adhesive. In this case, the end conditions, affecting how the two plates are bonded, play an important role in defining the capacity of the system.

#### **2.3.4.2 (iii) BII-E-C and (iv) BII-E-NC**

The variation of  $\xi_{be}$  with  $a/b$  is presented in Figure 2.9 for both the C and NC cases. The results for the C-cases can be interpreted as follows:

- For  $a/b = 3$  and 5, premature GFRP rupture is predicted before reaching the elastic buckling capacity of the bare steel plate. As such, the attachment of the GFRP does not provide any enhancement in the elastic buckling capacity of these strong plates.
- For  $a/b = 10$ , the failure mode is still governed by the rupture of the GFRP plate.

However, a certain level of magnification is achieved at this aspect ratio depending on the thickness of the GFRP plate.

- For  $a/b = 15$  and  $20$ , the system fails due to elastic buckling and the magnification factors achieved in those two aspect ratios are almost equal.

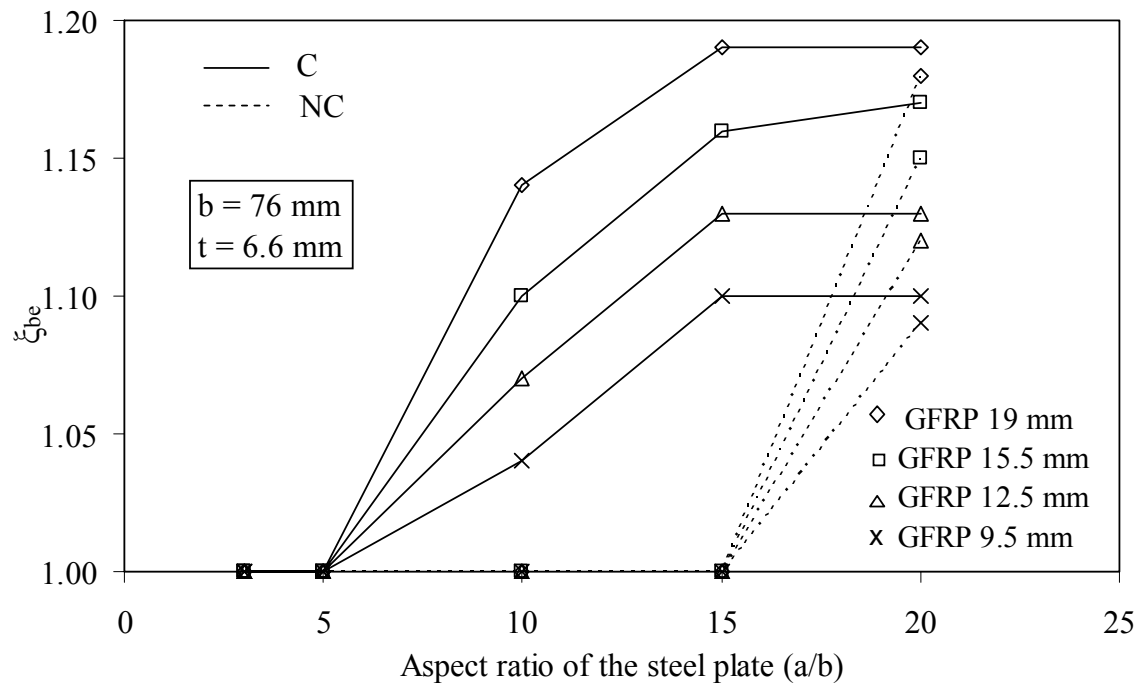


**Figure 2.9** Variation of elastic buckling magnification factors of type II plates with aspect ratio.

The results of the NC-type of end conditions can be interpreted by:

- For  $a/b = 3$  to  $15$ , premature shear failure of the adhesive is predicted. Once the adhesive fails, there is practically no bond between the GFRP and steel plates, and thereby, the GFRP does not contribute into the enhancement of the capacity of the retrofitted system.
- For  $a/b = 20$ , elastic buckling of the system is predicted for all GFRP plates. As

shown in the figure, the elastic buckling magnification factors for this aspect ratio are almost the same as the C-type plates.

### 2.3.4.3 (v) CI-E-C and (vi) CI-E-NC

The variations of  $\xi_{be}$  with the slenderness ratio of the Type I plates are presented in Figure 2.10. The figure presents the results for the plates that are relatively slender with  $b/t$  values of 10 and higher. The analyses of these slender plates reveal the following:

- The failure of all the cases reported in Figure 2.10 is governed by elastic buckling of the system, i.e. no premature failure in the adhesive or the GFRP plate is observed.

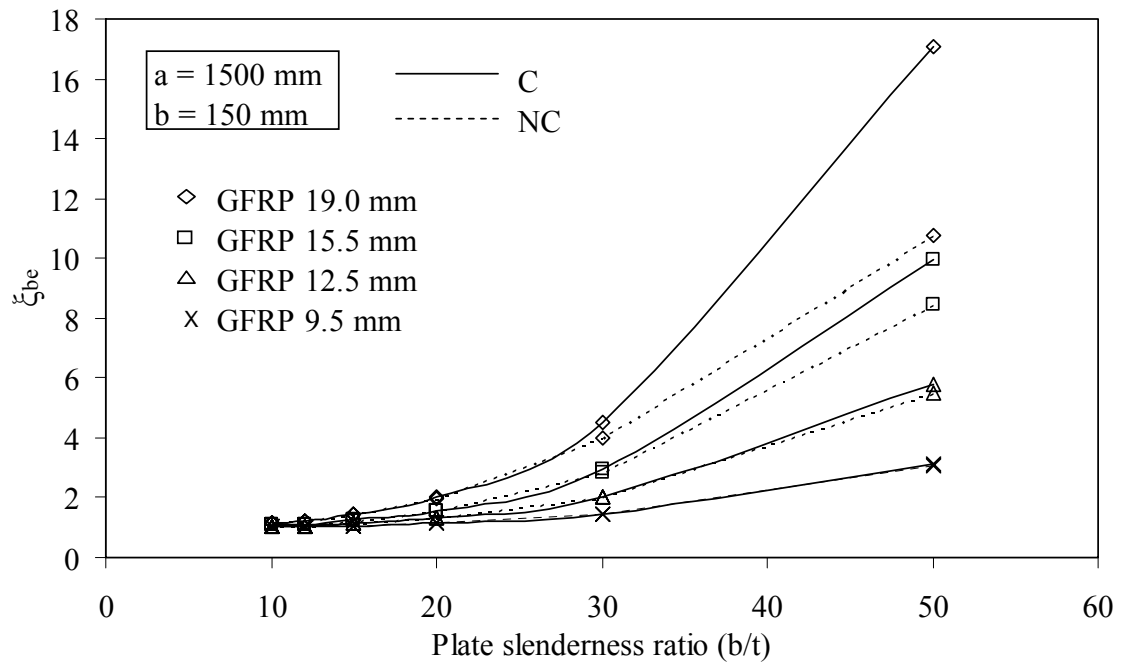


**Figure 2.10** Variation of elastic buckling magnification factors of type I plates with slenderness ratio.

- The elastic buckling magnification factor,  $\xi_{be}$ , increases as the slenderness ratios of the plates are increased.
- For  $b/t = 50$  and a GFRP plate thickness of 19.0 mm, the values of  $\xi_{be}$  reach 17.0 and 10.8 for the C and NC end conditions, respectively.
- The C-type of end conditions result in higher values for  $\xi_{be}$  compared to the NC-end conditions. Larger differences are observed for the thick GFRP plates. For the 9.5 mm GFRP, very minor difference is shown between the C and NC cases.

#### **2.3.4.4 (vii) DII-E-C and (viii) DII-E-NC**

The results of these analyses are presented in Figure 2.11. The analyses reveal the following:

- For the considered slenderness ratios with C-type of end conditions, the failure occurs due to elastic buckling of the systems, i.e. no premature failure either in adhesive or the GFRP plate is observed.
- For the NC-type end conditions, failure is also governed by elastic buckling with the exception of the cases of small slenderness ratio,  $b/t = 20$ , which are governed by adhesive shear failure.

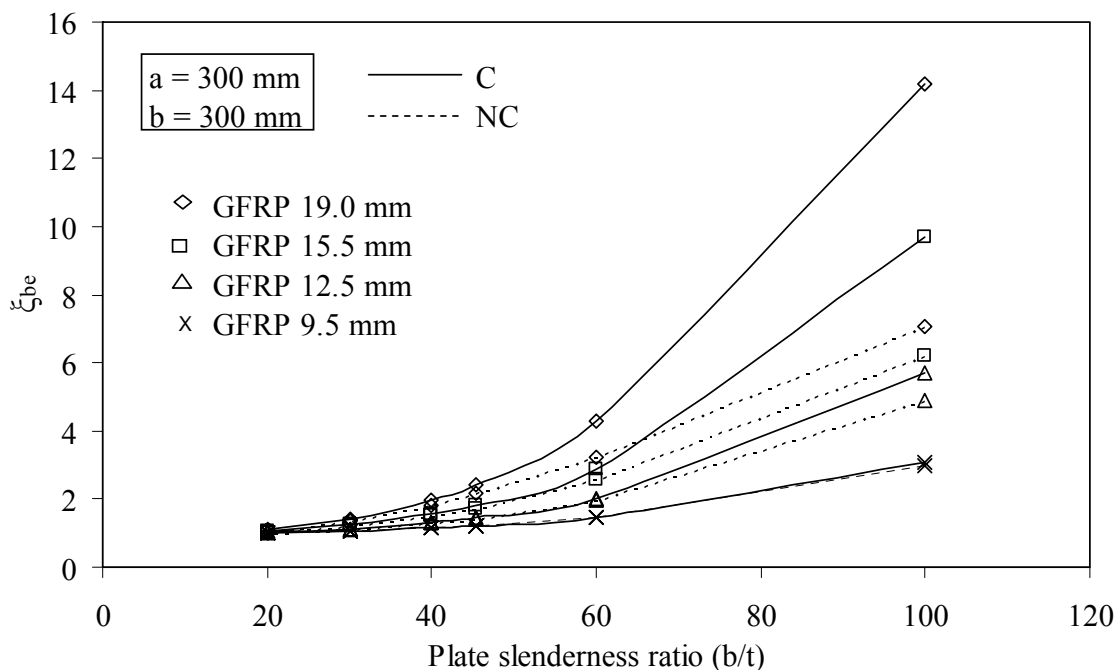


**Figure 2.11** Variation of elastic buckling magnification factors of type II plates with slenderness ratio.

#### 2.3.4.5 (ix) EI-E-C

This set of analysis is conducted to assess the effect of geometric imperfections. Figures 2.12 and 2.13 show the load-deflection curves obtained from various analyses. In these figures, the mid-point deflection of the plate “w” is normalized with respect to the plate thickness while the applied axial load “F” is normalized with respect to  $F_{cr}$ , where  $F_{cr}$  is the elastic buckling capacity of the bare perfect steel plate. The figures show plot for various level of initial imperfections. The interaction of the curve with the x-axis denotes the amplitude of initial geometric imperfection. The results of the analysis of the imperfect bare steels as well as the imperfect retrofitted plates with C-type and NC-type end conditions are presented in Figures 2.12 and 2.13, respectively.

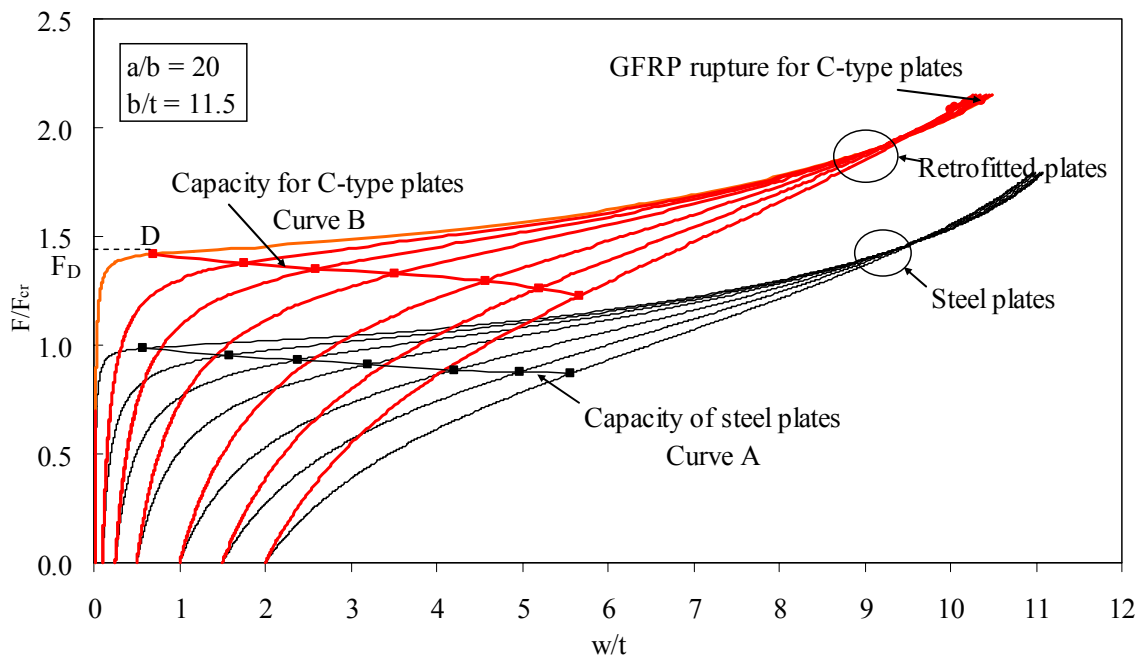


**Figure 2.12** Elastic responses of type I imperfect C-plates retrofitted with 12.5 mm GFRP plate.

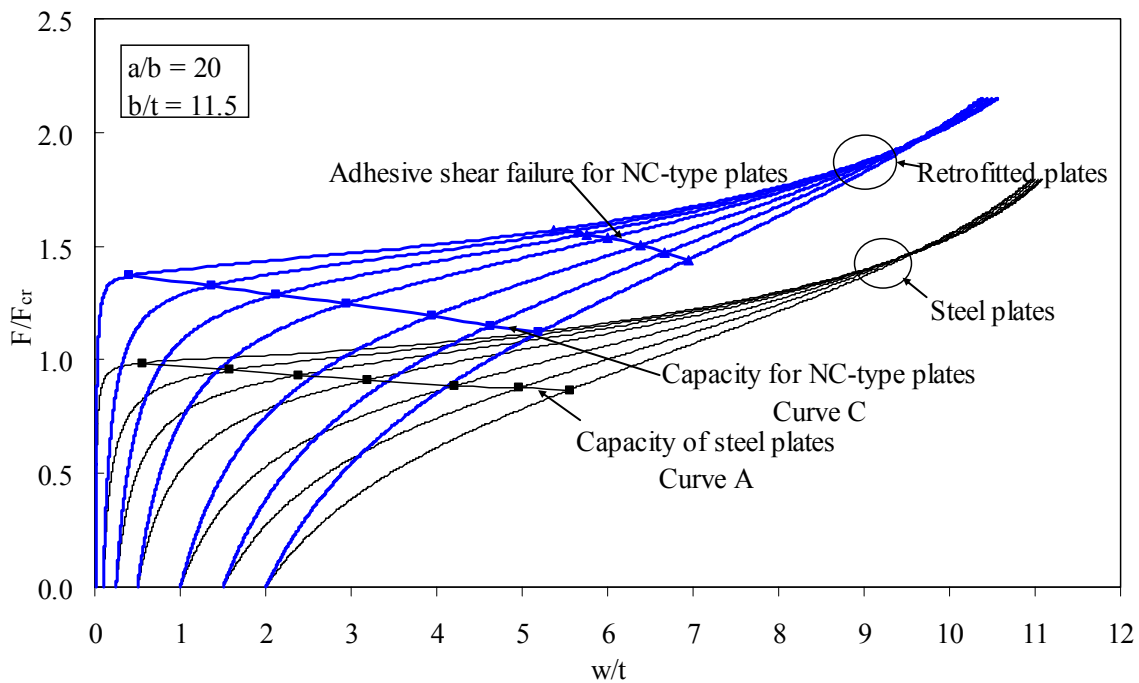


**Figure 2.13** Elastic responses of type I imperfect NC-plates retrofitted with 12.5 mm GFRP plate.

A hardening pattern is observed in all plots resulting from the analyses. This hardening behaviour is attributed to the membrane effect as reported by Bulson [18]. The limit loads for an imperfect steel plate was defined by Bulson [18] as the load at which the maximum strain  $\epsilon_{\max im}$  reaches the maximum strain of the corresponding perfect steel plate  $\epsilon_{\max per}$  occurring at the onset of buckling. This approach is used in the current study. In Figure 2.12, the normalized values of the limit loads of the bare steel as well as the retrofitted plates with C-type of end conditions are provided by Curves “A” and “B”, respectively, for various levels of geometric imperfections. Similarly, the normalized values of the limit loads for the retrofitted plates with NC-type of end conditions are provided by Curve “C” as shown in Figure 2.13. For the retrofitted cases, the limit loads can be governed by reaching the maximum strength capacities either in the adhesive or the GFRP plate. For the C-end conditions, the GFRP rupture precedes the adhesive failure. As shown in Figure 2.12, the GFRP rupture occurs at load values that exceed significantly the loads governed by maximum strains. As such, loads “F” calculated based on Curve “B” given in Figure 2.12 represent the limit loads of the retrofitted system.

The intersection of Curve “B” with the load-deflection curves in Figure 2.12 provides the limit loads  $F_{im}$  of the retrofitted system for various imperfection levels. The point “D” shown in Figure 2.12 represents the limit load for the case of perfect plate. The corresponding capacity of the retrofitted perfect plate “ $F_D$ ” can be calculated.

A parameter  $\lambda = F_{im}/F_D$  can be calculated for various imperfection levels. Similar calculation can be done for the bare steel plates. The variation of  $\lambda$  with the normalized value for the initial imperfection ( $w_0/t$ ) is provided in Figure 2.14 for the case of 9.5



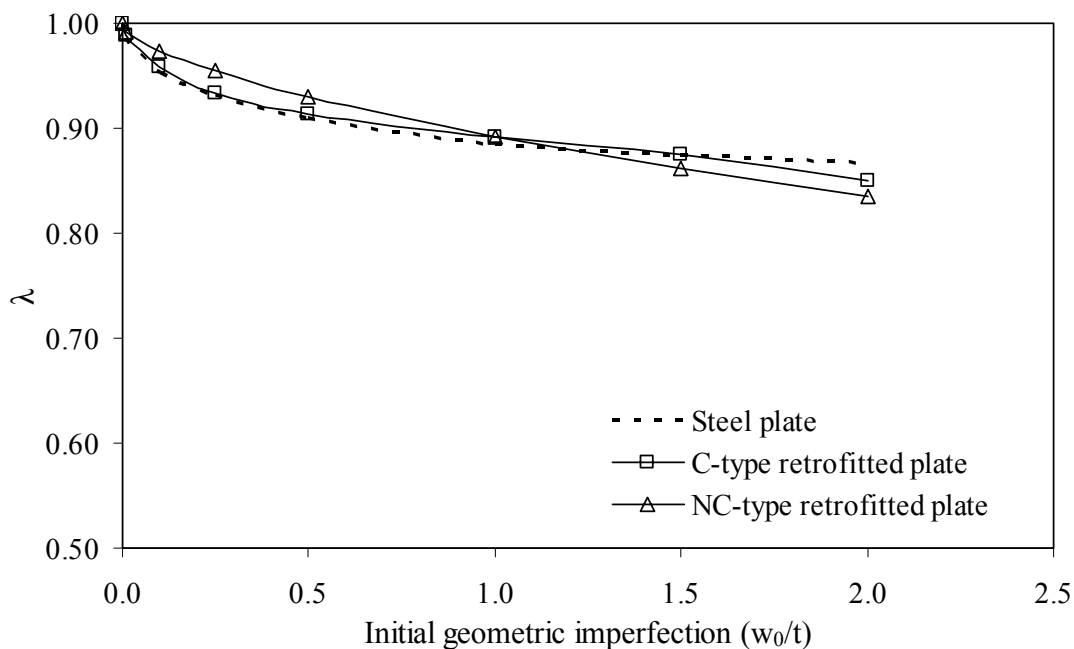


**Figure 2.14** Effect of geometric imperfection on type I plates retrofitted with 9.5 mm GFRP plate.

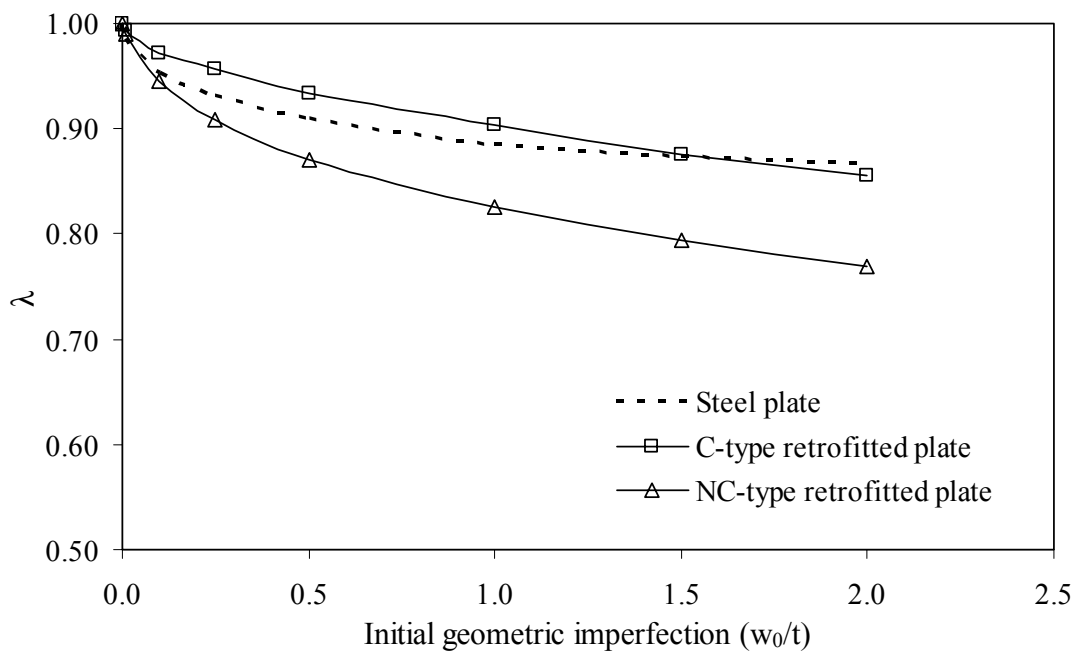


**Figure 2.15** Effect of geometric imperfection on type I plates retrofitted with 19.0 mm GFRP plate.

mm GFRP plate thickness. This figure can be used to estimate the reduction of the limit loads of the bare as well as the retrofitted steel plates due to presence of initial geometric imperfections. The figure shows that an imperfection value  $w_0/t = 0.5$  reduces the limit load at both the bare steel as well as the retrofitted plates to about 90% of their original capacities. Similar plots are provided in Figure 2.15 for the case of 19.0 mm GFRP plates.

#### **2.3.4.6 (x) EI-E-NC**

The same analysis procedure used in the previously reported EI-E-C case is employed in this part of the study. The normalized load-deflection curve associated with various imperfection levels is provided in Figure 2.13. For the NC-case, the adhesive shear failure precedes the GFRP rupture. Similar to the previous analysis, the limit loads corresponding to the maximum strain of the perfect plates at the onset of buckling are calculated (Curve C in Figure 2.13). The parameter  $\lambda$  reflecting the reduction in limit loads due to the effect of the geometric imperfections is also calculated. Comparison between Figures 2.12 and 2.13 indicates that despite the fact that the load-deflection curves have the same patterns, the limit loads of the NC plates are less than those of the C-plates. Also, Figure 2.14 shows that for the 9.5 mm GFRP plates, the variations of  $\lambda$  for both the C and NC cases are almost similar. However, as shown in Figure 2.15,  $\lambda$  has a smaller value for the NC case when a 19.0 mm GFRP plate is used.

#### **2.3.4.7 (xi) FII-E-C and (xii) FII-E-NC**

The variations of  $\lambda$  with  $w_0/t$  are presented for the two cases together with the bare steel plate in Figure 2.16 for a GFRP plate of 19.0 mm. An imperfection value of  $w_0/t = 0.5$

reduces the limit load for both the retrofitted C- and NC-plates to about 70% of their original capacities.

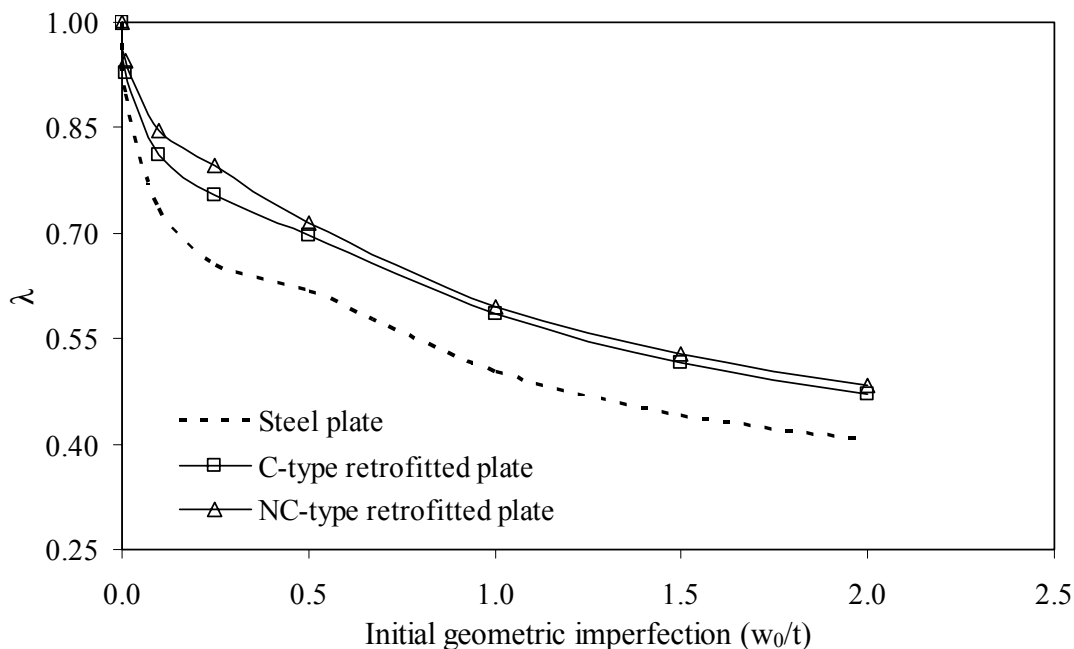


**Figure 2.16** Effect of geometric imperfection on type II plates retrofitted with 19.0 mm GFRP plate.

### 2.3.5 Results of Inelastic Buckling Analyses

#### 2.3.5.1 (i) AI-IE-C and (ii) AI-IE-NC

The inelastic buckling analysis of the bare steel plates reveals that for all the considered aspect ratios, yielding has preceded elastic buckling. As such, the stability of the bare steel plates is governed by inelastic buckling. For the C-type retrofitted plates, the GFRP plates reach their ultimate capacities before reaching a state of instability of the system. For such cases, the variation of inelastic buckling magnification factor,  $\xi_{\text{bine}}$ , with the aspect ratio  $a/b$  are provided in Figure 2.17. A significant improvement in the capacity of the retrofitted plates is shown for the C-type of end conditions with a maximum value of

$\xi_{b_{ine}}$  reaching 2.5 for the 19 mm GFRP plates. Figure 2.17 also indicates that no improvement in the behaviour is observed for the NC-type for all values of the GFRP plate thickness. This is mainly due to premature shear failure in the adhesive. Once the steel plates yield, their stiffnesses are reduced significantly and a major portion of any extra load is transferred to the GFRP plates through the adhesive. This leads to the observed premature adhesive failure.

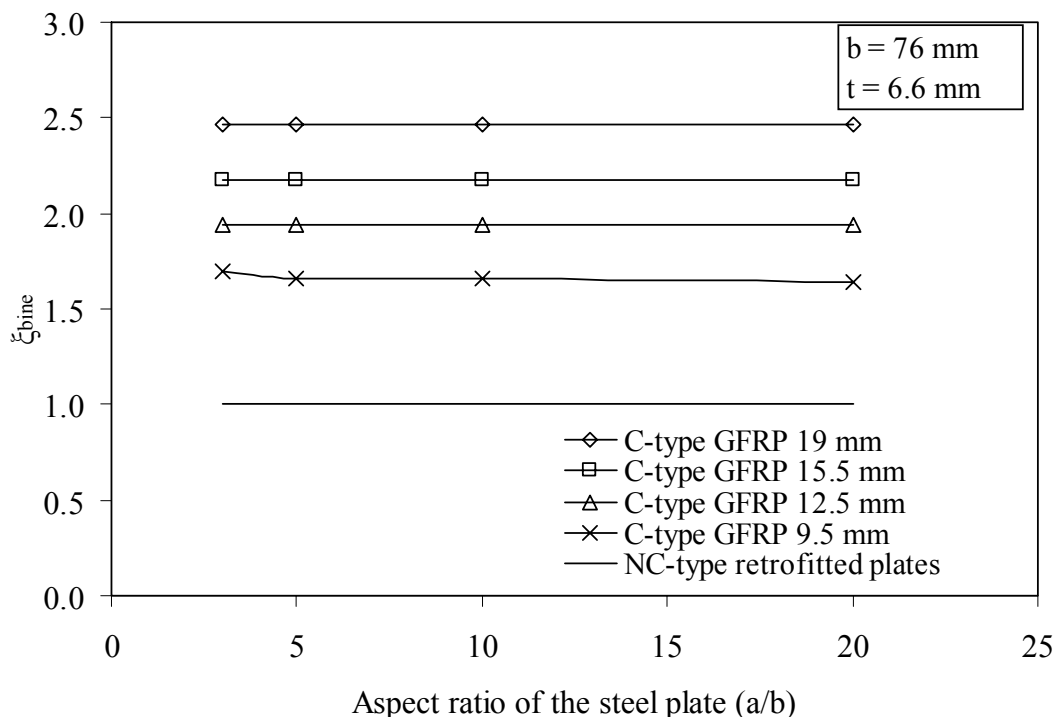


**Figure 2.17** Variation of inelastic buckling magnification factors of type I plates with aspect ratio.

### 2.3.5.2 (iii) BII-IE-C and (iv) BII-IE-NC

Similar to the analysis reported in the previous sub-section, the bare steel plates are shown to buckle inelastically. Also, no significant enhancement ( $\xi_{b_{ine}} = 1.1$ ) for the NC-type is observed due to premature shear failure of the adhesive.

The magnification factors observed in the C-type depend on the values of  $a/b$  and the thickness of the GFRP plates. Also, the mode of failure changes depending on the value of  $a/b$ . For  $a/b = 3$  and 5, failure is governed by rupture of GFRP plates. For those aspect ratios, the maximum value of  $\xi_{b\text{ine}} = 2.72$  for the 19.0 mm GFRP plate as shown in Figure 2.18. For  $a/b = 10$  and 20, failure is governed by inelastic buckling of the system.

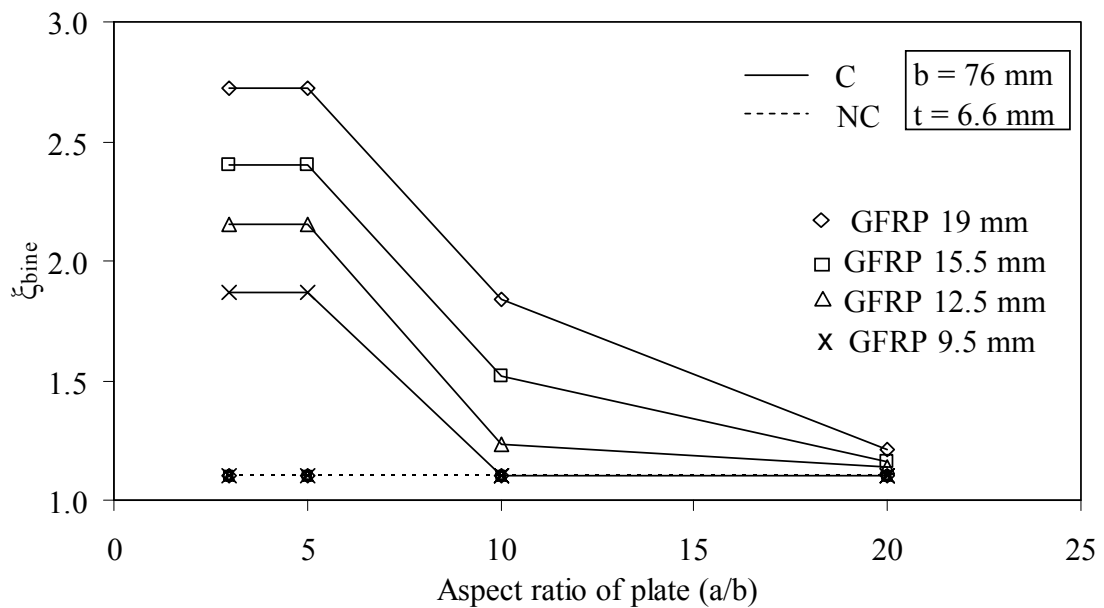


**Figure 2.18** Variation of inelastic buckling magnification factors of type II plates with aspect ratio.

### 2.3.5.3 (v) CI-IE-C and (vi) CI-IE-NC

The variation of  $\xi_{b\text{ine}}$  with  $b/t$  is given in Figure 2.19. Comparison between Figures 2.10 and 2.19 indicates that the plots provided in the two figures are almost identical. This is because, with the exception of  $b/t \leq 15$ , the failure of the C and NC plates is governed by elastic buckling. As such, the same observations stated in section 2.3.4.3 can be used to describe the behaviour of the analyses reported this section.

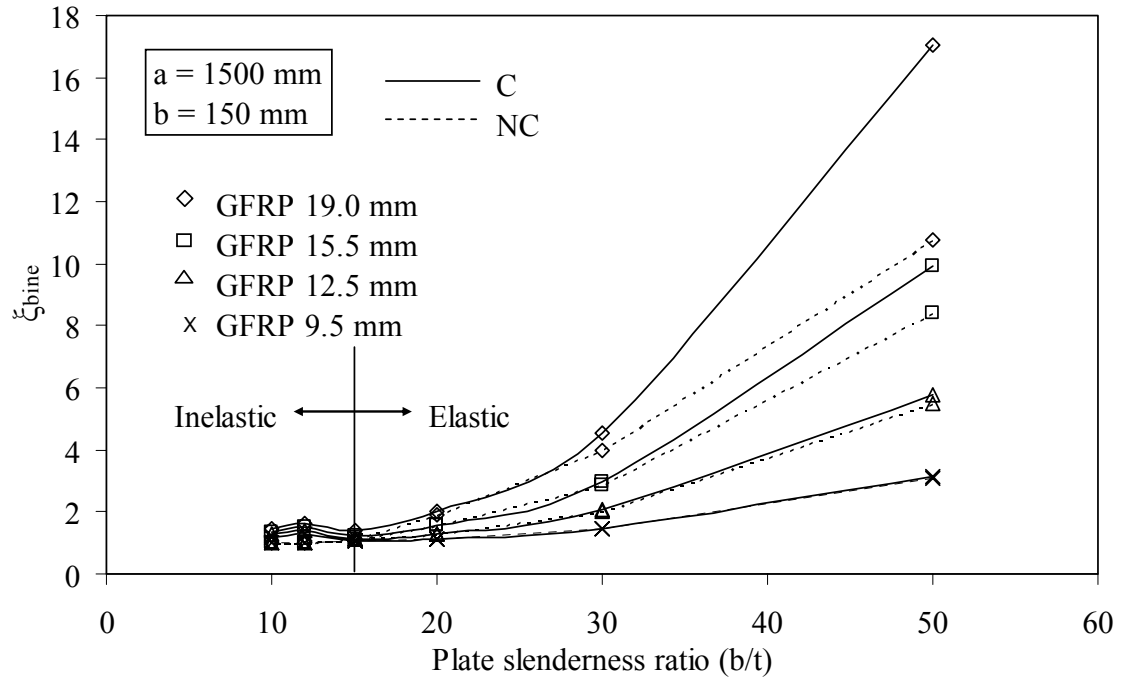


**Figure 2.19** Variation of inelastic buckling magnification factors of type I plates with slenderness ratio.

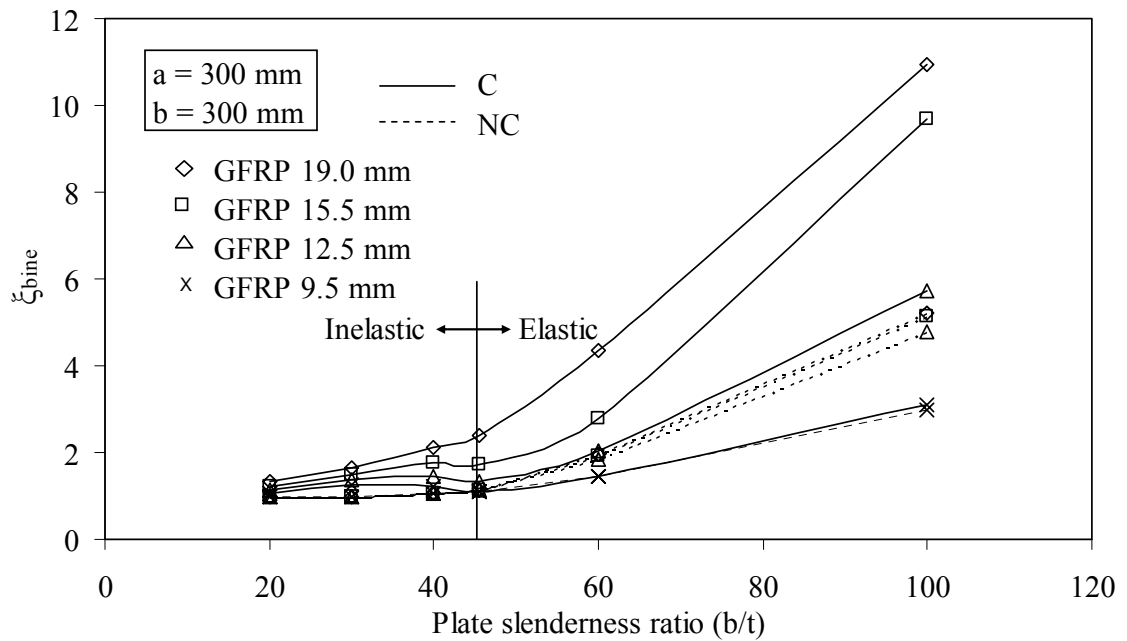


**Figure 2.20** Variation of inelastic buckling magnification factors of type II plates with slenderness ratio.

#### 2.3.5.4 (vii) DII-IE-C and (viii) DII-IE-NC

The variations of  $\xi_{\text{bine}}$  with b/t ratios of Type-II plates are presented in Figure 2.20 for both the C and NC end conditions. Again, comparison with Figure 2.11 indicates that the elastic and inelastic buckling analyses lead to very close results and almost similar trends.

#### 2.3.5.5 (ix) EI-IE-C

This set of inelastic analysis assesses the effect of geometric imperfections. The load-deflection curves associated with different imperfection amplitudes for the retrofitted plates with 9.5 mm GFRP are given in Figure 2.21. In this figure, the mid-point deflection of the plate “w” is normalized with respect to the plate thickness while the applied axial load “F” is normalized with respect to  $F_{\text{cr}}$ , where  $F_{\text{cr}}$  is the inelastic buckling capacity of the bare perfect steel plate. The failure of the bare and the retrofitted plates reported in Figure 2.21 is governed by inelastic buckling of the system. A comparison with the elastic buckling analysis of the imperfect plates can be made in view of Figure 2.12. Due to the loss of stiffness after yielding, no hardening behaviour is observed in the inelastic analyses.

Similar to the approach used in the elastic analysis, a parameter  $\lambda = F_{\text{im}}/F_{\text{D}}$  is calculated, where  $F_{\text{im}}$  is the limit load of the imperfect retrofitted plate and  $F_{\text{D}}$  is the limit load of the perfect retrofitted plates. The variation of  $\lambda$  with  $(w_0/t)$  is presented in Figure 2.22 for various GFRP plate thicknesses. As shown in the figure, the value  $\lambda$  reduces with the increase in the imperfection amplitude. It also depends on the thickness of the GFRP plate.

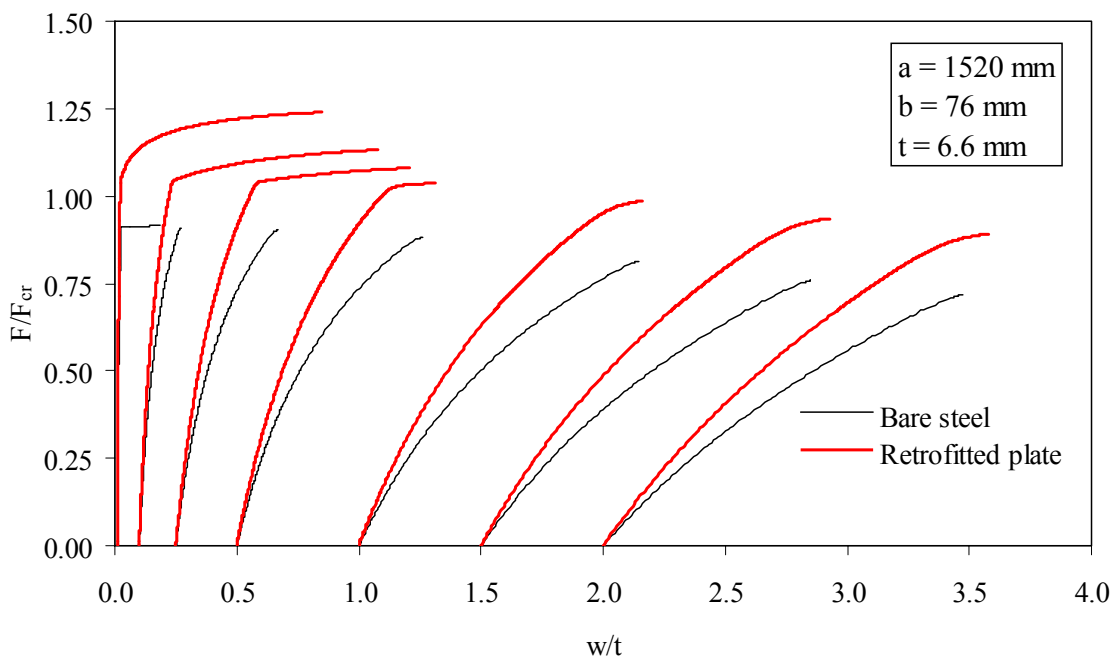


**Figure 2.21** Inelastic load-deflection responses of type I C-plates retrofitted with 9.5 mm GFRP for different imperfection amplitudes.

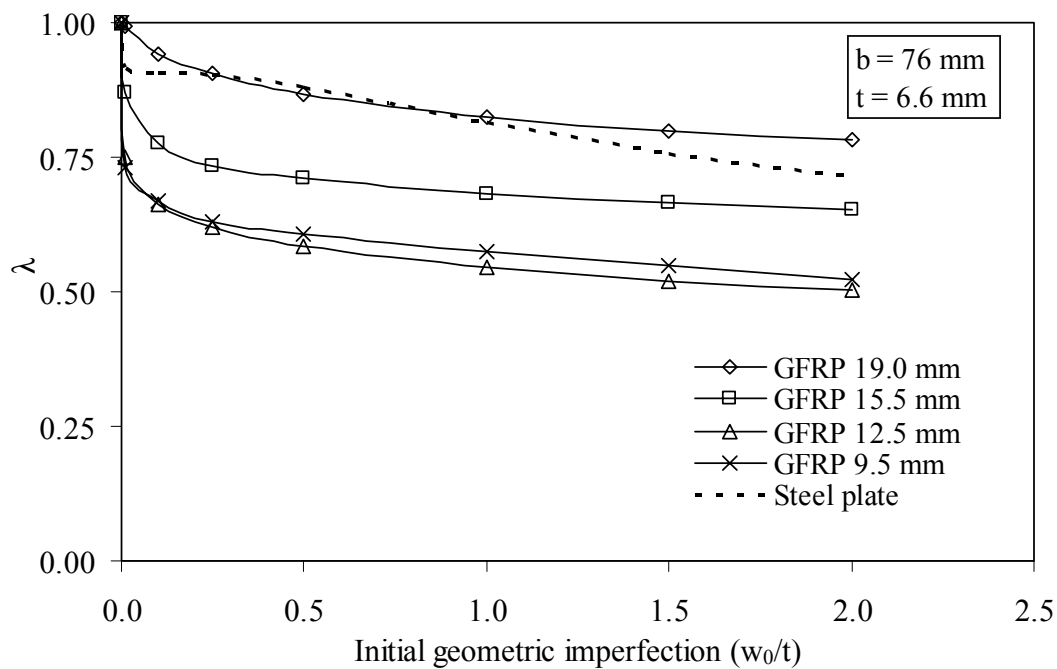


**Figure 2.22** Effect of geometric imperfection on type I C-plates.



**2.3.5.6 (x) EI-IE-NC**

The failure of Type-I plate with NC end condition is governed by premature shear failure of the adhesive, and, therefore, the effect of initial imperfection can not be assessed for such a case.

**2.3.5.7 (xi) FII-IE-C**

The load-deflection response pattern is identical to that of the EI-IE-C case for both the bare steel and the retrofitted plates. For the retrofitted plates with 9.5 mm GFRP, failure is governed by inelastic buckling of the system for initial geometric imperfection amplitude up to  $1.0t$ . For the amplitude of imperfection higher than  $1.0t$ , failure is governed by GFRP rupture. For the larger thickness addition of GFRP plates, failure is governed by GFRP rupture for all imperfection amplitudes. As the thickness of the GFRP increases, the failure mode is shifted from inelastic buckling of the system to the GFRP rupture. The parameter,  $\lambda$ , is plotted in Figure 2.23 for different imperfection amplitudes. From this figure, it is observed that the values of  $\lambda$  decrease with the increase of the imperfection amplitude. This pattern is observed for different GFRP thicknesses. It is observed that the rate of reduction of  $\lambda$  with  $(w_0/t)$  is higher for the bare steel plates compared to the retrofitted plate. The values of  $\lambda$  are 0.73 and 0.65 for the GFRP thicknesses of 9.5 mm and 19.0 mm, respectively, with an imperfection amplitude of  $0.5t$ . These values are 0.63 and 0.56 with an imperfection amplitude of  $2.0t$ .

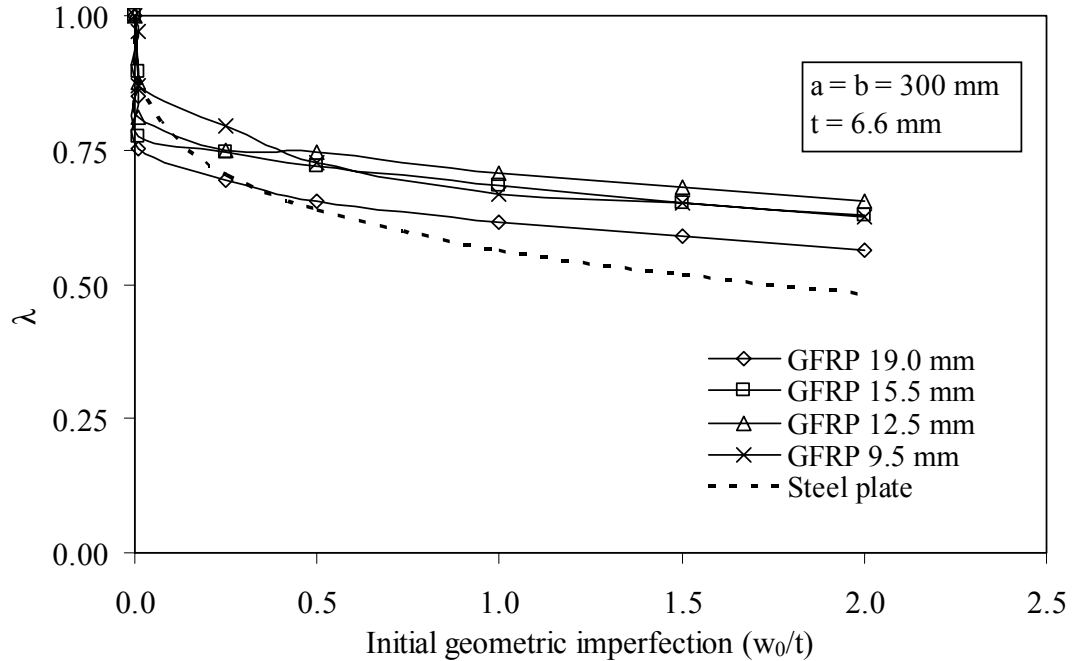


**Figure 2.23** Effect of geometric imperfection on type II C-plates.

### 2.3.5.8 (xii) FII-IE-NC

For the Type II-NC bonded plates, premature shear failure of the adhesive is observed, and, therefore, the effect of initial geometric imperfection can not be assessed for this case.

## 2.4 Conclusions

The enhancement in the buckling capacity of steel plates resulting from bonding GFRP plates is assessed in the current study using a finite element model developed in-house. In this model, a consistent degenerated shell element is used to simulate both the steel and GFRP plates. A continuous linear spring system is used to simulate the bond behaviour between the steel and GFRP plates. The mechanical properties of the adhesive used in the analysis are based on actual values determined experimentally from previous studies. The

finite element model is validated by comparing its prediction to the analyses available in the literature. The model is then used to evaluate enhancement in both the elastic and inelastic capacities. A buckling magnification factor defined as the ratio of the capacity of the retrofitted system to the capacity of the bare steel plate is evaluated. The capacity of the retrofitted system is governed by reaching the ultimate shear capacity of the adhesive, ultimate axial capacity of the GFRP, or instability of the system. The study considers three-sided as well as four-sided simply supported plates. In addition, two types of compatibility end conditions between the axial displacements of the steel and GFRP are considered. The C and NC type denote full and no compatibility conditions, respectively. The variation of the buckling magnification factor with the aspect ratio and slenderness ratio of the plate are determined for different GFRP plate thickness. In addition, the effect of the initial geometric imperfection on the capacity of the retrofitted system is assessed. The main conclusions that can be drawn from the conducted analyses are summarized as follows:

- Type I plates

- For C-type end condition and for a slenderness ratio of 11, the elastic buckling magnification factor ranges between 1.20 and 2.40 for GFRP additions of 9.5 mm to 19.0 mm, respectively. For the NC-plates, these factors range between 1.20 and 1.75. When inelastic buckling analyses are considered, these values range between 1.65 and 2.46 for the C-type, while no enhancement in the buckling capacity is observed for the NC-ended plates because of premature adhesive shear failure.

- For slender plates, much higher elastic buckling magnification factors are obtained. They reach values of 17 and 11 for the C and NC-plates, respectively, for a slenderness ratio of 50 and a 19 mm GFRP plate addition. The same values are obtained when inelastic behaviour is considered since the buckling occurs elastically for these slender plates.
- Type II plates
  - For C-type end condition and for a slenderness ratio of 11, both the elastic and the inelastic buckling magnification factors reach values of 1.10 and 1.20 for GFRP additions of 9.5 mm to 19.0 mm, respectively. Almost the same enhancement is observed for the NC-plates.
  - For slender plates having with slenderness ratio of 100 and with a 19.0 mm GFRP addition, elastic buckling magnification factors of 14 and 7 are obtained for the C and NC plates, respectively. Those values are reduced to 11 and 5.2, respectively, when inelastic analysis is considered.
- Failure modes of the retrofitted plates
  - The failure mode, either overall instability or material failure in the adhesive and/or the GFRP, depends on the slenderness ratio of the plate and the thickness of the GFRP addition. For plates with high slenderness ratio, failure occurs due to elastic instability of the system. For less slender plates, material failure in the form of GFRP rupture and adhesive shear failure are predicted for the C-plates and the NC-plates, respectively.

- Material failure of Type I retrofitted system is predicted at a slenderness ratio of 15 with a 9.5 mm GFRP plate. However, for the 19.0 mm GFRP plate, this type of failure starts at a slenderness ratio of 20.
  - For Type II plates, material failure of the system starts at a slenderness ratio of 45.45 for the 9.5 mm GFRP addition. This type of material failure is observed for all the considered range of slenderness ratio for the 19.0 mm GFRP plate.
- Effect of Initial geometric imperfection
- A parameter  $\lambda$  is calculated as the ratio of the capacity of the retrofitted system with initial geometric imperfection to the capacity of the system without any imperfection. In general, the results indicate that the value of  $\lambda$  decreases with the increase of amplitude of imperfections.
  - For the Type I plates with C-type end condition, and a 19.0 mm GFRP, the values of  $\lambda$  resulting from elastic analyses range between 1.00 and 0.86 for the imperfection amplitudes ranging between 0 and  $2.0t$ , where  $t$  is the thickness of the steel plate. This parameter  $\lambda$  ranges between 1.00 and 0.77 for the same imperfection range with the NC-end conditions. The above range of  $\lambda$  becomes 1.00 to 0.78 when inelastic analyses are considered for the C-type plates.
  - For Type II C-plates with 19.0 mm GFRP, the predicted values of  $\lambda$  are almost the same both for the C and NC-end conditions. For elastic analysis, these values range between 1.00 and 0.47 for the above mentioned range of imperfection amplitude. This range becomes between 1.00 and 0.56 when inelastic analysis is considered.

## 2.5 References

- [1] Saadatmanesh, H. and Ehsani, M. R., RC beams strengthened with GFRP plates. I: Experimental Study, *Journal of Structural Engineering*, ASCE 1991; 117(11): 3417-3433.
- [2] An, W., Saadatmanesh, H., and Ehsani, M. R., RC beams strengthened with FRP plates. II: Analysis and Parametric Study, *Journal of Structural Engineering*, ASCE 1991; 117(11): 3434-3455.
- [3] Saadatmanesh, H., Extending service life of concrete and masonry structures with fiber composites, *Construction and Building Materials* 1997; 11(5-6): 327-335.
- [4] Neale, K. W., FRPs for structural rehabilitation: a survey of recent progress, *Progress in Structural Engineering and Materials* 2000; 2(2): 133-138.
- [5] Sheikh, S. A., DeRose, D., and Mardukhi, J., Retrofitting of concrete structures for shear and flexure with fiber-reinforced polymers, *ACI Structural Journal* 2002; 99(4): 451-459.
- [6] Barros, J. A. O., Dias, S. J. E., and Lima, J. L. T., Efficacy of CFRP-based techniques for the flexural and shear strengthening of concrete beams, *Cement and Concrete Composites* 2007; 29(3): 203-217.
- [7] Tavakkolizadeh, M. and Saadatmanesh, H., Strengthening of steel–concrete composite girders using carbon fiber reinforced polymer sheets, *Journal of Structural Engineering*, ASCE 2003; 129(1): 30-40.
- [8] Colombi, P. and Poggi, C., Strengthening of tensile steel members and bolted joints using adhesively bonded CFRP plates, *Construction and Building Materials* 2006; 20(1-2): 22-33.

- [9] Silverstre, N., Young, B., and Camotim, D., Non-linear behaviour and load-carrying capacity of CFRP-strengthened lipped channel steel columns, *Engineering Structures* 2008; 30(10): 2613-2630.
- [10] Al-Saidy, H., Klaiber, F. W., and Wipf, T. J., Repair of steel composite beams with carbon fiber-reinforced polymer plates, *Journal of Composites for Construction*, ASCE 2004; 8(2): 163-171.
- [11] Shaat, A. and Fam, A., Axial loading tests on short and long hollow structural steel columns retrofitted using carbon fibre reinforced polymers, *Canadian Journal of Civil Engineering* 2006; 33(4): 458-470.
- [12] Accord, N. B. and Earls, C. J., Use of fiber-reinforced polymer composite elements to enhance structural steel member ductility, *Journal of Composites for Construction*, ASCE 2006; 10(4): 337-344.
- [13] Koziey, B. L. and Mirza, F. A., Consistent thick shell element, *Computers and Structures* 1997; 65(12): 513-541.
- [14] El Damatty, A., Korol, R. M., and Mirza, F. A., Large displacement extension of consistent shell element for static and dynamic analysis, *Computers and Structures* 1997; 62(6): 943-960.
- [15] El Damatty, A. and Abushagur, M., Testing and modeling of shear and peel behavior for bonded steel/FRP connections, *Journal of Thin-Walled Structures* 2003; 41(11): 987-1003.
- [16] Sen, R., Liby, L., and Mullins, G., Strengthening steel bridge sections using CFRP laminates, *Composites Part B: Engineering* 2001; 32(4): 309-322.
- [17] Miller, T. C., Chajes, M. J., Mertz, D. R., and Hastings, J. N., Strengthening of a

- steel bridge girder using CFRP plates, *Journal of Bridge Engineering*, ASCE 2001; 6(6): 514-522.
- [18] P. S. Bulson, *The stability of flat plates*, American Elsevier Publishing Company, New York, 1969.
- [19] Bakker, M. C. M., Rosmanit, M., and Hofmeyer, H., Prediction of the elasto-plastic post-buckling strength of uniformly compressed plates from the fictitious elastic strain failure, *Journal of Thin-Walled Structures* 2009; 47(1): 1-13.
- [20] El Damatty, A., Abushagur, M., and Youssef, M. A., Experimental and analytical investigation of steel beams rehabilitated using GFRP sheets, *Steel and Composite Structures* 2003; 3(6): 421-438.



**CHAPTER 3**

**IMPROVEMENT OF LOCAL BUCKLING BEHAVIOUR OF STEEL BEAMS  
THROUGH BONDING GFRP PLATES\***

### **3.1 Introduction**

Fiber-reinforced polymers (FRP) are versatile structural components that are used in the automotive, aerospace, and construction industries. Many investigations were carried out in the past to repair and strengthen concrete structures using FRP. A significant increase in the flexural and shear capacities of concrete and masonry structures was observed in these FRP applications. This process involves the application of FRP to the top, bottom, and sides of concrete members for the purpose of rehabilitating and retrofitting deteriorated structures and retrofitting schemes [1-8]. Recently a similar technique has been employed to improve the performance of metallic structures. Welding, bolting or adding steel cover plates to existing members are the common practice for rehabilitation and/or retrofitting of existing steel members. This approach, which involves adding steel plates, has some drawbacks such as potential corrosion, involvement of cumbersome false works, and the sensitivity of the rehabilitated system to fatigue due to stress concentration resulting from welding or bolting. FRP have the advantages of possessing a high strength-to-weight ratio, and an excellent resistance to corrosion and environmental degradation. They are also available in various forms and shapes and are easy to handle during construction. This makes the use of FRP an attractive solution for rehabilitation and retrofitting of steel structures.

---

\*A version of this chapter is prepared for publication in the *Journal of Composite Structures*.

A limited number of studies related to the application of FRP on metallic structures are available in the literature. Most of these studies focused on the application of FRP for enhancing the load carrying capacity or restoring the original strength of a deteriorated member [9-12]. Sen et al. [13] tested six steel beams with carbon FRP (CFRP) sheets bonded to the bottom flange of the beams in order to assess the increase in bending strength. The study revealed a considerable increase in the load carrying capacity of the beams. Miller et al. [14] also used CFRP sheets to strengthen four steel girders and the obtained results indicated that the stiffness of the rehabilitated girders increased by 10% to 37%. This application is susceptible to galvanic corrosion on the metal surface upon contact with seawater or water with de-icing salts, as carbon fibers are good electron conductors [15].

There is relatively little work done to investigate the use of adhesively bonded Glass Fiber Reinforced Polymer (GFRP) materials in retrofitting of steel structures. El Damatty et al. [16] studied analytical and experimental enhancement in the flexural capacity of I-shaped steel beam resulting from bonding GFRP plates to the beams' flanges. A significant improvement in the flexural capacity of the beams was observed in this application.

The capacity of steel members can be governed by buckling failure before developing their full plastic resistance when these elements are subjected to compressive stresses. This can happen for slender beams, where premature local buckling of the flanges and/or web can occur. FRP composite materials can be used to enhance the stability of steel members. Shaat and Fam [17] tested hollow structural square (HSS) steel column specimens wrapped with both longitudinal and transversely oriented CFRP sheets. From

the test results, it was observed that the axial strength increased approximately by 8 -18% and the axial stiffness by 4-28%. They suggested that transverse CFRP restrain outward-directed local buckling and, thereby, an increase in the capacity was observed. They also tested five slender HSS specimens with a constant slenderness ratio of 68, of which four specimens were strengthened by unidirectional CFRP sheets. The improvement in the axial strength of the columns ranged between 13% and 23% and failure occurred due to overall buckling. Accord and Earls [18] used a finite element model to study the effectiveness of using GFRP strips bonded to the compression flange of I-shaped cantilever members. The inelastic response of the strengthened I-shaped members during plastic hinge formation was assessed under an applied moment gradient. The adhesive layer between the steel and GFRP plates was modeled as an isotropic elastic material with a modulus of elasticity of 6900 MPa, which is about one fourth that of the GFRP material. Their work demonstrated that the presence of the GFRP strips enhances the structural ductility of the steel members because the GFRP strips provide effective bracing to the flange, and thus inhibit the formation of local buckling in the compression flange of the cross-section.

An experimental study was conducted by El Damatty and Abushagur [19] to determine the type of adhesive that can achieve the best bonding between a GFRP plate and a steel section. They considered the following adhesives:

- (i) High-strength epoxy
- (ii) Impregnating Resin Epoxy
- (iii) Epoxy paste adhesive
- (iv) DP-190 Translucent and Gray Epoxy adhesive

- (v) DP-180 Low-order Acrylic adhesive
- (vi) DP-100 plus Clear and Gray Epoxy adhesive
- (vii) Methacrylate : MA 300
- (viii) Methacrylate : MA 420

They conducted a number of shear lap tests to select the adhesive that develops the highest load resistance of specimens involving bonding GFRP plates to a HSS section. They found that methacrylate MA420 achieved the highest load resistance with a superior performance. This adhesive has been also used by Chakrabarti and Mosallam [20] to assess the improvement in the beam-to-column joint behaviour of steel frames with polymer composites.

The objective of the current research is to assess the improvement in the local buckling capacity of wide flange steel beams rehabilitated through bonding GFRP plates to their flanges. The study is conducted numerically using a finite element model developed in-house. In this numerical model, consistent degenerated shell elements are used to simulate various components of the steel beam as well as the GFRP plates. A set of linear spring system simulating the adhesive medium between the steel and GFRP plates is used in the model. The mechanical properties of the adhesive medium used in model are obtained from the previous tests conducted by El Damatty and Abushagur [19]. The geometric and material nonlinear effects as well as the initial geometric imperfection and residual stresses are included in the finite element model. Improvement in both the load carrying capacity and the deflection at failure of the retrofitted beams is assessed for different thickness additions of GFRP plates and various slenderness ratios of the steel beams. Various instability and strength failure modes in the steel, GFRP and adhesive are

considered in the study. Simply supported beams with center point and two-point loading system, and cantilever beams with free-end applied load are considered in the current study.

### **3.2 Finite Element Model**

In order to capture the local buckling behaviour of the retrofitted beams, shell elements are used to model various components of the system. The consistent subparametric shell element, shown in Figure 3.1, is used in this model. This shell element was formulated by Koziey and Mirza [21] and was then extended by El Damatty et al. [22] to include the effects of material and geometric non-linearities. The non-linear finite element model has the flexibility to incorporate either elastic-perfectly plastic or a bilinear strain hardening behaviour for steel. The material model is based on the von Mises yield criterion and its associated flow rule. This triangular element consists of 13 nodes of which 10 nodes are used to interpolate the displacements  $u$ ,  $v$ , and  $w$ , that act along the global axes  $x$ ,  $y$  and  $z$ , respectively. This element is free from the shear-locking phenomenon through employing a consistent formulation that involves a cubic interpolation for displacements and a quadratic interpolation for rotations. The rotational degrees of freedom  $\alpha$ ,  $\beta$ ,  $\varphi$ , and  $\psi$  are associated with the corner and mid-side nodes, where rotations  $\alpha$  and  $\varphi$  are about the local  $y'$  axis and rotations  $\beta$  and  $\psi$  are about the local  $x'$  axis, where  $y'$  and  $x'$  are located in a plane tangent to the mid-surface. The rotations  $\alpha$  and  $\beta$  provide a linear variation of displacements through the thickness, simulating bending deformations, while  $\varphi$  and  $\psi$  lead to a cubic variation of the through-thickness displacements, simulating shear deformations. An assembly of consistent shell elements is used to model the top flange,

bottom flange, web of the steel sections and the GFRP retrofitting plates. A special interface element, compatible with the consistent shell element, is used to simulate the adhesive layer bonding the GFRP plates to the steel sections.

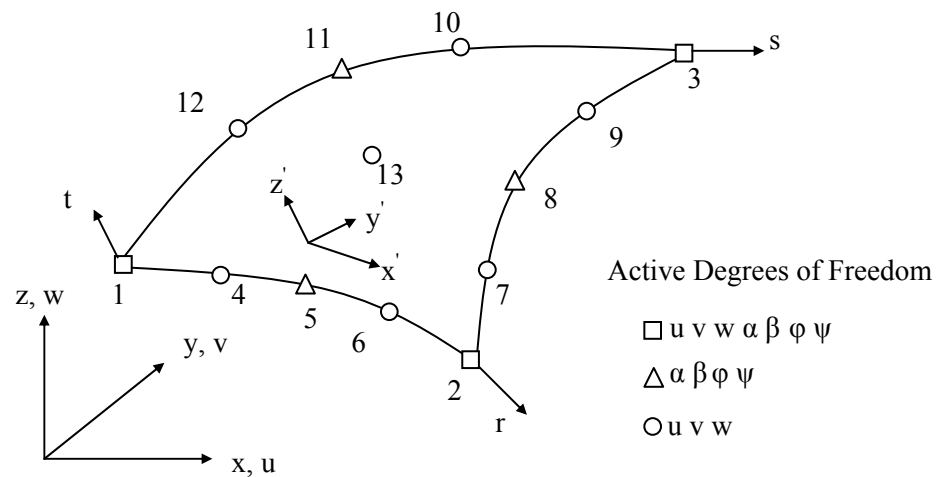


**Figure 3.1** Shell element coordinate system and nodal degrees of freedom [21].

### 3.2.1 Interface Element Model

The bond between the steel and GFRP plates plays a vital role in determining the effectiveness of using GFRP plates for enhancing the local buckling capacity of steel I-shaped beams. It is observed from the previous studies that the failure of adhesive limited the capacity of the retrofitted members. The analytical study conducted by Sen et al. [13] predicted that high peeling stresses could cause failure of the epoxy at the end of the CFRP laminated steel members. This was also observed in the experimental and analytical study conducted by Miller et al. [14]. An assumption of perfect bond between the steel and GFRP sections can overestimate the stiffness and/or the strength of the retrofitted system.

The shear and peeling stiffnesses of the adhesive can be represented by a three-dimensional continuous linear spring system. El Damatty and Abushagur [19] conducted a large number of shear lap tests for GFRP plates and steel sections bonded together using the MA420 methacrylate adhesive, which has shown to provide the best performance among different adhesives for such an application. In the same study, El Damatty and Abushagur [19] incorporated the results of the tests into an analytical model and estimated the characteristics of a continuous spring system simulating both the shear and peel stiffnesses of the adhesive. The constants of the continuous spring system used in the current study are based on the results of this investigation. A sketch of the interface element used in the current study to simulate the adhesive is provided in Figure 3.2. In this element, the shear behaviour is simulated using in-plane springs in two perpendicular directions, while the peeling behaviour is simulated by an out-of-plane spring system. This interface element is compatible with the consistent shell element used to model the steel and GFRP plates. One face of the interface element coincides with a shell element modeling the steel flanges, while the other face coincides with the shell element modeling the GFRP plates. The interface element has only displacement degrees of freedom along the three perpendicular global directions, which are compatible with the displacement degrees of the consistent shell element. It should be noted that the constants of the continuous spring systems in shear,  $K_s$  and in peeling,  $K_p$  have unit of Force/length<sup>3</sup>.

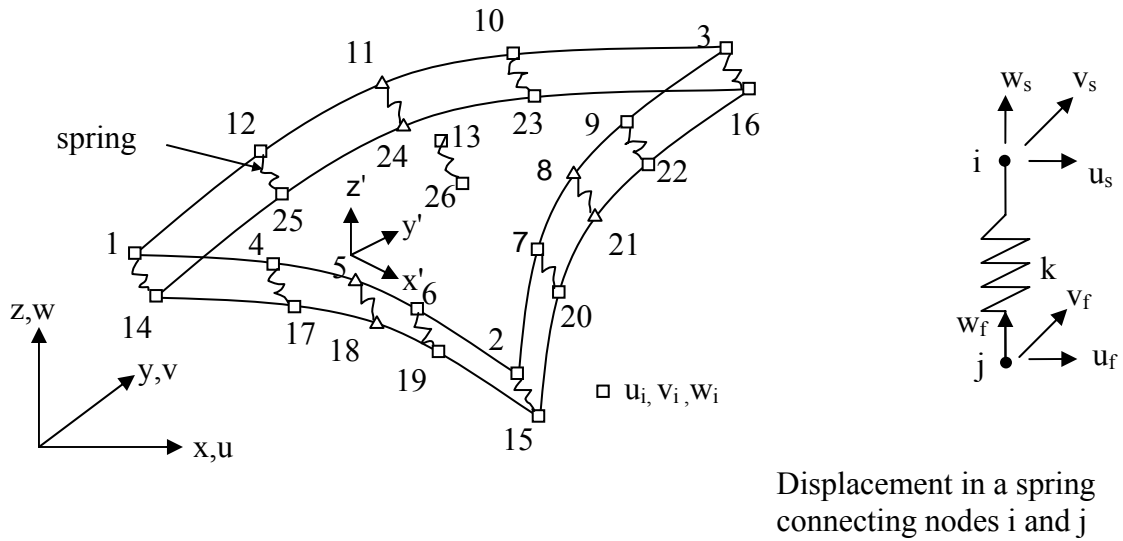


**Figure 3.2** Interface elements between steel and GFRP plates used in the model.

### 3.2.2 Assumed Initial Geometric Imperfection Shape of Beam

The effect of initial geometric imperfection of the beams is incorporated into the model as initial strains included in the nonlinear stiffness matrix of the shell elements. The following initial imperfection function  $w_0(x, y)$  is introduced in the finite element model for the flange of the steel beam and the attached GFRP plate [23]:

$$w_0(x, y) = A \cos \frac{\pi x}{b} \sin \frac{m\pi y}{a} \quad (3.1)$$

In the above equation,  $A$  is the amplitude of initial imperfection,  $a$  and  $b$  are the length and width of the compression flange of beams, respectively.  $m$  is the half-wavelength number along the longitudinal direction of the beams. The length of a half-wavelength is considered to be equal to the width of the flange [23]. A sketch of a beam with initial geometric imperfection is shown in Figure 3.3. The study considers the two types of boundary conditions shown in Figures 3.4 (a) and (b).



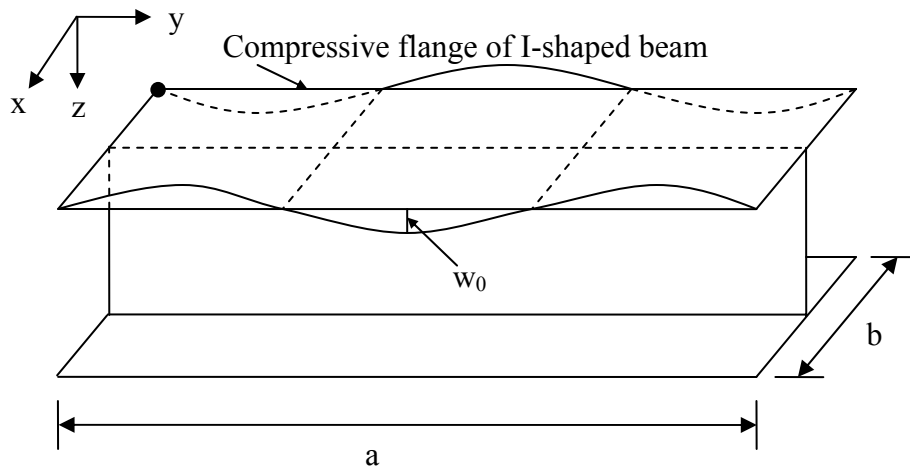
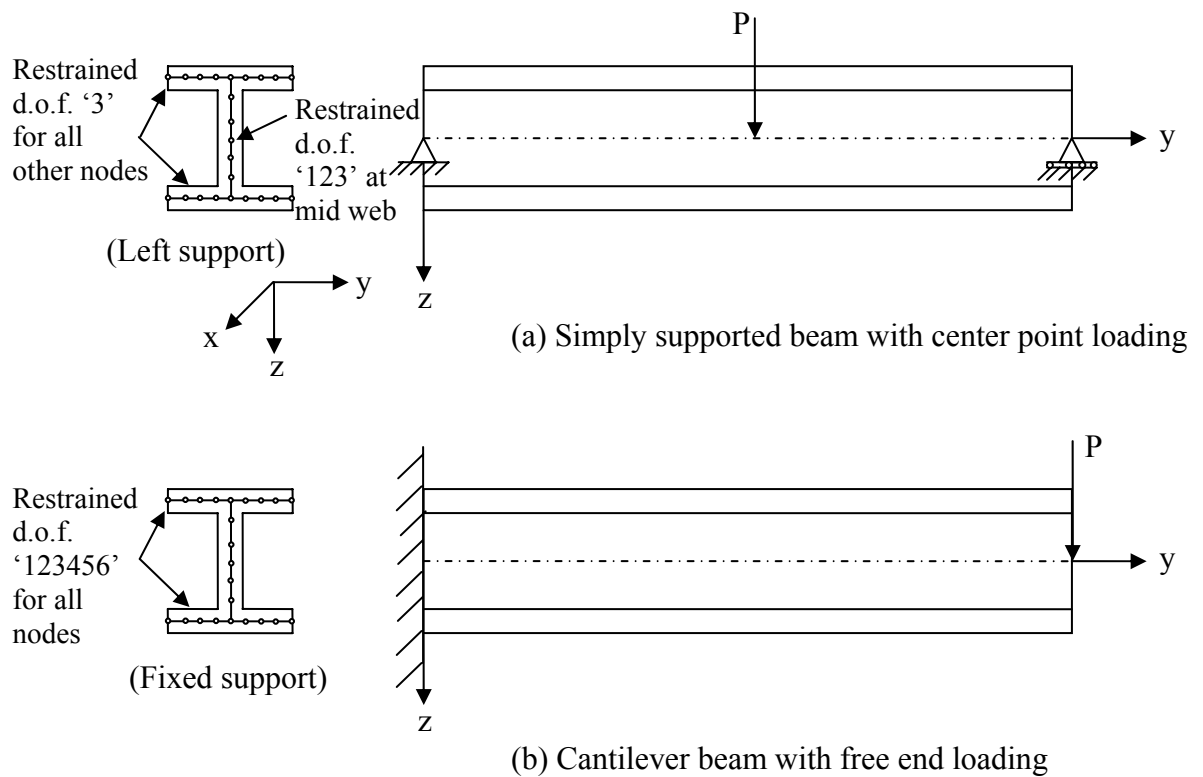


**Figure 3.3** Initial geometric imperfection shape of the beam used in the model.



Note: The degrees of freedom notation (d.o.f.) '123' corresponds to translations in x-, y-, and z-axes, whereas '456' corresponds to rotations about x-, y-, and z-axes, respectively

**Figure 3.4** Boundary conditions of the steel beam used in the model.

At the two edges of the simply supported beam, the displacements are totally restrained at the centroidal (center) node, while only the vertical displacement is restrained at all other nodes. For the cantilever beam, all the nodes at the clamped edge have both the displacement and rotation degrees of freedom restrained. The centerline nodes of the top and bottom flanges of the beam are restrained in x-direction to prevent any kind of lateral torsional buckling.

### 3.2.3 Assumed Residual Stresses Distribution of Section of Beams

Residual stresses develop in hot rolled as well as in built up steel sections due to the welding process. These stresses can affect the local buckling capacity of the members. The distribution of residual stresses assumed in the flanges and web of the I-shaped steel section is shown in Figure 3.5. This distribution is compatible with the findings of the experimental program conducted by Hasham and Rasmussen [24] on plastic and slender welded I-shaped built-up sections.

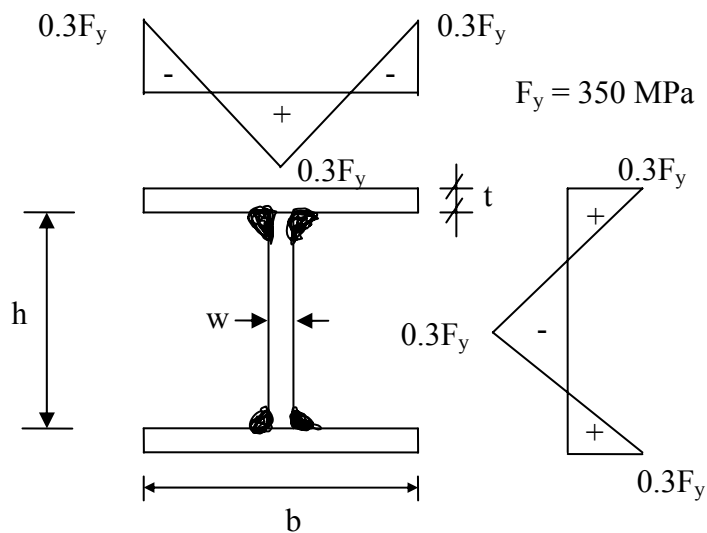


**Figure 3.5** Assumed residual stresses pattern of steel section used in the model.

The residual stresses are incorporated into the finite element model as initial axial stresses.

### 3.2.4 Validation of Finite Element Model

The finite element model is validated through comparison with numerical and experimental results available in the literature. The first validation example involves a bare steel beam that was modelled numerically by Accord and Earls [18]. They considered two I-shaped cantilever beams both having span length of 3.81 m and loaded by a point load acting at the free end of the beams. In the current study, the same beams are modelled using the consistent shell elements. Figure 3.6 shows the relation between the applied load and the deflection at the tip of the cantilever for both specimens indicating an excellent agreement.

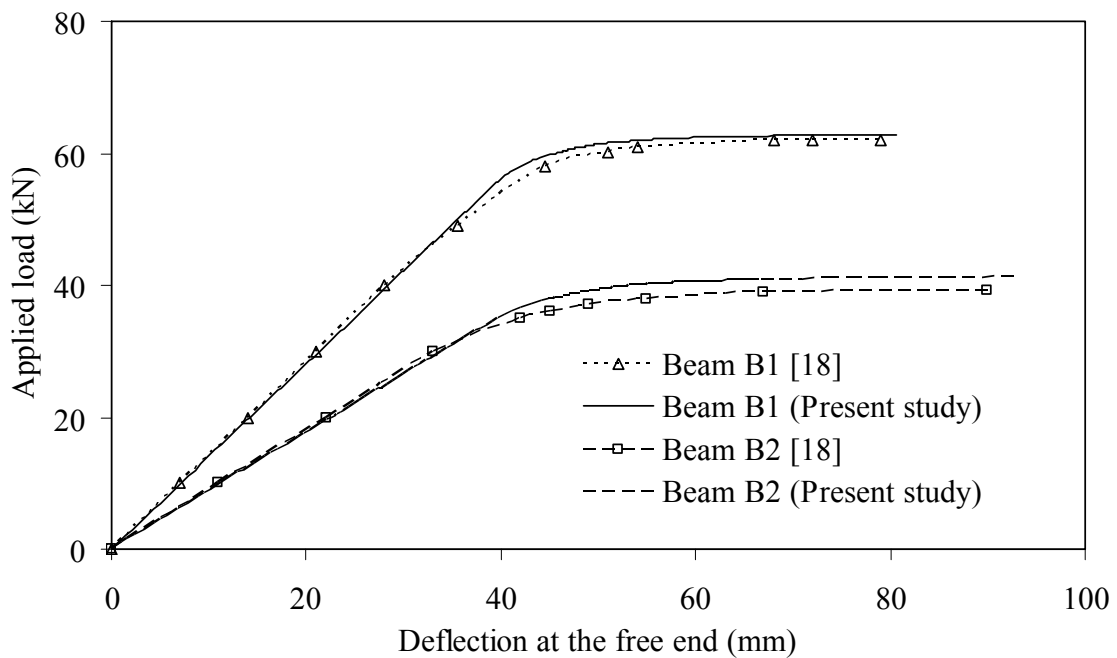


**Figure 3.6** Comparison of load-deflection responses of the bare steel beams.

The second validation example also involves steel cantilever beams that were previously tested by Daali and Korol [25]. The beams were loaded monotonically through a point load applied at the tip of the cantilever. The authors reported the values of the peak loads resisted by the beams. Those results are reported in Table 3.1 together with the dimensions of the beams and the maximum loads obtained from numerical modelling conducted in the current study. The comparison shows an excellent agreement between the numerical and experimental results.

**Table 3.1** Comparison of predicted and observed values of maximum load capacity.

Reference	Specimen no.	b (mm)	t (mm)	d (mm)	w (mm)	L (m)	Observed load, $P_m$ (kN)	Predicted load, $P_p$ (kN)	$P_p/P_m$
Daali and Korol [25]	A0	101.0	5.7	303	5.1	2.125	47.6	51.25	1.07
	B0	101.0	5.7	303	5.1	1.210	85.6	85.5	1.00
	P1	165.0	9.7	310	5.8	2.125	112.1	115.0	1.03

El Damatty et al. [16] conducted an experimental program for steel beams strengthened using GFRP sheets. The tests considered wide flange beams W150 x 37. GFRP plates with 19 mm thickness were bonded to the top and bottom flanges of the steel beams. Tests were conducted with and without the addition of the GFRP plates. The beams had a span length of 2800 mm and were tested using a two-point loading system with simply supported end conditions. The steel beams had the following mechanical properties: yield strength,  $F_y = 363$  MPa, modulus of elasticity,  $E_s = 2 \times 10^5$  MPa, and Poisson's ratio,  $\nu_s = 0.3$ . The GFRP plates had the following mechanical properties: rupture strength,  $\sigma_f = 206.8$  MPa, modulus of elasticity,  $E_f = 1.72 \times 10^4$  MPa, and Poisson's ratio,  $\nu_f = 0.33$ . A

methacrylate adhesive, MA 420, was used to bond the steel and GFRP elements. In view of the study conducted by El Damatty and Abushagur [19], the used adhesive system has the following mechanical properties:

$$K_s = 21.79 \text{ N/mm}^3; K_p = 2.26 \text{ N/mm}^3$$

$$\text{and } \sigma_s = 15.5 \text{ MPa and } \sigma_p = 4.0 \text{ N/mm}.$$

where  $K_s$  and  $K_p$  are the stiffness values for the spring system simulating the shear and peel rigidities of the adhesive, respectively, as explained in Section 3.2.1.  $\sigma_s$  and  $\sigma_p$  are the allowable shear strength and peel strength of the adhesive, respectively. Figure 3.7 shows the relation between the applied load and the mid-span deflection of the beams for both the bare and retrofitted beams obtained from the experiments and the current numerical study. An excellent agreement is shown between the two sets of results.

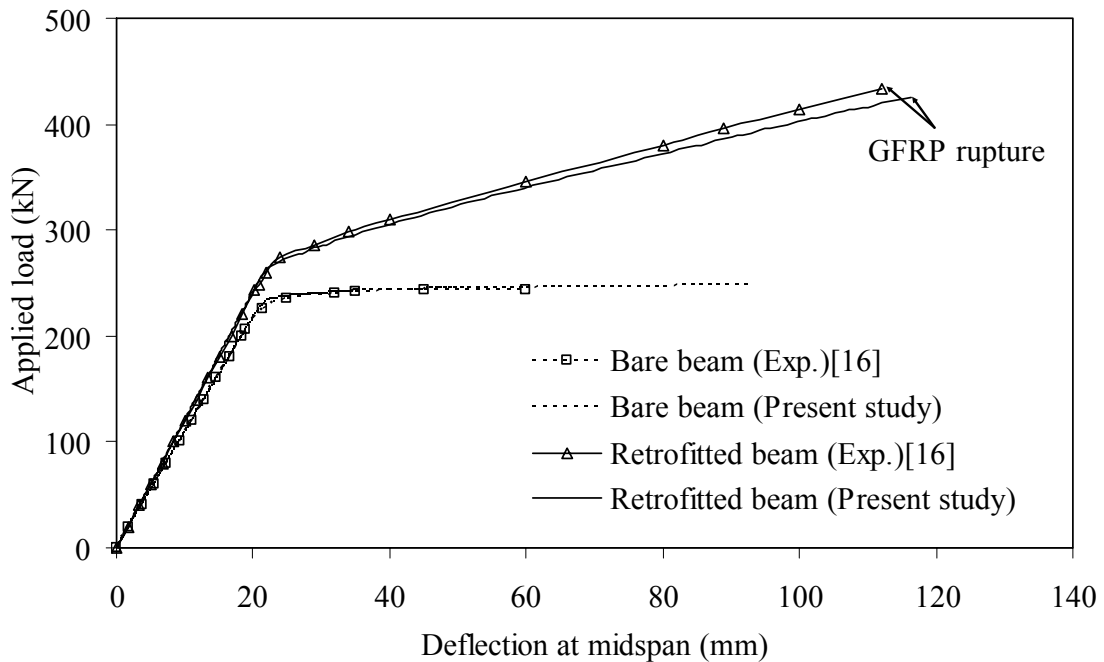


**Figure 3.7** Comparison of predicted and measured load-deflection responses of the bare and retrofitted steel beams with GFRP.

### 3.3 Description of Analysis of Retrofitted Beams

#### 3.3.1 Geometric Properties of Beams

In the current study, doubly symmetric wide flange built-up steel beams are considered. In order to encompass a wide range of flange slenderness values, beams having  $b_f/2t_f$  values of 10, 15, 20, 25 and 30 are analyzed. For each flange slenderness ratio, five different web dimensions are considered. The maximum considered value for the web slenderness ratio  $h/w$  is 60. This assures compactness according to the Canadian Institute of Steel Construction (CISC) specification for a yield stress and a modulus of elasticity of steel of 350 MPa and  $2 \times 10^5$  MPa, respectively [26]. The span,  $L$ , of the beams is 2000 mm. For all the considered beams, the span to depth ratio  $L/h$  ranges between 5.7 and 13.3.

Improvement in the local buckling behaviour of retrofitted steel beams with different thicknesses of GFRP plates under transverse loads is studied. The thicknesses of GFRP plates used in the analyses are 6.35 mm, 9.5 mm, 12.5 mm, 15.5 mm, and 19.0 mm, respectively. It is also assumed that the GFRP plates are bonded only to the compression flange of the beams and they cover the entire span. Geometric properties of the considered beams are given in Table 3.2. Beams are defined as B1 to B25 for different cross sections. The study also considers the effect of post-yielding strain hardening of steel, residual stresses, and initial geometric imperfections on the capacity of the retrofitted beams.

In terms of boundary conditions and loading, three types of beams are considered in the study. Those are:

- (i) Cantilever beam (CF1) subjected to a point load at its tip

- (ii) Simply supported beam (SS1) subjected to point load at its center and
- (iii) Simply supported beam (SS2) subjected to a two-point load with uniform stress in-between the loads.

**Table 3.2** Properties of wide flange built-up sections used in the parametric studies.

Flange width, $b_f$ (mm)	Flange thickness, $t_f$ (mm)	$b_f/2t_f$	Beam No.	Web depth, $h$ (mm)	Web thickness, $w$ (mm)	$h/w$
150	7.5	10	B1	150	7.5	20
			B2	150	5	30
			B3	200	5	40
			B4	200	4	50
			B5	300	6	50
150	5	15	B6	150	7.5	20
			B7	150	5	30
			B8	200	5	40
			B9	200	4	50
			B10	300	6	50
150	3	25	B11	150	7.5	20
			B12	150	5	30
			B13	200	5	40
			B14	200	4	50
			B15	300	6	50
300	7.5	20	B16	300	7.5	40
			B17	300	6	50
			B18	325	6	54.2
			B19	350	6	58.3
			B20	350	7.5	46.7
300	5	30	B21	300	6	50
			B22	300	7.5	40
			B23	325	6	54.2
			B24	350	6	58.3
			B25	350	7.5	46.7

### 3.3.2 GFRP and Adhesive Properties

The GFRP plates used in the retrofitting scheme are manufactured using the pultrusion process and have the following mechanical properties: (i) tensile and compressive bending strength = 206.8 MPa, flexural modulus = 17,200 MPa, and Poisson's ratio = 0.33. These values are provided by the manufacturer and are confirmed through tests [16].

Based on El Damatty and Abushagur [19] tests, the methacrylate adhesive (MA420) with a thickness of 0.79 mm is used to bond the flange of the beam and the GFRP plate. The average values for the spring constants simulating the shear and peeling stiffness of the adhesive are 21.79 N/mm<sup>3</sup> and 2.26 N/mm<sup>3</sup>, respectively. The allowable shear strength and peeling strength of this adhesive are about 15.5 MPa and 4.0 N/mm, respectively, based on the information provided by the manufacturer and confirmed through tests [19].

### 3.3.3 Mesh Sensitivity Analysis of Beams

A number of analyses with different mesh sizes are performed on both bare steel beams and retrofitted beams with different thicknesses of GFRP plates. From the analyses, it is concluded that 720 elements for the bare beams and 960 elements for the retrofitted beams predict the behaviour with good accuracy. For the bare beams, the 720 elements are divided equally between the two flanges and the web; 240 elements for each. For the retrofitted beams, 240 extra elements are used to model the GFRP plate attached to the compression flanges. The 240 triangular elements have 120 rectangular divisions with 60 along the length and 2 along the width of the beams.



### 3.4 Effect of GFRP Plate Thickness on the Buckling Improvement Factors

The load carrying capacities of the retrofitted beam as well as the maximum deflection of the beams at failure are obtained from the analyses. The increase in the load carrying capacity of the beam is expressed by a load improvement factor  $\mu_L$  defined by

$$\mu_L = \frac{\text{Load capacity of the retrofitted beam}}{\text{Load capacity of the corresponding bare beam}}$$

Similarly, a deflection improvement factor  $\mu_\Delta$  is defined by

$$\mu_\Delta = \frac{\text{Deflection value at failure of the retrofitted beam}}{\text{Deflection value at failure of the corresponding bare beam}}$$

Results of all the conducted analyses are presented in Tables 3.1 to 3.15 in Appendix I. In these tables, the load and deflection improvement factors are provided for the retrofitted beams using different GFRP thicknesses and for the three types of boundary conditions. A discussion about the behaviour and failure modes of the beam is provided in the next sub-section.

#### 3.4.1 Cantilever Beams with Free-end Loading (CF1)

The modes of failure of the bare steel beams are as follows:

- B1 to B10 ( $b_f/2t_f = 10$  and  $15$ ) and B16 to B20 ( $b_f/2t_f = 20$ ): Inelastic buckling of the steel section,
- B11 to B15 ( $b_f/2t_f = 25$ ): Yielding of the steel section
- B21 to B25 ( $b_f/2t_f = 30$ ): Elastic buckling of the system

As expected, slender bare steel beams result in elastic buckling whereas inelastic buckling following full plastification of the section is predicted for plastic beams. The failure modes of the bare beams are independent of the  $h$  and  $w$  values of the web of the

beams.

The failure modes of the retrofitted beams depend on the value of the thickness of the GFRP plate and the flange slenderness ratio,  $b_f/2t_f$ , of the beams. For a specific slenderness ratio, the load and deflection improvements are shown to be insensitive to the web dimensions.

The failure of the retrofitted beam B1 ( $b_f/2t_f = 10$ ) is governed by GFRP rupture for all the considered GFRP plate thicknesses. No premature failure in the adhesive is observed before the retrofitted beams reach their maximum load capacities. The load–deflection responses of beam B1 are presented in Figure 3.8 for different GFRP plate thicknesses. A load improvement factor,  $\mu_L = 1.13$  and a deflection improvement factor,  $\mu_\Delta = 1.48$  are predicted for the addition of 6.35 mm GFRP plate. These factors increase to 1.27 and 2.90, respectively, for the case of 19.0 mm GFRP plate. This trend is observed for all the retrofitted beams with smaller slenderness ratios.

For slender beams with  $b_f/2t_f$  ratio of 30, the following modes of failure for the retrofitted beams are predicted:

- GFRP 6.35 mm: Elastic buckling of the system
- GFRP 9.5 mm and 12.5 mm: Yielding of steel
- GFRP 15.5 mm and 19.0 mm: GFRP rupture

The load and deflection improvement factors corresponding to 6.35 mm thick GFRP plate are 1.09 and 1.04, respectively. These factors increase to 1.76 and 5.80, respectively when a 19.0 mm GFRP plate is used. The load-deflection responses of beam B25 ( $b_f/2t_f = 30$ ) are provided in Figure 3.9. The plots show the obvious improvement in the load and deflection capacities of this slender beam as a result of the GFRP addition. The plots also

indicate that the improvement in deflection is more significant than that of load.

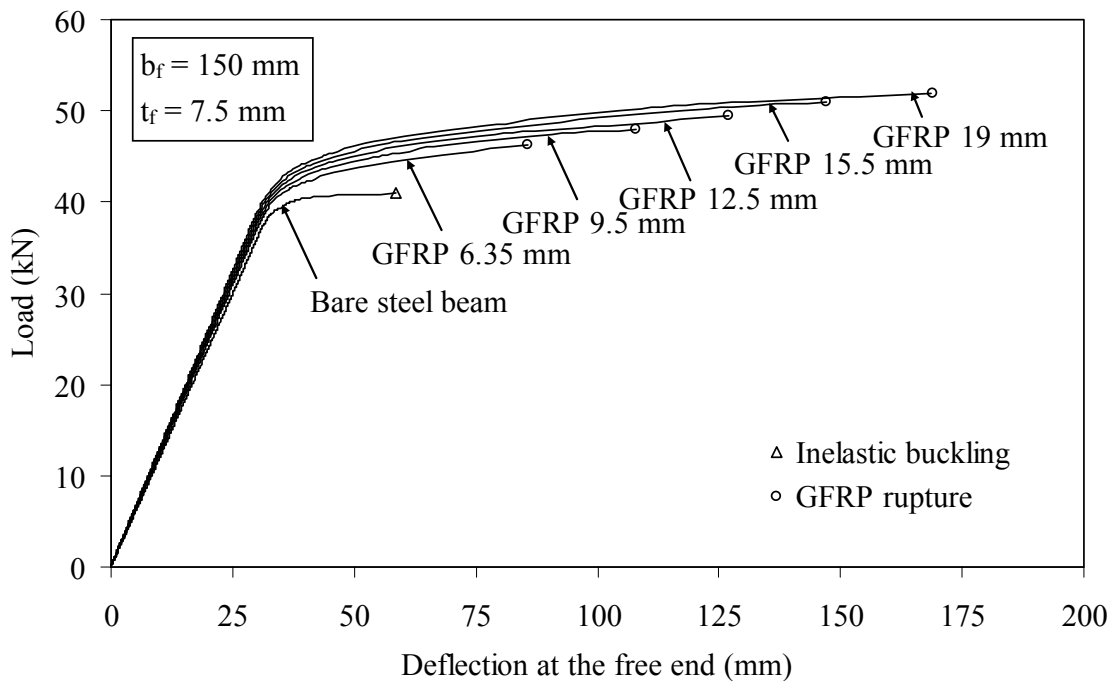


**Figure 3.8** Load-deflection responses of cantilever retrofitted beam B1 ( $b_f/2t_f = 10$ ).

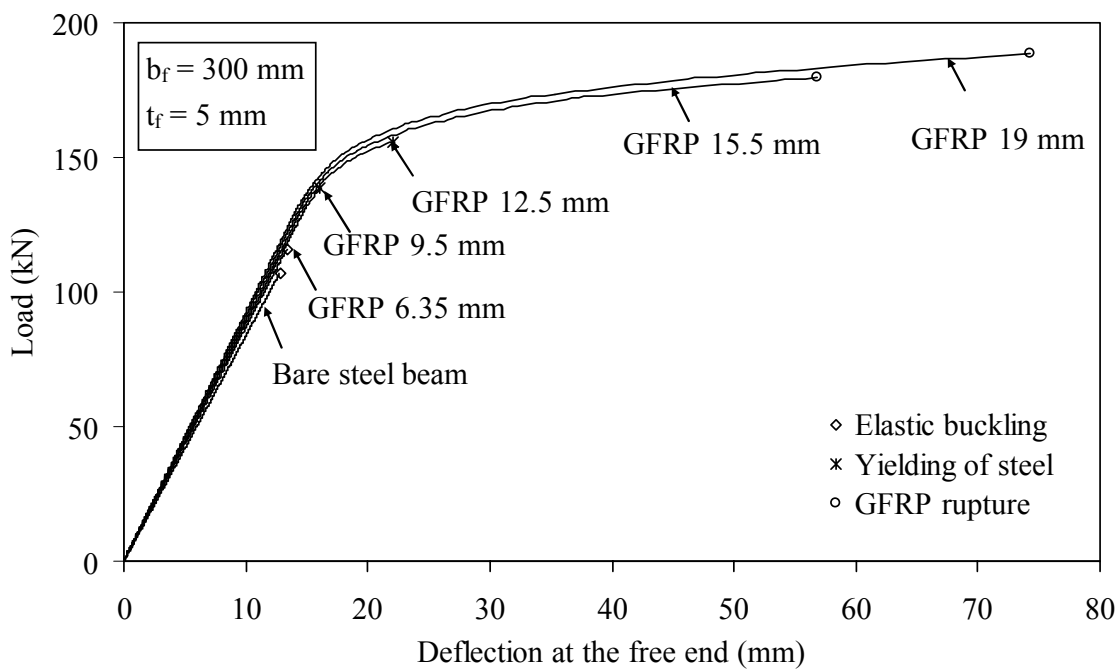


**Figure 3.9** Load-deflection responses of cantilever retrofitted beam B25 ( $b_f/2t_f = 30$ ).

### 3.4.2 Simply Supported Beams with Center Point Loading (SS1)

The failure modes of the SS1 bare steel beams are the same as that of the CF1 beams with exception of beams B16 to B20. These beams reach a state of instability after the extreme fiber of the beam yield, but before reaching a stage of full section plastification. The failure modes of the retrofitted beams with different GFRP plates are also identical to that of the CF1 beams. The improvement factors,  $\mu_L$  and  $\mu_\Delta$ , are 1.25 and 3.05, respectively, for beam B1 with 19.0 mm GFRP plates whereas these values are 1.68 and 5.95, respectively, for beam B25 for the same GFRP addition.

### 3.4.3 Simply Supported Beams with Two-Point Loading (SS2)

The failure modes of bare SS2 beams are the same as that of the SS1 beams with exception of beams B11 to B20. These beams fail by elastic buckling. The failure modes of the retrofitted beams with different GFRP plates are also different for the slenderness ratio,  $b_f/2t_f$ , of 20 to 30. Inelastic overall buckling of the system is observed for larger thickness addition of GFRP plates instead of GFRP rupture of the CF1 and SS1 systems. The failure of the retrofitted beam B1 is governed by GFRP rupture for all GFRP thicknesses. The load-deflection responses of this beam are plotted in Figure 3.10. The load and deflection improvement factors,  $\mu_L$  and  $\mu_\Delta$ , are 1.34 and 5.09, respectively, for a 19.0 mm GFRP plate.

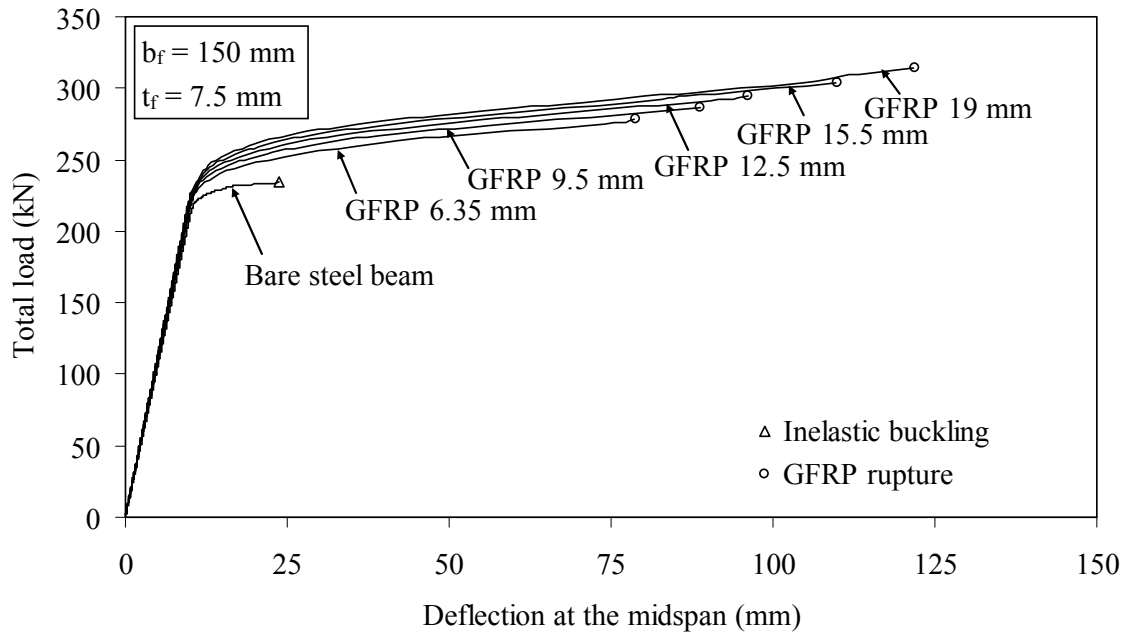


**Figure 3.10** Load-deflection responses of simply supported retrofitted beam B1 with two-point loading.

For beam B25, the modes of failure depend on the GFRP plate as shown below.

- GFRP 6.35 mm and 9.5 mm: Elastic buckling of the system
- GFRP 12.5 mm: Yielding of steel
- GFRP 15.5 mm : GFRP rupture and
- GFRP 19.0 mm: Inelastic buckling of the system

The load-deflection responses of beam B25 are presented in Figure 3.11. The predicted factors,  $\mu_L$  and  $\mu_{\Delta}$ , are 1.85 and 8.71, respectively, for beam B25 with a 19.0 mm GFRP plate.

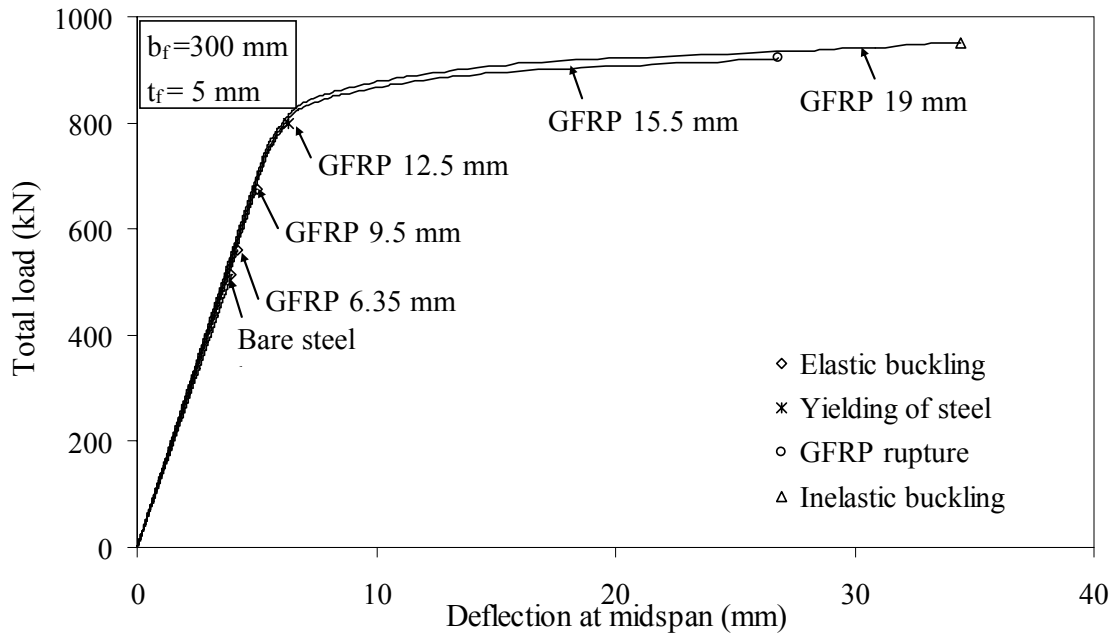


**Figure 3.11** Load-deflection responses of simply supported retrofitted beam B25 with two-point loading.

In general, it is shown from the analyses and the figures that as the thickness of the GFRP plate increases both the load and deflection at failure increase. However, the improvement rate in the deflection is higher than that of the load for the same addition of GFRP plate. It is also observed that in case of slender beams, the improvement factors of both the load and deflection are higher than that of plastic beams.

### 3.5 Influence of Strain Hardening Behaviour of Steel on the Capacities of the Retrofitted Beams

The behaviour of the retrofitted beams is assessed in this section while considering the strain hardening behaviour of steel. The steel beams with slenderness ratio,  $b_f/2t_f$ , of 10 and 30 are considered for the three mentioned loading systems. The strain hardening

modulus of bare steel is assumed 0.5% of the elastic modulus of steel [27]. The analyses show that both the load and deflection at failure of the beams with  $b_f/2t_f = 10$  increase when the strain hardening behaviour of steel is considered. The load capacity increases by 5% whereas deflection at failure increases by 99% for beam B1 of the CF1 system. This pattern of enhancement in load and deflection is also observed for the SS1 and SS2 systems. For the beams with  $b_f/2t_f$  equal to 30, the capacity does not vary as the failure occurs due to elastic buckling of the system.

### 3.5.1 CF1 Beams

The variation in the load and deflection capacities of the retrofitted cantilever beams with and without including the strain hardening behaviour of steel is shown in Figure 3.12. In this figure, the load variation is presented as  $P_{1000}/P_0$ , where  $P_{1000}$  and  $P_0$  are the load capacities of the retrofitted beams with and without strain hardening, respectively. The deflection variation at failure is presented as  $\Delta_{1000}/\Delta_0$ , where  $\Delta_{1000}$  and  $\Delta_0$  are deflections at failure of the beams with and without strain hardening, respectively. It is observed that the failure mode of the retrofitted beams is the same with and without strain hardening. From this figure, it is shown that the inclusion of strain hardening increases both the load and deflection at failure for beam B1 for all the considered GFRP thicknesses. However, for the slender beam B25, small improvement is observed only for the larger thickness addition of GFRP plates. For the slender beams with smaller GFRP thicknesses, elastic buckling and onset of yielding of the steel are the dominant modes of failure minimizing the effect of strain hardening on the capacity improvements of the retrofitted beams.

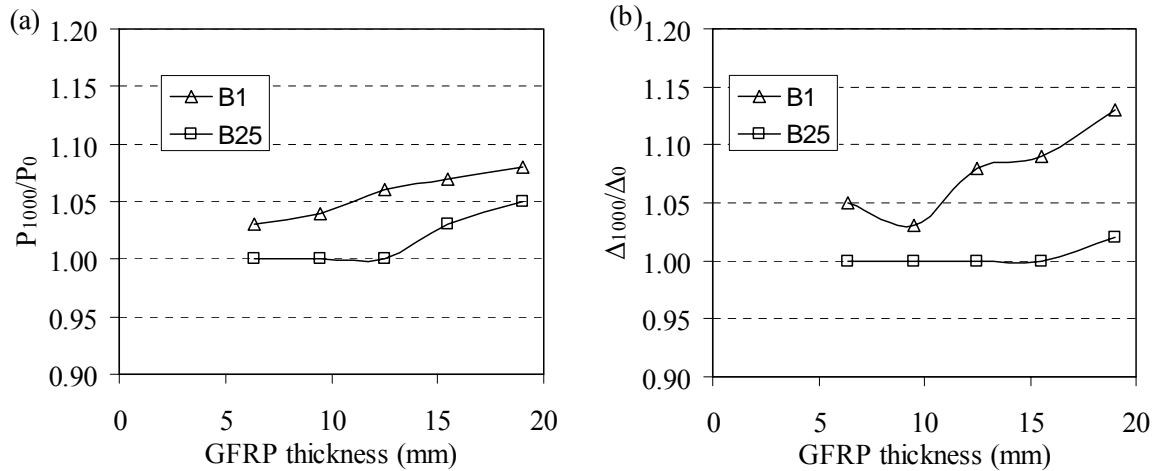


**Figure 3.12** Variation of capacities of retrofitted CF1 beams with and without strain hardening of steel (a) load and (b) deflection.

### 3.5.2 SS1 Beams

For SS1 system, the load and deflection variations due to strain hardening of steel are almost the same as the CF1 system.

### 3.5.3 SS2 Beams

An increase in the load capacity and a decrease in the deflection are observed for the beams of  $b_f/2t_f$  of 10 with the SS2 system. The failure of these retrofitted beams is governed by GFRP rupture. The stiffnesses of the beams after yielding increase by considering the strain hardening of steel. This results in higher capacity and lower deflection at failure of the beams. For the slender beam B25, failure modes are identical with that of elastic-perfectly plastic beams for the GFRP additions up to 12.5 mm. However, inelastic buckling of the retrofitted beam is predicted for a 15.5 mm GFRP addition. This leads to an improvement in the load capacity and a reduction in the



deflection at failure of the beam. For beam B25 with 19.0 mm GFRP plate, failure of the beam is governed by GFRP rupture instead of inelastic buckling. This results in improving both the load carrying capacity and deflection at failure as shown in Figure 3.13.

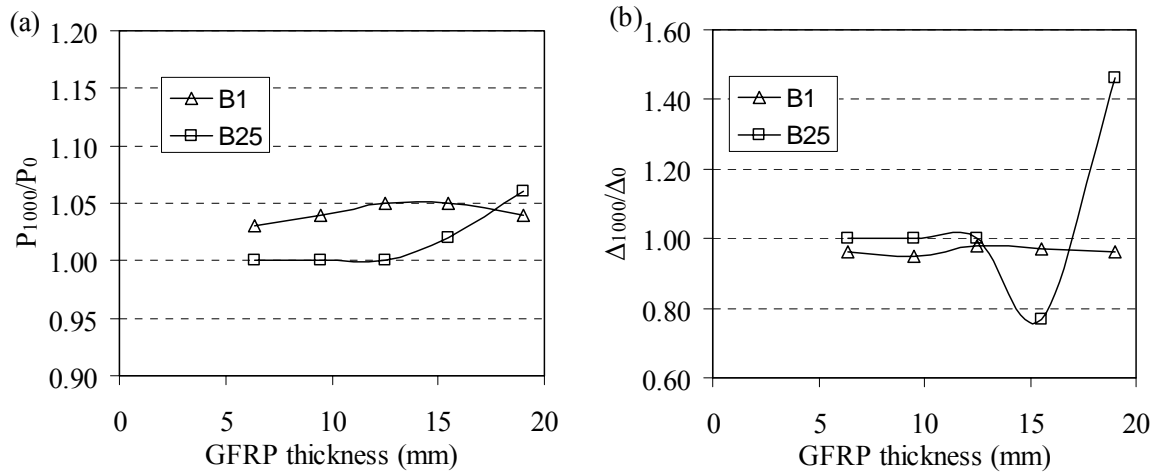


**Figure 3.13** Variation of capacities of retrofitted SS2 beams with and without strain hardening of steel (a) load and (b) deflection.

### 3.6 Influence of Geometric Imperfections on the Capacities of Retrofitted Beams

A parametric study is conducted on the beams of slenderness ratios of 10 and 30 to assess the effect of initial geometric imperfections on the behaviour of the retrofitted beams. The boundary conditions of the beams considered in this analysis are the CF1 and SS2 systems. The initial geometric imperfection shape is assumed for the compression flange of the I-shaped steel beams and is expressed by Equation (3.1). For the retrofitted beams, this initial geometric imperfection shape is applied on both the compressive flange of the steel beams and the GFRP plates attached to that flange. The amplitude of imperfection is considered  $0.001t$ ,  $0.01t$ ,  $0.1t$ ,  $0.25t$ , and  $0.5t$ , respectively, where  $t$  is the thickness of the

compressive flange of the steel beam. The above values lead to a maximum imperfection that is less than  $L/500$ , where  $L$  is the span length of the beam.

The perfect bare steel beam B1 of slenderness ratio of 10 fails by inelastic buckling due to the plastification of steel. The initial imperfections reduce the capacity of the bare steel beams by 6% and 9% due to an imperfection amplitude of 3.75 mm for the CF1 and SS2 systems, respectively. However, an imperfection amplitude less than 0.075 mm for the bare beam B1 of the system SS2 results in higher deflection at failure. As the imperfection amplitudes increase, the load carrying capacity as well as the deflection at failure decrease. For beam B25 of slenderness ratio of 30, failure is governed by elastic buckling. Any initial geometric imperfection will result in an increase in the load carrying capacity of the beams. The increase in load capacity is attributed to the membrane effect of the flanges of the elastic steel beams. This type of hardening behaviour is shown for steel plates that are governed by classical elastic buckling [28-29]. This behaviour is predicted for bare slender beam B25. The failure loads increase by 15% and 30% for an initial imperfection amplitude of 2.5 mm for the CF1 and SS2 beams, respectively.

### **3.6.1 CF1 Beams**

The improvement pattern of retrofitted beams B1 with slenderness ratio of 10 shows that as the initial geometric imperfection increases the load carrying capacity decreases. This trend is shown for the retrofitted beams with 6.35 mm to 19 mm GFRP plates. The failure mode of the beams is the same as that of the beams without any geometric imperfection. The variations in the load and deflection at failure are presented as  $P_{imp}/P_0$  and  $\Delta_{imp}/\Delta_0$ , respectively, where  $P_{imp}$  and  $\Delta_{imp}$  are the load and deflection capacities of the imperfect

beam, respectively and  $P_0$  and  $\Delta_0$  are the load and deflection capacities of the perfect beam, respectively. Such variations are given in Figure 3.14 for beam B1 for different amplitude of imperfections. For retrofitted beam B25 with 6.35 mm GFRP, failure is governed by elastic buckling of the system, leading to an increase in both the load and deflection at failure. This increase in load and deflection is also predicted for the beams with 9.5 mm and 12.5 mm GFRP plates. However, failure of the beams with 15.5 mm and 19.0 mm GFRP plates shows a reduction in both the load and deflection due to presence of geometric imperfections. This reduction in capacities is due to the failure mode of such beams. These beams fail by a GFRP rupture. Any imperfection in these beams will trigger the failure of the beams earlier resulting in reduction in the load and deflection at failure. The variation in the load and deflection at failure of beams B25 is presented in Figure 3.15.

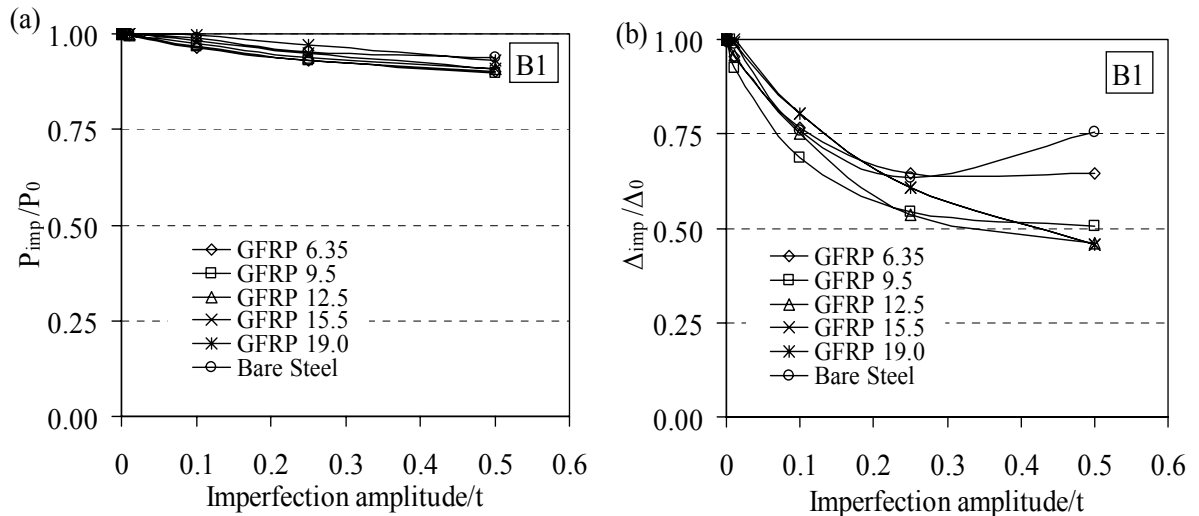


**Figure 3.14** Influence of geometric imperfection on the capacities of CF1 beams B1 (a) load and (b) deflection.

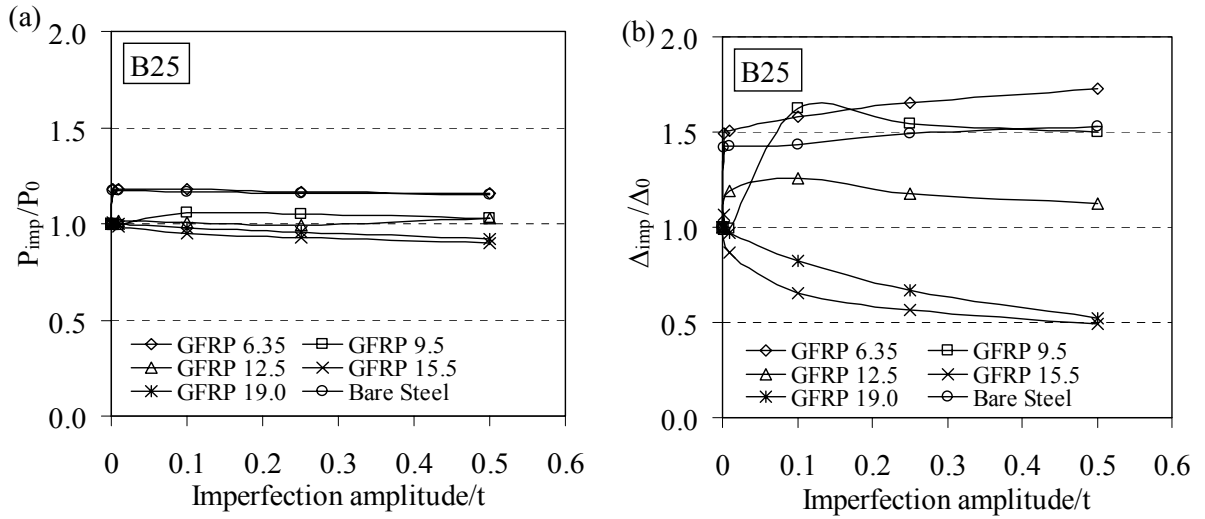


**Figure 3.15** Influence of geometric imperfection on the capacities of CF1 beams B25 (a) load and (b) deflection.

**3.6.2 SS2 Beams**

The results of the SS2 retrofitted beams follow the same trend of variation as that of the CF1 beams. The variations in the load and deflection at failure are plotted in Figures 3.16 and 3.17 for beams B1 and B25, respectively.

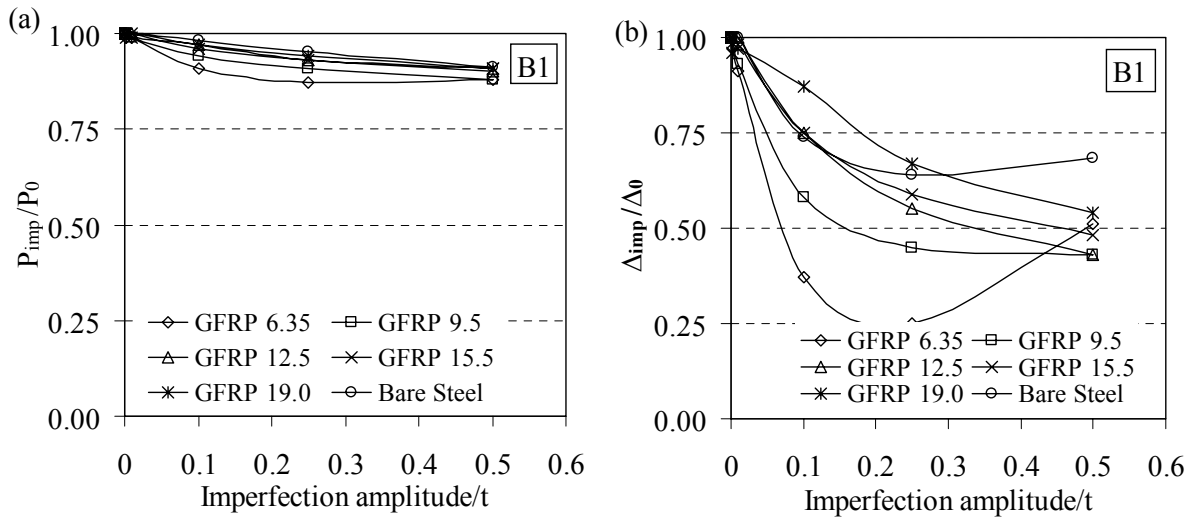


**Figure 3.16** Influence of geometric imperfection on the capacities of SS2 beams B1 (a) load and (b) deflection.

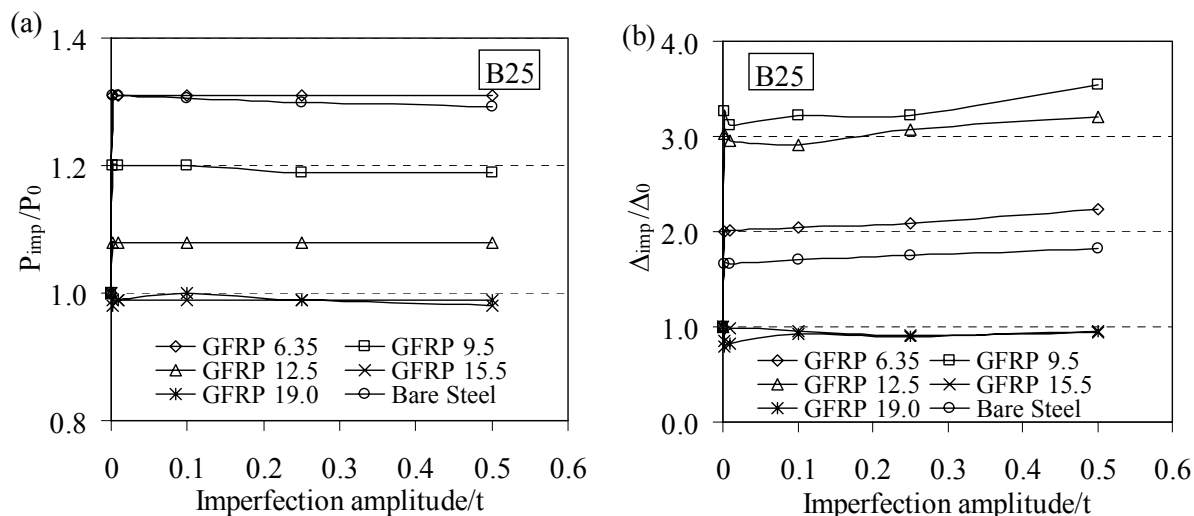


**Figure 3.17** Influence of geometric imperfection on the capacities of SS2 beams B25 (a) load and (b) deflection.

### 3.7 Influence of Residual Stresses in Steel Section on the Capacities of Retrofitted Beams

The effect of residual stresses of steel on the load and deflection improvements of the retrofitted beams is assessed for the slenderness ratios,  $b/t$ , of 10 and 30. CF1 and SS2 systems are considered in this part of the study. The magnitude and distribution of the residual stresses for steel considered in these analyses are as shown in Figure 3.5. The residual stresses are shown to have no significant effect on the load carrying capacity of the bare steel beams with  $b/t$  ratio of 10. However, they increase the deflection at failure of beams B1 and B2 for both the CF1 and SS2 systems. On the other hand, residual stresses are shown to reduce both the load and the deflection of the bare beams of  $b/t$  of 30. The values of the load and deflection at failure of beam B25 are reduced to 75% of the values without residual stresses for the two support conditions.

There is no significant effect of residual stresses on the load and deflection capacities of

the retrofitted beams B1. The failure modes, with and without residual stresses, are shown to remain identical. For the retrofitted beams B25, the failure modes are identical to that of the beams without residual stresses. However, for those SS2 retrofitted beams which fail by elastic buckling and onset of yielding of the steel section, the load and the deflection capacities at failure decrease. This reduction in capacity is presented in Figure 3.18 as  $P_{res}/P_0$  and  $\Delta_{res}/\Delta_0$  for the load and deflection at failure, respectively, where  $P_{res}$  and  $\Delta_{res}$  are the load and deflection capacities of the beams with inclusion of residual stresses.

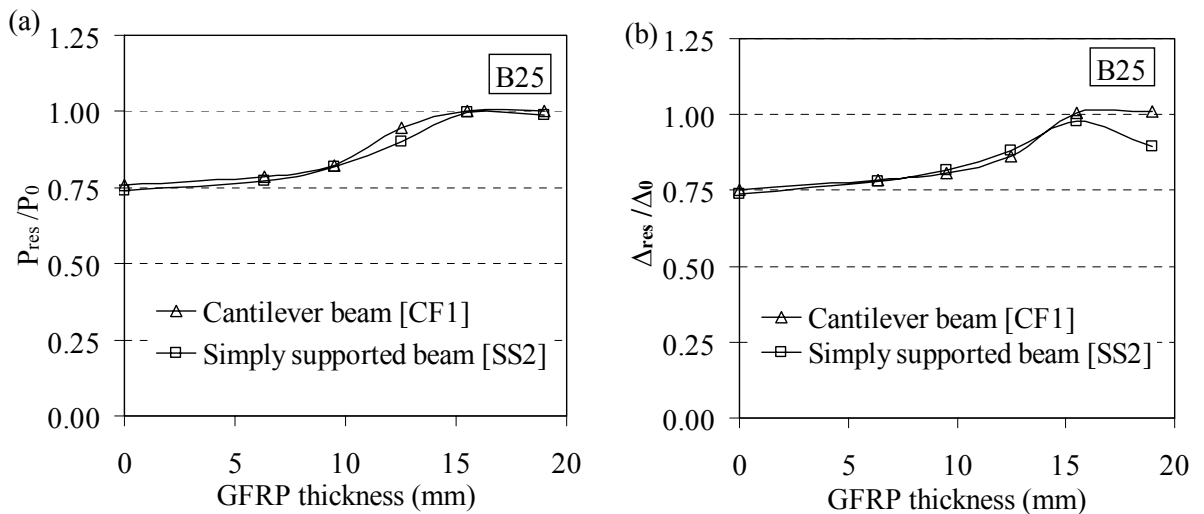


**Figure 3.18** Influence of residual stresses of steel on the capacities of beams B25 (a) load and (b) deflection.

### 3.8 Effect of Span Length of the Beams on the Improvement Factors

The effect of span length of the beams on the improvement factors of the retrofitted beams is studied for the beams having  $b_f/2t_f$  ratios of 10 and 30 for both the CF1 and SS2 systems. Only perfect beams without any initial geometric imperfection and residual

stresses are considered in these analyses. With the exception of the span length of the beam, the material and geometric properties are kept constant. Three span lengths of 2000 mm, 4000 mm, and 6000 mm are considered, respectively.

### 3.8.1 CF1 Beams

For retrofitted beams B1, the failure modes are identical for the three considered span lengths. The load and deflection improvement factors are plotted in Figure 3.19 versus the span length of the beams. From this figure, it is shown that there is little variation in the improvement factors of the beams with the span length. This pattern of variation of the improvement factors is also observed for slender beams B25 as shown in Figure 3.20.

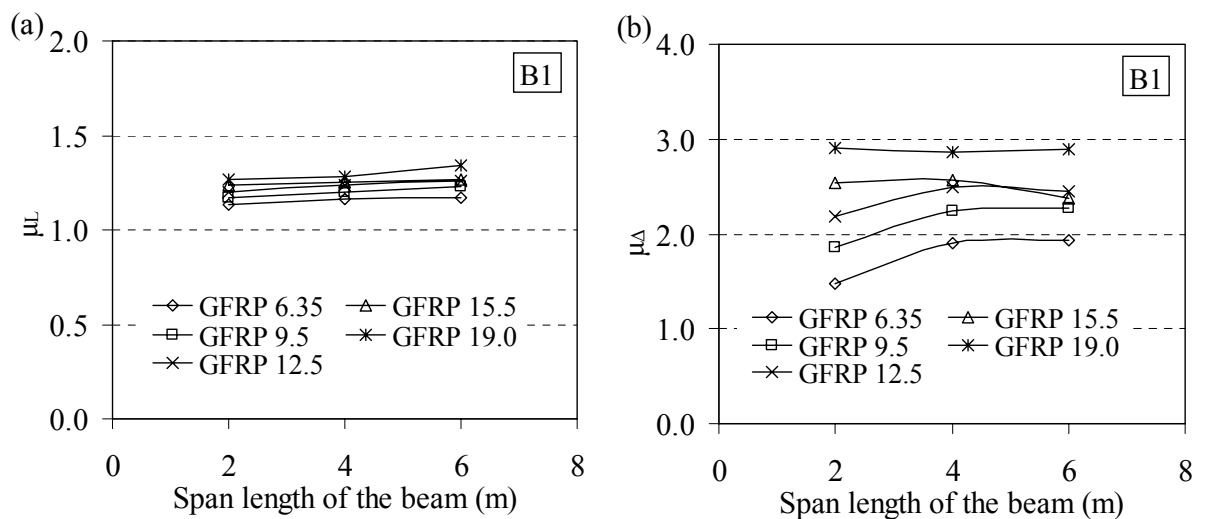


**Figure 3.19** Effect of span length on the Improvement factors of CF1 beams B1 (a) load and (b) deflection.

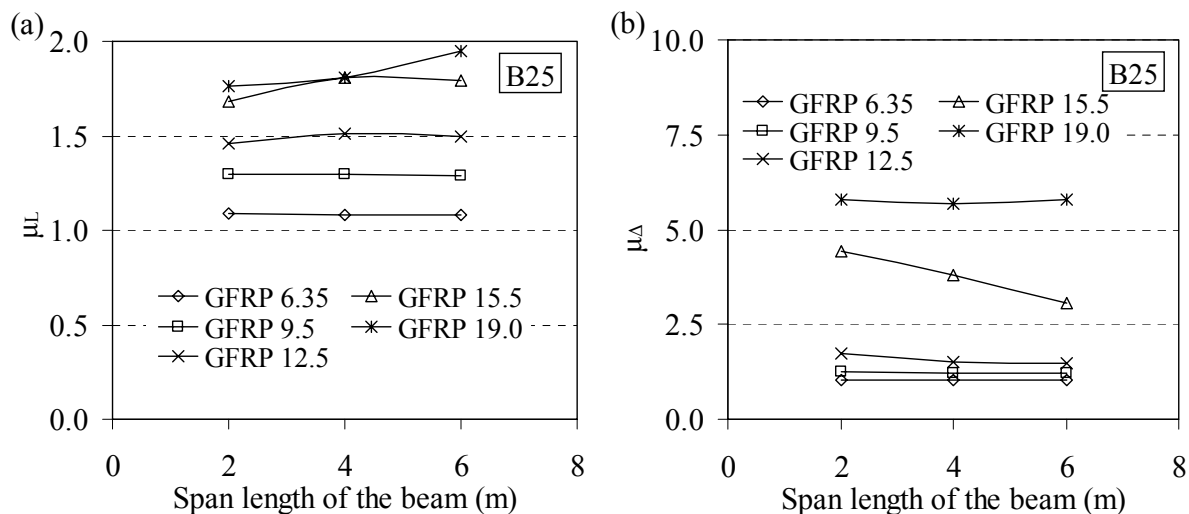


**Figure 3.20** Effect of span length on the Improvement factors of CF1 beams B25 (a) load and (b) deflection.

Elastic buckling of the system is predicted for beams B25 with GFRP additions up to 12.5 mm. However, the failure mode of 15.5 mm retrofitted beam changes to inelastic buckling for the spans of 4m and 6m compared to the GFRP rupture for the 2m span. The beams become more slender as the span length increases and this changes the failure modes from GFRP rupture to inelastic buckling. For the beams with 19.0 mm GFRP, the failure pattern is the same for the different span lengths. As the beam becomes more slender with longer span length, an addition of 19.0 mm GFRP plate shows some variation in improving the load capacities of the retrofitted beams.

### 3.8.2 SS2 beams

The failure pattern of beams B1 is identical for the considered span length except the beam with 19.0 mm GFRP plate. For beams retrofitted with 19.0 mm GFRP plates, shear failure of the adhesive is predicted for the spans of 4m and 6m, while GFRP rupture is



observed for the 2m span. However, an increase in the load capacity is shown in expense of the deflection for longer span length as shown in Figure 3.21. Uniform stresses are developed between the two applied loads of this type of loading and boundary conditions of beams. Bare steel beams fail by plastification of steel. As the span length increases, the beam becomes more slender and the region with uniform stress also increases. The steel beams retrofitted with GFRP plates become stiffer for the beams with longer span than that of the shorter span. This results in an increase in the load capacity and a decrease in the deflection at failure of the retrofitted beams with longer span length.

For slender beams B25, there is little increase in the load carrying capacity for 19.0 mm GFRP addition. As the failure mode changes from GFRP rupture to inelastic buckling with 15.5 mm GFRP at longer span length, the deflection at failure decreases as shown in Figure 3.22. Therefore, the span length has an effect on the improvement factors of the retrofitted beams when large GFRP thicknesses are used.

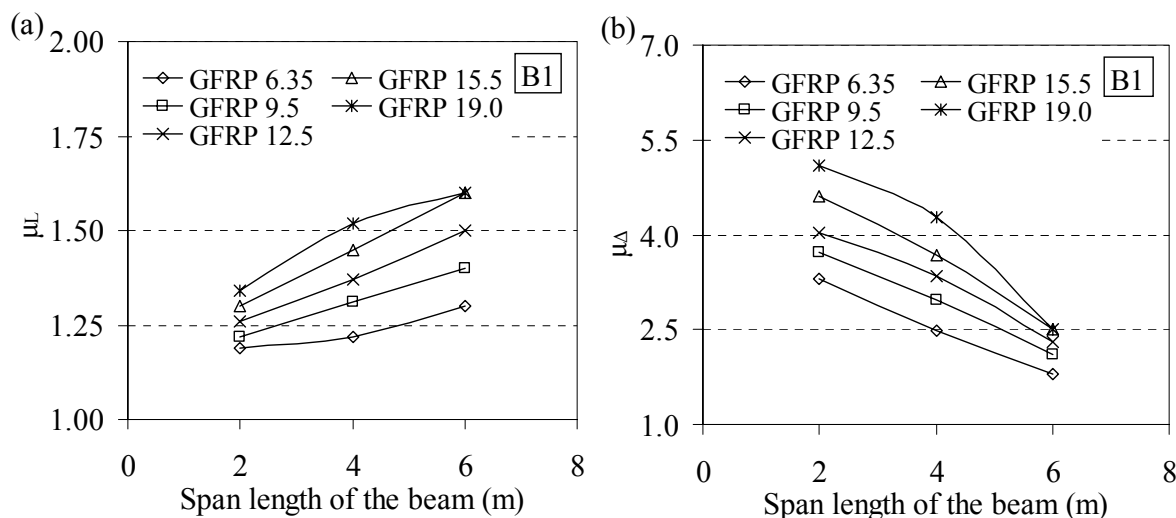


**Figure 3.21** Effect of span length on the Improvement factors of SS2 beams B1 (a) load and (b) deflection.

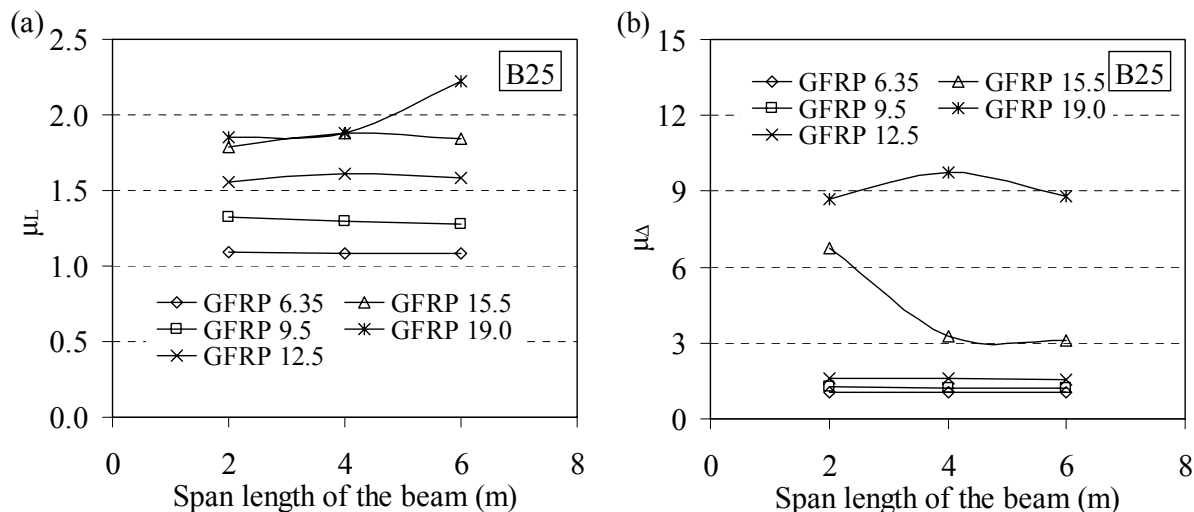


**Figure 3.22** Effect of span length on the Improvement factors of SS2 beams B25 (a) load and (b) deflection.

### 3.9 Conclusions

A finite element model developed in-house is used to assess the improvement in the behaviour of steel beams retrofitted by bonding GFRP to their compression flanges. The consistent degenerated thick shell element is used to model both the steel beams and GFRP plates. A set of linear spring system is used to simulate the bond behaviour between the flange of steel beam and the GFRP plate. A special interface element is used to simulate the actual adhesive strength and stiffness properties. The mechanical properties of the adhesive are based on real values determined experimentally from previous studies. The model is validated through comparison with numerical and experimental results available in literature for both bare steel beams and steel beams retrofitted with GFRP. The enhancement in the load and deflection at failure of the retrofitted beams is assessed for cantilever and simply supported boundary conditions using various GFRP plate thicknesses. The study also considers the effect of strain

hardening of steel, initial geometric imperfections, and residual stresses of steel on the variation of the capacities of beams. Finally, the effect of various span lengths of beams on the improvement factors and modes of failure is discussed.

The following conclusions can be drawn from the conducted analyses:

- The addition of GFRP plates to the compression flange of wide flange steel beams increases both the load carrying capacity and deflection at failure. However, the improvement factor is higher for the slender beams than that of plastic beams.
- For a specific slenderness ratio of the flange of the beams, the improvement in the load capacity is independent of the web dimensions of the beams. This trend is observed for both the plastic and slender beams.
- For the plastic beams, the modes of failure are governed by GFRP rupture. No premature failure in adhesive is shown before the beams reach their capacities.
- The mode of failure of the retrofitted slender beams ranges from elastic buckling of the system to GFRP rupture when the thickness of the GFRP is varied from 6.35 mm to 19.0 mm.
- The strain hardening behaviour of steel has little effect on the improvement of both the load and deflection capacities of the retrofitted beams. Only retrofitted beams which fail by GFRP rupture show improvement in the capacity due to the inclusion of strain hardening.
- The initial geometric imperfection has a significant effect on both the load and deflection capacities of the plastic beams. However, for the retrofitted beams that fail by elastic buckling, the inclusion of the geometric imperfection increases both the load and deflection capacities due to membrane effect of the compressive

flange of the beam. The improvement ratios with and without geometric imperfection of these beams are insensitive to the amplitude values.

- Residual stresses of steel have an insignificant effect on the load and deflection improvements of the plastic beams. However, they reduce both the load and the deflection for the retrofitted slender beams that fail by elastic buckling and onset of yielding of the system.
- The effect of different span lengths on the load and deflection improvement factors is insignificant for the cantilever support condition. For the simply supported beams with two-point loading system, the load capacity increases in expense of a decrease in the deflection at failure. The failure modes of the retrofitted beams also change from GFRP rupture to shear failure of the adhesive for the longer span.

### **3.10 References**

- [1] Saadatmanesh, H. and Ehsani, M. R., RC beams strengthened with GFRP plates. I: Experimental study, *Journal of Structural Engineering*, ASCE 1991; 117(11): 3417-3433.
- [2] Saadatmanesh, H., Extending service life of concrete and masonry structures with fiber composites, *Construction and Building Materials* 1997; 11(5-6): 327-335.
- [3] Neale, K. W., FRPs for structural rehabilitation: a survey of recent progress, *Progress in Structural Engineering and Materials* 2000; 2(2): 133-138.
- [4] Sheikh, S. A., DeRose, D., and Mardukhi J., Retrofitting of concrete structures for shear and flexure with fiber-reinforced polymers, *ACI Structural Journal* 2002;

- 99(4): 451- 459.
- [5] Mufti, A. A., FRPs and FOSs lead to innovation in Canadian civil engineering structures, *Construction and Building Materials* 2003; 17(6-7): 379-387.
- [6] Van Den Einde, L., Zhao, L., and Seible, F., Use of FRP composites in civil engineering applications, *Construction and Building Materials* 2003; 17(6-7): 389-403.
- [7] Nanni, A., North American design guidelines for concrete reinforcement and strengthening using FRP: principles, applications, and unresolved issues, *Construction and Building Materials* 2003; 17(6-7): 439-446.
- [8] Barros, J. A. O., Dias, S. J. E., and Lima, J. L. T., Efficacy of CFRP-based techniques for the flexural and shear strengthening of concrete beams, *Cement and Concrete Composites* 2007; 29(3): 203-217.
- [9] Hollaway, L. C., The evaluation of and the way forward for advanced polymer composites in the civil infrastructure, *Construction and Building Materials* 2003; 17(6-7): 365-378.
- [10] Tavakkolizadeh. M. and Saadatmanesh, H., Strengthening of steel–concrete composite girders using carbon fiber reinforced polymer sheets, *Journal of Structural Engineering, ASCE* 2003; 129(1): 30-40.
- [11] Colombi, P. and Poggi, C., Strengthening of tensile steel members and bolted joints using adhesively bonded CFRP plates, *Construction and Building Materials* 2006; 20(1-2): 22-33.
- [12] Karbhari, V. M. and Shulley, S. B., Use of composites for rehabilitation of steel structures–determination of bond durability, *Journal of Materials in Civil*

- Engineering, ASCE 1995; 7(4): 239-245.
- [13] Sen, R., Liby, L., and Mullins, G., Strengthening steel bridge sections using CFRP laminates, *Composites Part B: Engineering* 2001; 32(4): 309-322.
- [14] Miller, T. C., Chajes, M. J., Mertz, D. R., and Hastings, J. N., Strengthening of a steel bridge girder using CFRP plates, *Journal of Bridge Engineering*, ASCE 2001; 6(6): 514-522.
- [15] Tavakkolizadeh, M. and Saadatmanesh, H., Galvanic corrosion of carbon and steel in aggressive environments, *Journal of Composites for Construction*, ASCE 2001; 5(3): 200-210.
- [16] El Damatty, A., Abushagur, M., and Youssef, M. A., Experimental and analytical investigation of steel beams rehabilitated using GFRP sheets, *Steel and Composite Structures* 2003; 3(6): 421-438.
- [17] Shaat, A. and Fam, A., Axial loading tests on short and long hollow structural steel columns retrofitted using carbon fiber reinforced polymers, *Canadian Journal of Civil Engineering* 2006; 33(4): 458-470.
- [18] Accord, N. B. and Earls, C. J., Use of fiber-reinforced polymer composite elements to enhance structural steel member ductility, *Journal of Composites for Construction*, ASCE 2006; 10(4): 337-344.
- [19] El Damatty, A. and Abushagur, M., Testing and modeling of shear and peel behavior for bonded steel/FRP connections, *Journal of Thin-Walled Structures* 2003; 41(11): 987-1003.
- [20] Chakrabarti, P. R. and Mosallam, A. S., Performance of welded steel beam-to-column joints seismically retrofitted with polymer composites & steel stiffeners,

- Fiber Composites in Infrastructure Conference, Tuscan, Arizona, USA ICCI-1998, pp. 160 – 174.
- [21] Koziey, B. L. and Mirza, F. A., Consistent thick shell element, *Computers and Structures* 1997; 65(12): 513-541.
- [22] El Damatty, A., Korol, R. M., and Mirza, F. A., Large displacement extension of consistent shell element for static and dynamic analysis, *Computers and Structures* 1997; 62(6): 943-960.
- [23] Hasham, A. S. and Rasmussen, K. J. R., Interaction curves for locally buckled I-section beam-columns, *Journal of Constructional Steel Research* 2002; 58(2): 213-241.
- [24] Hasham, A. S. and Rasmussen, K. J. R., Section capacity of thin-walled I-section beam-columns, *Journal of Structural Engineering, ASCE* 1998; 124(4): 351-359.
- [25] Daali, M. L. and Korol, R. M., Low cycle fatigue damage assessment in steel beams, *Structural Engineering and Mechanics* 1995; 3(4): 341-358.
- [26] Canadian Institute of Steel Construction (CISC), *Handbook of Steel Construction*, 10<sup>th</sup> edition, 2010, Canada.
- [27] M. Bruneau, C. Uang, and A. Whittaker, *Ductile Design of Steel Structures*, McGraw-Hills Companies, Inc., 1998.
- [28] P. S. Bulson, *The stability of flat plates*, American Elsevier Publishing Company, New York, 1969.
- [29] Bakker, M. C. M., Rosmanit, M., and Hofmeyer, H., Prediction of the elasto-plastic post-buckling strength of uniformly compressed plates from the fictitious elastic strain failure, *Journal of Thin-Walled Structures* 2009; 47(1): 1-13.

**CHAPTER 4**

**SEISMIC PERFORMANCE OF MOMENT RESISTING STEEL FRAMES**

**RETROFITTED AT BEAMS' FLANGES WITH GFRP PLATES\***

#### **4.1 Introduction**

The seismic design of a steel moment resisting frame (SMRF) is usually based on the concept of strong column/weak beam in which the energy is dissipated through formation of plastic hinges near the column faces. In these frames, normally Class 1 beams (plastic section) are used, where the slenderness ratios of the flanges and web are relatively low. These design guidelines are well documented in steel construction manuals [1-2]. The ductility of SMRF depends primarily on failure modes like the fracture of beam flange-to-column welds for welded connections, the lateral torsional buckling of the beams, and the flange/web local buckling.

Most of the research conducted after the 1994 Northridge (US) and the 1995 Kobe (Japan) earthquakes focused on preventing the brittle weld fractures observed in welded SMRF as reported by Nakashima et al. [3] and Uang et al. [4]. Although with the help of new design guidelines, brittle fractures can be satisfactorily mitigated, local buckling of beam flanges and webs is still a concern for the ductility and stability of the members. In current seismic design codes, local instability is prevented by limiting the flange/web slenderness ratios. However, the rotation capacities expected from beam-column connections have been increased as a result of the research of the post-Northridge and the post-Kobe earthquakes. So, existing structures that lack adequate slenderness ratios might

---

\*A version of this chapter is prepared for publication in the *Canadian Journal of Civil Engineering*.



be prone to local buckling and require retrofitting. If the structures at present are subjected to more loads than the design loads specified in old design codes, they may also require retrofitting.

Fiber Reinforced Plastic (FRP) sheets are commonly used for seismic upgrading of existing reinforced concrete (RC) structures. FRP materials have several advantages such as lightweight, superior strength, and high stiffness-to-weight ratios. They also have a high corrosion resistance and can easily be bonded to concrete members. Research studies on the seismic retrofit of RC frames, including strengthening deficient members such as beams, columns and beam-to-column joints to increase strength, stiffness, and/or ductility, have been carried out by many researchers [5-9]. The use of FRP to enhance the overall seismic performance of RC frames by increasing lateral strength, reducing drift and/or increasing ductility has also been carried out by some researchers [10-12].

The application of FRP composites has been recently extended to the repair and strengthening of steel members. However, most of the research works focused on the use of FRP for enhancing the load carrying capacity or restoring the strength of deteriorated members [13-18]. Generally, high modulus carbon FRP (CFRP) laminates, which have elastic modulus similar to that of steel, are preferred in flexural and shear strengthening applications. A few studies are available in the literature that reports the improvement of local buckling capacity of steel sections using FRP. Syed-Ahmed [19] numerically studied the performance of retrofitted I-beams, where CFRP strips were used in the compression region of the webs of the beams. The parametric studies showed that the local buckling of the webs could be delayed resulting in an increase in strength of the beams. A finite element study conducted by Accord and Earls [20] also showed the

improvement of the rotation capacity and strength of glass FRP (GFRP) strengthened cantilever I-beams. An experimental study was conducted by El-Tawil et al. [21] on CFRP-wrapped double channel built-up members subjected to reverse cyclic loading. The plastic hinge regions of the beams were retrofitted with CFRP strips to assess the improvement in the local and global instabilities of the members. From the test results, it was shown that the application of CFRP increases the size of the yielded plastic hinge region, and thereby reduces the occurrence of local buckling and delays the lateral torsional buckling of the members.

In the Chapter 3, the behaviour of steel beams retrofitted with GFRP plates was characterized in terms of their capacities and deflections at failure. The objective of the current chapter is to assess the global lateral behaviour of steel moment resisting frames whose beams are strengthened with GFRP plates. Two different existing frames, representing a three-story and a nine-story building are considered. In addition, generic frames with two different slenderness ratios for the beams of the existing three-story frame are analyzed. GFRP plates are assumed to be bonded to both the top and bottom flanges of the W-shape steel girders. Detailed finite element analysis, in which all the components of the girders are simulated using shell elements, is first conducted in order to determine the moment-rotation characteristics of the retrofitted girders. The nonlinear numerical simulation takes into account the flexibility of the adhesive based on realistic values obtained from previously conducted tests. Various modes at failure such as elastic and inelastic buckling, shear and peeling failure of the adhesive, and GFRP rupture are considered in these analyses. The characteristics of the retrofitted beams are implemented into a nonlinear model where the columns and the beams of the rigid frames are

simulated using frame elements. The seismic performance level, in terms of ductility and overstrength factors, are obtained from nonlinear static pushover analyses conducted on the retrofitted frames. Comparison is made with the seismic performance level of the original frames.

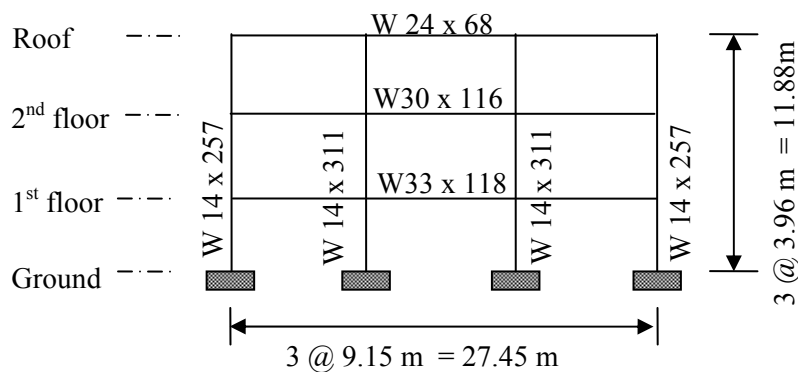
## **4.2 Description of Steel Frames Used in the Study**

### **4.2.1 Original Steel Frames**

The three- and nine-story frames used in this study were designed by Brandow and Johnston Associates for the SAC Phase II Steel project (1996). The three- and nine-story buildings meet the local seismic code requirements and represent typical low- and medium-rise buildings designed for the Los Angeles, California region, respectively.

The three-story (3-story) structure is 36.58 m x 54.87 m in plan and 11.88 m in elevation. The span length of the frame is 27.45 m. The bays are 9.15 m on center and the typical floor height is 3.96 m. The lateral load-resisting system of the building is comprised of steel perimeter moment resisting frames. Both the columns and beams of the frame are wide flange sections. The yield strength of the columns is 345 MPa while that of the beams is 248 MPa. The seismic mass of the structure is comprised of various components including the steel framing, floor slabs, ceiling/flooring, mechanical/electrical, partitions, roofing, and a penthouse located on the roof the buildings. The seismic mass of the first and second levels is  $9.57 \times 10^5$  kg and the third level is  $1.04 \times 10^6$  kg. The seismic mass of the entire structure is  $2.95 \times 10^6$  kg. The column bases are considered fixed at the ground level. The exterior column size is W14 x 257 and the interior column size is W14 x 311. The column cross sections are constant throughout the height of the building. The

fundamental period of this building is 1.00 seconds as determined by Akbas et al. [22]. The nine-story (9-story) structure is 45.75 m x 45.75 m in plan, and 37.17 m in elevation. The bays are 9.15 m on center and the typical story height except the basement and ground levels is 3.96 m. The floor-to-floor height for the basement is 3.65 m and that of the first floor is 5.49 m. The beams and columns of this frame consist also of wide flange sections having the same material properties as the 3-story frame. The steel perimeter MRF is the lateral load-resisting system. The bases of the columns are considered pinned at the ground level. However, concrete foundation walls and surrounding soil are considered to restrain the structure at the ground level from moving laterally. The seismic masses are  $9.65 \times 10^5$  kg,  $1.01 \times 10^6$  kg,  $9.89 \times 10^5$  kg, and  $1.07 \times 10^6$  kg for the ground, first, second to eighth, and ninth level, respectively. The seismic mass above the ground level of the entire structure is  $9.00 \times 10^6$  kg. The exterior and interior columns have similar cross-sections. The fundamental period of the structure is 2.10 seconds as determined by Akbas et al. [22]. An elevation view of the considered frames with their member sizes is presented in Figure 4.1.



(a) 3-story frame

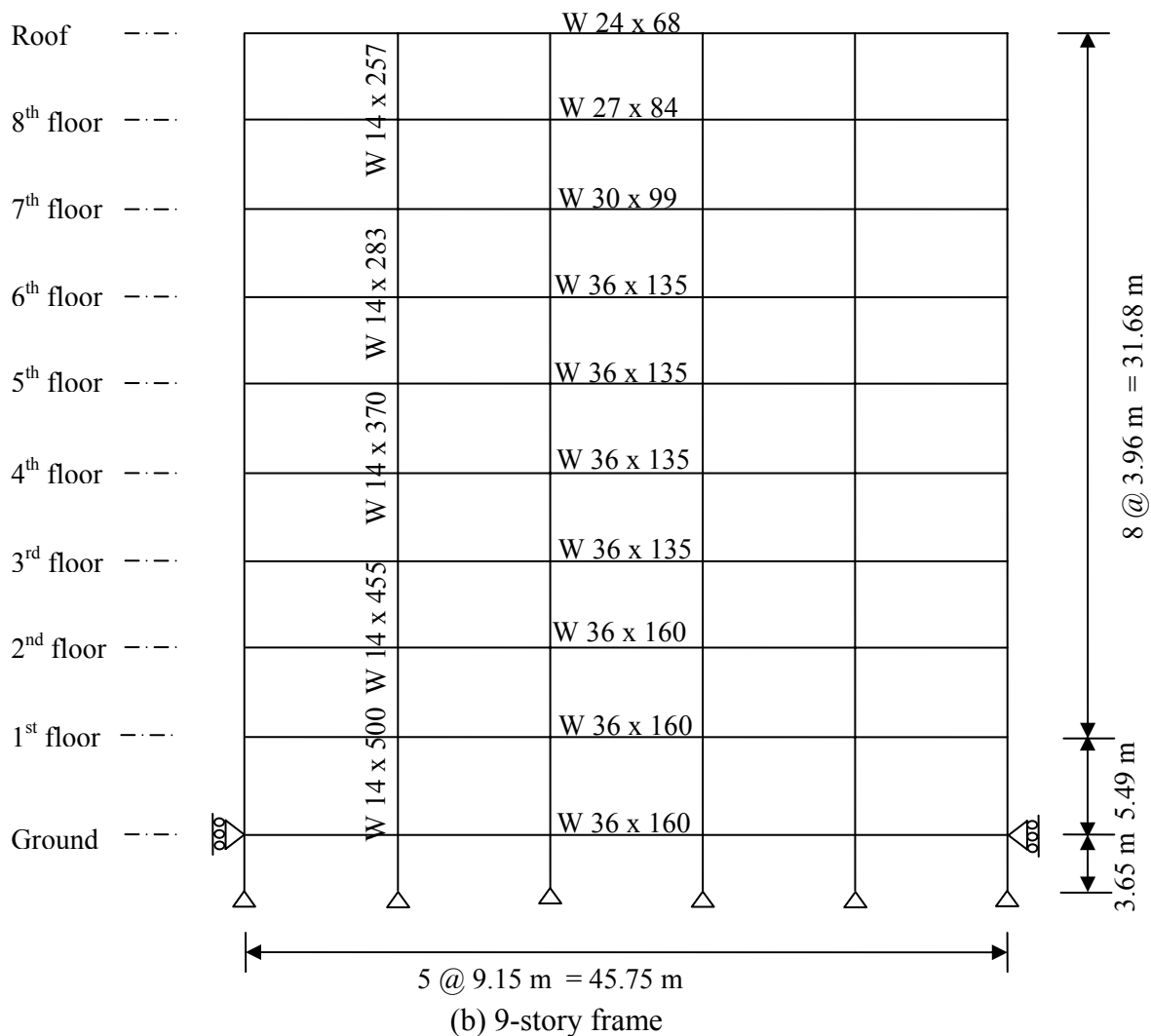


**Figure 4.1** Elevation of the original frames considered in the present study.

#### 4.2.2 Generic 3-story Steel Frames

Analyses are conducted on generic frames having beams with the same inertias of the original 3-story frames but with different slenderness ratios for the flanges of the beams. Two different slenderness ratios for the flanges of the beams are considered,  $b/t = 25$  and  $30$ . Slenderness ratio,  $b/t = 25$ , generates beams that develop a capacity higher than the yield moment but less than the plastic moment. On the other hand, beams with

slenderness ratio,  $b/t$ , of 30 develop a moment capacity close to the yield moment of the member.

### 4.2.3 Retrofitted Steel Frames with GFRP Plates

#### 4.2.3.1 3-story Frames

Two retrofitting scheme cases are considered in the pushover analyses. These cases are shown in Figure 4.2. In Case (a), the beams of the frame are retrofitted only at the middle bay of the frame, which is labeled as F3-B1. For Case (b), the beams are retrofitted along the entire three spans of the frame, which is labeled as F3-B3. For each case, two types of retrofitting pattern are used. In the first type, beams of the three levels of the frames are retrofitted with the same thickness of GFRP plates and these frames are labeled as F3-B1-C and F3-B3-C for the retrofitted middle bay and total spans, respectively.

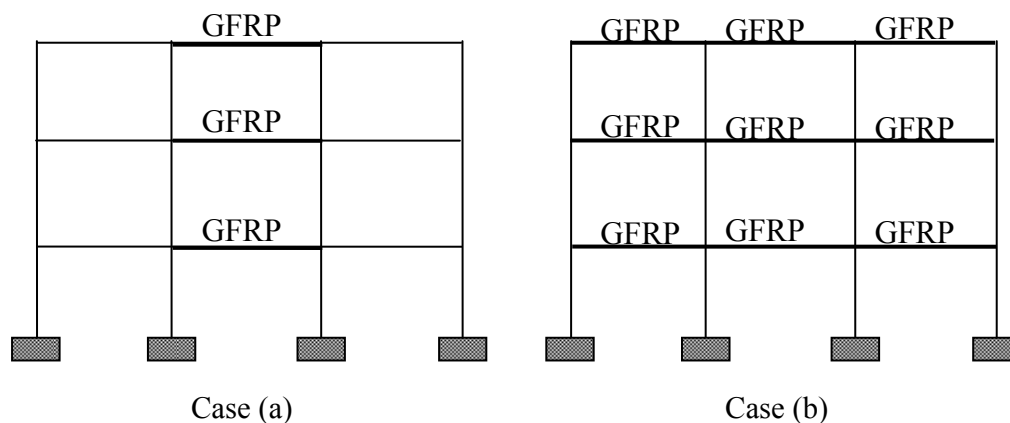


**Figure 4.2** Retrofitting schemes for the 3-story frame.

In the second type, a larger thickness of GFRP plates at the bottom story than that of the upper story is considered and these frames are labeled as F3-B1-V and F3-B3-V for the

retrofitted middle bay and total spans, respectively. Nonlinear static pushover (NSP) analyses are carried out for each case to assess the enhancement in the seismic performance of the retrofitted frames in comparison to the original frames.

#### ***4.2.3.2 9-story Frames***

Three cases are considered for the 9-story frame to assess the seismic performance of the frame with different thicknesses of GFRP plates. Case (a) involves retrofitting of the beams only at the center bay (F9-B1 frame). Case (b) and Case (c) involve the retrofitting of the beams of the frame at the middle 3-bay (F9-B3 frame) and the entire spans (F9-B5 frame), respectively. For each case, two types of retrofitted pattern that are identical to that of the 3-story frame are considered. These result in three frames labeled F9-B1-C, F9-B3-C, and F9-B5-C for the retrofitted scheme of an equal thickness of GFRP plates for all the beams of the frame. For the variable thickness of the GFRP plates along the height, the three frames are labeled as F9-B1-V, F9-B3-V, and F9-B5-V.

#### ***4.2.3.3 Generic 3-story Frames***

To assess the seismic performance for the generic slender frames, steel beams retrofitted with different thicknesses of GFRP plates are used in the NSP analyses. The analyses are carried out for all the cases as mentioned for the retrofitted 3-story frame in subsection 4.2.3.1. The retrofitted frames are labeled as GF3-B1-C and GF3-B3-C for the equal thickness addition of GFRP plates on the middle bay and total spans, respectively. For the addition of variable thickness of GFRP plates, the frames are termed as GF3-B1-V and GF3-B3-V for the middle bay and total spans, respectively.

### **4.3 Moment-Rotation Relationships for Beams of the Frame**

#### **4.3.1 Finite Element Model**

A finite element model, based on shell element discretization that is developed in-house and considers realistic strength values for the adhesive and GFRP plates, is used to determine the moment-rotation relationship of steel beams retrofitted with GFRP plates. The details of the model and its validation are presented in the previous chapters. In this model, a consistent shell element that was formulated by Koziy and Mirza [23] and was then extended by El Damatty et al. [24] to include the effects of material and geometric nonlinearities is used to model the flanges and web of the steel beams as well as the GFRP plates. This element is free from the shear-locking phenomenon observed in many isoparametric shell elements when used to model thin shell structures. The nonlinear finite element model has the flexibility to incorporate either an elastic-perfectly plastic or a bilinear strain hardening behaviour for steel. The material model is based on the von Mises yield criterion and its associated flow rule. A special interface element, compatible with the consistent shell element, is used to simulate the adhesive layer bonding the GFRP plates to the flanges of the steel beams. Steel beams with yield strength of 248 MPa and an elastic modulus of  $2 \times 10^5$  MPa are considered in the study. A bilinear strain hardening with a post-yielding modulus equal to 3% of the elastic modulus of steel is considered in the numerical analysis. For the retrofitted beams, different thicknesses of GFRP plates are bonded to both the top and bottom flanges of the beams. The thicknesses of the considered GFRP plates range from 6.35 mm to 19.0 mm. The material properties of the GFRP plate and the adhesive are similar to those used in the experimental study conducted by El Damatty et al. [25-26] and are given below.



For the GFRP plates:

- (i) Tensile or compressive strength = 206.8 MPa
- (ii) Modulus of elasticity =  $1.72 \times 10^4$  MPa
- (iii) Poisson's ratio = 0.33

For the adhesive:

- (i) Shear stiffness,  $K_s = 21.79 \text{ N/mm}^3$
- (ii) Peeling stiffness,  $K_p = 2.26 \text{ N/mm}^3$
- (iii) Allowable shear strength,  $\sigma_s = 15.5 \text{ MPa}$
- (iv) Allowable peel strength,  $\sigma_p = 4.0 \text{ N/mm}$

A number of analyses with different mesh sizes are performed on both bare steel beams and retrofitted beams with different thicknesses of GFRP plates. From the analyses, it is concluded that 576 elements for the bare beams and 960 elements for the retrofitted beams predict the behaviour with good accuracy. For the bare beams, the 576 elements are divided equally between the two flanges and the web: 192 elements for each. For the retrofitted beams, 192 elements are used to model each GFRP plate attached to the flanges of beams. The 192 triangular elements have 96 rectangular divisions with 48 along the length and 2 along the width of the beams. A typical finite element mesh for a W-shaped cantilever beam is presented in Figure 4.3.

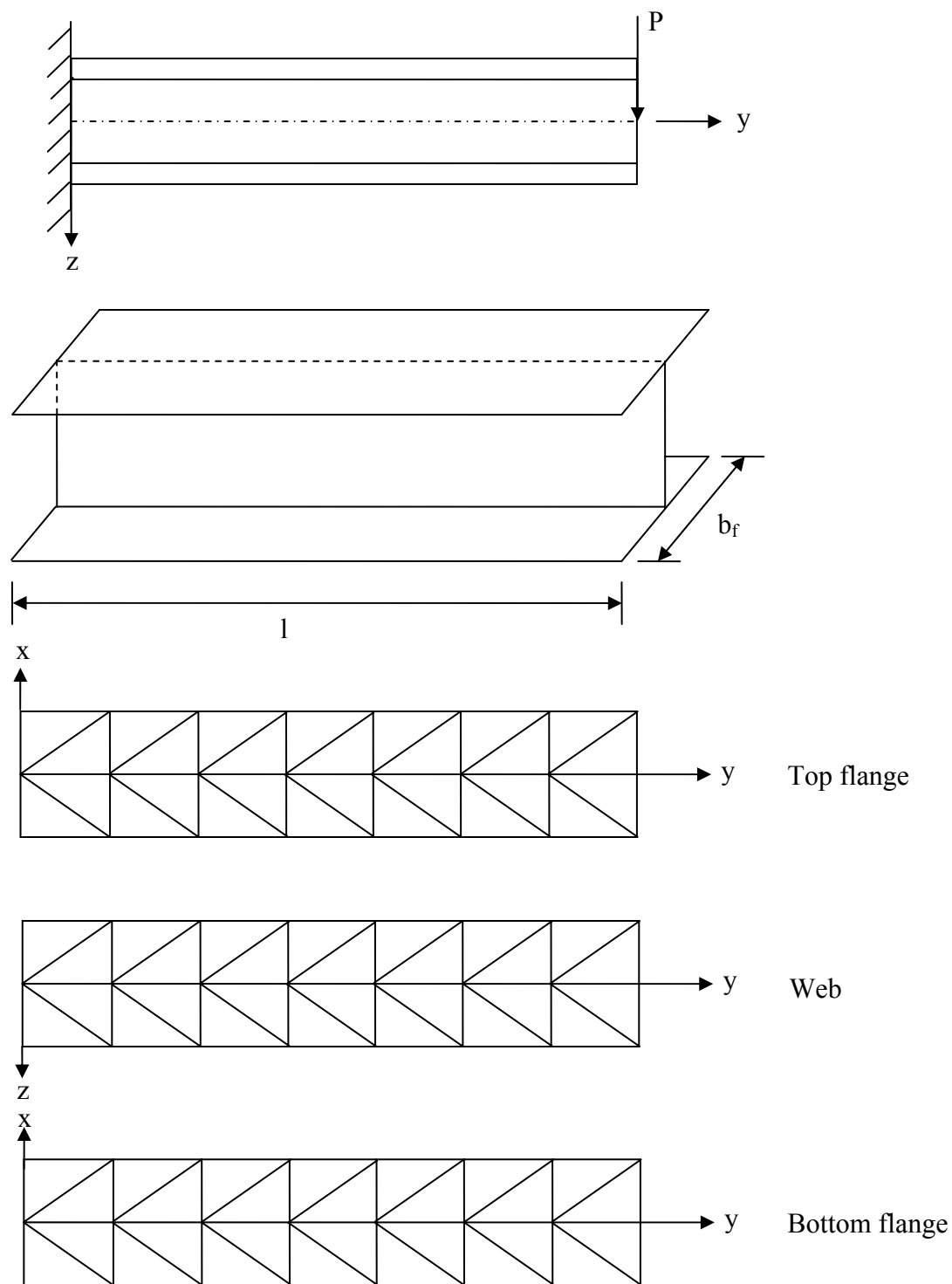


**Figure 4.3** A typical finite element mesh for a W-shaped cantilever beam.

### 4.3.2 Determination of Moment (M)-Rotation ( $\theta$ ) Relationships of Beams

The plastic hinges that simulate the moment-rotation relationship are based on the assumption that all inelastic deformations are concentrated in a hinge of zero length located at each end of the girder. The moment capacity of a section of the girder is calculated considering a cantilever beam subjected to a point load at its free end. Based on the assumption of a point of contraflexure at mid-length of the girder, the length of the cantilever beam used is half the span length of the girder. Using the shell element model, steel beams with and without GFRP plates, as shown in Figure 4.4 (b), are loaded incrementally till the member fails by one of the following failure modes: (i) elastic buckling of the system, (ii) inelastic buckling of the system, (iii) full plastification of steel, (iv) shear failure of the adhesive, (v) peeling failure of the adhesive, and (vi) GFRP rupture. A typical load (P)-deflection ( $\Delta$ ) relationship of a steel beam with and without GFRP plates is presented in Figure 4.5 (a).

The deflection ( $\Delta$ ) at the free end of the cantilever depends on the applied load (P), span length (l) and flexural stiffness (EI) of the section. This deflection can be expressed as:

$$\Delta = Pl^3/(3EI_{\text{eff}}) \quad (4.1)$$

where,  $EI_{\text{eff}}$  is the effective flexural stiffness of the beam.

The rotation capacity ( $\theta$ ) at the end of a girder, shown in Figure 4.4 (a), can be expressed by:

$$\theta = \Delta/l \quad (4.2)$$

This deflection  $\Delta$  can be considered as the same deflection at the end of a cantilever beam with a free-end point loading as shown in Figure 4.4 (b).

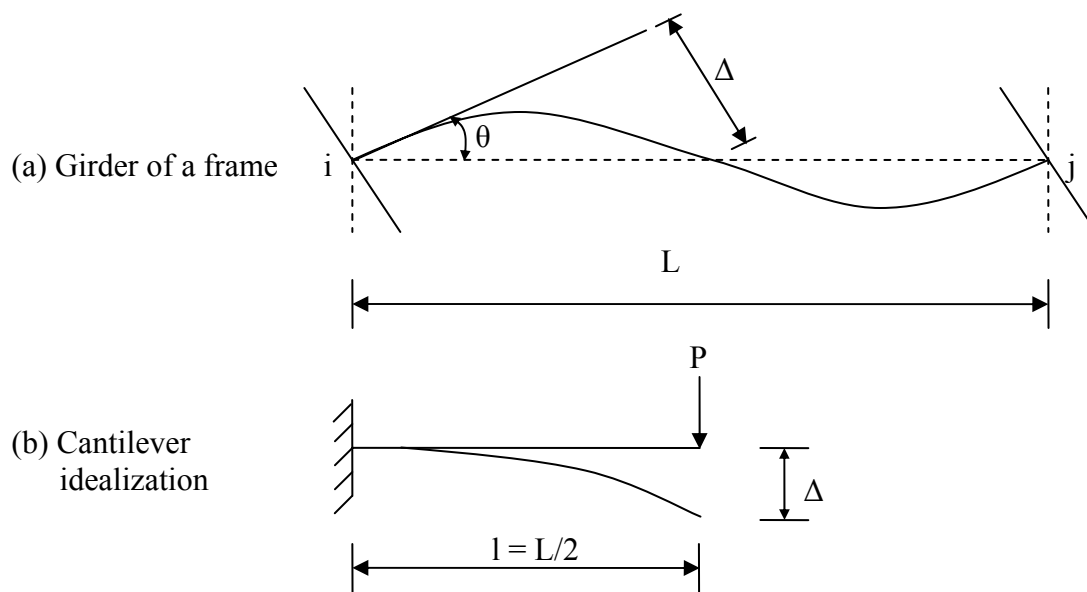


**Figure 4.4** Derivation of the rotation capacity at the end of a girder of a frame.

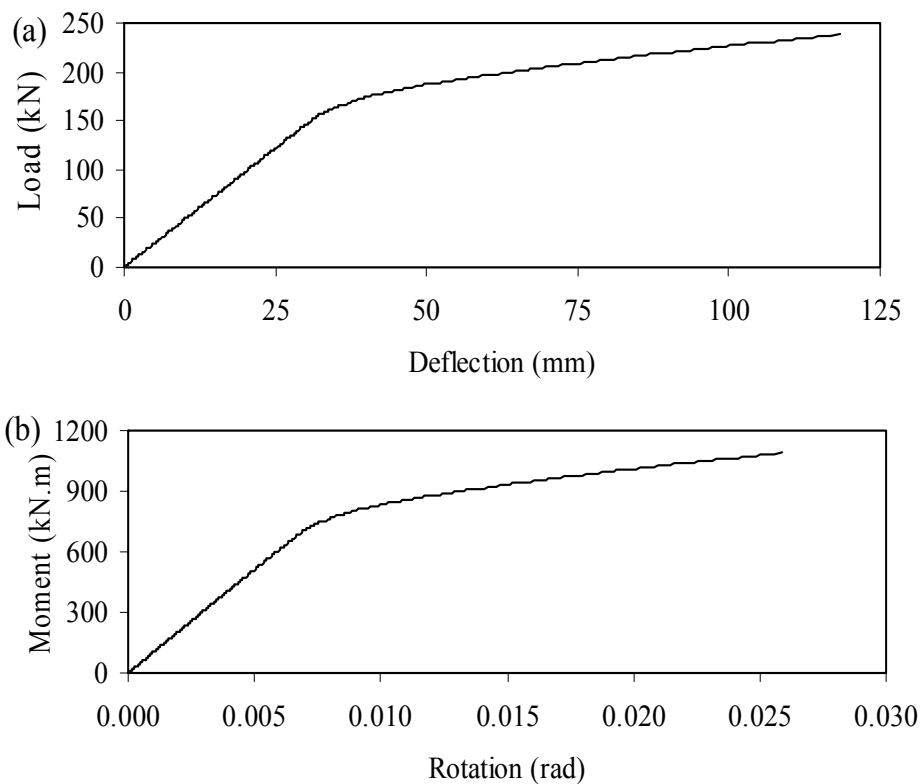


**Figure 4.5** Typical (a) P- $\Delta$  and (b) M- $\theta$  relationships of a beam.

The rotation capacity ( $\theta$ ) for a moment capacity ( $M = Pl$ ) can be obtained by replacing  $\Delta$  in Equation (4.2) as:

$$\theta = M l / (3EI_{\text{eff}}) \quad (4.3)$$

$$\Rightarrow M/\theta = (3EI_{\text{eff}})/l = (P/\Delta) * l^2$$

As such, M- $\theta$  relationship of a beam, shown in Figure 4.5(b), will follow the same pattern of the P- $\Delta$  relationship of the beam as shown in Figure 4.5(a).

### 4.3.3 Idealization of Moment (M)-Rotation ( $\theta$ ) Relationships of Beams

A typical M- $\theta$  relation for a steel member as idealized by the Federal Emergency Management Agency (FEMA) 356[27] regulations is shown in Figure 4.6.

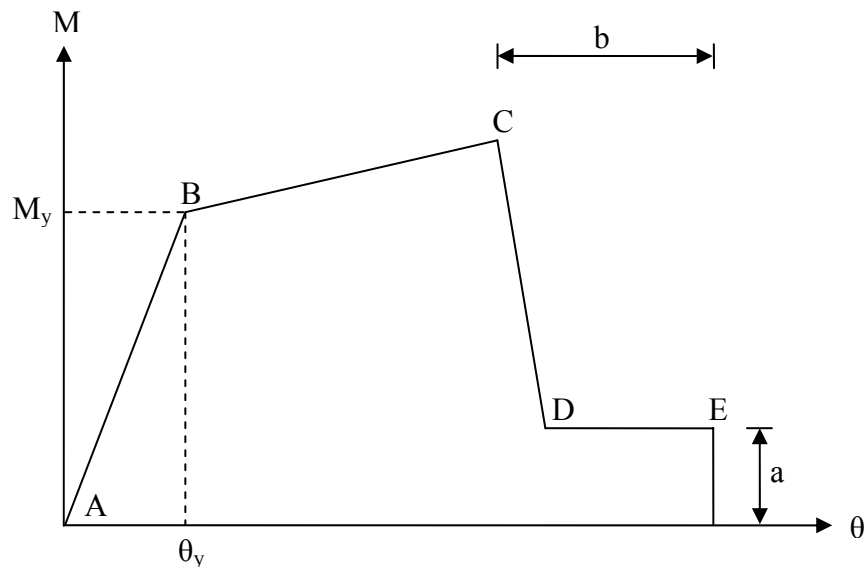


**Figure 4.6** Generalized moment-rotation (M- $\theta$ ) relationship of steel elements.

In this figure, a linear response is assumed until reaching an effective yield point “B”. The strain hardening behaviour of steel is considered in the region BC with a slope that is typically between 0-10% of the elastic slope. Point C has an ordinate that represents the maximum strength of the steel component, and an abscissa value equal to the rotation at which significant strength degradation begins (line CD). A sharp (vertical) transition between points C and D can result in computational difficulties and inability to converge when used as modeling input in computerized analysis software. A small slope may be provided between these two points to avoid this computational instability [27]. Beyond point D, the steel component responds with substantially reduced strength until point E is reached. At a deformation greater than E, the component strength is essentially zero [27]. FEMA356 also provides information for the capacity and rotation values for the residual capacity region (line DE). This capacity depends on the slenderness ratios of the flange and web of the beam under flexural actions. The parameters  $a$  and  $b$  shown in Figure 4.6 represent the residual capacity and extending of the rotation in this residual region, respectively. The recommended values for these parameters, as stated by FEMA356 [27], are  $a = 0.2M_y$  and  $b = 2\theta_y$  where,  $M_y$  and  $\theta_y$  are the effective yield moment capacity and the rotation capacity corresponding to the effective yield capacity, respectively.

The actual and bilinear idealized  $M-\theta$  relationships for a typical beam are shown in Figure 4.7. In this figure, dotted lines (line ABCDE) represent the idealized  $M-\theta$  relationship for the beam. Point C denotes the maximum capacity of the beam. The effective yield point “B” is determined by idealizing the actual response (curve AC) with a bilinear (line ABC) response, which will result the same energy under the curve AC as plotted in Figure 4.7.

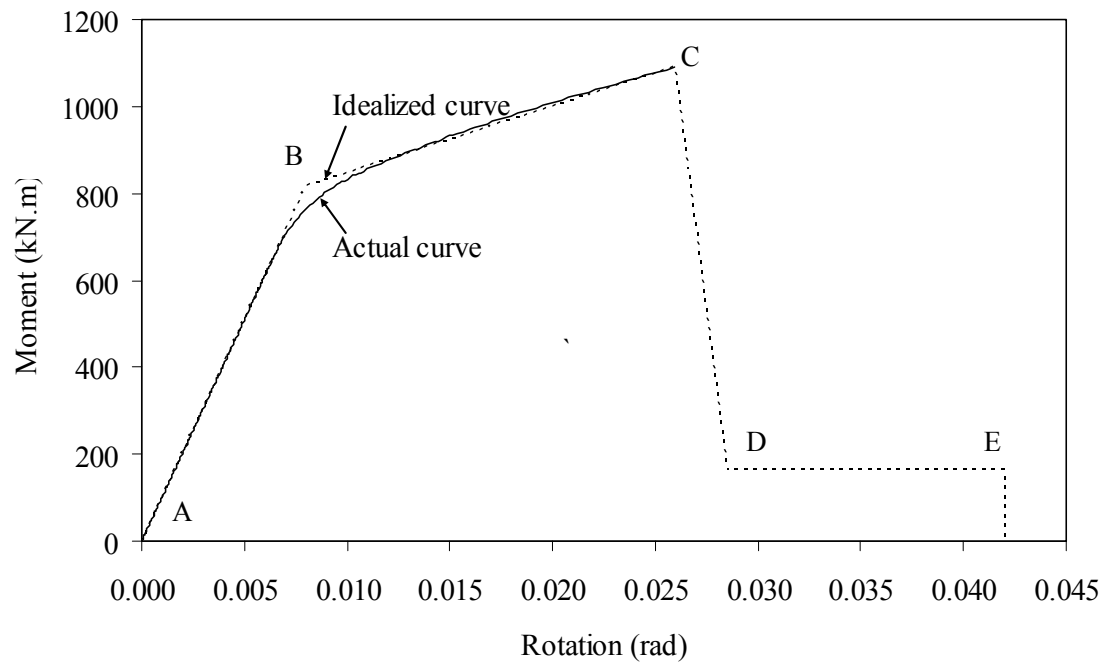


**Figure 4.7** Actual and idealized moment-rotation ( $M-\theta$ ) relationships of steel beams.

#### 4.3.4 Original 3-story and 9-story Frames

A discussion about the moment-rotation relationship obtained from the shell element modeling of the beams is presented in this sub-section. The analyses indicate that all the bare beams of the 3-story and 9-story frames fail by inelastic buckling following full plastification of the steel section. For both the 3-and 9-story frames, the mode of failure of all the retrofitted beams for various GFRP thicknesses is shown to be governed by shear failure of the adhesive. As an illustration, the moment-rotation relationship of the top story beam of the 3-story frame with and without GFRP plates is presented in Figure 4.8.

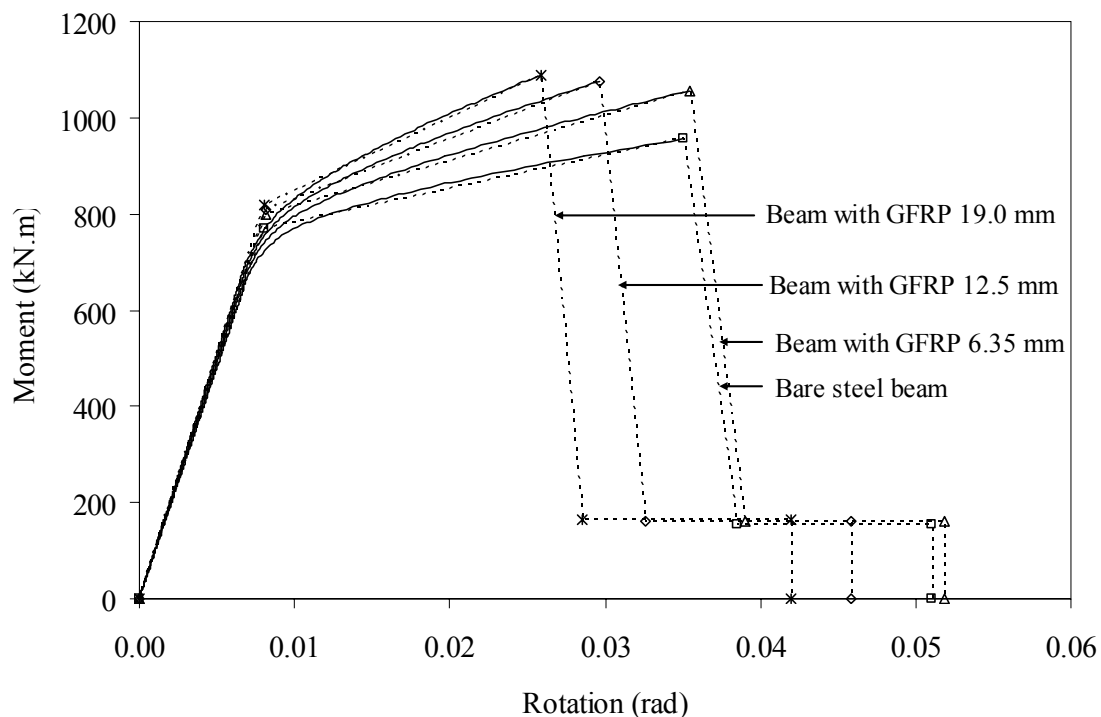


**Figure 4.8** Moment-rotation relationships of the top floor beams of the 3-story frame retrofitted with GFRP plates.

The analyses indicate that the moment capacity of the retrofitted beams enhances by 10% to 14% for the addition of 6.35 mm to 19.0 mm GFRP plates, respectively. The moment capacities of the retrofitted beams increase as the thickness of GFRP plates are increased. However, the deflection capacity at failure of the retrofitted beams reduces with the addition of larger thickness of GFRP plates. Therefore, the rotation capacity of the retrofitted beams is shown to decrease for a larger GFRP thickness addition. The pattern provided in Figure 4.8 is typical for all the beams of the 3- and 9-story frames considered in the study.



#### 4.3.5 Generic 3-story Frames with Beams of $b/t = 25$

A typical moment-rotation relationship of the top floor beam of the generic 3-story frame is presented in Figure 4.9. The generic bare beam fails by yielding of steel. As predicted, the addition of the GFRP plates increases the moment capacities of the bare beams. The retrofitted beam with a 6.35 mm GFRP plate fails by inelastic buckling. Once the portion of the steel beam yields, the load sharing of the yielded portion is transferred to the GFRP plate through the adhesive. If the load-carrying capacity of the GFRP plate alone is less than that of the transferred load then the total system fails by buckling. But for the larger thickness addition of GFRP plates, failure is governed by the shear capacity of the adhesive. A very large improvement in the rotation capacity is predicted for the larger GFRP retrofitted beams as the bonded plates eliminate inelastic buckling of the system.

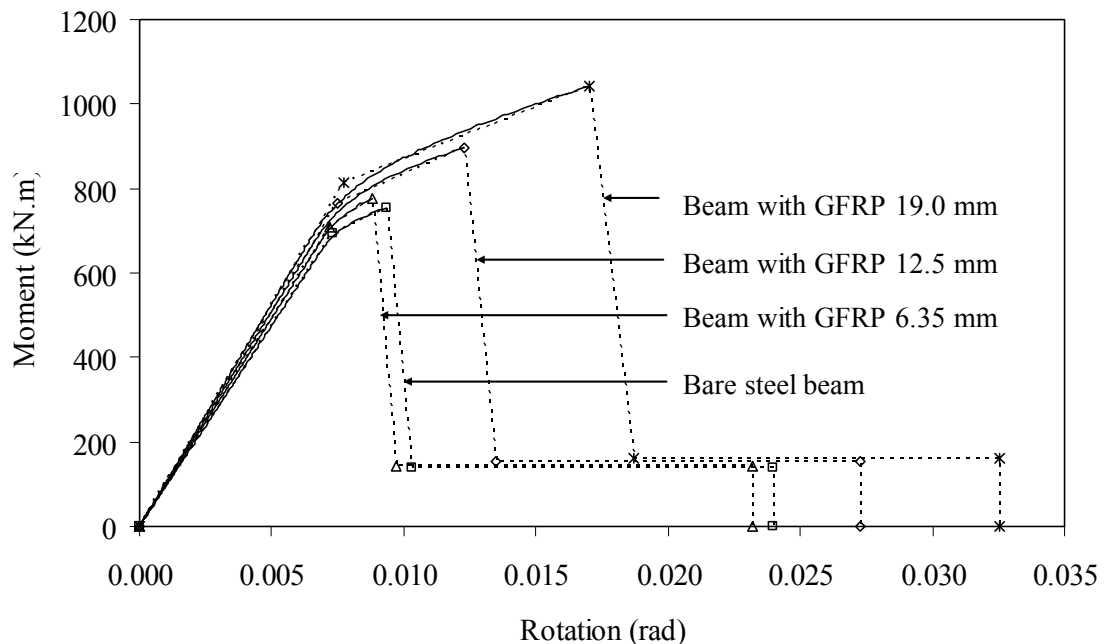


**Figure 4.9** Moment-rotation relationships of the top floor beams of the generic 3-story frame having  $b/t = 25$ .

#### 4.3.6 Generic 3-story Frames with Beams of $b/t = 30$

The moment-rotation relationships for both the bare and retrofitted beams at the top floor are presented in Figure 4.10. The bare steel beam fails by elastic buckling of the steel section. The retrofitted beam with a 6.35 mm GFRP plate also fails by elastic buckling. This results in a small increase in the moment capacity. However, the rotation capacity of the retrofitted beam remains almost unchanged. The added 6.35 mm GFRP plate is not shown to be sufficient to prevent the elastic buckling failure mode of the beam. The retrofitted beam with 19.0 mm GFRP plates fails by inelastic buckling of the steel section with a very large increase in both the moment and rotation capacities as shown in Figure 4.10.

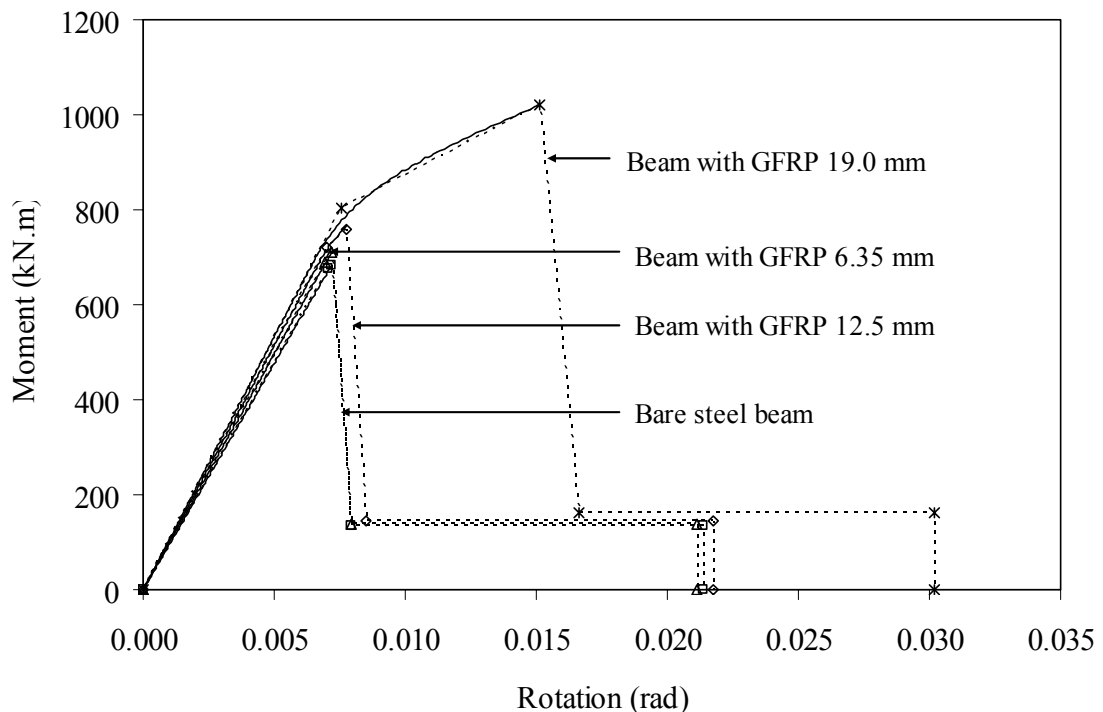


**Figure 4.10** Moment-rotation relationships of the top floor beams of the generic 3-story frame having  $b/t = 30$ .

#### **4.4 Nonlinear Static Pushover Analysis of Frames**

A global pushover curve generated through a pushover analysis can be used to assess the seismic performance of structures. This curve represents the relationship between a global deformation parameter (roof displacement) and a global strength parameter (base shear) obtained by subjecting the structure to a lateral load pattern. FEMA 440 [28] has shown that using multiple load patterns do not improve the accuracy of the pushover analysis significantly. Therefore, a single lateral load pattern based on the first mode shape of the frame is used in this study.

Nonlinear static pushover (NSP) analyses of the frame are carried out using the Structural Analysis Program (SAP) 2000 [29]. The moment-rotation relationships of the beams obtained in Section 4.3 that simulate the plastic hinge properties are assigned to the end of the frame elements of the beams. Plastic hinge properties that account for axial loads and bending moments and are predefined for steel members in the program SAP2000 are used for the columns.

##### **4.4.1 Ground Motions**

Ground excitations considered in this study are obtained from a set of twenty ground motions corresponding to the Los Angeles urban area. These ground motions were established for the FEMA/SAC Steel Project [30] and correspond to the design earthquake spectra involving firm soil with 10% exceedance probability in fifty years. Figure 4.11 shows the elastic mean plus one standard deviation(s) pseudo-acceleration and displacement spectra corresponding to the set of ground motions.

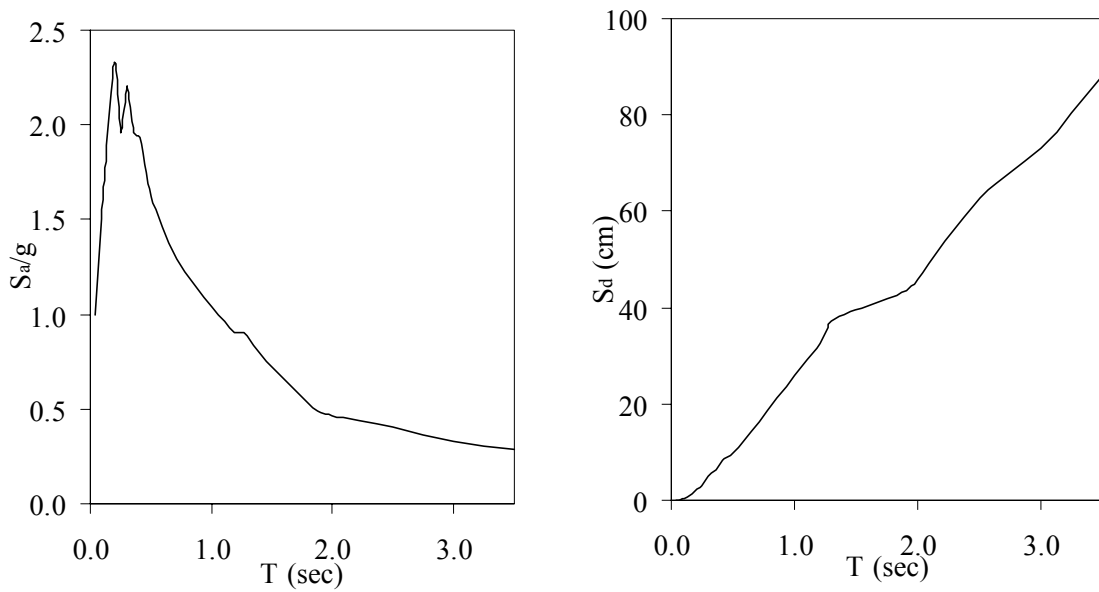


**Figure 4.11** Elastic spectra corresponding to the set of ground motions under consideration [30].

#### 4.4.2 Distribution of Seismic Forces along the Height of the Frame

In the NSP analysis, a constant gravity load, equal to the total dead weight of the building is applied on each frame. The lateral force,  $F_i$ , applied at any floor level  $i$  can be obtained in accordance with the requirements of FEMA 356 [27] as:

$$F_i = V_d \frac{w_i h_i^k}{\sum_{j=1}^N w_j h_j^k} \quad (4.4)$$

$$C_{vi} = \frac{w_i h_i^k}{\sum_{j=1}^N w_j h_j^k} \quad (4.5)$$

where,

$V_d$  = Design base shear determined following the equivalent lateral force procedure defined in the ASCE7-05[31].

$C_{vi}$  = Lateral load distribution factor at floor level  $i$

$w_i$  = Weight at the floor level  $i$

$h_i$  = Height at the floor level  $i$

$N$  = Total number of stories

$k$  = A parameter that accounts for higher modes.  $k$  can be expressed as follows:

$$k = \begin{cases} 1 & \text{for } T_1 \leq 0.5 \text{ s} \\ 1 + 1/2(T_1 - 0.5) & \text{for } 0.5 \text{ s} \leq T_1 \leq 2.5 \text{ s} \\ 2 & \text{for } T_1 \geq 2.5 \text{ s} \end{cases}$$

where,  $T_1$  is the fundamental period of vibration of the frame.

The distribution factors,  $C_{vi}$ , obtained using Equation 4.5, are presented in Table 4.1 for the 3-story and 9-story frames.

**Table 4.1** Distribution of story level shear force for NSP analyses.

Building	Story level	Story weight (kN)	Distribution factors, $C_{vi}$
3-story	Roof	5100	0.559
	2 <sup>nd</sup> floor	4707	0.310
	1 <sup>st</sup> floor	4707	0.130
9-story	Roof	5296	0.284
	8 <sup>th</sup> floor	4805	0.209
	7 <sup>th</sup> floor	4805	0.164
	6 <sup>th</sup> floor	4805	0.125
	5 <sup>th</sup> floor	4805	0.091
	4 <sup>th</sup> floor	4805	0.062
	3 <sup>rd</sup> floor	4805	0.038
	2 <sup>nd</sup> floor	4805	0.020
	1 <sup>st</sup> floor	5002	0.007

#### 4.4.3 Effective Fundamental Period

The effective fundamental period,  $T_e$ , of the building in the direction under consideration is determined using the force-displacement relationship of the pushover analysis of the frames. It is calculated using the secant stiffness at a base shear force equal to 60% of the yield force,  $V_y$ . The effective fundamental period,  $T_e$  can be obtained from the following expression in accordance with the guidelines specified in FEMA 273 [32]:

$$T_e = T_i \sqrt{\frac{K_i}{K_e}} \quad (4.6)$$

where,

$T_i$  = Elastic fundamental period in the direction under consideration

$K_i$  = Elastic lateral stiffness of the frame in the direction under consideration

$K_e$  = Effective lateral stiffness of the frame under consideration

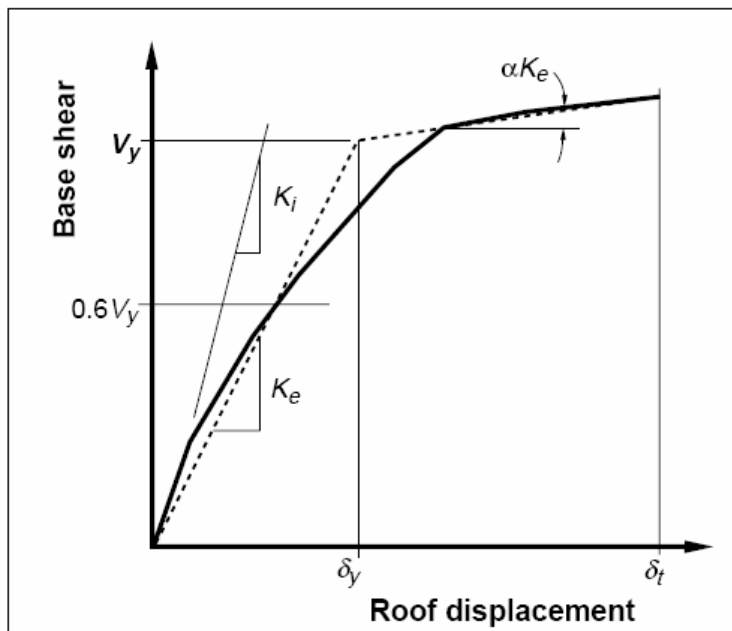


**Figure 4.12** Calculation of effective stiffness,  $K_e$  [32].

Values of  $K_i$  and  $K_e$  can be calculated from the global pushover curves as shown in Figure 4.12 following FEMA 273 [32]. From the global pushover curves of the frames, the values of  $K_i$  and  $K_e$  are predicted to be almost equal for both the bare and GFRP retrofitted frames considered in the current study.

#### 4.4.4 Target Displacement

In the nonlinear static pushover procedure, lateral load is increased monotonically until the displacement of the control node reaches the target displacement. According to the National Earthquake Hazards Reduction Program (NEHRP) guidelines [32], the building should have enough capacity to withstand a specified roof displacement for an earthquake. This is called the target displacement and is defined as an estimate of the likely building roof displacement in the design earthquake. The target displacement,  $\delta_t$ , can be determined according to the guidelines [32] using the following expression:

$$\delta_t = C_0 C_1 C_2 C_3 S_a \frac{T_e^2}{4\pi^2} g \quad (4.7)$$

where,

$T_e$  = Effective fundamental period in seconds.

$C_0$  = Modification factor to relate spectral displacement and likely building roof displacement. It depends on the number of stories of the frame. The value of  $C_0$  can be obtained from Table 3-2 of FEMA 273 [32].

$C_1$  = Modification factor to relate expected maximum inelastic displacements to displacements calculated from linear elastic response.

$C_2$  = Modification factor to represent the effect of hysteresis shape on the maximum

displacement response. The factor  $C_2$  depends on the frame type and performance level of the building. For ordinary SMRF frame with immediate occupancy,  $C_2 = 1.0$ .

$C_3$  = Modification factor to represent increased displacements due to dynamic P- $\Delta$  effects. For buildings with positive post-yield stiffness,  $C_3 = 1.0$ .

$g$  = Acceleration due to gravity

$S_a$  = Response spectrum acceleration at the effective fundamental period and damping ratio of the building obtained from Figure 4.11.

Table 4.2 summarizes the values assigned to the different parameters and coefficients involved in the estimation of the target roof displacements.

**Table 4.2** Parameters and coefficients used in the estimation of roof displacements of the frames.

Frame	$T_i$ (s)	$T_e$ (s)	$S_a/g$	$C_0$	$C_1$	$C_2$	$C_3$
3-story	1.00	1.00	1.05	1.2	1.0	1.0	1.0
9-story	2.10	2.10	0.50	1.3	1.0	1.0	1.0

#### 4.4.5 Parameters for Seismic Performance Assessment of Frames

In order to evaluate the seismic performance of the steel frames, the following parameters are used:

- (i) Target displacement-

The building should have enough capacity to withstand a specific roof displacement for an earthquake.



## (ii) Interstory drift index-

An interstory drift index is defined as the lateral deflection of a floor relative to the one immediately below it divided by the distance between the floors of a frame. FEMA356 [27] recommendations specify interstory drift index thresholds of 0.7%, 2.5% and 5% for the immediate occupancy, life safety and collapse prevention performance levels, respectively. The maximum interstory drift ratio of a frame is calculated from the pushover analysis of the frame when it reaches its target displacement.

## (iii) Response modification factor-

A response modification factor (or the seismic force reduction factor) is used to reduce the elastic strength demand due to an earthquake event. This factor is intended to account for overstrength and ductility inherent in the structural system [33]. The overstrength factor is defined as the ratio of the actual lateral strength ( $V_y$ ) to the design lateral strength ( $V_d$ ) as shown in Figure 4.13. The design base shear,  $V_d$ , overstrength factor,  $\Omega_d$ , and ductility factor,  $\mu$  are described as follows:

$$V_d = V_e / (\Omega_d \mu), \quad \Omega_d = V_y / V_d, \quad \mu = \Delta_m / \Delta_y \quad (4.8)$$

where,  $V_e$  and  $V_y$  are the elastic base shear and shear capacity at a yield strength of the frame, respectively.  $\Delta_m$  and  $\Delta_y$  are the maximum and yield displacements of the system, respectively. Thus, the response modification factor,  $R$  can be expressed as:

$$R = \Omega_d \mu = \text{overstrength factor} \times \text{ductility factor} \quad (4.9)$$

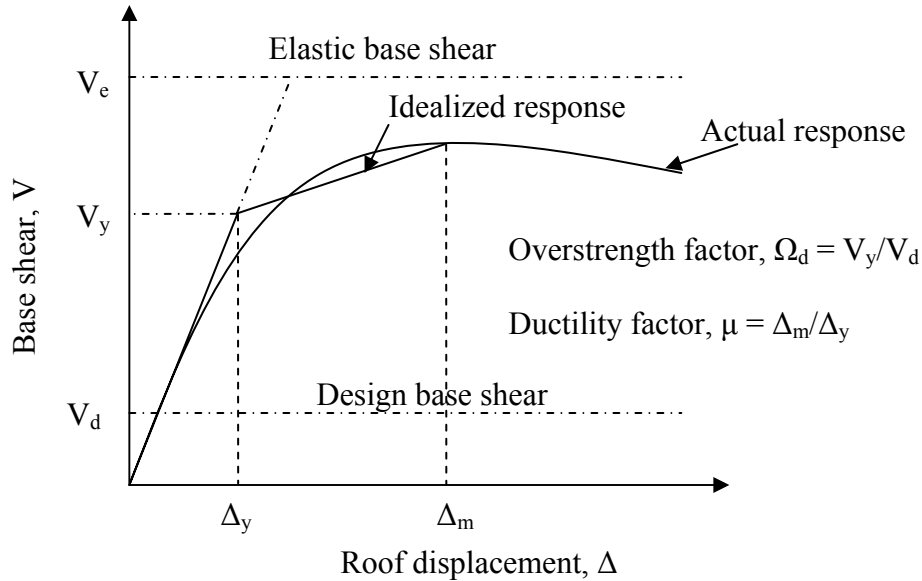


**Figure 4.13** Description of overstrength and ductility factors for a structural response.

FEMA273 [32] provisions are used to determine the equivalent structural yield displacement,  $\Delta_y$  and yield strength,  $V_y$  using the obtained capacity curve of each frame. In these guidelines, the target displacement,  $\delta_t$ , and its corresponding base shear,  $V_t$ , are used to determine the yield strength and yield displacement.

#### 4.4.6 Steps for NSP Analysis of Frames

The following steps are used for NSP analysis of each frame:

- A computer model is developed for each frame using the structural analysis program SAP2000. In this model, plastic hinges are assigned at the end of each frame member.
- A single lateral load pattern based on the first mode shape of the frame is applied gradually until the failure of the frame occurs. The lateral load pattern, provided in Table 4.1, is used for the bare as well as retrofitted frames.

- Target displacement, interstory drift index, and seismic response factors for each frame are calculated to evaluate the seismic performance of the frames.
- To calculate the target displacement of each frame, Equation 4.7 is used. The parameters used for the target displacement calculation are provided in Table 4.2.
- Overstrength and ductility factors are determined first to calculate the response modification factors for each frame.
- To calculate overstrength and ductility factors, the effective yield point is evaluated first. The effective yield lateral strength and the displacement corresponding to the yield strength are determined by following the FEMA273 [32] guidelines, shown in Figure 4.13, through the use of obtained global pushover curves for frames.
- The overstrength and ductility factors for each frame are calculated by using Equation 4.8. The response modification factor for each frame is obtained by using Equation 4.9.

#### **4.5 Results of NSP Analysis of Original Frames**

Figure 4.14 shows the results of the pushover analyses for the 3- and 9- story original steel frames. Target displacements of the frames obtained for the considered ground motions are shown in the same figure.

Figure 4.15 summarizes the maximum interstory drift demands expected in the frames according to the NSP analyses. From Figure 4.15(a), it is observed that the interstory drift index is 3% at the target displacement for the 3-story frame, which is higher than the recommended Life Safety performance level. However, this drift index is 3.6% when the maximum shear capacity,  $V_m$  is considered.

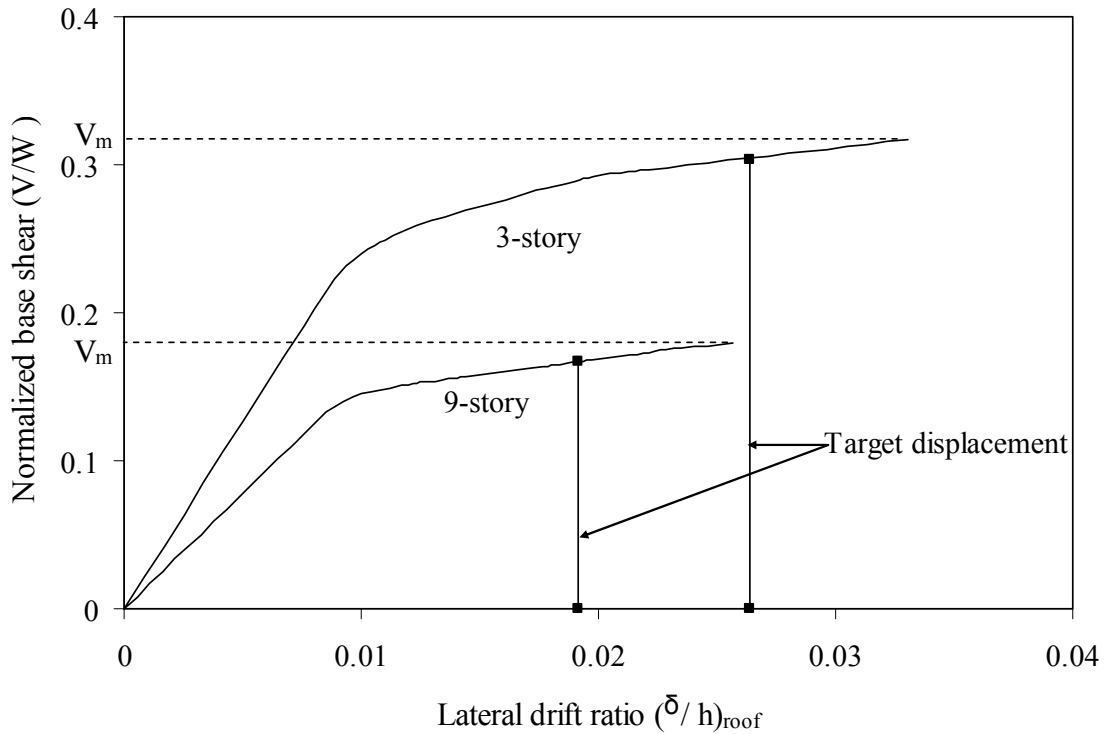


**Figure 4.14** Pushover curves for the 3- and 9-story original steel frames.

For the 9-story frames, the interstory drift index is presented in Figure 4.15(b). It is also shown that the interstory drift index exceeds the Life Safety performance level at the maximum shear capacity. But it is well below the Life Safety performance level for the shear capacity at the target displacement as shown in Figure 4.15(b).

The overstrength and ductility factors for the original 3-story frame are 3.56 and 3.27, respectively, as obtained from Figure 4.16(a). The response modification factor is predicted as 11.6 for the 3-story frame.

The overstrength and ductility factors for the original 9-story frame are 2.84 and 2.76, respectively, as obtained from Figure 4.16(b). This results in a response modification factor,  $R$  for the 9-story frame of 7.8.

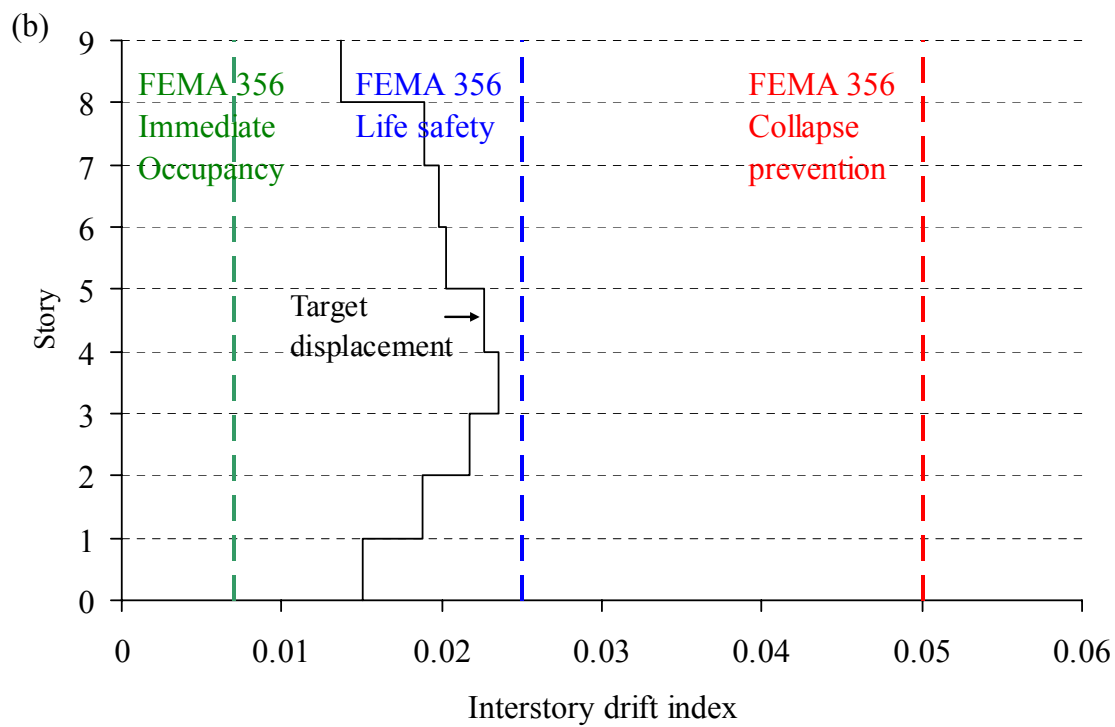
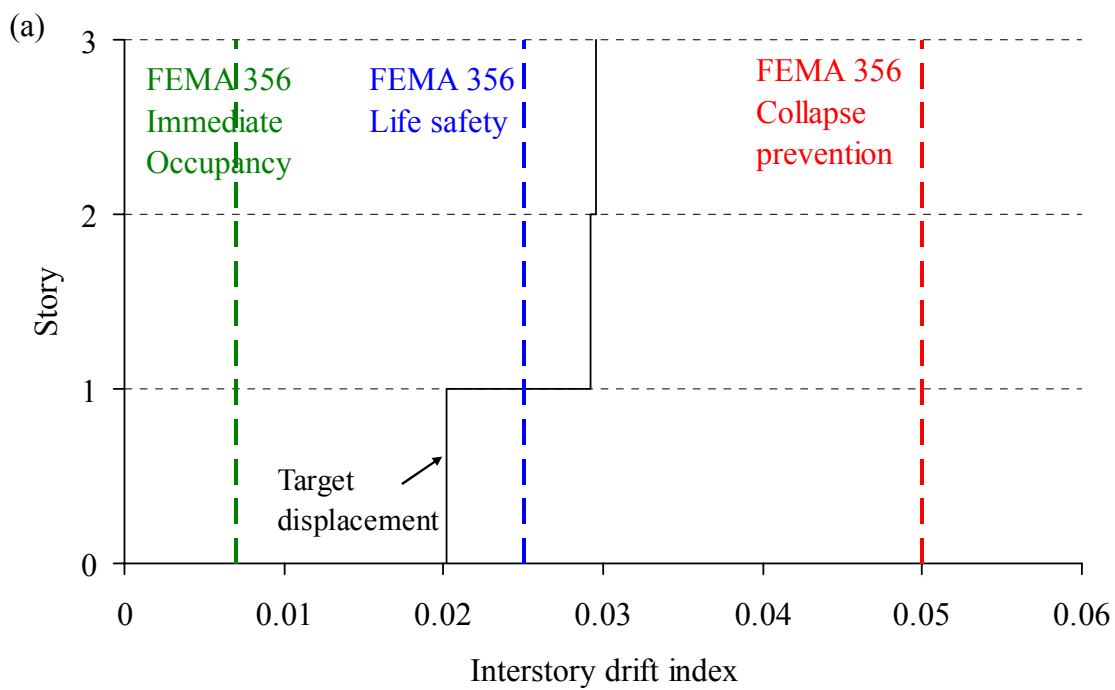


**Figure 4.15** Interstory drift indexes for the original steel frames (a) 3-story (b) 9-story.

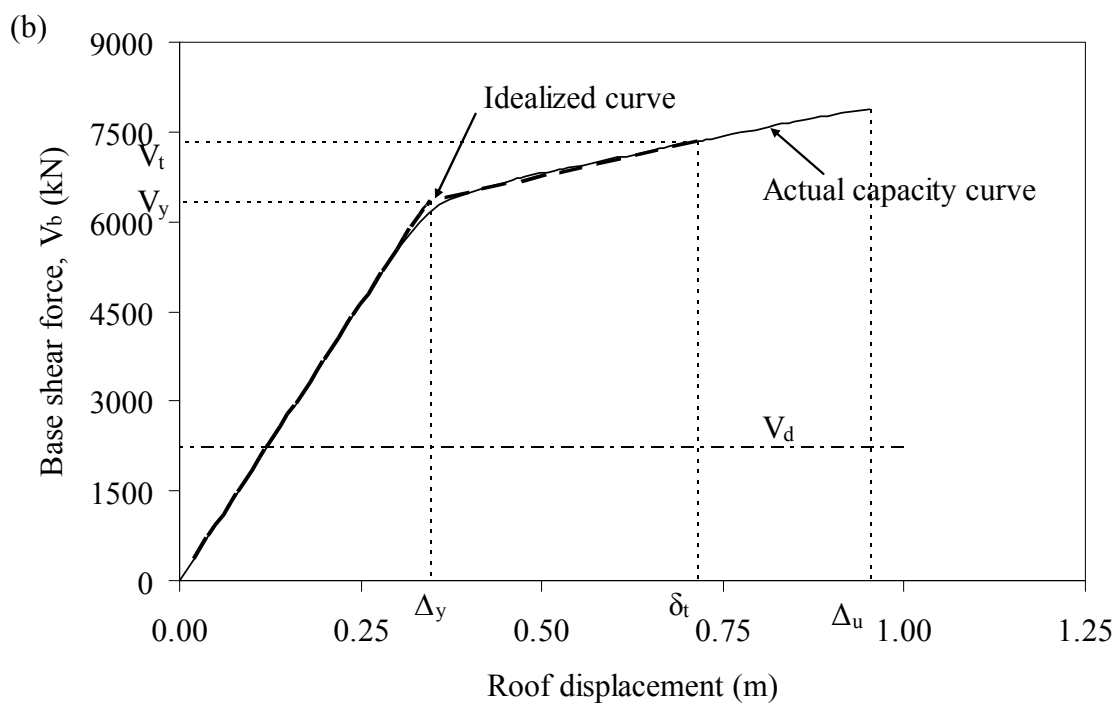
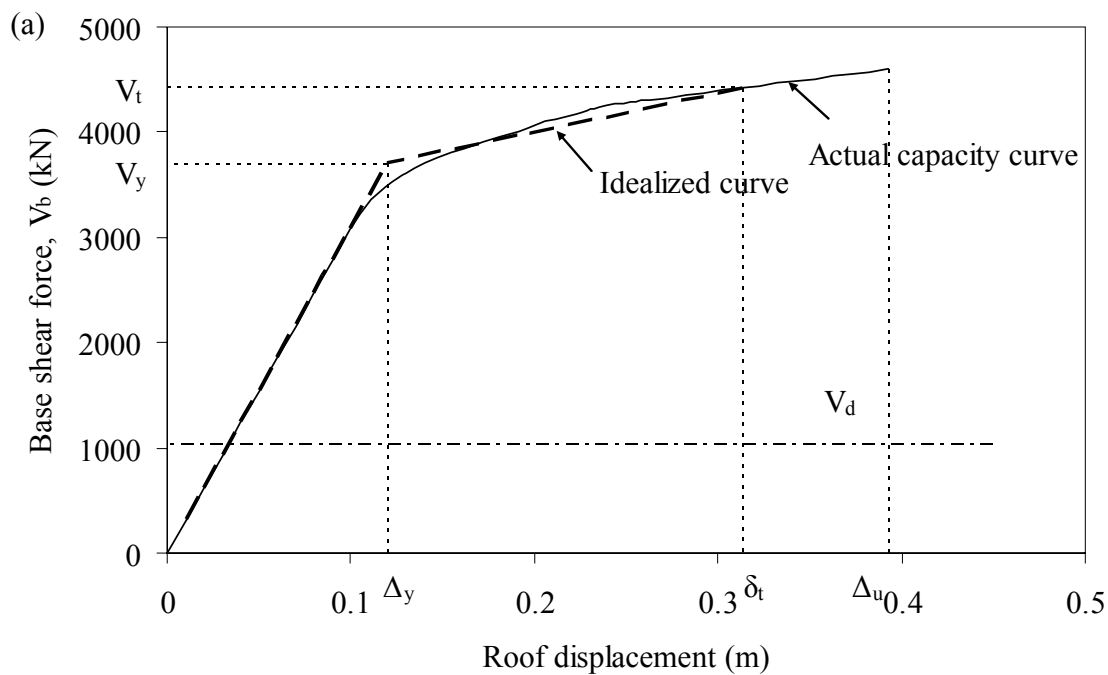


**Figure 4.16** Capacity and idealized curves of original steel frames for the evaluation of seismic performance parameters (a) 3-story and (b) 9-story.

#### 4.5.1 Results of NSP Analysis of Retrofitted 3-story Frames

From the pushover analyses of the frames, it is predicted that the beams retrofitted with a 6.35 mm GFRP plate result in a load capacity comparable to that of a 19.0 mm GFRP plate for the two retrofitted cases mentioned in subsection 4.2.3.1. The retrofitting scheme with Case (a) of F3-B1-C and F3-B1-V frames develops also comparable capacity curves with that of Case (b) of F3-B3-C and F3-B3-V frames as shown in Figure 4.17. The maximum load-carrying capacity enhances by 5% and 8% for the F3-B1-C and F3-B3-C frames, respectively. However, the F3-B3-C frame with a 6.35 mm GFRP plate generates higher displacement at the maximum load. On the other hand, frame F3-B3-C having a GFRP plate of 19.0 mm results in maximum load for the 3-story retrofitted frame.

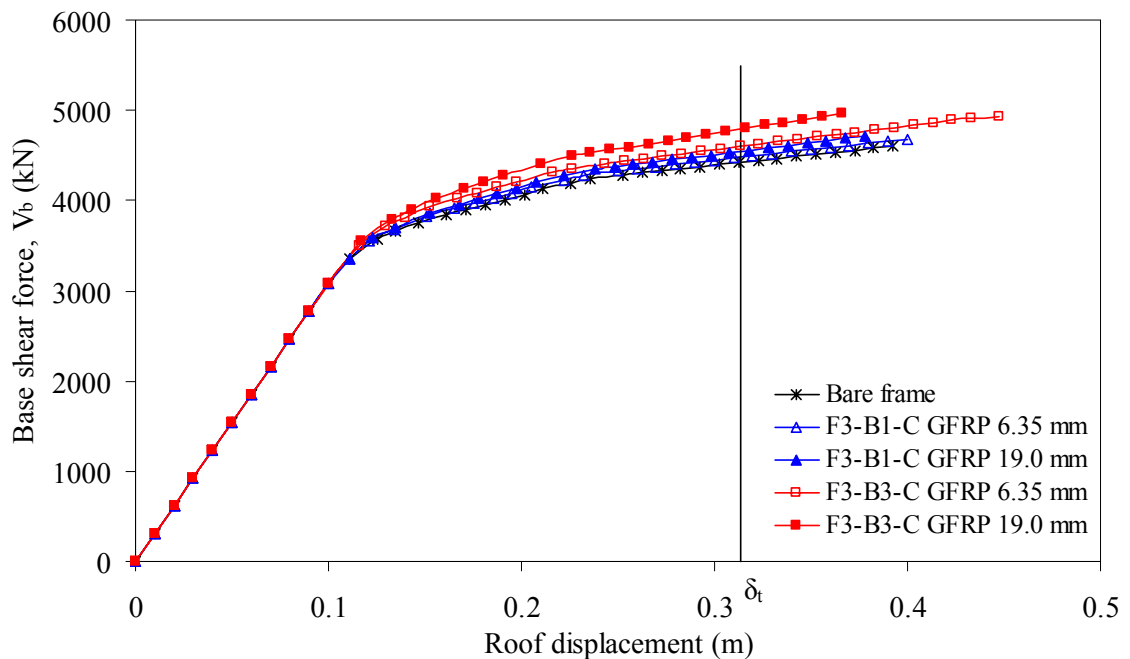


**Figure 4.17** Capacity curves for the 3-story retrofitted frames.

For the retrofitted frame F3-B3-C with a 19.0 mm GFRP plate, the overstrength and ductility factors are 3.77 and 2.88, respectively, and results in a modification factor of 10.8. The yield strength and yield displacement of the retrofitted frame increase by 5.8% in comparison to the original 3-story frame as obtained from Figure 4.18. The interstory drift index of the retrofitted frame at the same base shear force of the target displacement of the 3-story original frame is presented in Figure 4.19. From the figure, it is shown that the drift index reduces 27% at the top story. The drift indexes are well below the FEMA356 Life Safety performance level for the retrofitted frame.

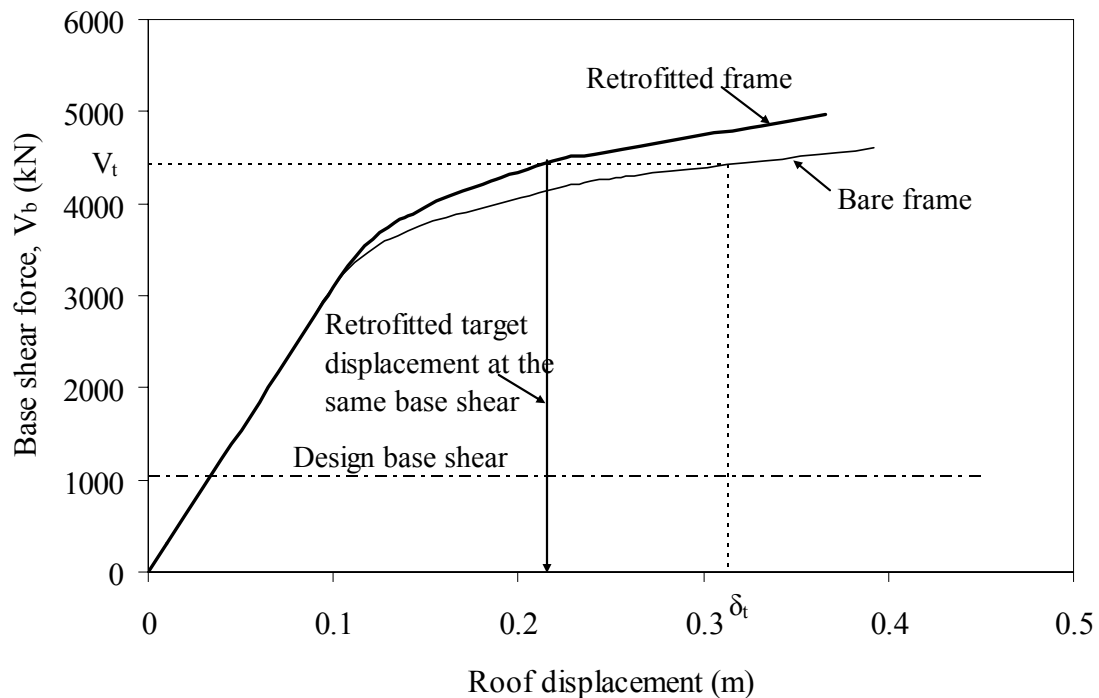


**Figure 4.18** Capacity improvement for the F3-B3-C frame retrofitted with 19.0 mm GFRP plates.



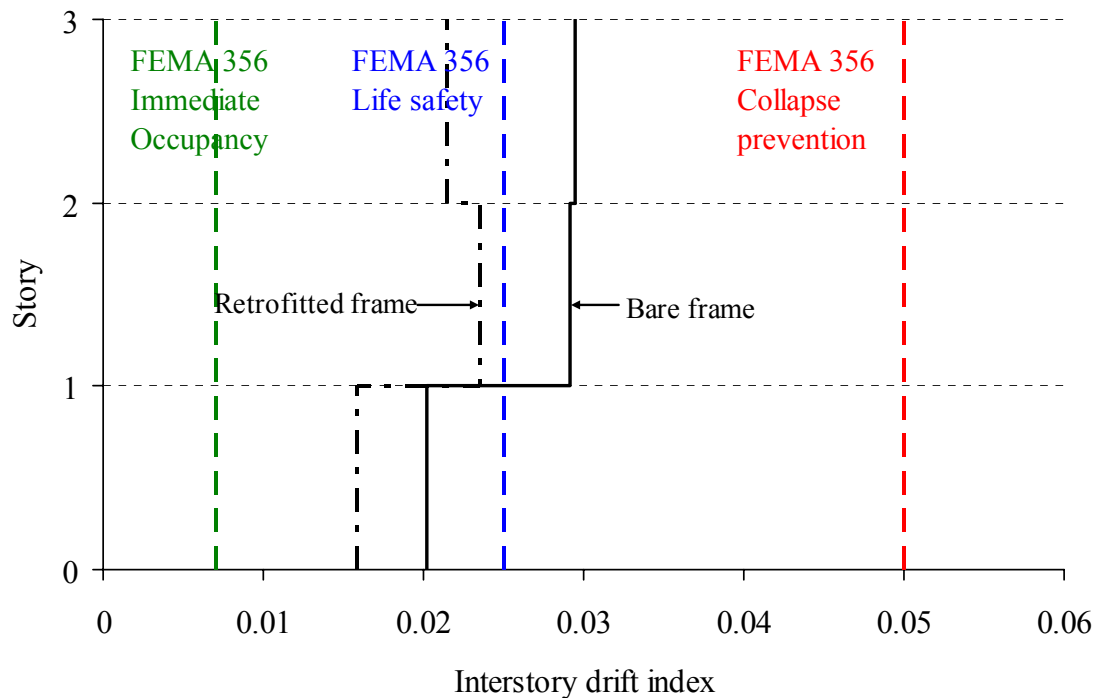


**Figure 4.19** Interstory drift indexes for the F3-B3-C frame with 19.0 mm GFRP plates.

#### 4.5.2 Results of NSP Analysis of Retrofitted 9-story Frames

The capacity curves for the 9-story retrofitted frames with GFRP plates are presented in Figure 4.20. From the curves, it is observed that F9-B5-C with different thicknesses of GFRP plates result in higher load capacities than that of F9-B1-C and F9-B3-C frames for the same GFRP additions. It is also predicted that the load capacity of the F9-B1-C frame is slightly higher than that of the F9-B1-V frame for the same thickness of GFRP plates. This pattern is repeated for the F9-B1, F9-B3, and F9-B5 retrofitted frames. From Figure 4.20, it is revealed that the F9-B5-C frame with a 6.35 mm GFRP plate results in a better performance for the displacement at maximum load while that of an addition of 19.0 mm GFRP develops a higher strength.

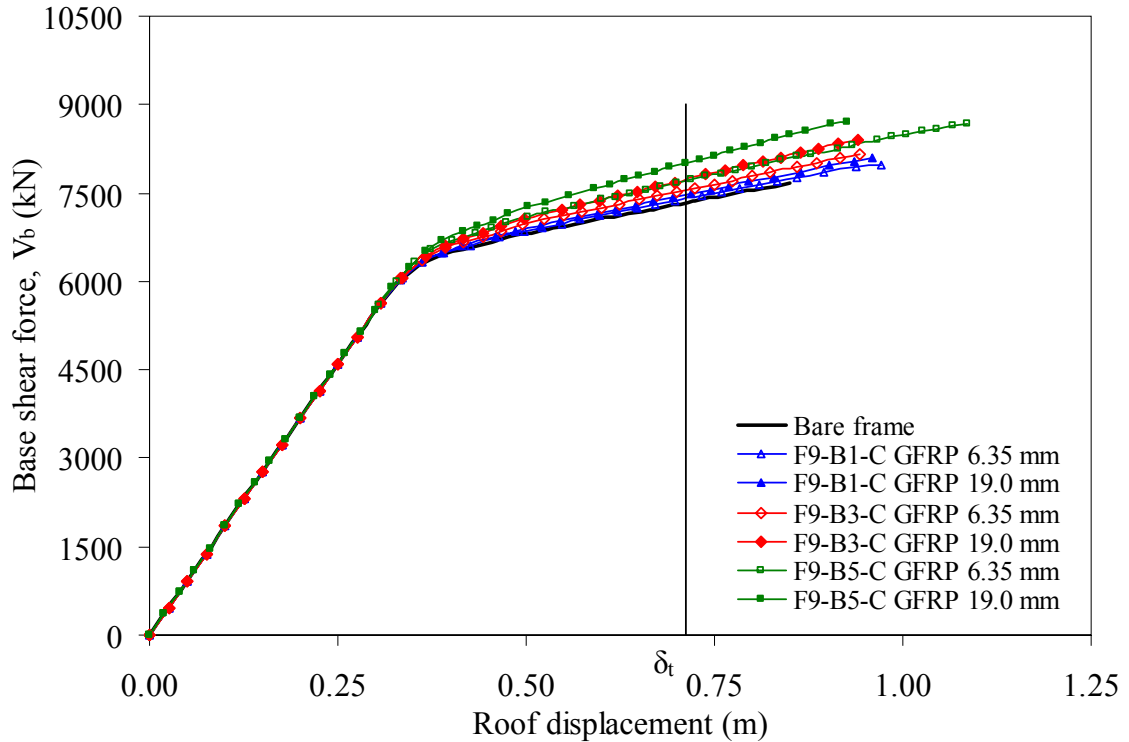


**Figure 4.20** Capacity curves for the retrofitted 9-story frames.

The overstrength and ductility factors for the F9-B5-C frames with a 6.35 mm GFRP plate are 2.92 and 3.05, respectively. The yield strength of the retrofitted frame increases by 3% in comparison to the original frame. The response modification factor,  $R$  for this frame is 8.9, which is 13% higher than that of the original frame. The interstory drift index at each floor is within the Life Safety performance level.

#### 4.6 Results of NSP Analysis of Generic 3-story Frames

The overstrength and ductility factors for the original generic frame with  $b/t = 25$  are 3.25 and 1.76, respectively. This frame has a response modification factor,  $R$  of 5.7. On the other hand, this factor,  $R$  is 4.5 with overstrength and ductility factors of 2.96 and 1.51,

respectively, for the frame with  $b/t = 30$ . The generic frames do not satisfy the target displacement requirements. The interstory drift indexes for the two bare frames are well below the Life Safety performance level.

#### **4.6.1 Results of NSP Analysis of Retrofitted Generic Frames with $b/t = 25$**

From the NSP analyses of the retrofitted frames, it is observed that the load and displacement capacities of the GF3-B3-C frame are higher than those of the GF3-B1-C frames for the same addition of GFRP plates. It is also shown that the capacities of the GF3-B3-V frames are higher than those of the GF3-B1-V frames. Retrofitted frame GF3-B3-C with 19.0 mm GFRP results in a higher load-carrying capacity and higher displacement as shown in Figure 4.21. For this case, the lateral load capacity increases by 25% in comparison to the parent frame. The displacement capacity enhances by 40% at the maximum base shear for this frame. Only this retrofitted frame satisfies the target displacement requirement. The interstory drift indexes of the retrofitted frame with 6.35 mm to 15.5 mm GFRP satisfy the Life Safety performance level at the maximum base shear of the frame. For the retrofitted frame with 19.0 mm GFRP, the interstory drift index at the maximum base shear of the frame shows a close threshold of the Life Safety performance level. Figure 4.22 shows the interstory drift indexes of the frames at the maximum base shear level of the parent frame. From the figure, it is shown that the retrofitted frame with 19.0 mm GFRP plates can reduce the interstory drift index by 37% at the top floor level. The overstrength and ductility factors for the retrofitted frame with 19.0 mm GFRP plates are 3.84 and 2.1, respectively. This results in a response modification factor of 8.0, which is 41% higher than that of the parent frame.

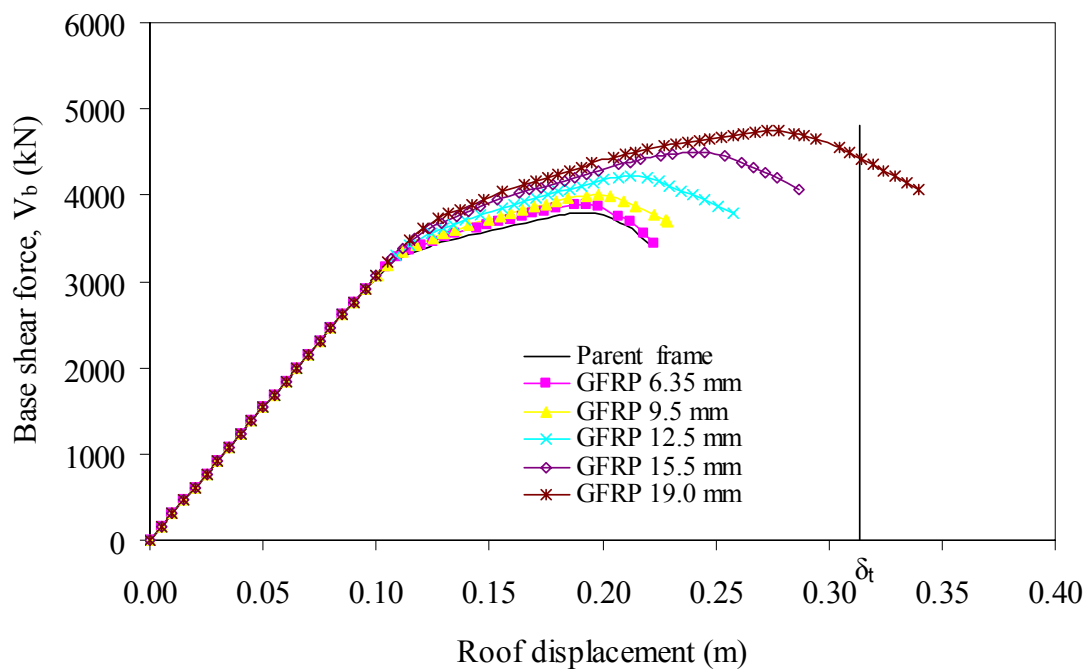


**Figure 4.21** Capacity curves for the GF3-B3-C retrofitted frames with  $b/t=25$ .

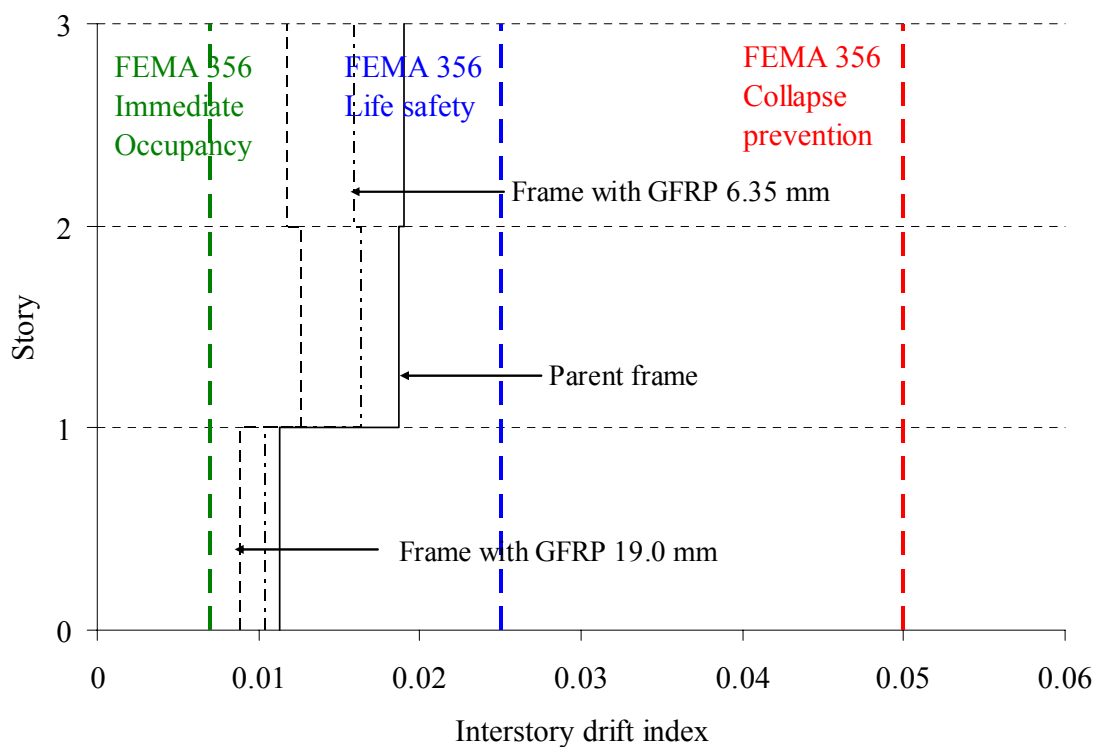


**Figure 4.22** Interstory drift indexes for the GF3-B3-C frames with  $b/t = 25$ .

#### 4.6.2 Results of NSP Analysis of Retrofitted Generic Frames with $b/t = 30$

From the NSP analyses, it is revealed that the enhancement pattern of the retrofitted frames with  $b/t = 30$  is the same as that of the frames with  $b/t = 25$ . Frame GF3-B3-C with 19.0 mm GFRP results in a higher load-carrying capacity and a higher displacement as shown in Figure 4.23. The enhancement in the base shear capacity is 25% and that of displacement is 31% in comparison to the parent frame at the maximum base shear. The overstrength, ductility, and response modification factors are 3.40, 1.73, and 5.9, respectively. The response modification factor for the GF3-B3-C frame with 19.0 mm GFRP enhances by 30% in comparison to the corresponding parent frame. The interstory drift indexes are well below the Life Safety performance level as shown in Figure 4.24. However, none of these frames, including both the bare and retrofitted frames, satisfies the target displacement requirements.

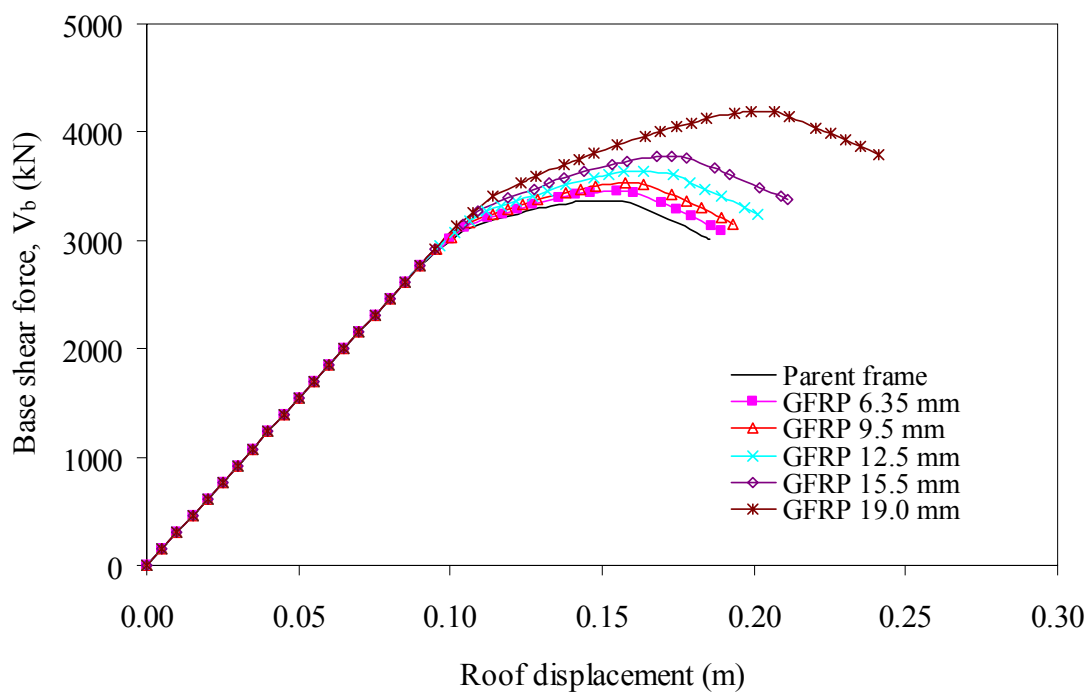


**Figure 4.23** Capacity curves for the GF3-B3-C retrofitted frames with  $b/t = 30$ .

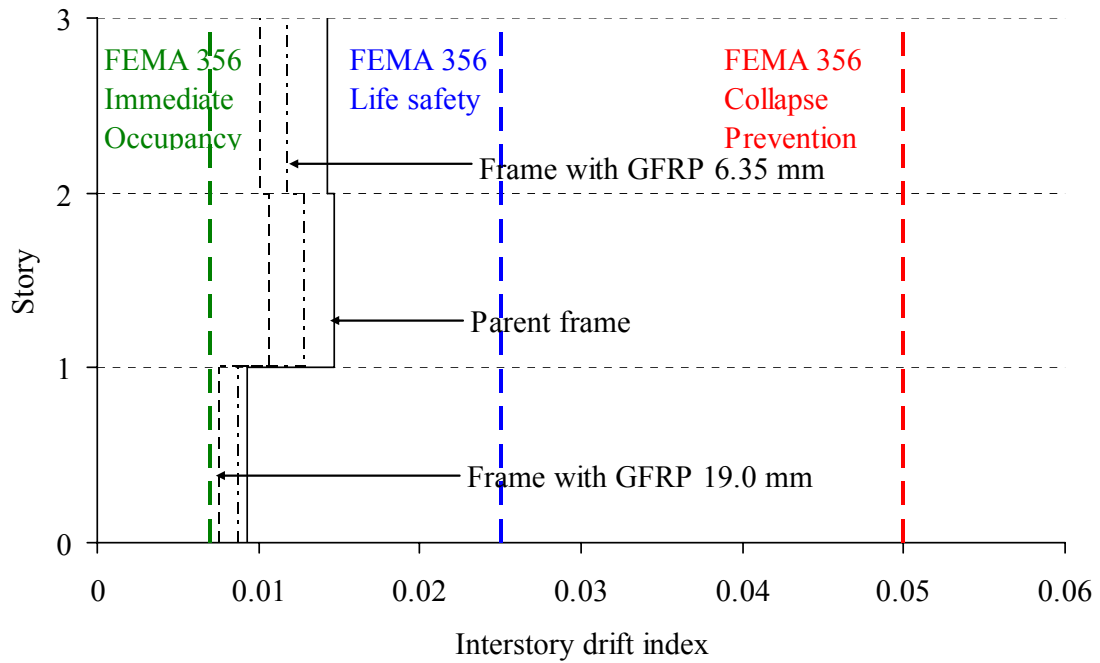


**Figure 4.24** Interstory drift indexes for the GF3-B3-C frames with  $b/t = 30$ .

#### 4.7 Conclusions

Nonlinear static pushover analyses are carried out on both the original and retrofitted frames with various thicknesses of GFRP plates added to their beams' flanges. The thickness of GFRP plate ranges from 6.35 mm to 19.0 mm. The moment-rotation relationships of the beams used in the analyses are based on realistic strengths and stiffness values of the GFRP plate and the adhesive obtained from a previous experimental study. The plastic hinge properties simulating the moment-rotation behaviour of the beams and columns are assigned at the end of the frame members. A single lateral load pattern based on the first mode shape of the frame is increased monotonically until the failure of the frame occurs. The response modification factor, in terms of overstrength and ductility factors, is determined using the capacity curves obtained from the pushover analyses. Enhancement in the lateral load capacity as well as

the response modification factors of each frame is discussed. The interstory drift index of each frame is then compared to the values provided by the FEMA regulations. The following conclusions can be drawn from the current study:

- The strength of the adhesive limits both the moment and deflection capacities at failure of the retrofitted beams. For slender beams, inelastic buckling of the steel sections is the dominant mode of failure for GFRP plate addition. The failure of plastic beam sections is governed by shear failure of the adhesive.
- The lateral load-carrying capacity of the retrofitted frames with plastic beam sections does not increase significantly as the shear failure of the adhesive limits full utilization of the strength capacity of the added GFRP plates.
- The interstory drift indexes of the existing 3-story and 9-story frames are reduced significantly due to addition of GFRP plates. For the considered 3-story original frame, interstory drift index reduces by 27% at the top story level, and thereby, satisfies the threshold of the Life Safety performance level.
- The response modification factors for the 3-story bare and retrofitted frames are almost the same with an increase of 5.8% yield capacity of the retrofitted frame. For the 9-story frame, the response modification factor increases by 13% due to an addition of 19.0 mm GFRP plates to the flanges of the beams of the frame.
- For the frames with slender beams, both the lateral load-carrying capacity and deflection at failure are enhanced by adding GFRP plates. As the thickness of GFRP plate increases, the failure mode of the beam shifts from elastic buckling to shear failure of the adhesive, and thereby increases both the load and deflection capacities of the frame.

- For the frames with the slender beams of a ratio of 25, the lateral load and displacement capacities of the retrofitted frames with a 19.0 mm GFRP increase by 25% and 40%, respectively, in comparison to the bare frame. This retrofitted frame satisfies the target displacement requirements.
- The response modification factors for the retrofitted slender frames show a very large improvement in comparison to the corresponding bare frames. These factors increase by 41% and 30% for the retrofitted frames with 19.0 mm GFRP plates and with a slenderness ratio of 25 and 30 for the flange of the beams, respectively.

#### **4.8 References**

- [1] Canadian Institute of Steel Construction (CISC), Handbook of Steel Construction, 10<sup>th</sup> edition, 2010, Canada.
- [2] American Institute of Steel Construction (AISC), Steel Construction Manual, 14<sup>th</sup> edition, 2011, USA.
- [3] Nakashima, M, Suita, K., Morisako, K. and Maruoka, Y., Tests of welded beam-column subassemblies I: Global behaviour, Journal of Structural Engineering, ASCE 1998; 124(11): 1236-1244.
- [4] Uang, C., Yu, Q. K., Noel, S., and Gross, J., Cyclic testing of steel moment connections rehabilitated with RBS or welded haunch, Journal of Structural Engineering, ASCE 2000; 126(1): 57-68.
- [5] Shahawy, M. A., Arockiasamy, M., Beitelmant, T., and Sowrirajan, R., Reinforced concrete rectangular beams strengthened with CFRP laminates, Journal of Composites Part B: Engineering 1996; 27:225-233.



- [6] Rabinovitch, O. and Frostig, O., Experiments and analytical comparison of RC beams strengthened with CFRP composites, *Journal of Composites Part B: Engineering* 2003; 34:663-677.
- [7] Binici, B. and Mosalam, K., Analysis of reinforced concrete columns retrofitted with fiber reinforced polymer lamina, *Journal of Composites Part B: Engineering* 2007; 38: 265-276
- [8] Parvin, A. and Granata, P., Investigation on the effects of fiber composites at concrete joints, *Journal of Composite Part B: Engineering* 2000; 31:499-509.
- [9] Antonopoulos, C. P. and Triantafillou, T. C., Analysis of FRP-strengthened RC beam-column joints, *Journal of Composites for Construction, ASCE* 2002; 6(1): 41-51.
- [10] Balsamo, A., Colombo, A., Manfredi, G., Negro, P., and Prota, A., Seismic behavior of a full scale RC frame repaired using CFRP laminates, *Engineering Structures* 2005; 27:769-780.
- [11] Zou, X. K., Teng, J. G., De Lorenzis, L., and Xia, S. H., Optimal performance-based design of FRP jackets for seismic retrofit of reinforced concrete frames, *Journal of Composites Part B: Engineering* 2007; 38: 584-597.
- [12] Di Ludovico, M., Prota, A., Manfredi, G., and Cosenza, E., Seismic strengthening of an under-designed RC structure with FRP, *Earthquake Engineering and Structural Dynamics* 2008; 37: 141-162.
- [13] Sen, R., Liby, L. and Mullins, G., Strengthening steel bridge sections using CFRP laminates, *Journal of Composites Part B: Engineering* 2001; 32(4): 309-322.
- [14] Miller, T. C., Chajes, M. J., Mertz, D. R. and Hastings, J. N., Strengthening of a

- steel bridge girder using CFRP laminates, *Journal of Bridge Engineering*, ASCE 2001; 6(6): 514-522.
- [15] Van Den Einde, L., Zhao, L., and Seible, F., Use of FRP composites in civil engineering applications, *Construction and Building Materials* 2003; 17(6-7): 389-403.
- [16] Tavakkolizadeh, M. and Saadatmanesh, H., Strengthening of steel–concrete composite girders using carbon fiber reinforced polymer sheets, *Journal of Structural Engineering*, ASCE 2003; 129(1): 30-40.
- [17] Colombi, P. and Poggi, C., Strengthening of tensile steel members and bolted joints using adhesively bonded CFRP plates, *Construction and Building Materials* 2006; 20(1-2): 22-33.
- [18] Shaat, A. and Fam, A., Axial loading tests on short and long hollow structural steel columns retrofitted using carbon fiber reinforced polymers, *Canadian Journal of Civil Engineering* 2006; 33(4): 458-470.
- [19] Sayed-Ahmed E. Y., Strengthening of thin-walled steel I-section beams using CFRP strips. In: *Proceedings of the 4th international conference on advanced composite materials in bridges and structures*, Calgary, 2004.
- [20] Accord, N. B. and Earls, C. J., Use of fiber-reinforced polymer composite elements to enhance structural steel member ductility, *Journal of Composites for Construction*, ASCE 2006; 10(4): 337-344.
- [21] El-Tawil, S., Ekiz, E., Goel, S., and Chao, S-H., Retraining local and global buckling behavior of steel plastic hinges using CFRP, *Journal of Constructional Steel Research* 2011; 67(3): 261-269.

- [22] Akbas, B., Tugsal, U. M., and Kara, F. I., An evaluation of energy response and cumulative plastic rotation demand in steel moment-resisting frames through dynamic/static pushover analyses, *The structural Design of Tall and Special Buildings* 2009; 18: 405-426.
- [23] Koziey, B. L. and Mirza, F. A., Consistent thick shell element, *Computers and Structures* 1997; 65(12): 513-541.
- [24] El Damatty, A., Korol, R. M., and Mirza, F. A., Large displacement extension of consistent shell element for static and dynamic analysis, *Computers and Structures* 1997; 62(6): 943-960.
- [25] El Damatty, A., Abushagur, M. and Youssef, M. A., Experimental and analytical investigation of steel beams rehabilitated using GFRP sheets, *Steel and Composite Structures* 2003; 3: 421-438.
- [26] El Damatty, A. and Abushagur, M., Testing and modeling of shear and peel behaviour for bonded steel/FRP connections, *Journal of Thin-Walled Structures* 2003; 41: 987-1003.
- [27] Federal Emergency Management Agency, Prestandard and commentary for the seismic rehabilitation of buildings. Report FEMA 356, Washington, DC, 2000.
- [28] Federal Emergency Management Agency (FEMA) 440, Improvement of nonlinear static seismic analysis procedures, Washington DC, 2005.
- [29] Structural Analysis Program SAP2000 nonlinear version 10.1.0, Analysis reference manual. Berkeley (California): Computers and Structures Inc.; 2011.
- [30] Somerville, P. G., Smith, N., Punyamurthula, S., and Sun, J., Development of ground motion time histories for phase 2 of the FEMA/SAC steel Project, Report

SAC/ BD-97/04, SAC Joint Venture, 1997.

[31] American Society of Civil Engineers (ASCE), Minimum Design Loads for Buildings and Other Structures, 2006, USA.

[32] Federal Emergency Management Agency (FEMA), NEHRP provisions for the seismic rehabilitation of buildings, Reports FEMA 273 and 274, Washington (DC), 1997.

[33] Federal Emergency Management Agency (FEMA), NEHRP recommended provisions for seismic regulations for new buildings and other structures, (FEMA 450) Washington (DC), 2004.

## CHAPTER 5

### TESTING AND PREDICTION OF SHEAR AND PEELING BEHAVIOUR OF BONDED STEEL/GFRP JOINTS UNDER CYCLIC LOADING\*

#### 5.1 Introduction

Bonded joints are commonly used in aerospace and aeronautical structures. The application of adhesively bonded joints between steel members and glass fiber reinforced polymer (GFRP) plates for the retrofitting schemes of metallic structures has increased in recent years. The alternative in connecting plastic and metallic elements is mechanical fastening, which requires drilling holes resulting in unfavourable stress concentration near the holes. This stress concentration can be eliminated by using bonded joints, which provide efficient load transfer between composite parts through a uniform distribution of stresses over a larger area compared to discrete bolted or welded joints. Adhesive bonding also has the advantage of ease of application. However, enhancement in load and deflection capacities of retrofitted members depends largely on the adhesive that is used to bond the two elements. Therefore, it is important to estimate the strength and stiffness of the bonded joints in order to accurately assess the improvement in performance of steel members retrofitted with GFRP plates.

A number of studies have been conducted to predict the performance of bonded joints under monotonic loading. Khalili et al. [1] studied the stress distribution in the adhesive and the failure of a single lap joint under static in-plane and out-of-plane loadings by means of a three-dimensional finite element analysis. In this study, the adhesive layer

---

\*A version of this chapter is prepared for publication in the *International Journal of Adhesion and Adhesives*.

was assumed to be linear elastic because of its brittle nature. Kim et al. [2] also studied the behaviour of composite single lap bonded joints considering the failure of composite adherends and the adhesive using a finite element analysis. An elastic-perfectly plastic model of the adhesive and a delamination failure criterion were used in their study. From the obtained numerical results, they showed that the maximum joint strength is achieved when the adhesive and the delamination failures occur at the same time. Also, a number of numerical and experimental studies have led to a reasonable insight on the properties of adhesives under monotonic static loading [3-8].

El Damatty and Abushagur [9] conducted an experimental study to quantify the adhesive properties and strength of shear-lap joints under monotonic static loading. They tested a large number of adhesives to select the one suitable for bonding steel and GFRP plates. They found that a methacrylic adhesive system that is used in the automotive industry is the best type for such an application. A number of shear lap tests were conducted in their study and the failure load, displacement, and strains were recorded to determine the properties of the adhesive. They also presented the properties of the adhesive as a collection of linear continuous springs and used the test results to determine the stiffness of these springs.

Although a number of research studies have analyzed bonded joints under monotonic loadings, the behaviour of bonded joints under cyclic loading has not yet been studied. The repeated cyclic loading on bonded joints may result in cracks in the adhesive, which might reduce the capacity and stiffness of the joint compared to the monotonic load case. This might be a critical factor when designing a bonded joint in a seismic region.

The objective of the current study is to assess the strength of bonded steel/GFRP joints under cyclic loading. An experimental program is conducted on bonded steel/GFRP joints under both monotonic and cyclic loadings. The experimental program is divided into two phases. In the first phase, a preliminary test is performed on two types of methacrylate adhesive, MA300 and AO420, to determine the strength capacity of the joint under monotonic loading. The considered bond size is 76 x 51 mm and the joint is subjected to monotonic downward loading. In the second phase, a number of shear lap tests are conducted on the joint under both monotonic and cyclic loadings using the adhesive that has provided higher strength in the first phase. Two different sizes of bonded areas of the adhesive are considered in the second phase to assess the effect of the bond size on the capacity of the joints. The considered bond sizes are 76 x 51 mm and 50 x 25 mm, respectively. The thickness of the adhesive used in both phases of the experiments is the optimum value as suggested by the manufacturer. The study also focuses on quantifying the adhesive stiffness properties under cyclic loading and their variation with different amplitudes of the cyclic loading. A previously developed analytical model is used to determine the spring constant simulating the shear behaviour of the adhesive. A finite element model developed in-house is used to predict the spring constant simulating the peel behaviour of the adhesive.

## **5.2 Experimental Program**

### **5.2.1 Test Specimens**

The bonded specimens used in the tests are hollow structural steel (HSS) sections and GFRP plates. The HSS columns have cross-sectional dimensions of 203 mm x 203 mm x

13 mm, length of 550 mm, and are made of M350 steel. The mechanical properties of the HSS section as specified by the manufacturer are: yield strength,  $\sigma_y = 350$  MPa, modulus of elasticity,  $E_s = 2 \times 10^5$  MPa, and Poisson's ratio,  $\nu_s = 0.30$ . Pultruded GFRP plates (EXTREN 525) of 19 mm thickness are used as adherends in the tests. The GFRP plates are supplied by the manufacturer in a large panel of 2.4 m x 1.2 m. The pultruded sheet consists of a large number of GFRP layers with either unidirectional or random arrangement of fibers. A polyester non-woven fabric layer covers each side of the GFRP plates and these layers are removed in order to achieve proper bonding with the steel sections. Based on the information provided by the manufacturer, the mechanical properties of the GFRP plates are flexural strength,  $\sigma_f = 206.8$  MPa,  $E_f = 1.38 \times 10^4$  MPa, and  $\nu_f = 0.31$ .

For bonded GFRP/steel joints, failure can occur at the adherend, adhesive, or the interface between these two media [10]. The failure mode of GFRP/steel joints depends on the bonding area and the type of adhesive. If the bonded area is large enough and/or the adhesion is strong, either a rupture of GFRP or steel yielding can happen. However, in this study no premature failure in either GFRP plate or the steel section is observed as the joint design is done in such a way that the failure capacity of the bonded components is higher than that of the adhesive. In the first phase of the experimental program, steel/GFRP joints with bond size of 76 x 51 mm are subjected to monotonic downward loading. Two methacrylate adhesives, MA300 and AO420, are considered in this phase. MA300 adhesive offers a combination of high strength and stiffness as well as an ability to bond a wide range of materials. On the other hand, methacrylate adhesive Plexus AO420 is the standard choice for composites bonding applications in the transportation



industry, because it requires virtually no surface preparation. In addition, this product provides a unique combination of outstanding impact resistance and superior toughness. El Damatty and Abushagur [9] recommended AO420, as this product achieved the highest load resistance with a superior performance in their experimental study.

In the second phase, two different sizes for the bonded joints with areas of 76 x 51 mm and 50 x 25 mm are used to assess the strength and stiffness properties of the joints and the adhesives. Both monotonic and cyclic tests are conducted on a number of specimens for the two bonded surface dimensions to assess the size effect and the degradation of stiffness and of strength due to reverse in loading direction.

### **5.2.2 Specimen Preparation**

The quality of the bonded joint depends strongly on the surface preparation of the adherends. To achieve good bond strength and durability, a roughened surface, cleaned of contaminants (particularly any chemicals, wax, or grease resulting from environmental exposure or after the composite fabrication process), has to be ensured. For the preparation of the steel specimen, sand blast is used to remove any rust or grease from the surfaces of steel. It is then cleaned using methanol in order to remove any dirt. Finally, a primer Plexus PC 120 is applied to the surface as recommended by the manufacturer of adhesives.

The GFRP plates are prepared for testing first by removing the non-structural layers of polyester non-woven fabric, which encase the glass-reinforced fiber. The adherence face of the GFRP plate is cleaned using alcohol methanol acid to avoid any contamination. The adhesive is first applied to the GFRP plates and then attached the steel column. It is

stated by the manufacturer that the optimum thickness of the adhesive is 0.79 mm. This thickness is controlled using four steel spacer disks located at the edges of the GFRP plates, which are attached to the steel sections and are then clamped using a C-clamp adjusted to obtain the optimum thickness of the adhesive. For the first phase of testing, two adhesive types are considered. Two specimens of each adhesive type are prepared and are subjected to monotonic loading. For the second phase, the adhesive used in the experiments is the one that is shown to provide higher strength capacity of the joint during the first phase. In the second phase, specimens are prepared in five different batches in the lab. The specimens are then allowed to cure at room temperature for 2 to 7 days. Figure 5.1 shows typical specimens prepared for the tests.

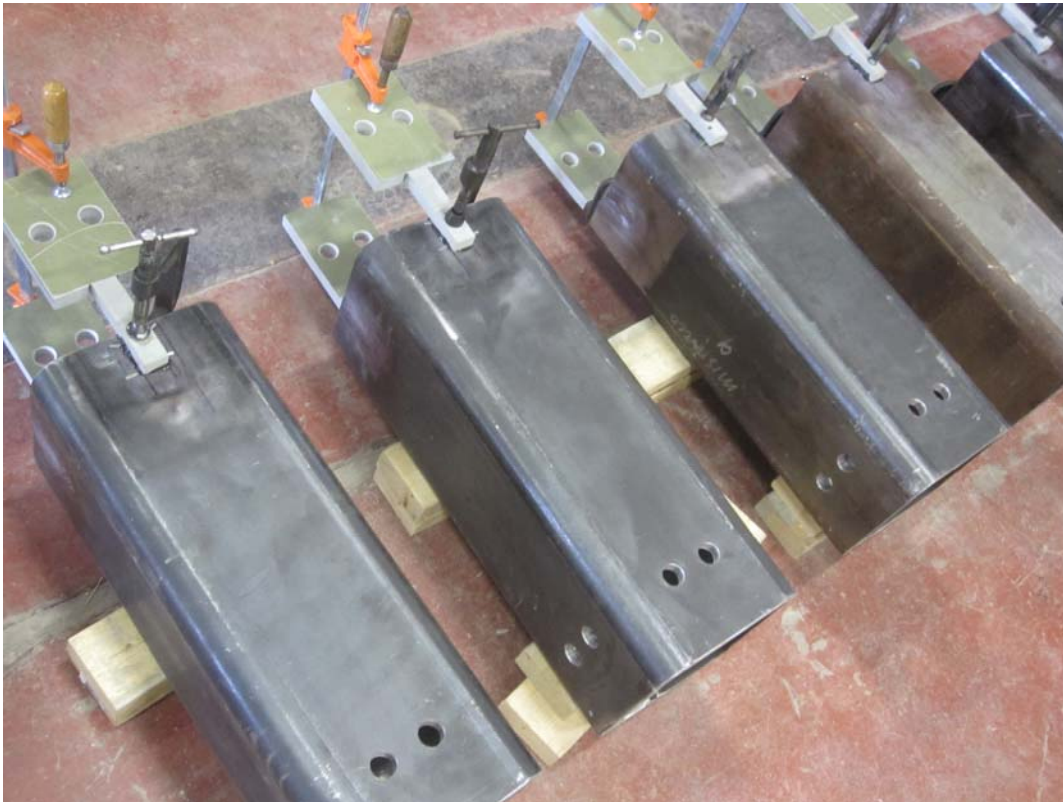


**Figure 5.1** A photo of prepared test specimens (bonded size = 50 x 25 mm).

For each batch of the second phase, a number of tests are performed both for monotonic and cyclic loading as listed below:

- Batch A- 1 downward, 1 upward , and 2 cyclic loadings (bond size: 76 x 51 mm)
- Batch B-1 downward, 1 upward, and 1 cyclic loadings (bond size: 76 x 51 mm)
- Batch C- 1 downward, 1 upward, and 1 cyclic loadings (bond size: 50 x 25 mm)
- Batch D- 1 downward, 1 upward, and 2 cyclic loadings (bond size: 50 x 25 mm)
- Batch E-1 downward, 1 upward, and 1 cyclic loadings (bond size: 50 x 25 mm)

For each batch of prepared specimens, the sequence of testing is monotonic downward, monotonic upward, and then cyclic loadings. An effort is made to test the specimens of each batch in the same day. However, some of the cyclic tests are done on the next day of the tested monotonic downward and upward specimens due to space and time constraints in the lab. As such in some cases, the age of the cured specimens for the cyclic loading is one day higher than that of the corresponding monotonic tests. However, the tested adhesive achieves almost 100% strength in one day, as stated by the manufacturer, minimizing the age effect of the cured specimens on the test results.

### **5.2.3 Loading Procedure and Displacement Measurement**

The steel/GFRP bonded assembly shown in Figure 5.2, is connected to the MTS testing machine, which has a capacity of 250 kN. The bottom steel plate attached to the steel HSS column section is firmly bolted to the floor whereas the top steel plate attached to the GFRP plate is connected to the actuator of the machine. The monotonic downward and upward loads are applied in a displacement-controlled manner using a rate of 0.5 mm/min. The MTS machine records the values of the applied load as well as the actuator

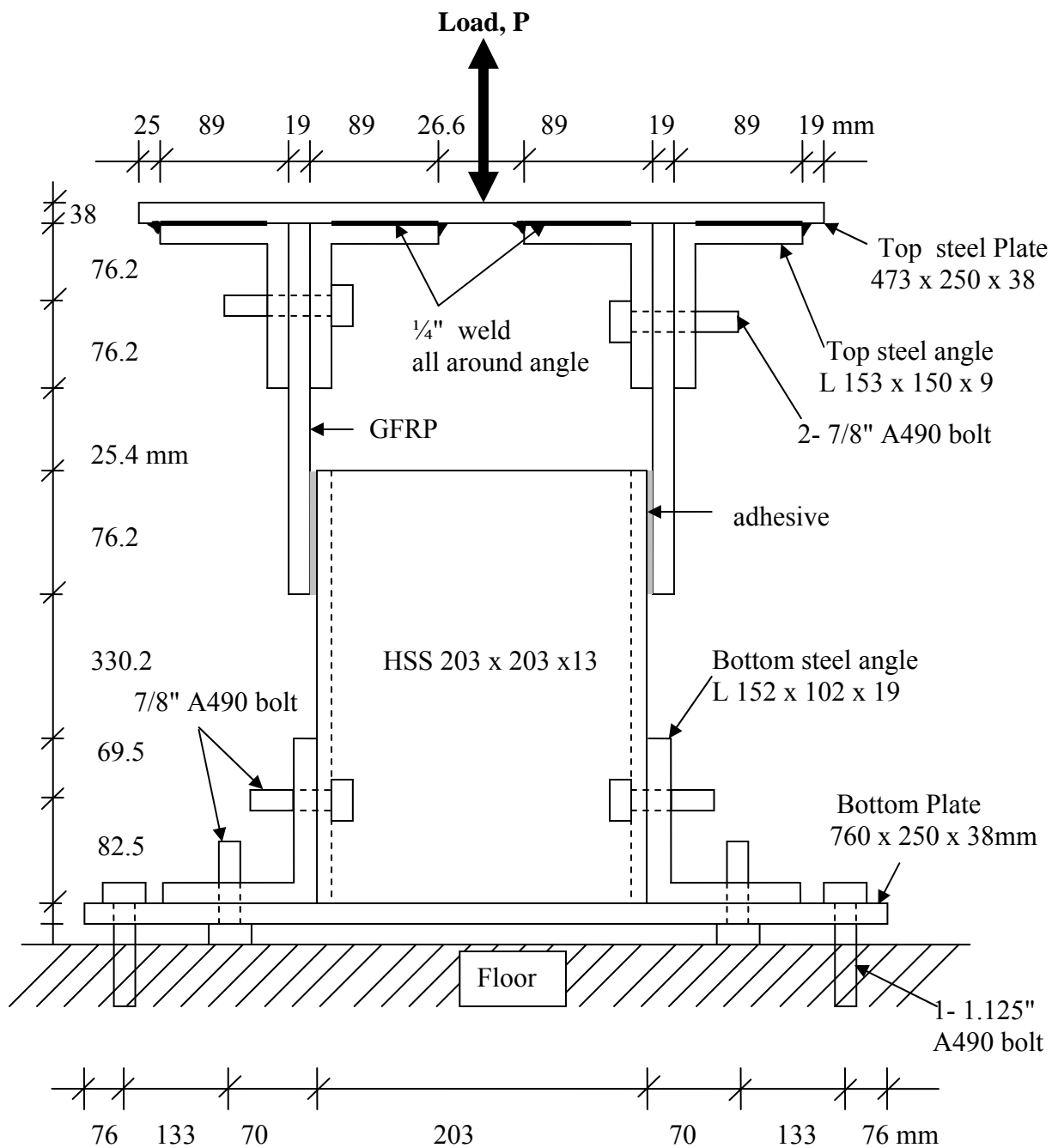
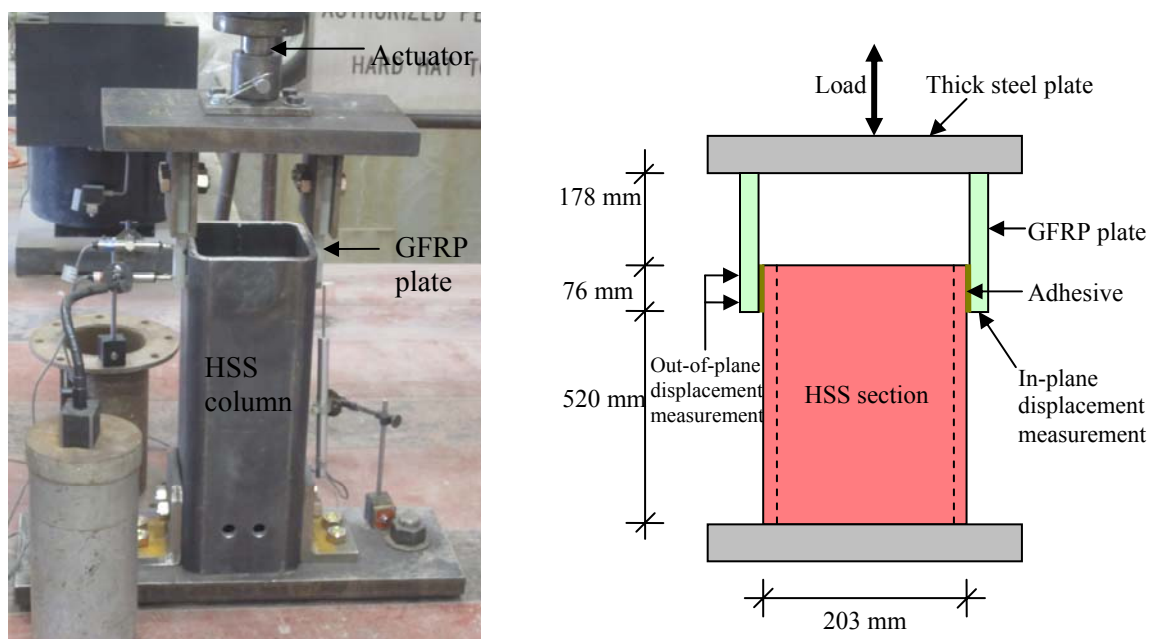


**Figure 5.2** Schematic of a shear lap test setup.

movement. In order to quantify the stiffness properties of the adhesive, a number of measurements for vertical (in-plane) displacement and out-of-plane displacement at the

outer face of GFRP plates are conducted in a number of tests. Electromagnetic displacement transducers for measurements of in-plane displacement are located at the bottom of the GFRP plates. Two transducers to measure the out-of-plane displacements are located 10 mm below the upper edge and 10 mm above the lower edge of the bonded GFRP plate as shown in a photo and schematic of the test setup provided in Figure 5.3.



(a) Photo of the setup

(b) Schematic of the setup

**Figure 5.3** A photo of the shear lap test setup.

All the cyclic tests are conducted in a load-controlled manner. Quasi-static loads are applied on the steel/GFRP assembly in each cycle of loading. Tests are conducted in an air-conditioned environment at temperatures ranging from 22-26<sup>0</sup>C. Generally, the behaviour of steel beams under cyclic loading is determined following the loading protocol of the American Institute of Steel Construction (AISC) seismic provisions

(AISC 2005) [11]. In this loading protocol, specified rotations are imposed on the test specimen. In each rotation value, a number of specified cycles are used to assess the cyclic behaviour of steel beams. In the current study, load amplitudes are considered to assess the cyclic behaviour of adhesively bonded steel/GFRP joints. For each load amplitude, the same number of cycles provided in the AISC 2005 seismic provisions [11] for cyclic testing is followed. The load amplitude ratio  $\lambda_L$ , is defined as the ratio of the applied load to the maximum capacity of the joint of the corresponding batch under monotonic loading. The applied load amplitude ratios are selected as 0.375, 0.5, 0.75, 0.80, 0.85, 0.90, 0.95, and 1.00, respectively. For ratios up to 0.75, six cycles are applied and for that of 0.80, four cycles are applied. For ratio higher than 0.80, only two cycles are applied in each load step. The loading protocol for the cyclic tests is shown in Figure 5.4.

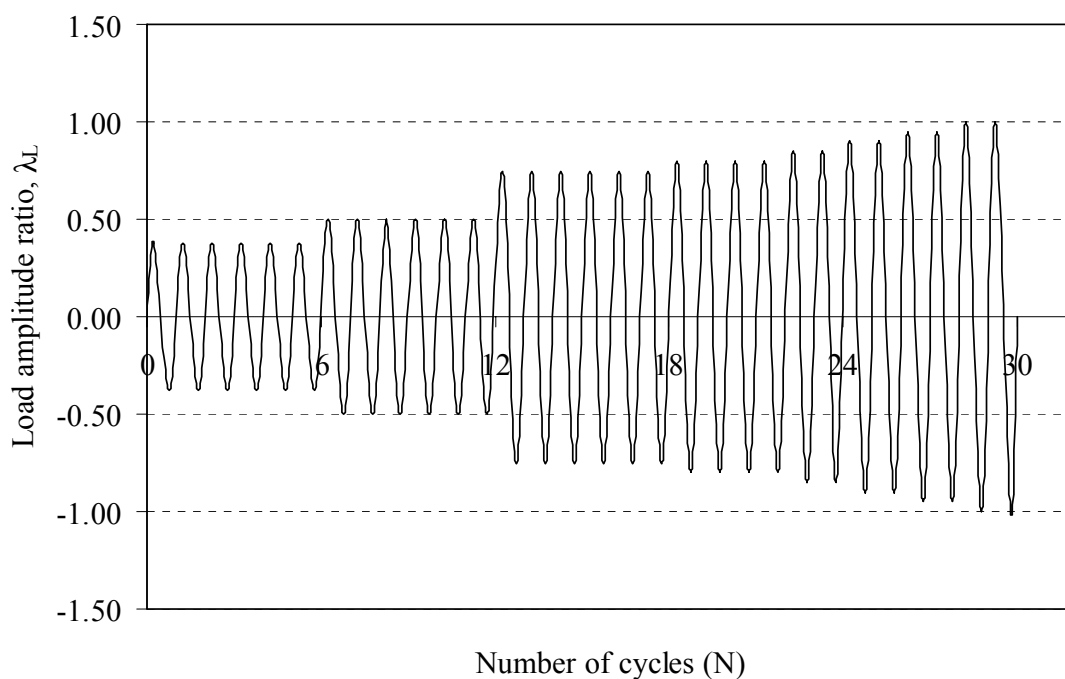


**Figure 5.4** Loading protocol used in the cyclic tests.

#### **5.2.4 Classification of Failure Modes of Adhesive in a Bonded Joint**

According to the ASTM standard D5573-99 [12], there are seven classes of failure modes in adhesive joints. They are as follows:

(1) Adhesive failure (ADH) (sometimes referred to as interfacial failure): separation appears at the adhesive–adherend interface.

(2) Cohesive failure (COH): separation is within the adhesive.

(3) Thin-layer cohesive failure (TLC) (sometimes referred to as interphase failure): failure similar to cohesive failure, except that the failure is very close to the adhesive–substrate interface, characterized by a “light dusting” of adhesive on one substrate surface and a thick layer of adhesive left on the other surface.

(4) Fiber-tear failure (FT): failure occurring exclusively within the FRP matrix, characterized by the appearance of reinforcing fibers on both ruptured surfaces.

(5) Light-fiber-tear failure (LFT): failure occurring within the FRP adherend, near the surface, characterized by a thin layer of the FRP resin matrix visible on the adhesive, with few or no glass fibers transferred from the adherend to the adhesive.

(6) Stock-break failure (SB): separation is within the adherend but outside the bonded region.

(7) Mixed failure: any combination of two or more different classes.

### **5.3 Results of Phase I Tests**

A preliminary experimental program is conducted considering the two methacrylate adhesives systems, MA300 and AO420. Two specimens for each type of adhesive with an adhesive bond size of 76 x 51 mm are tested under monotonic downward loadings.

The failure loads and the type of failure of the joints are determined for each type of adhesive. For both types, failure is shown to be governed by adhesive failure. The adhesive has been completely detached from the GFRP plate surface. A photo of a typical mode of failure of the adhesive is presented in Figure 5.5.



**Figure 5.5** A photo of a mode of failure of the adhesive.

The maximum strength of the bonded joints for the two types of adhesive is presented in Figure 5.6. From the figure, it is shown that the strength performance of the Plexus AO420 bonded steel/GFRP joints is better than that of the Plexus MA300 bonded joints. Therefore, the second phase of experimental program, which involves cyclic testing, is conducted using the adhesive AO420.



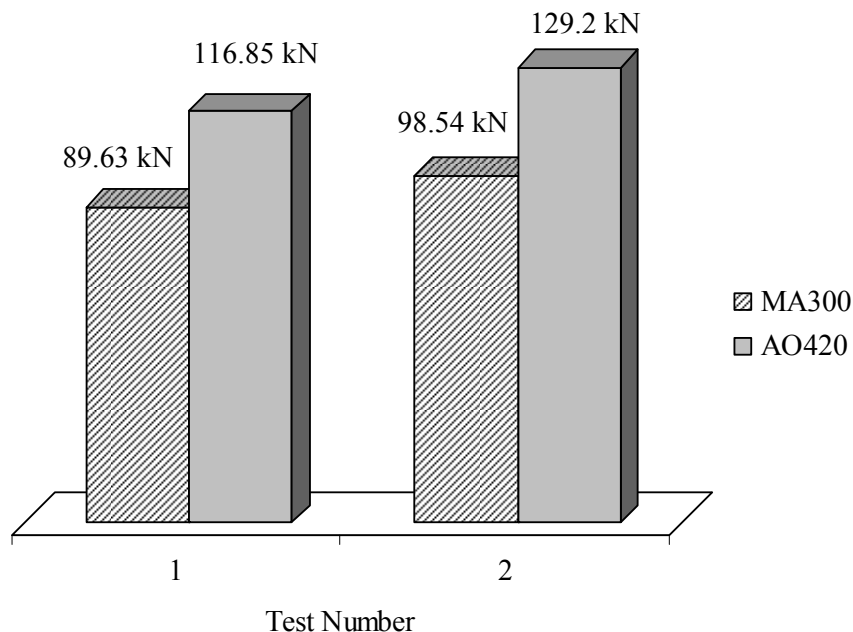


**Figure 5.6** Strength comparisons between the bonded joints with the adhesives of MA300 and AO420 in Phase I tests.

#### 5.4 Results of Phase II Tests

From the test results of Phase II, it is shown that all the bonded joint specimens fail by the adhesive failure mode under monotonic loadings. The ultimate failure of all the specimens occurs in a sudden manner, without any suggestive sign. The typical failure mode is the same as in Phase I tests shown in Figure 5.5. All the conducted monotonic tests result in a linear load-deflection curve followed by a brittle adhesive failure. A typical load-deflection curve for the shear lap joints under both monotonic downward and upward loadings is provided in Figure 5.7.

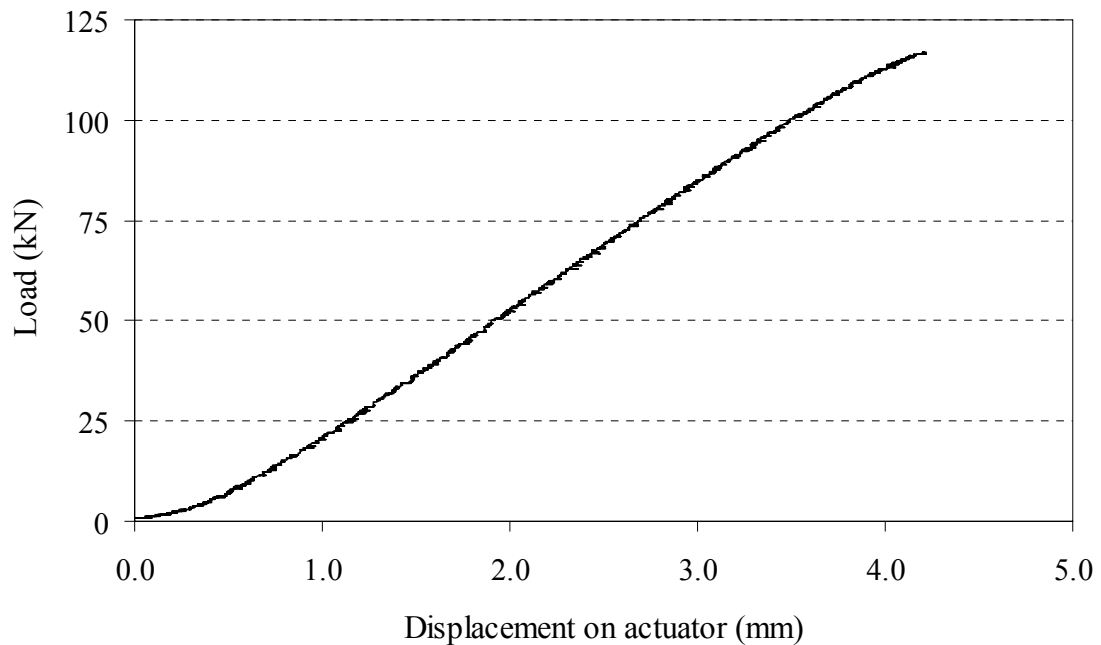


**Figure 5.7** Typical load-deflection response of a monotonic shear lap test.

The test results are presented in Table 5.1 for the bonded areas of 76 x 51 mm and 50 x 25 mm. Considering a two-dimensional linear elastic analysis and assuming constant stress, the adhesive stresses can be expressed by  $P/(bl)$ , where  $P$  is the load applied on the bonded joint,  $b$  is the joint width, and  $l$  is the joint length. This value of force/area can be interpreted as the average shear stress acting on the adhesive layer. It is, in fact, the basis for quoting adhesive shear strength in many standards such as ASTM [13] and ISO [14]. Also, it can be used for the sake of comparison between the monotonic and cyclic strength values. From the table, it is shown that the average shear stress at failure is 12.90 MPa under cyclic loading in comparison to 15.5 MPa under monotonic loading.

**Table 5.1** Test results of bonded steel/GFRP shear lap joints.

Batch no.	Bond area (mm x mm)	Monotonic failure load (kN)		Monotonic failure load /bonded area (N/mm <sup>2</sup> )		Cyclic failure load (kN)	Cyclic failure load/area (N/mm <sup>2</sup> )
		Downward loading	Upward loading	Downward loading	Upward loading		
A-1	76 x 51	116.85	117.13	15.07	15.11	103.26	13.32
A-2	76 x 51					104.20	13.44
B-1	76 x 51	129.20	119.23	16.66	15.38	124.20	16.02
C-1	50 x 25	41.28	36.55	16.51	14.62	30.50	12.20
D-1	50 x 25	35.10	41.81	14.04	16.72	29.53	11.81
D-2	50 x 25					31.53	12.61
E-1	50 x 25	37.83	37.89	15.13	15.16	27.33	10.93
Average:				15.48	15.40		12.90

From Table 5.1, it is observed that the strength capacity of the bonded joints under cyclic loading has been reduced in comparison to the monotonic loadings by about 17%. Therefore, it is recommended to reduce the strength capacity of steel/GFRP bonded joints in seismic regions by a similar percentage.

Failure of all the cyclic-tested specimens is shown to be governed by adhesive failure. Separation of the adhesive is observed from the GFRP plate for all the batches of Phase II cyclic tests. A typical load-deflection pattern of the tested specimens under cyclic loading is provided in Figure 5.8.

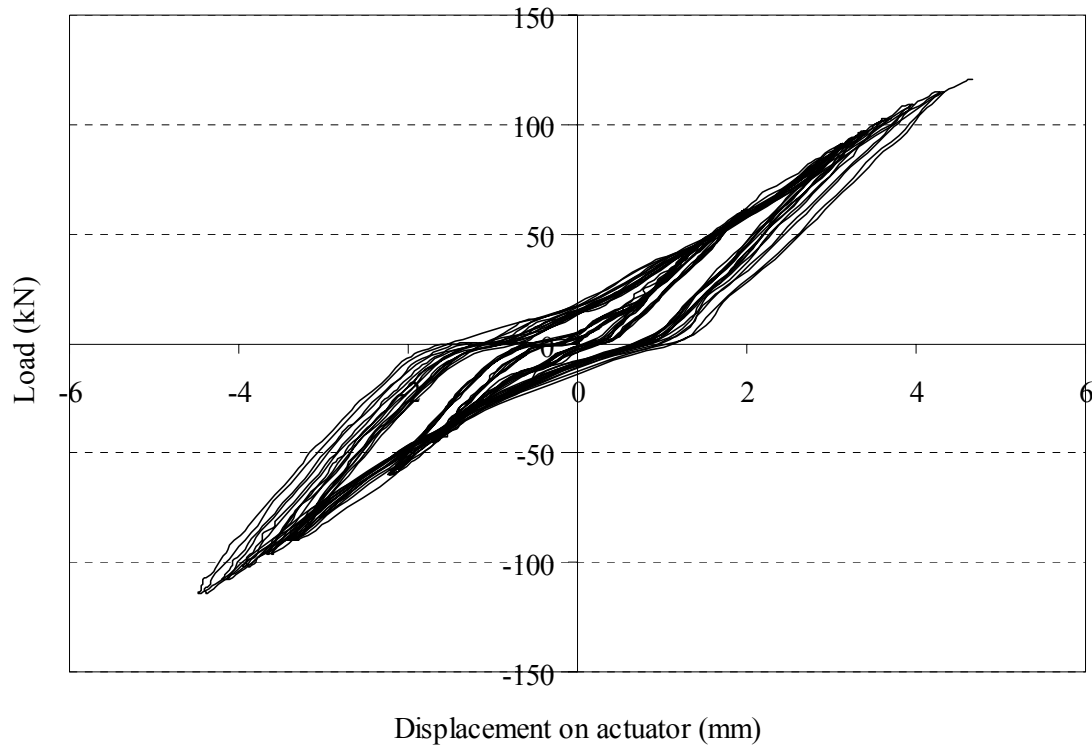


**Figure 5.8** Typical load-deflection response of a cyclic shear lap test.

### 5.5 Effect of Bond Size on the Capacity of Steel/GFRP Joints

From the test results presented in Table 5.1, no clear trend of the effect of the bonded area of the adhesive on the strength of the joints can be concluded. The load-deflection and the failure pattern of the 76 x 51 mm bonded adhesive are identical with that of the bonded joints of 50 x 25 mm. In both cases, the failure is governed by an adhesive failure for all the tested specimens under both monotonic and cyclic loadings. Therefore, the variation of the bonded size does not seem to have a significant effect on the shear capacity of the steel/GFRP joints. However, the results indicate that under cyclic loading, the reduction in strength relative to the monotonic loading is more pronounced for smaller bonded area.

## 5.6 Analytical Prediction of the Shear Stiffness of the Adhesive

Shear spring constants simulating the shear stiffness of an adhesive can be predicted analytically using a closed-form solution. A free body diagram of a GFRP plate tested in this study is provided in Figure 5.9. In this figure,  $K_s$  is a continuous spring (with unit of force/volume) simulating the shear stiffness of the adhesive. In the shear lap tests, a GFRP plate is subjected to in-plane stresses resulting from the vertical load as well as the bending stresses due to the eccentricity between the load and the vertical support system, “ $K_s$ ”.

### 5.6.1 Prediction of Shear Stiffness of the Adhesive under Monotonic Loading

The GFRP sheet can be treated as a plate resting on elastic supports. The steel section has high stiffness compared to both the GFRP plate and the adhesive and can be assumed to be infinitely rigid. The solution of the differential equation governing the in-plane behaviour of the GFRP sheets is provided below.

The vertical forces acting on an infinitesimal element ( $dx$ ) are shown in Figure 5.9b. In this figure,  $u$ ,  $\sigma$ ,  $b$ ,  $t$ ,  $E$  are the in-plane displacement, mid surface axial stress, width, thickness, and modulus of elasticity of the GFRP sheet, respectively. Considering the vertical equilibrium of forces acting on the infinitesimal element and using the relation  $\sigma = E du/dx$ , the following second-order differential equation is obtained [9].

$$\frac{d^2u}{dx^2} - \omega^2 u = 0 \quad (5.1)$$

where

$$\omega^2 = \frac{K_s}{Et} \quad (5.2)$$

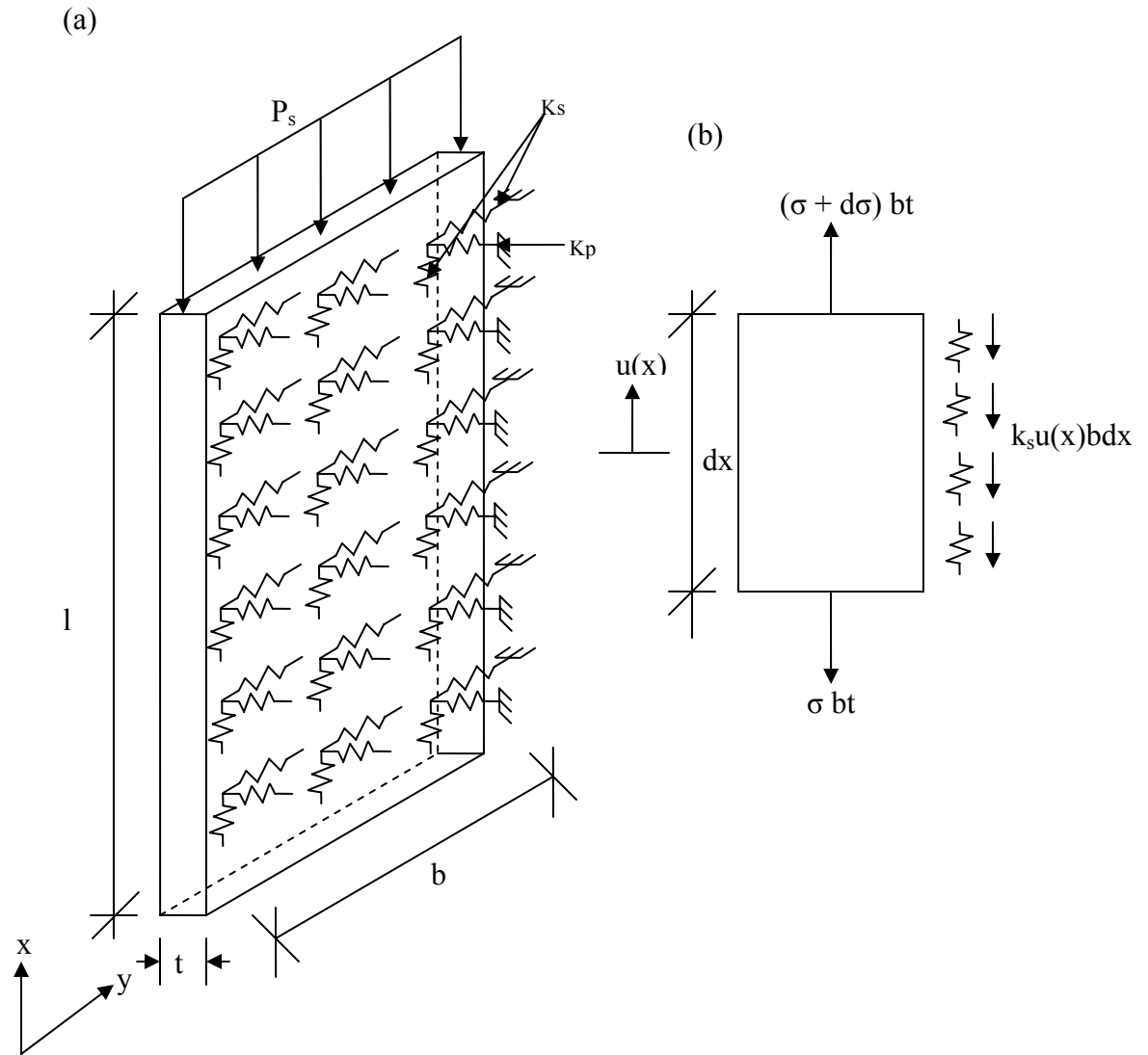


**Figure 5.9** A free body diagram of GFRP plate that bonded to steel elements.

The axial load is applied at the top ( $x = l$ ) of the GFRP plate, while the bottom ( $x = 0$ ) of the plate is free. As such, the boundary conditions at the two edges of the plate are given as:

$$x = 0, \quad \frac{du}{dx} = 0$$

$$x = l, \quad \frac{du}{dx} = -\frac{P_s}{btE}$$

where,  $P_s$  is the load acting on one GFRP plate and is equal to half of the total load applied in the experiment i.e.  $P_s = P/2$ .

The solution satisfying the differential equation and the above boundary conditions is given by:

$$u(x) = -\frac{P_s}{btE\omega \sinh(\omega l)} \cosh(\omega x) \quad (5.3)$$

Using the above expression, the relationship between the applied load ( $P = 2P_s$ ) and the measured bottom deflection of the plate will be given as:

$$P = -2btE\omega \sinh(\omega l) u(0) \quad (5.4)$$

Based on the load-deflection curves ( $P$  versus  $u(0)$ ) obtained experimentally, the above expression can be used to evaluate  $\omega$  and consequently the spring constant  $K_s$  using Equation (5.2). The values obtained from processing ten monotonic tests including upward and downward loadings are provided in Table 5.2. These shear stiffness values range between 20.42 and 30.81 N/mm<sup>3</sup> with an average value of 23.61 N/mm<sup>3</sup>. As an illustration, the distribution of axial displacement  $u(x)$  along the height of the GFRP plate is provided in Figure 5.10, evaluated according to Equation (5.3) above for a  $K_s$  value of 23.29 N/mm<sup>3</sup> (corresponding to test C25-1).

The distribution of shear stresses that occur in the adhesive system can be evaluated once the value of  $K_s$  is estimated. This distribution  $\sigma_s(x)$  is obtained by multiplying the spring constant  $K_s$  by the axial displacement profile, i.e.,

$$\sigma_s(x) = K_s u(x) \quad (5.5)$$

As such, the shear stress distribution will follow the typical profile of an axial displacement provided in Figure 5.10 with maximum values occurring at the top edge of the adhesive. The maximum shear stresses that occur at the adhesive are provided also in Table 5.2. The shear strength of the adhesive ranges between 12.1 MPa and 15.5 MPa as provided by the manufacturer. From Table 5.1, it is shown that the average shear stress at the failure of the bonded joints is 15.5 MPa. It is observed from Table 5.2 that the maximum shear stress for all the tested specimens exceeds these strength values. However, strength values provided by the manufacturer are based on the average shear stress over the entire bonded area and the values shown in Table 5.2 are for the maximum shear stress developed in the adhesive layer at the edge of steel/GFRP joints.

**Table 5.2** Summary of test results and processing of shear lap monotonic tests.

Type of test	Bonded area	Specimen no.	Failure load (kN)	Vertical displacement at failure at the bottom of GFRP plate (mm)	Shear stiffness, $K_s$ (N/mm <sup>3</sup> )	Maximum shear stress (MPa)
Downward Loading	76 mm x 51 mm	C51-1	116.85	0.677	20.57	17.4
		C51-2	129.20	0.736	20.91	19.3
	50 mm x 25 mm	C25-1	41.28	0.682	23.29	17.8
		C25-2	35.10	0.433	30.81	15.5
		C25-3	37.83	0.575	25.23	16.4
Upward Loading	76 mm x 51 mm	T51-1	117.13	0.600	23.07	17.7
		T51-2	119.23	0.662	21.41	17.8
	50 mm x 25 mm	T25-1	36.55	0.692	20.42	15.6
		T25-2	41.81	0.615	26.04	18.1
		T25-3	37.89	0.598	24.34	16.3
Average:					23.61	17.2
Standard Deviation:					3.05	1.15



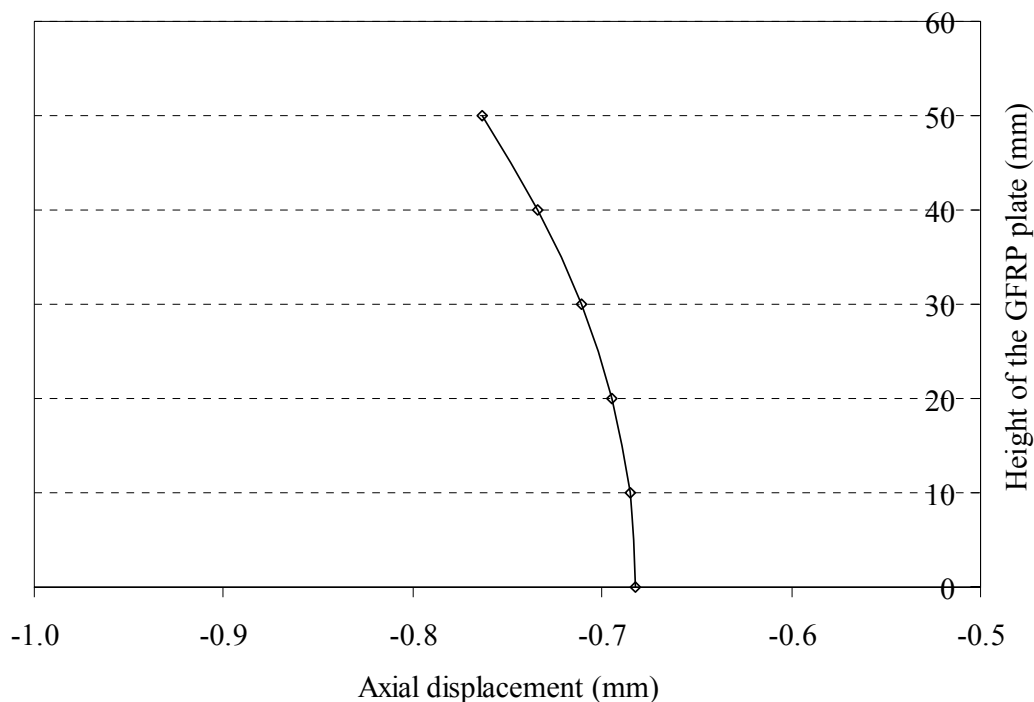


**Figure 5.10** Distribution of axial displacements along the height of GFRP plate (C25-1).

### 5.6.2 Prediction of Shear Stiffness of the Adhesive under Cyclic Loading

The shear stiffness of the adhesive under cyclic loading can be determined following the procedure presented for monotonic loading in subsection 5.6.1. The same procedure can be used since the load is applied in a quasi-static manner and linear load-deflection behaviour of the joint has been shown in each cycle of loading. For each cycle, the applied load and the corresponding displacement measured at the bottom of the GFRP plate are used to calculate the shear spring constants simulating the shear behaviour of the adhesive under cyclic loading.

The variation of the shear stiffness of the adhesive with the number of cycles is presented in Figures 5.11(a) and 5.11(b) of the joint with bond area of 76 x 51 mm for the upward and downward loadings, respectively. CYC51-1, CYC51-2, CYC51-3 denote the cyclic

test specimens corresponding batches of A-1, A-2, and B-1, respectively. No specific trend of degradation of the shear stiffness of the adhesive is observed in any number of cycles even when the amplitude of the load is increased.

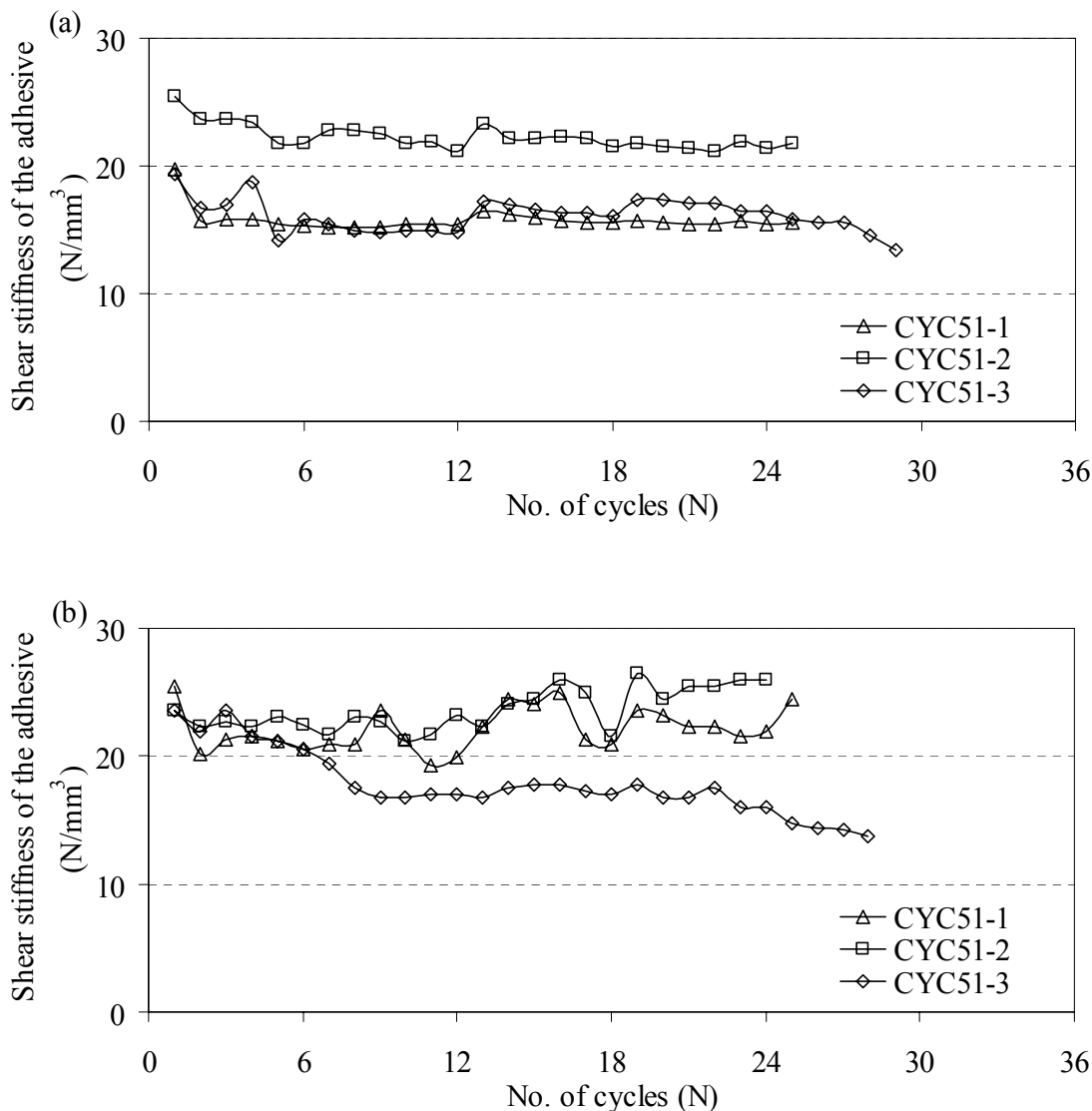


**Figure 5.11** Variation of the shear stiffness of the adhesive under cyclic loading (bond size = 76 x 51 mm) (a) upward loading and (b) downward loading.

The shear stiffness values of the adhesive are determined also for the joints with the 50 x 25 mm bonded area. CYC25-1, CYC25-2, CYC25-3, and CYC25-4 denote the cyclic test

specimens corresponding batches of C-1, D-1, D-2, and E-1, respectively. The shear stiffness values do not also show any specific trend of degradation under different load amplitudes of the cyclic loading. However, degradation in the shear stiffness of the adhesive is shown for the cyclic test CYC25-3 at a load amplitude ratio of 0.75. This pattern of the reduction in stiffness is similar for both the upward and downward loadings as shown in Figure 5.12.

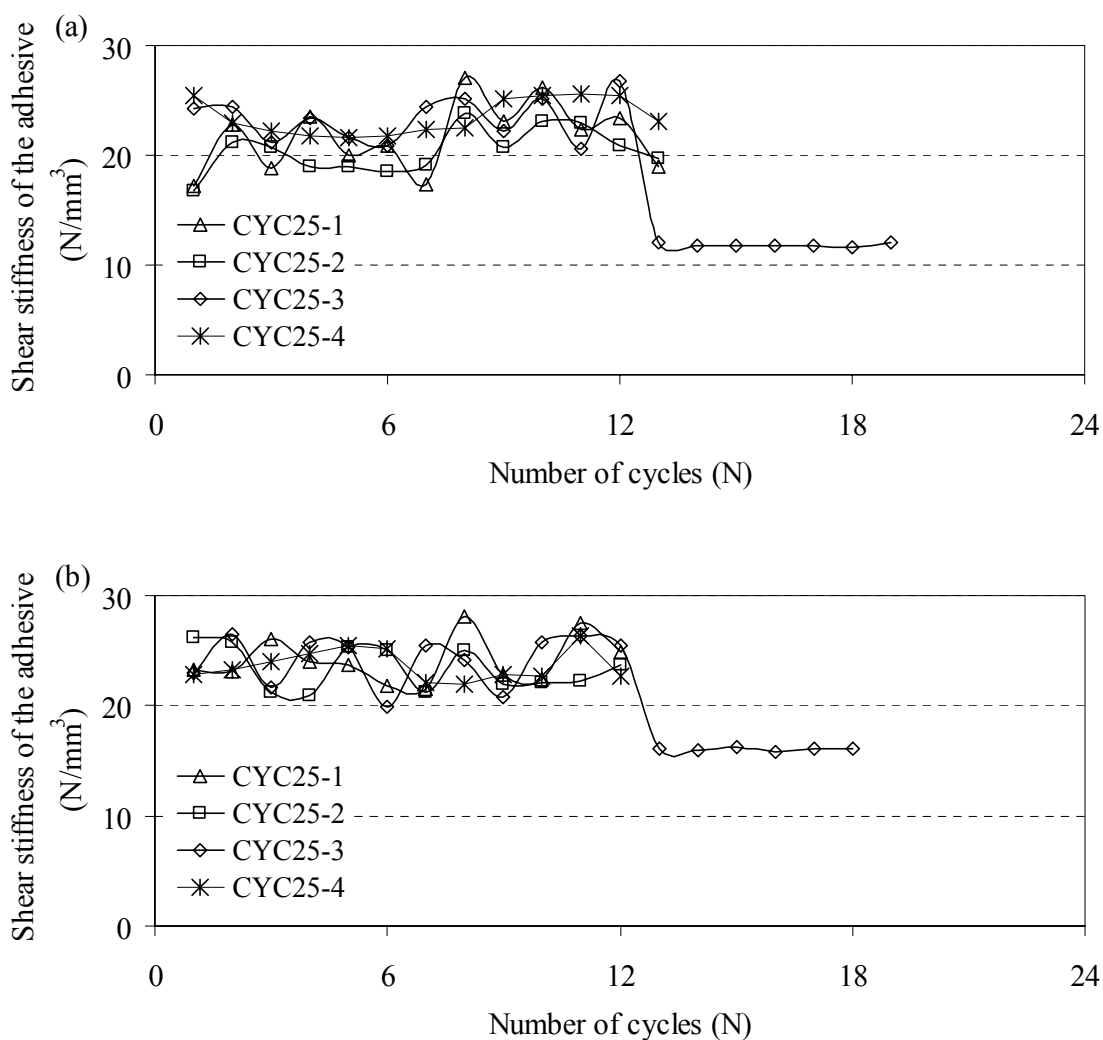
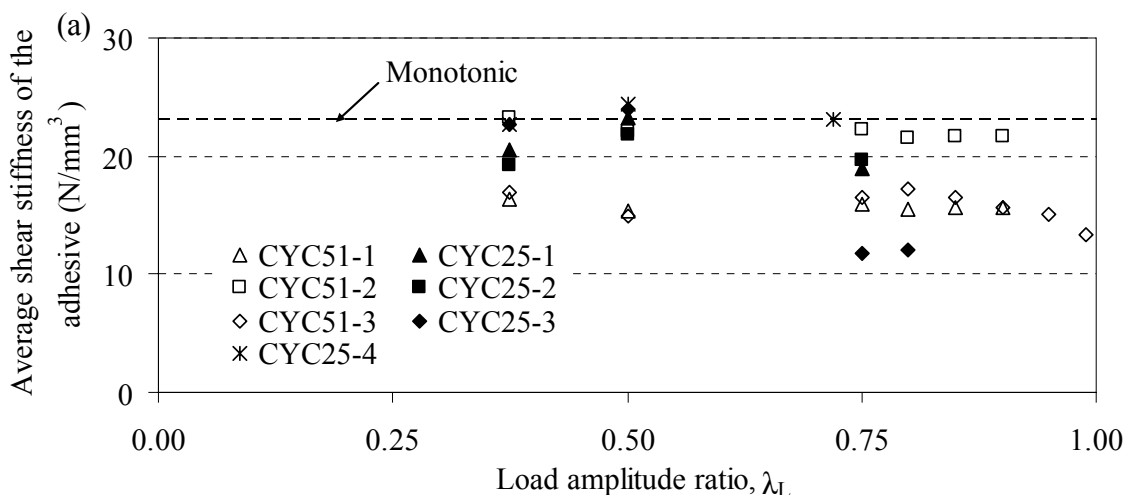


**Figure 5.12** Variation of the shear stiffness of the adhesive under cyclic loading (bond size = 50 x 25 mm) (a) upward loading and (b) downward loading.

Maximum shear stress in the adhesive occurs at the top edge of the bonded steel/GFRP connection. The maximum shear stress in the adhesive of the 76 x 51 mm bonded joint is determined to be equal to 17.2 MPa in an upward loading cycle of the test CYC51-3. The maximum shear stress developed in the adhesive layer of the 50 x 25 mm joints is predicted to have a value of 13.1 MPa for the cyclic test CYC25-3.

For each load amplitude, average values of the shear stiffness are calculated over the specified number of cycles. These stiffness values are presented in Figure 5.13 in comparison to the corresponding values under monotonic loading. From the figure it is shown that shear stiffness values under monotonic loading are higher than those under cyclic loading. This trend is observed for both the joints of the 76 x51 mm and 50 x 25 mm bonded areas.

For each load amplitude, average shear stresses developed in the adhesive layer are also determined over the specified number of cycles. The variation of the average shear stress is presented in Figure 5.14 with different load amplitudes of the cyclic loading. From the figure, it is concluded that the average shear stress developed in the adhesive layer is not affected with the considered bonded areas of the adhesive.



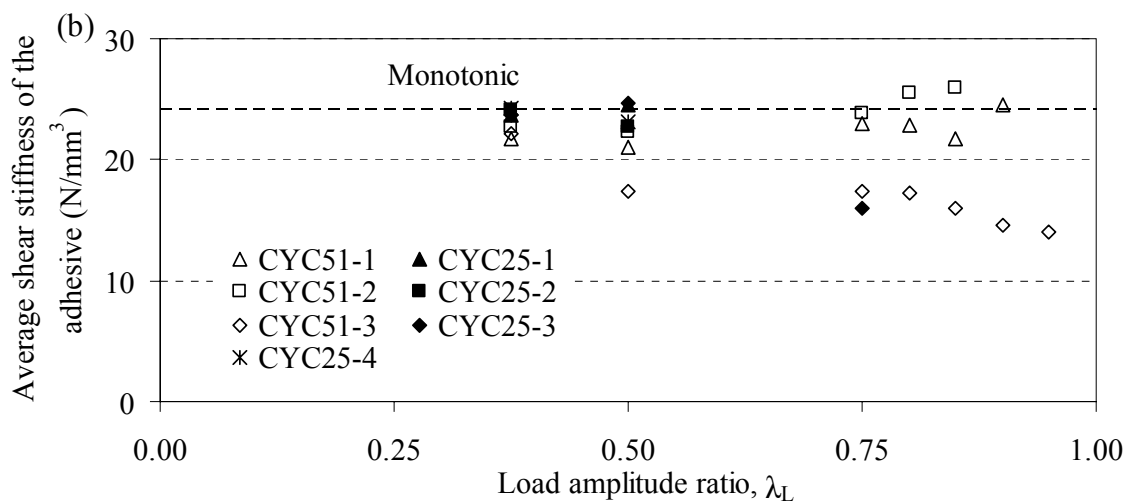


**Figure 5.13** Effect of the amplitudes of cyclic loading on the shear stiffness of the adhesive (a) upward loading and (b) downward loading.

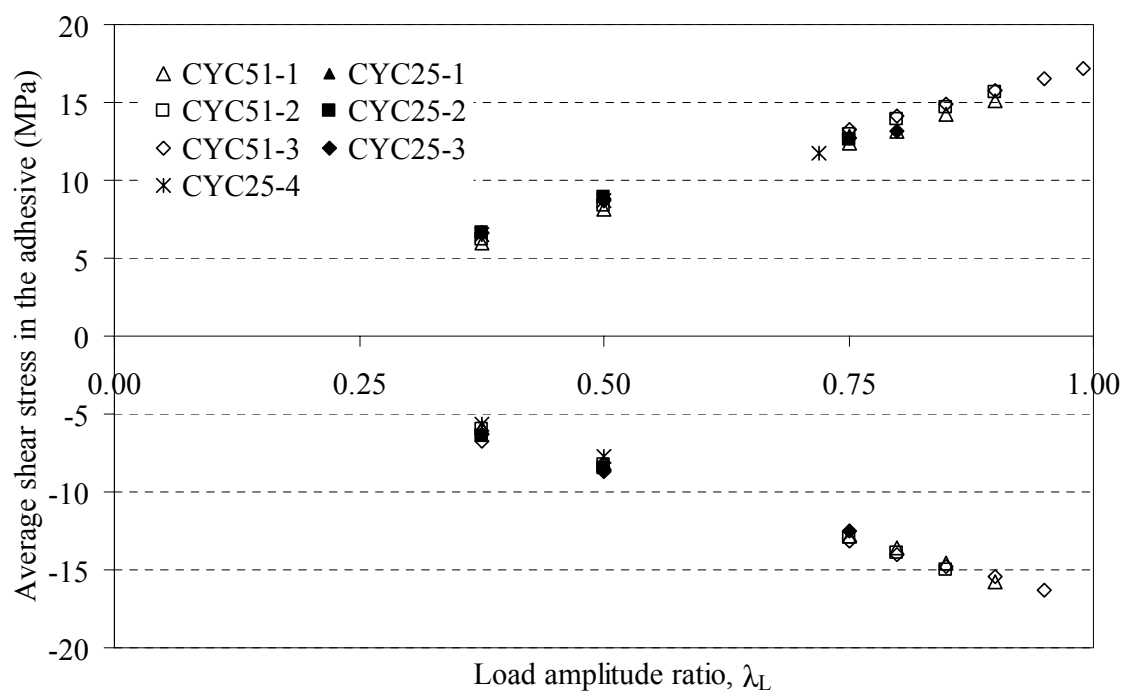


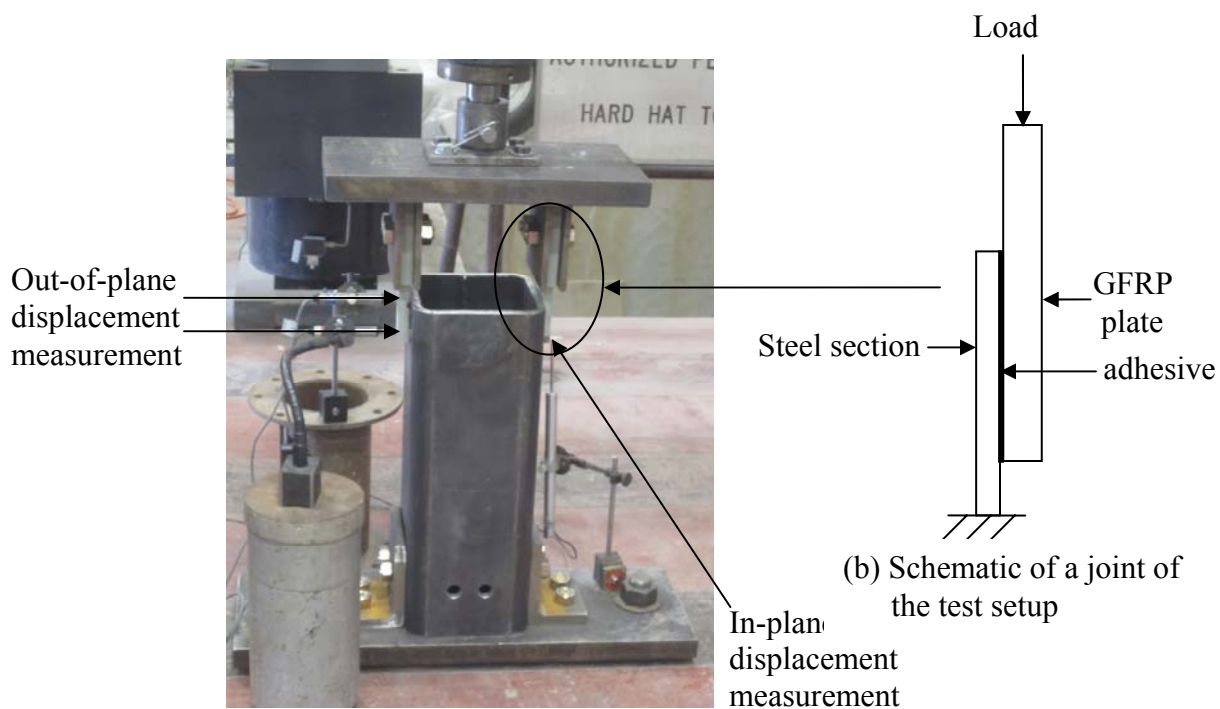
**Figure 5.14** Variation of average shear stress developed in the adhesive with different amplitudes of cyclic loading.

## 5.7 Numerical Prediction of Peeling Stiffness of the Adhesive

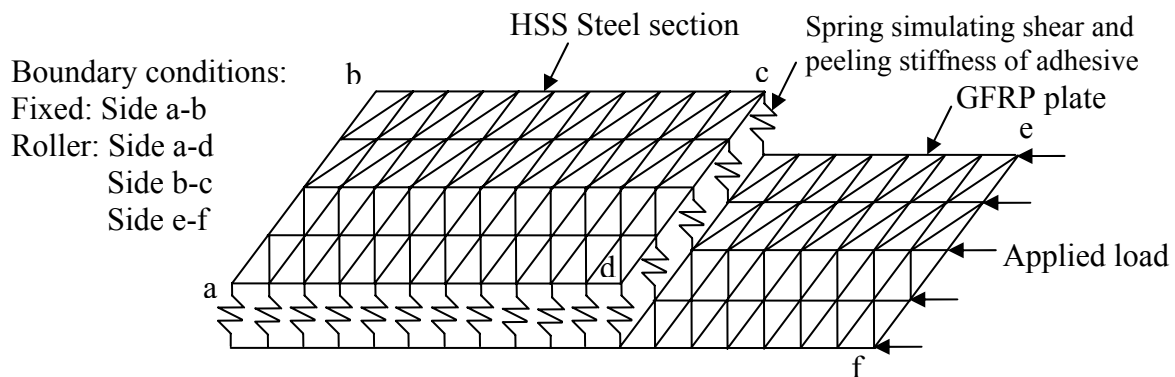
A finite element modeling of the bonded joint is carried out to predict the peeling stiffness of the adhesive under both monotonic and cyclic loadings. The numerical model is based on a consistent degenerated triangular subparametric shell element that was developed by Koziy and Mirza [15] and was then extended by El Damatty et al. [16] to include the effects of geometric and material nonlinearities. Both the steel and GFRP plates are modelled using an assembly of consistent shell elements. This shell element is free from the shear-locking phenomenon observed in many isoparametric degenerated shell elements when used to model thin shell structures.

A special 26 noded contact element is developed in Chapter 2 to model the continuous spring simulating the shear and peel behaviour of the adhesive. In a continuum, horizontal in-plane springs represent the shear behaviour while the spring in out-of-plane represents the peeling behaviour of the adhesive. Thus, the model of this special spring system allows the adhesive to incorporate the bond behaviour between the steel HSS section and the GFRP plate. The geometry and boundary conditions of the joint used in the numerical analysis of a typical single lap joint is shown in Figure 5.15. The part of the HSS attached to the adhesive is modelled as a steel plate. This steel plate has the same thickness of the HSS section but has high flexural stiffness in comparison to the bonded joint. The boundary conditions of the steel plate are considered to be roller supports which allow displacement along the direction of the loading. The sides a-d and b-c of the steel plate, shown in Figure 5.15(c), are considered to be restrained in the out-of-plane direction to account for the higher flexural stiffness of the HSS section. The bottom of the steel plate (side a-b) is assumed to be fixed. The GFRP plate side (side: e-f) that is

connected to steel bolts to transfer the load from the actuator to the joint can be considered to have a roller support condition which allows in-plane displacement while restraining out-of-plane displacement.



(a) Photo of a test setup



(c) Meshed model and boundary conditions of the connecting plates for the adhesive joint

**Figure 5.15** Geometry and boundary conditions for the joint of a bonded shear lap test.

The thickness of the GFRP plate after removing the nonstructural layers is 18 mm. The length of the GFRP plate, from the lower edge of the bonded adhesive to the steel bolts at which load is transferred from the actuator to the GFRP plate, is 176 mm for joints of bonded area of 76 x 51 mm and 150 mm for that of the 50 x 25 mm joints. A length measurement is performed on the GFRP plates attached to the two opposite sides of the HSS column at the bolted and the bonded joint locations of each cured specimen. This is done to detect any eccentricity in loading involved in the cured specimen during testing. The difference between the measured centerline distances of the attached GFRP plates at the bolted and bonded locations is termed as an eccentricity of the applied load. This eccentricity is accounted for in the numerical model by applying a concentrated moment (equal to the applied axial load multiplied by the eccentricity) at the point of application of the load.

The numerical model is first used to compute the shear stiffness of the adhesive by conducting the following steps:

- The experimental load and the concentrated moment are applied to the model.
- A trial value of shear stiffness of the adhesive ( $K_s$ ) is assumed. The in-plane displacement at the bottom of the GFRP plate is obtained from the analysis and then compared to the corresponding experimental measurement.
- The value of  $K_s$  is changed gradually until the value providing goal match, in terms of in-plane displacement, is obtained with the experimental result.

The distribution of mid-surface axial displacement of the GFRP plate along the bonded height of the plate obtained from the numerical model is compared with the same distribution determined using the analytical solution obtained using Equation (5.3).



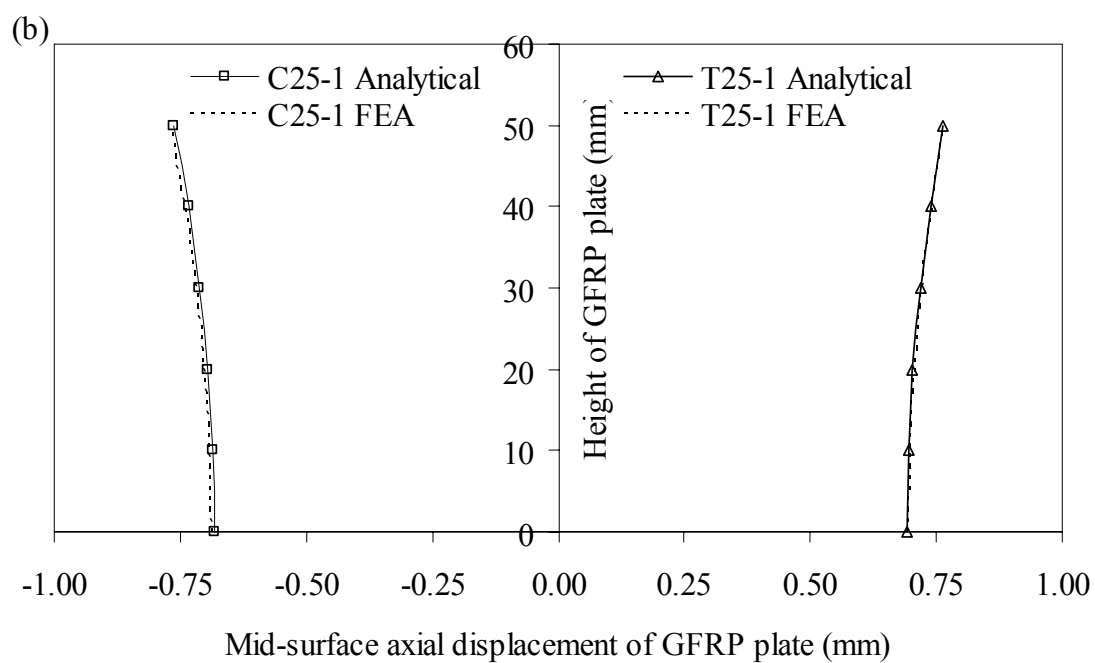
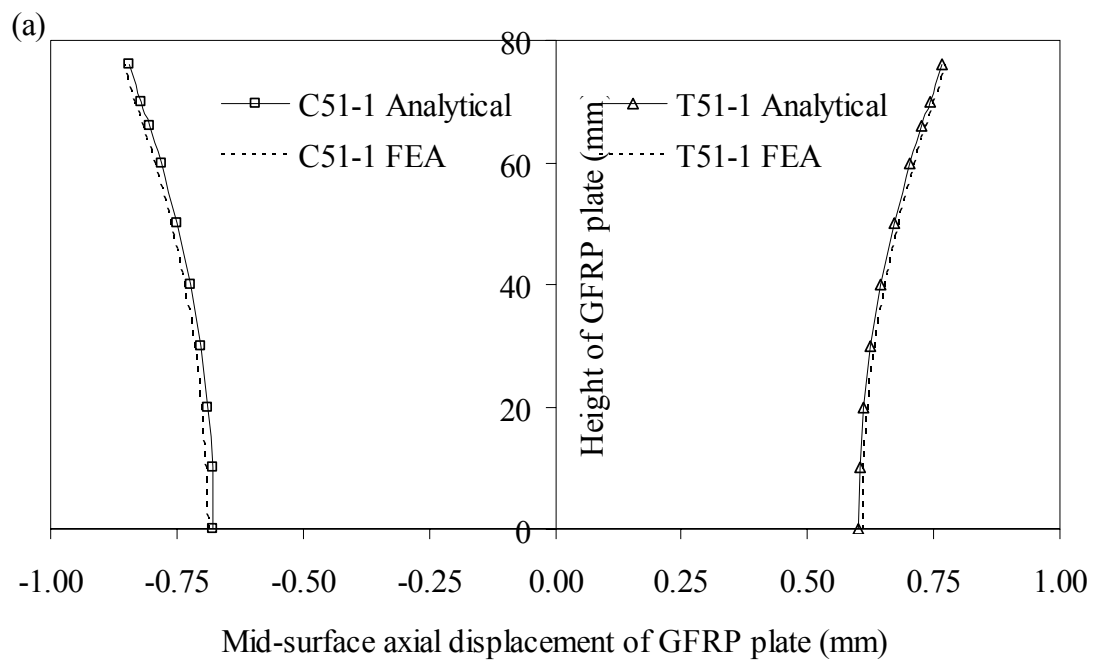


**Figure 5.16** Comparison of mid-surface axial displacements of GFRP plate along the height of the plate (a) 76 x 51 mm and (b) 50 x 25 mm.

Such comparisons are provided in Figure 5.16. The comparisons are made for both the bonded areas of the 76 x 51 mm and 50 x 25 mm. From this figure, it is shown that the numerical model captures the mid-surface axial displacement profile of the GFRP plate with a very good agreement with the analytical solution.

The numerical model is then used to compute the peeling stiffness of the adhesive. The locations of the measured out-of-plane displacements at the outer face of the GFRP plate are shown in Figure 5.15. The measurement points are located at 10 mm below and above the bonded edges of the GFRP plate. Knowing the failure load, out-of-plane displacements, and the eccentricity of load of each test, the following steps are used to calculate the peeling stiffness of the adhesive:

- For a specific test, the experimental load, shear stiffness of the adhesive ( $K_s$ ), and the concentrated moment resulting from the eccentricity are incorporated into the numerical model.
- A trial value of peeling stiffness of the adhesive ( $K_p$ ) is assumed and this value is changed iteratively in the model in order to match the measured out-of-plane displacements of the GFRP plate.
- The  $K_p$  value corresponding to matched values between the numerical prediction and the measured values for the out-of-plane displacement is determined.

The relation between the applied load and the out-of-plane displacements obtained from the numerical simulation and the experimental results are given in Figure 5.17. From this figure, it is shown that the model captures the out-of-plane displacements with loading

history in a good agreement for the monotonic downward test (C51-1).

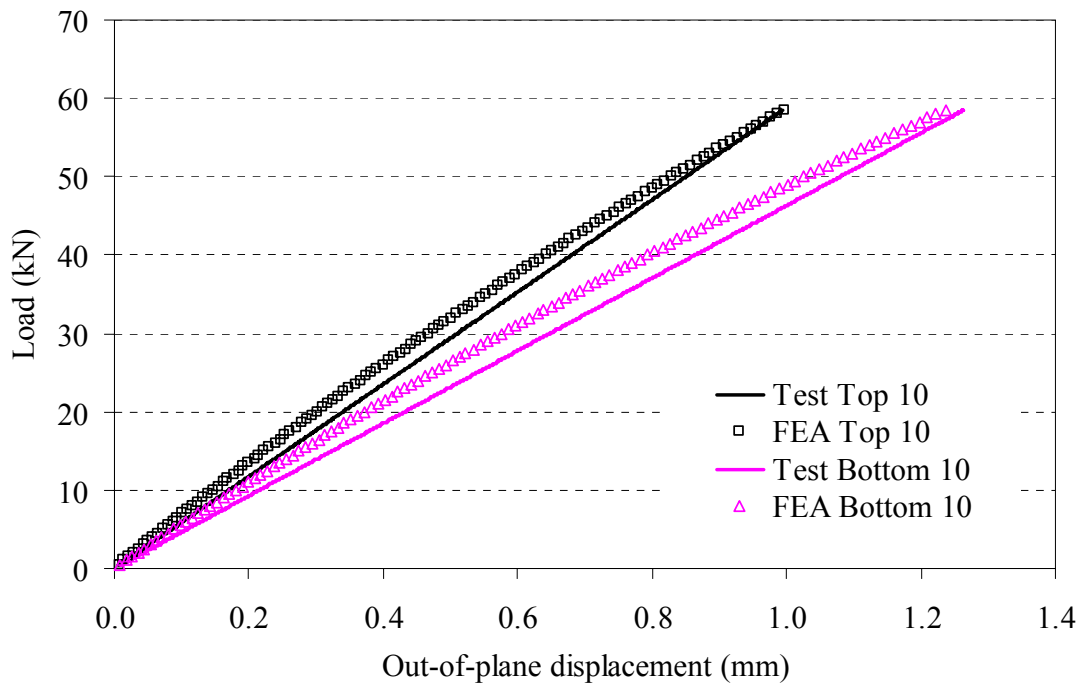


**Figure 5.17** Typical load vs. out-of-plane displacement diagrams measured by tests and predicted by the model (C51-1).

The peeling stiffness values of the adhesive predicted by the numerical model are presented in Table 5.3 for the monotonic tests. These peeling stiffness values range between  $1.05 \text{ N/mm}^3$  and  $2.00 \text{ N/mm}^3$  with an average value of  $1.50 \text{ N/mm}^3$ .

**Table 5.3** Prediction of peeling stiffness of adhesive under monotonic loadings.

Specimen no.	Peeling stiffness, $K_p$ (N/mm <sup>3</sup> )
C51-1	1.24
C51-2	1.93
C25-1	1.05
C25-2	1.80
C25-3	1.30
T51-1	1.35
T51-2	2.00
T25-1	1.22
T25-2	1.49
T25-3	1.58

The model is then used to determine the peeling stiffness of the adhesive under cyclic loading. For each amplitude of cyclic loading, the same steps described above are used to determine the corresponding value of peeling stiffness. The predicted peeling stiffness of the adhesive is shown in Figure 5.18 for the cyclic tests CYC51-1 and CYC25-1. From this figure, no appreciable degradation of the peeling stiffness due to cyclic loadings is observed. For each load amplitude, the peeling stiffness of the adhesive in the initial cycle is predicted to have a lower value than that of the rest of the cycles. This pattern of stiffness variation is shown for all the load amplitudes considered in the cyclic tests. However, at the maximum load amplitude of the test CYC51-1, the peeling stiffness under downward loading degrades more than that of the initial cycle of loading. It is also predicted that the bonded area of the adhesive has an insignificant effect on the variation of the peeling stiffness of the adhesive.

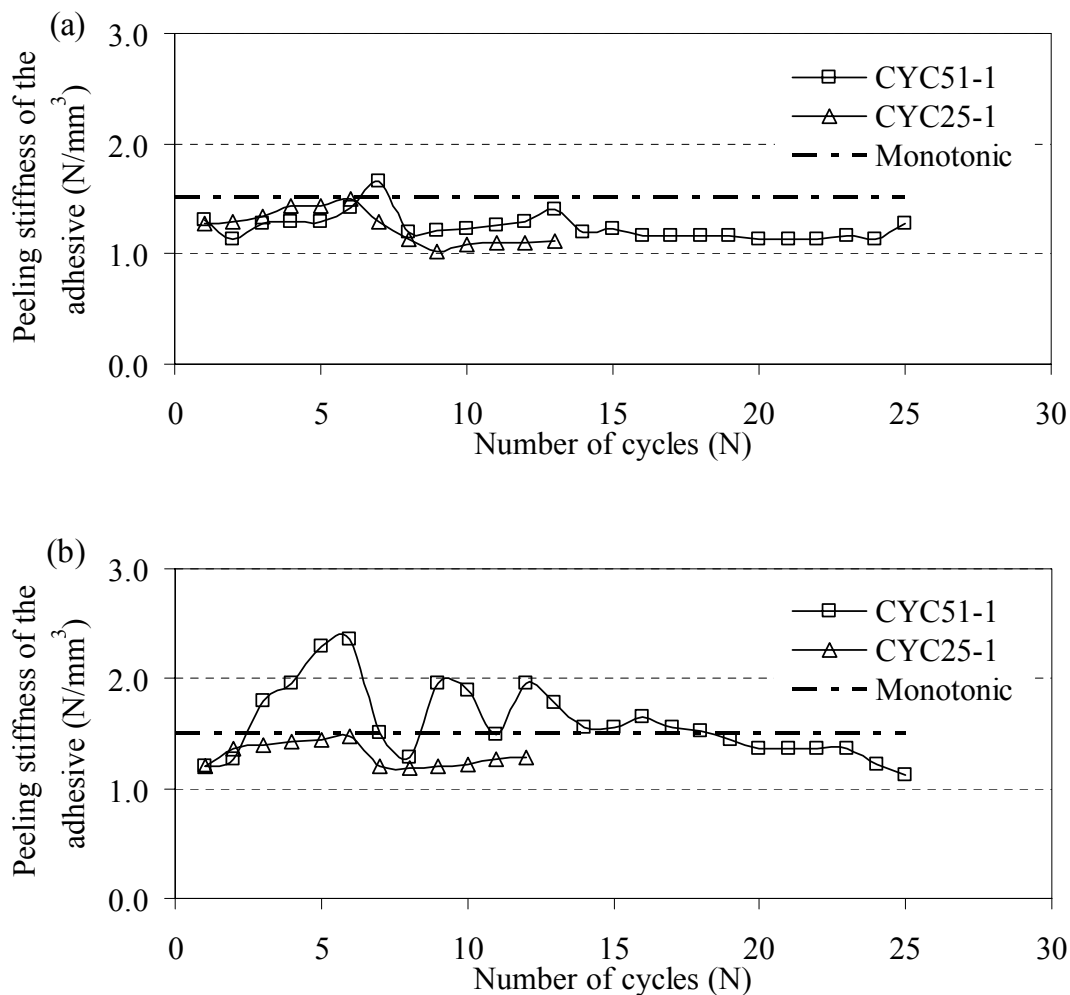


**Figure 5.18** Effect of cyclic loading on the variation of peeling stiffness of the adhesive (a) upward loading and (b) downward loading.

## 5.8 Summary and Conclusions

An experimental, analytical and numerical investigation is conducted to assess the strength and stiffness behaviour of bonded steel/glass fiber reinforced plastic (GFRP) plate connections under both monotonic and cyclic loadings. A number of shear lap tests, in which GFRP plates are bonded to hollow structural steel sections, are performed. During the tests, the in-plane and out-of-plane displacements of the GFRP are measured

using displacement transducers. Two types of methacrylate adhesives of MA300 and AO420 are used in monotonic tests to determine the strength capacities of the bonded joints in the first phase of the experimental program. From the test results obtained from this phase, it is shown that the methacrylate adhesive AO420 provides higher strength compared to the MA300 adhesive. In the second phase of the experimental program, a number of shear lap tests are conducted using the adhesive AO420 to assess the strength and stiffness of the joints under both monotonic and cyclic loadings. Two different sizes of the bonded area are considered to assess the size effect on the strength and stiffness of the steel/GFRP joints.

A system of continuous in-plane and out-of-plane springs is used to simulate the adhesive medium. A previously developed analytical solution is used to determine the shear stiffness of the adhesive under both monotonic and cyclic loadings. A numerical model developed in-house is used to predict the peeling stiffness of the adhesive. However, the spring constants simulating the shear and peeling behaviour of the adhesive evaluated in this study are limited to the type of adhesive used in the bonded joints. For such an adhesive system, these spring constants can be used to simulate any GFRP/steel connection subjected to both monotonic and cyclic loadings. The study also provides an estimation of the maximum shear stresses developed in the adhesive layer at the edge of the steel/GFRP joints under both the monotonic and cyclic loadings.

The main conclusions that can be drawn from the study are as follows:

- The strength of steel/GFRP bonded joints under cyclic loading reduces by about 17% in comparison to under monotonic loadings.

- The size of the bonded areas has no significant effect on the strength capacity of the joints under monotonic loadings.
- The average shear stiffness of the adhesive is determined to be  $23.61 \text{ N/mm}^3$  under monotonic loading. For various amplitude of cyclic loading, no specific trend of degradation of the shear stiffness of the adhesive is predicted.
- The effect of the size of the bonded area of the adhesive is insignificant on the shear stiffness values.
- Maximum shear stress developed in the adhesive layer does not show significant variation within the different cycles of an amplitude ratio of loading. This stress value is also shown to be independent of the considered bonded areas of the joint.
- The average peeling stiffness of the adhesive is predicted to have a value of  $1.50 \text{ N/mm}^3$  under monotonic loading. No specific trend of degradation of the peeling stiffness of the adhesive is shown with the load amplitude ratios of cyclic loading.

## 5.9 References

- [1] Khalili, S. M. R., Khalili, S., Pirouzhshemi, M. R., Shokuhfar, A., and Mittal, R. K., Numerical study of lap joints with composite adhesives and composite adherends subjected to in-plane and transverse loads, *International Journal of Adhesion and Adhesives* 2008; 228: 411-418.
- [2] Kim, K-S., Yi, Y-M., Cho, G-R., and Kim, C-G., Failure prediction and strength improvement of uni-directional composite single lap joints, *Composite Structures* 2008; 82: 513-520.
- [3] Tong, L., Bond shear strength for adhesive bonded double-lap joints, *International*

- Journal of Solids Structures 1994; 31:2919–2931.
- [4] Tong, L., Strength of adhesively bonded single-lap and lap shear joints, International Journal of Solids Structures 1998; 35(20):2601-2616.
- [5] Her, S-C., Stress analysis of adhesively bonded lap joints, Composite Structures 1999; 47:673-678.
- [6] Wanga, Z. Y., Wang, L., Guo, W., Deng, H., Tong, J. W., and Aymerich, F., An investigation on strain/stress distribution around the overlap end of laminated composite single-lap joints, Composite Structures 2009; 89:589-595.
- [7] Diaz, J., Romera, L., Hernandez, S., and Baldomir, A., Benchmarking of three-dimensional finite element models of CFRP single-lap bonded joints, International Journal of Adhesion and Adhesives 2010; 30: 178-189.
- [8] Nemes, O. and Lachaud, F., Double-lap adhesive bonded-joints assemblies modelling, International Journal of Adhesion and Adhesives 2010; 30: 288-297.
- [9] El Damatty, A. and Abushagur, M., Testing and modeling of shear and peel behavior for bonded steel/FRP connections, Journal of Thin-Walled Structures 2003; 41(11): 987-1003.
- [10] Zhao, X. L. and Zhang, L., State-of-the-art review on FRP strengthened steel structures, Engineering Structures 2007; 29(8): 1807-1823.
- [11] American Institute of Steel Construction (AISC), Seismic provisions for structural steel buildings, ANSI/AISC 341-05, Chicago, IL, 2005.
- [12] American Society for Testing and Materials, ASTM D5573-99, 2005, “Classifying Failure Modes in Fiber-Reinforced-Plastic (FRP) Joints”, [www.astm.org](http://www.astm.org)
- [13] American Society for Testing and Materials, ASTM D3165-07, “Strength Properties



of Adhesives in Shear by Tension Loading of Single-Lap-Joint Laminated Assemblies”, [www.astm.org](http://www.astm.org)

[14] International Organization for Standardization, ISO 4587:2003, “Adhesives- Determination of Tensile lap-Shear Strength of Rigid-to-Rigid Bonded Assemblies” [www.iso.org](http://www.iso.org)

[15] Koziey, B. L. and Mirza, F. A., Consistent thick shell element, Computers and Structures 1997; 65(12): 513-541.

[16] El Damatty, A., Korol, R. M., and Mirza, F. A., Large displacement extension of consistent shell element for static and dynamic analysis, Computers and Structures 1997; 62(6): 943-960.

## **CHAPTER 6**

### **CONCLUSIONS**

#### **6.1 General**

The research conducted and reported in this thesis consists of two main parts. The first part involves the assessment of using glass fiber reinforced polymer (GFRP) plates in enhancing the buckling capacity and deflection behaviour of retrofitted steel plates, beams, and moment resisting frames. An interface element to bond the steel and GFRP plates is developed first. This element can simulate the shear and peeling behaviour of the adhesive in a bonded joint. A finite element model that is developed in-house to consider bonded adhesive behaviour as well as the geometric and material nonlinear effects is used to assess the enhancement in buckling capacity of the retrofitted steel plates, beams, and moment resisting frames. In the second part of the study, an experimental program is conducted on the adhesively bonded joints under cyclic loading to assess the strength and stiffness of the joints. Both monotonic and cyclic tests are conducted on the bonded joints to assess their load-carrying capacities as well as the stiffness properties of the adhesive. Two different bond sizes are considered in the experimental program to study the effect of the adhesive bonded area on the strength capacity and stiffness of the joints.

#### **6.2 Summary and Conclusions**

The following are the main conclusions that can be drawn and summarized from this study:

- Enhancement in buckling capacity is higher for GFRP retrofitted slender steel

plates than that of the thicker plates.

- Constrained end conditions of GFRP plates in a retrofitted system always result in a higher capacity than that of the non-constrained plates.
- For the constrained ended GFRP plates, GFRP rupture is the dominant mode of failure of the retrofitted plates. However, shear failure of the adhesive is governed for the non-constrained GFRP plates.
- Initial geometric imperfection reduces the capacity of retrofitted steel plates.
- Improvements in load and deflection at failure are higher for GFRP retrofitted slender beams than that of the plastic beam sections.
- GFRP rupture is the governing mode of failure for retrofitted plastic steel beams. For slender beams, elastic buckling to GFRP rupture are the modes of failure that limit their capacities.
- Elastic buckling of the system is shown for slender steel beams with smaller thickness addition of GFRP plates. However, GFRP rupture is predicted for the larger GFRP plate additions for such beams.
- Initial geometric imperfections reduce both the load and deflection capacities of the retrofitted beams with GFRP plates.
- The effect of strain hardening behaviour and residual stresses of steel is insignificant on the load and deflection improvements of retrofitted beams. However, retrofitted beams which fail by GFRP rupture show improvement in the capacity due to the inclusion of strain hardening. Residual stresses reduce both the load and deflection improvements for retrofitted beams which fail by elastic buckling.

- Different span length of the beams does not show variations in the load and deflection improvements. However, span length changes the failure modes of retrofitted beams.
- The enhancement in the lateral load capacity of retrofitted moment resisting frames with plastic beam sections is not significant as shear failure of the adhesive limits the full utilization of the strength capacity of added GFRP plates.
- Interstory drift indexes can be reduced significantly for the GFRP retrofitted frames having plastic beam sections.
- For slender frames, both the lateral load capacity and deflection at failure can be enhanced significantly by retrofitting beams' flanges with GFRP plates.
- The response modification factor of a moment resisting frame can be improved significantly by retrofitting slender beams of the frame with GFRP plates.
- The strength capacity of steel/GFRP bonded joints under cyclic loading reduces by 17% in comparison to that under monotonic loading.
- The size of adhesive bonded areas has no significant effect on the variation in the strength capacity of the joints under cyclic loading.
- No specific trend of degradation of shear and peel stiffnesses of the adhesive is predicted under cyclic loading.

### **6.3 Recommendations for Future Research**

For further research, the following investigations related to the improvement of the buckling behaviour of the elements of steel structures are suggested:

- The analysis conducted in this study can be extended to only a portion of the steel sections instead of bonding the entire steel plate and the flanges of steel beams.
- The developed numerical model can be extended to achieve the optimum size of the GFRP plate and bonded areas of the adhesive to achieve a specific enhancement in capacity and/or deflection of structures.
- Similar studies can be conducted to assess the improvement in the web buckling and the lateral torsional buckling of the steel girders.
- The improvement in lateral load behaviour of GFRP strengthened steel structures can be studied considering the retrofitted elements of the structures under fire conditions.
- A full-scale experimental study can be performed to assess the performance of GFRP strengthened steel beams under cyclic loadings.
- A small-scale experiment can also be done on the GFRP retrofitted moment resisting frames to assess their performance in enhancing the lateral load-carrying capacities.

# APPENDIX I

This appendix provides the results of load and deflection capacities of retrofitted steel beams with different thickness additions of GFRP plates. All the conducted analysis results of retrofitted beams are presented in Table format. Tables 3.1 to 3.5 provide the load and deflection values for cantilever beams with free end loading. Tables 3.6 to 3.10 provide the results for simply supported beams with center point loading. Tables 3.11 to 3.15 provide the results for simply supported beams under two-point loading systems. The results of analyses of retrofitted beams are presented in terms of load and deflection at failure as well as their improvement ratios. Different failure modes of the beams are also mentioned. In the tables,  $\mu_L$  represents the load improvement factor as the ratio of the load capacity of the retrofitted beam to the load capacity of the corresponding bare steel beam. Deflection improvement factor is presented by  $\mu_\Delta$  as the ratio of deflection value of the retrofitted beam to the deflection value at failure of the corresponding bare steel beam.

**Table 3.1** Predicted values of load and deflection of the retrofitted cantilever beams ( $b_f = 150$  mm and  $t_f = 7.5$  mm) with free end loading.

h (mm)	w (mm)	Bare steel beam			Retrofitted beam					
		Load (kN)	Defl. (mm)	Failure mode*	GFRP (mm)	Load (kN)	Defl. (mm)	$\mu_L$	$\mu_\Delta$	Failure mode*
150	7.5	41	58	IB	6.35	46.2	86	1.13	1.48	G
					9.5	48	108	1.17	1.86	G
					12.5	49.4	127	1.20	2.19	G
					15.5	51	147	1.24	2.54	G
					19.0	52	168	1.27	2.90	G
150	5.0	38.2	65	IB	6.35	43	97	1.13	1.49	G
					9.5	44.2	116	1.16	1.78	G
					12.5	45.6	150	1.20	2.31	G
					15.5	46.6	184	1.22	2.84	G
					19.0	47.2	201	1.24	3.09	G
200	5.0	52.4	44	IB	6.35	59.6	73	1.14	1.66	G
					9.5	61.6	91	1.18	2.09	G
					12.5	63.6	107	1.21	2.46	G
					15.5	65.4	138	1.25	3.15	G
					19.0	66.4	156	1.27	3.55	G
200	4.0	50.5	41	IB	6.35	57.2	77	1.13	1.85	G
					9.5	59	95	1.17	2.29	G
					12.5	60.8	122	1.20	2.93	G
					15.5	62	150	1.23	3.63	G
					19.0	63	177	1.25	4.27	G
300	6.0	89.5	36	IB	6.35	100.4	46	1.12	1.30	G
					9.5	106.2	60	1.19	1.67	G
					12.5	109.6	68	1.22	1.91	G
					15.5	112.8	79	1.26	2.23	G
					19.0	117	95	1.31	2.67	G

\* EI = Elastic buckling, G = GFRP rupture, IB = Inelastic buckling, Y = Yielding of steel

**Table 3.2** Predicted values of load and deflection of the retrofitted cantilever beams ( $b_f = 150$  mm and  $t_f = 5.0$  mm) with free end loading.

h (mm)	w (mm)	Bare steel beam			Retrofitted beam					
		Load (kN)	Defl. (mm)	Failure mode*	GFRP (mm)	Load (kN)	Defl. (mm)	$\mu_L$	$\mu_\Delta$	Failure mode*
150	7.5	29.3	52	IB	6.35	34	81	1.16	1.56	G
					9.5	35.8	101	1.22	1.94	G
					12.5	37.4	126	1.27	2.41	G
					15.5	39	160	1.33	3.07	G
					19.0	40	185	1.36	3.55	G
150	5.0	26.6	51	IB	6.35	30.8	86	1.16	1.69	G
					9.5	32.4	115	1.22	2.26	G
					12.5	33.6	150	1.26	2.93	G
					15.5	34.8	199	1.31	3.91	G
					19.0	35.8	237	1.34	4.64	G
200	5.0	37.7	46	IB	6.35	43.8	68	1.16	1.47	G
					9.5	45.8	88	1.21	1.90	G
					12.5	48	108	1.27	2.33	G
					15.5	49.8	147	1.32	3.18	G
					19.0	51	180	1.35	3.88	G
200	4.0	35.8	42	IB	6.35	41.6	73	1.16	1.75	G
					9.5	43.4	91	1.21	2.17	G
					12.5	45.2	123	1.26	2.95	G
					15.5	46.6	167	1.30	3.99	G
					19.0	47.8	206	1.34	4.94	G
300	6.0	67.6	35	IB	6.35	79	52	1.17	1.50	G
					9.5	83.2	60	1.23	1.72	G
					12.5	86.6	69	1.28	1.99	G
					15.5	89.6	82	1.33	2.36	G
					19.0	93.8	99	1.39	2.84	G

\* EI = Elastic buckling, G = GFRP rupture, IB = Inelastic buckling, Y = Yielding of steel



**Table 3.3** Predicted values of load and deflection of the retrofitted cantilever beams ( $b_f = 150$  mm and  $t_f = 3.0$  mm) with free end loading.

h (mm)	w (mm)	Bare steel beam			Retrofitted beam					
		Load (kN)	Defl. (mm)	Failure mode*	GFRP (mm)	Load (kN)	Defl. (mm)	$\mu_L$	$\mu_\Delta$	Failure mode*
150	7.5	19	36	Y	6.35	23.4	60	1.23	1.69	Y
					9.5	26.6	110	1.40	3.07	G
					12.5	28.2	135	1.48	3.78	G
					15.5	29.8	183	1.57	5.14	G
					19.0	30.8	213	1.62	5.98	G
150	5.0	16.5	34	Y	6.35	20.6	60	1.25	1.80	Y
					9.5	23	113	1.39	3.38	G
					12.5	24.6	172	1.49	5.14	G
					15.5	26	230	1.58	6.88	G
					19.0	27.2	266	1.65	7.94	G
200	5.0	23.6	26	Y	6.35	29.8	46	1.26	1.80	Y
					9.5	33.8	93	1.43	3.63	G
					12.5	36	118	1.53	4.60	G
					15.5	37.8	171	1.60	6.65	G
					19.0	38.8	200	1.64	7.79	G
200	4.0	21.6	25	Y	6.35	26.2	34	1.21	1.37	Y
					9.5	31.4	94	1.45	3.82	G
					12.5	33.2	137	1.54	5.55	G
					15.5	35	207	1.62	8.39	G
					19.0	36.2	247	1.68	10.0	G
300	6.0	44.7	18	Y	6.35	57.4	37	1.28	2.01	Y
					9.5	64.8	60	1.45	3.21	G
					12.5	68.6	73	1.53	3.93	G
					15.5	71.6	88	1.60	4.75	G
					19.0	75.6	103	1.70	5.54	G

\* EI = Elastic buckling, G = GFRP rupture, IB = Inelastic buckling, Y = Yielding of steel

**Table 3.4** Predicted values of load and deflection of the retrofitted cantilever beams ( $b_f = 300$  mm and  $t_f = 7.5$  mm) with free end loading.

H (mm)	w (mm)	Bare steel beam			Retrofitted beam					
		Load (kN)	Defl. (mm)	Failure mode*	GFRP (mm)	Load (kN)	Defl. (mm)	$\mu_L$	$\mu_\Delta$	Failure mode*
300	7.5	159	25	IB	6.35	166	23	1.04	0.93	IB
					9.5	176	32	1.11	1.30	IB
					12.5	186	48	1.17	1.95	G
					15.5	192	63	1.21	2.55	G
					19.0	199	81	1.25	3.28	G
300	6	149	20	IB	6.35	156	21	1.05	1.05	IB
					9.5	161	23	1.08	1.15	IB
					12.5	174	39	1.17	1.98	IB
					15.5	183	67	1.23	3.41	G
					19.0	189	101	1.27	5.15	G
325	6	163	18	IB	6.35	171	19	1.05	1.05	IB
					9.5	176	21	1.08	1.15	IB
					12.5	190	34	1.17	1.86	IB
					15.5	201	63	1.24	3.42	G
					19.0	208	92	1.28	5.04	G
350	6	177	17	IB	6.35	185	18	1.05	1.08	IB
					9.5	191	20	1.08	1.14	IB
					12.5	206	31	1.17	1.80	IB
					15.5	220	59	1.25	3.45	G
					19.0	227	82	1.28	4.78	G
350	7.5	191	22	IB	6.35	199	20	1.04	0.92	IB
					9.5	211	27	1.10	1.24	IB
					12.5	225	44	1.18	1.99	G
					15.5	232	54	1.22	2.47	G
					19.0	241	71	1.26	3.21	G

\* EI = Elastic buckling, G = GFRP rupture, IB = Inelastic buckling, Y = Yielding of steel

**Table 3.5** Predicted values of load and deflection of the retrofitted cantilever beams ( $b_f = 300$  mm and  $t_f = 5$  mm) with free end loading.

h (mm)	w (mm)	Bare steel beam			Retrofitted beam					
		Load (kN)	Defl. (mm)	Failure mode*	GFRP (mm)	Load (kN)	Defl. (mm)	$\mu_L$	$\mu_\Delta$	Failure mode*
300	6	73	12.6	El	6.35	80	13.3	1.09	1.05	El
					9.5	98	16	1.34	1.27	Y
					12.5	118	22	1.62	1.73	Y
					15.5	138	70	1.90	5.55	G
					19.0	144	112	1.98	8.81	G
300	7.5	88	14.5	El	6.35	96	15.3	1.09	1.05	El
					9.5	115	18.5	1.31	1.27	Y
					12.5	130	26	1.47	1.80	Y
					15.5	147	66	1.67	4.51	G
					19.0	154	92	1.75	6.34	G
325	6	80	11.8	El	6.35	87	12.4	1.09	1.05	El
					9.5	107	15	1.33	1.26	Y
					12.5	129	20	1.62	1.69	Y
					15.5	151	57	1.89	4.82	Y
					19.0	160	99	2.00	8.39	G
350	6	87	11.1	El	6.35	95	11.6	1.09	1.05	El
					9.5	115	14	1.33	1.26	Y
					12.5	141	18.8	1.62	1.69	Y
					15.5	165	50	1.89	4.53	Y
					19.0	175	89	2.01	8.03	G
350	7.5	107	12.8	El	6.35	116	13.4	1.09	1.04	El
					9.5	139	16.1	1.3	1.26	Y
					12.5	156	22	1.46	1.73	Y
					15.5	180	57	1.68	4.43	G
					19.0	189	74	1.76	5.80	G

\* El = Elastic buckling, G = GFRP rupture, IB = Inelastic buckling, Y = Yielding of steel

**Table 3.6** Predicted values of load and deflection of the retrofitted simply supported beams ( $b_f = 150$  mm and  $t_f = 7.5$  mm) with center point loading.

h (mm)	w (mm)	Bare steel beam			Retrofitted beam					
		Load (kN)	Defl. (mm)	Failure mode*	GFRP (mm)	Load (kN)	Defl. (mm)	$\mu_L$	$\mu_\Delta$	Failure mode*
150	7.5	161	13.3	IB	6.35	181	25	1.13	1.88	G
					9.5	188	30	1.17	2.23	G
					12.5	193	35	1.20	2.61	G
					15.5	197	37	1.23	2.82	G
					19.0	201	41	1.25	3.05	G
150	5.0	148	12	IB	6.35	166	24	1.12	2.04	G
					9.5	172	30	1.16	2.54	G
					12.5	176	35	1.19	2.93	G
					15.5	180	42	1.21	3.49	G
					19.0	183	46	1.23	3.84	G
200	5.0	204	9.7	IB	6.35	229	19	1.12	1.95	G
					9.5	237	22	1.16	2.28	G
					12.5	243	25	1.19	2.6	G
					15.5	248	29	1.21	3.02	G
					19.0	253	34	1.24	3.54	G
200	4.0	195	9.1	IB	6.35	217	19	1.11	2.10	G
					9.5	224	24	1.15	2.64	G
					12.5	229	27	1.17	3.02	G
					15.5	233	32	1.19	3.54	G
					19.0	237	36	1.21	3.92	G
300	6.0	349	8.0	IB	6.35	387	13	1.11	1.64	G
					9.5	404	15	1.16	1.92	G
					12.5	418	17	1.20	2.18	G
					15.5	429	19	1.23	2.39	G
					19.0	441	22	1.26	2.74	G

\* EI = Elastic buckling, G = GFRP rupture, IB = Inelastic buckling, Y = Yielding of steel

**Table 3.7** Predicted values of load and deflection of the retrofitted simply supported beams ( $b_f = 150$  mm and  $t_f = 5.0$  mm) with center point loading.

h (mm)	w (mm)	Bare steel beam			Retrofitted beam					
		Load (kN)	Defl. (mm)	Failure mode*	GFRP (mm)	Load (kN)	Defl. (mm)	$\mu_L$	$\mu_\Delta$	Failure mode
150	7.5	116	12.8	IB	6.35	139	21	1.20	1.61	G
					9.5	141	31	1.22	2.44	G
					12.5	147	38	1.27	2.96	G
					15.5	151	42	1.30	3.28	G
					19.0	156	49	1.34	3.83	G
150	5.0	105	11.8	IB	6.35	122	24	1.16	2.01	G
					9.5	127	34	1.21	2.90	G
					12.5	131	39	1.25	3.33	G
					15.5	137	50	1.31	4.25	G
					19.0	141	57	1.35	4.84	G
200	5.0	148	10	IB	6.35	168	16.5	1.14	1.65	G
					9.5	179	23	1.21	2.33	G
					12.5	187	30	1.26	3.04	G
					15.5	192	35	1.30	3.47	G
					19.0	197	41	1.33	4.08	G
200	4.0	140	9.7	IB	6.35	158	15.9	1.13	1.63	G
					9.5	168	24	1.20	2.48	G
					12.5	174	29	1.24	3.02	G
					15.5	179	37	1.28	3.76	G
					19.0	185	45	1.32	4.60	G
300	6.0	265	8.1	IB	6.35	299	12.4	1.13	1.52	G
					9.5	319	15.4	1.20	1.90	G
					12.5	336	18.7	1.27	2.29	G
					15.5	349	21.5	1.32	2.64	G
					19.0	362	25.4	1.36	3.12	G

\* EI = Elastic buckling, G = GFRP rupture, IB = Inelastic buckling, Y = Yielding of steel

**Table 3.8** Predicted values of load and deflection of the retrofitted simply supported beams ( $b_f = 150$  mm and  $t_f = 3.0$  mm) with center point loading.

h (mm)	w (mm)	Bare steel beam			Retrofitted beam					
		Load (kN)	Defl. (mm)	Failure mode*	GFRP (mm)	Load (kN)	Defl. (mm)	$\mu_L$	$\mu_\Delta$	Failure mode*
150	7.5	75	9.2	Y	6.35	91	14.2	1.21	1.53	Y
					9.5	104	30	1.39	3.26	G
					12.5	112	44	1.49	4.72	G
					15.5	117	50	1.56	5.38	G
					19.0	120	49	1.60	5.33	IB
150	5.0	64	8.6	Y	6.35	79	13.4	1.23	1.58	Y
					9.5	91	32	1.42	3.75	G
					12.5	100	46	1.56	5.36	IB
					15.5	100	42	1.56	4.87	IB
					19.0	102	43	1.59	5.00	IB
200	5.0	91	6.7	Y	6.35	115	11.2	1.26	1.67	Y
					9.5	132	24	1.44	3.60	G
					12.5	142	37	1.55	5.50	G
					15.5	148	43	1.62	6.41	G
					19.0	152	45	1.66	6.72	IB
200	4.0	83	6.5	Y	6.35	101	8.5	1.21	1.29	Y
					9.5	123	27	1.47	4.17	G
					12.5	132	40	1.58	6.08	G
					15.5	136	43	1.63	6.57	IB
					19.0	145	46	1.74	7.06	IB
300	6.0	187	7.1	Y	6.35	222	10.3	1.18	1.43	G
					9.5	249	15	1.33	2.13	G
					12.5	269	20	1.43	2.85	G
					15.5	283	25	1.51	3.50	G
					19.0	295	29	1.57	4.07	G

\* EI = Elastic buckling, G = GFRP rupture, IB = Inelastic buckling, Y = Yielding of steel

**Table 3.9** Predicted values of load and deflection of the retrofitted simply supported beams ( $b_f = 300$  mm and  $t_f = 7.5$  mm) with center point loading.

h (mm)	w (mm)	Bare steel beam			Retrofitted beam					
		Load (kN)	Defl. (mm)	Failure mode*	GFRP (mm)	Load (kN)	Defl. (mm)	$\mu_L$	$\mu_\Delta$	Failure mode*
300	7.5	603	6.7	Y	6.35	626	6.8	1.04	1.01	Y
					9.5	648	9.0	1.07	1.34	Y
					12.5	682	17.2	1.13	2.55	G
					15.5	700	21.5	1.16	3.19	G
					19.0	714	23.3	1.18	3.47	G
300	6	567	6.5	Y	6.35	587	6.9	1.03	1.06	Y
					9.5	597	7.4	1.05	1.13	Y
					12.5	630	16.1	1.11	2.48	IB
					15.5	634	18	1.12	2.75	IB
					19.0	689	24	1.21	3.64	G
325	6	619	6.1	Y	6.35	640	6.6	1.03	1.06	Y
					9.5	650	6.9	1.05	1.12	IB
					12.5	682	15	1.10	2.44	IB
					15.5	693	18	1.12	2.91	IB
					19.0	703	21	1.14	3.45	IB
350	6	671	5.9	Y	6.35	693	6.2	1.03	1.05	Y
					9.5	705	6.6	1.05	1.13	IB
					12.5	749	15.8	1.12	2.68	IB
					15.5	753	18.1	1.12	3.06	IB
					19.0	766	20.1	1.14	3.40	IB
350	7.5	720	6.1	Y	6.35	746	6.1	1.04	1.00	Y
					9.5	774	8.3	1.07	1.34	IB
					12.5	812	15.5	1.13	2.51	IB
					15.5	832	18.1	1.16	2.94	G
					19.0	854	21.8	1.19	3.55	G

\* EI = Elastic buckling, G = GFRP rupture, IB = Inelastic buckling, Y = Yielding of steel

**Table 3.10** Predicted values of load and deflection of the retrofitted simply supported beams ( $b_f = 300$  mm and  $t_f = 5$  mm) with center point loading.

h (mm)	w (mm)	Bare steel beam			Retrofitted beam					
		Load (kN)	Defl. (mm)	Failure mode*	GFRP (mm)	Load (kN)	Defl. (mm)	$\mu_L$	$\mu_\Delta$	Failure mode*
300	6	280	3.9	El	6.35	306	4.2	1.09	1.06	El
					9.5	374	5.1	1.33	1.28	El
					12.5	448	6.6	1.60	1.69	IB
					15.5	512	23.3	1.83	5.92	G
					19.0	522	24.6	1.86	6.26	IB
300	7.5	341	4.4	El	6.35	372	4.7	1.09	1.06	El
					9.5	440	5.6	1.29	1.27	IB
					12.5	486	7.0	1.42	1.60	IB
					15.5	554	21	1.62	4.79	G
					19.0	576	28	1.69	6.37	G
325	6	308	3.7	El	6.35	336	3.9	1.09	1.06	El
					9.5	408	4.8	1.32	1.28	El
					12.5	490	6.2	1.59	1.67	IB
					15.5	560	21.3	1.82	5.72	G
					19.0	588	30.6	1.91	8.23	G
350	6	336	3.5	El	6.35	366	3.7	1.09	1.06	El
					9.5	442	4.5	1.32	1.27	El
					12.5	534	5.9	1.59	1.66	IB
					15.5	612	20.4	1.82	5.76	G
					19.0	638	27.6	1.90	7.76	G
350	7.5	414	4.0	El	6.35	448	4.2	1.08	1.05	El
					9.5	528	5.0	1.27	1.26	Y
					12.5	588	6.3	1.42	1.59	IB
					15.5	672	18.2	1.62	4.58	G
					19.0	698	23.7	1.68	5.95	G

\* El = Elastic buckling, G = GFRP rupture, IB = Inelastic buckling, Y = Yielding of steel



**Table 3.11** Predicted values of load and deflection of the retrofitted simply supported beams ( $b_f = 150$  mm and  $t_f = 7.5$  mm) with two-point loading.

h (mm)	w (mm)	Bare steel beam			Retrofitted beam					
		Load (kN)	Defl. (mm)	Failure mode*	GFRP (mm)	Load (kN)	Defl. (mm)	$\mu_L$	$\mu_\Delta$	Failure mode*
150	7.5	117	24	IB	6.35	139	79	1.19	3.31	G
					9.5	143	89	1.22	3.73	G
					12.5	147	96	1.26	4.04	G
					15.5	152	110	1.30	4.61	G
					19.0	157	121	1.34	5.09	G
150	5.0	109	25	IB	6.35	128	83	1.17	3.28	G
					9.5	136	105	1.25	4.14	G
					12.5	145	118	1.33	4.67	G
					15.5	148	118	1.36	4.67	G
					19.0	153	125	1.40	4.93	G
200	5.0	150	17	IB	6.35	168	39	1.12	2.25	G
					9.5	174	49	1.16	2.80	G
					12.5	181	68	1.21	3.88	G
					15.5	190	88	1.27	5.08	G
					19.0	201	111	1.34	6.38	G
200	4.0	141	12	IB	6.35	153	26	1.08	2.22	G
					9.5	165	51	1.17	4.30	G
					12.5	173	77	1.22	6.48	G
					15.5	175	83	1.24	6.99	G
					19.0	178	91	1.26	7.62	IB
300	6.0	252	11.3	IB	6.35	278	22	1.10	1.96	G
					9.5	288	25	1.14	2.20	G
					12.5	297	28	1.18	2.51	G
					15.5	304	33	1.21	2.90	G
					19.0	310	37	1.23	3.28	G

\* EI = Elastic buckling, G = GFRP rupture, IB = Inelastic buckling, Y = Yielding of steel

**Table 3.12** Predicted values of load and deflection of the retrofitted simply supported beams ( $b_f = 150$  mm and  $t_f = 5.0$  mm) with two-point loading.

h (mm)	w (mm)	Bare steel beam			Retrofitted beam					
		Load (kN)	Defl. (mm)	Failure mode*	GFRP (mm)	Load (kN)	Defl. (mm)	$\mu_L$	$\mu_\Delta$	Failure mode*
150	7.5	84	25	IB	6.35	101	56	1.20	2.22	IB
					9.5	109	78	1.29	3.10	G
					12.5	114	88	1.35	3.49	G
					15.5	120	92	1.42	3.65	G
					19.0	122	93	1.45	3.67	IB
150	5.0	76	24	IB	6.35	91	56.9	1.19	2.33	IB
					9.5	92	53.4	1.20	2.13	IB
					12.5	94	55.3	1.23	2.27	IB
					15.5	94	51.1	1.23	2.10	IB
					19.0	95	50.9	1.24	2.09	G
200	5.0	107	20	IB	6.35	128	46	1.19	2.32	G
					9.5	135	64	1.25	3.18	G
					12.5	146	73	1.35	3.61	G
					15.5	150	77	1.39	3.85	G
					19.0	158	87	1.47	4.32	G
200	4.0	102	20	IB	6.35	118	37	1.15	1.86	IB
					9.5	127	61	1.24	3.02	G
					12.5	127	55	1.24	2.73	IB
					15.5	139	74	1.36	3.67	IB
					19.0	146	80	1.43	4.01	IB
300	6.0	192	20.7	IB	6.35	220	24.2	1.14	1.16	G
					9.5	233	29.5	1.21	1.42	G
					12.5	245	39	1.27	1.88	G
					15.5	254	45	1.32	2.17	G
					19.0	262	53	1.36	2.57	G

\* EI = Elastic buckling, G = GFRP rupture, IB = Inelastic buckling, Y = Yielding of steel

**Table 3.13** Predicted values of load and deflection of the retrofitted simply supported beams ( $b_f = 150$  mm and  $t_f = 3.0$  mm) with two-point loading.

h (mm)	w (mm)	Bare steel beam			Retrofitted beam					
		Load (kN)	Defl. (mm)	Failure mode*	GFRP (mm)	Load (kN)	Defl. (mm)	$\mu_L$	$\mu_\Delta$	Failure mode*
150	7.5	51	10.2	El	6.35	67	25.5	1.31	2.50	IB
					9.5	75	44	1.46	4.33	IB
					12.5	77	45	1.50	4.43	IB
					15.5	79	46	1.54	4.56	IB
					19.0	81	47	1.58	4.62	IB
150	5.0	45	10.2	El	6.35	55	15.4	1.21	1.51	IB
					9.5	63	35	1.38	3.45	IB
					12.5	64	34	1.41	3.34	IB
					15.5	65	35	1.43	3.40	IB
					19.0	66	34	1.45	3.30	IB
200	5.0	65	7.9	El	6.35	80	13	1.23	1.65	IB
					9.5	95	38	1.46	4.87	IB
					12.5	98	41	1.50	5.20	IB
					15.5	101	44	1.55	5.51	IB
					19.0	103	45	1.58	5.72	IB
200	4.0	55	7.2	El	6.35	68	8.7	1.23	1.22	IB
					9.5	88	39	1.59	5.40	IB
					12.5	89	36	1.61	5.09	IB
					15.5	90	35	1.63	4.92	IB
					19.0	92	36	1.66	5.08	IB
300	6.0	120	5.6	El	6.35	157	12.8	1.31	2.31	IB
					9.5	185	32	1.54	5.67	G
					12.5	201	50	1.68	9.04	G
					15.5	209	55	1.75	9.88	G
					19.0	214	54	1.79	9.73	IB

\* El = Elastic buckling, G = GFRP rupture, IB = Inelastic buckling, Y = Yielding of steel

**Table 3.14** Predicted values of load and deflection of the retrofitted simply supported beams ( $b_f = 300$  mm and  $t_f = 7.5$  mm) with two-point loading.

h (mm)	w (mm)	Bare steel beam			Retrofitted beam					
		Load (kN)	Defl. (mm)	Failure mode*	GFRP (mm)	Load (kN)	Defl. (mm)	$\mu_L$	$\mu_\Delta$	Failure mode*
300	7.5	420	7.3	El	6.35	432	7.8	1.03	1.07	IB
					9.5	440	9.7	1.05	1.32	IB
					12.5	445	11	1.06	1.50	IB
					15.5	449	12.2	1.07	1.66	IB
					19.0	457	20.6	1.09	2.81	IB
300	6	372	10.2	El	6.35	374	12.1	1.01	1.19	Y
					9.5	375	13.2	1.01	1.29	Y
					12.5	375	13.2	1.01	1.29	Y
					15.5	375	13.1	1.01	1.28	Y
					19.0	378	20.6	1.02	2.02	Y
325	6	402	9.7	El	6.35	404	11	1.00	1.13	Y
					9.5	404	10.8	1.00	1.11	Y
					12.5	405	12.3	1.01	1.27	Y
					15.5	405	12	1.01	1.24	Y
					19.0	406	13.7	1.01	1.41	Y
350	6	433	10.2	El	6.35	434	10.5	1.00	1.03	Y
					9.5	435	11.8	1.00	1.16	Y
					12.5	435	11.5	1.00	1.13	Y
					15.5	436	13.3	1.01	1.30	Y
					19.0	436	13.1	1.01	1.28	Y
350	7.5	495	6.7	El	6.35	509	7.5	1.03	1.12	IB
					9.5	516	8.8	1.04	1.32	IB
					12.5	522	10.3	1.05	1.54	IB
					15.5	525	11.4	1.06	1.71	IB
					19.0	527	11.7	1.06	1.75	IB

\* El = Elastic buckling, G = GFRP rupture, IB = Inelastic buckling, Y = Yielding of steel

**Table 3.15** Predicted values of load and deflection of the retrofitted simply supported beams ( $b_f = 300$  mm and  $t_f = 5$  mm) with two-point loading.

h (mm)	w (mm)	Bare steel beam			Retrofitted beam					
		Load (kN)	Defl. (mm)	Failure mode*	GFRP (mm)	Load (kN)	Defl. (mm)	$\mu_L$	$\mu_\Delta$	Failure mode*
300	6.0	173	3.9	El	6.35	191	4.2	1.10	1.07	El
					9.5	235	5.0	1.35	1.30	El
					12.5	305	6.8	1.76	1.75	IB
					15.5	343	21.5	1.98	5.53	IB
					19.0	346	25.7	1.99	6.60	IB
300	7.5	212	4.4	El	6.35	231	4.6	1.09	1.05	El
					9.5	280	5.6	1.32	1.26	El
					12.5	333	7.2	1.57	1.63	IB
					15.5	384	27.8	1.81	6.33	IB
					19.0	388	27.4	1.83	6.23	IB
325	6	190	3.7	El	6.35	210	3.9	1.10	1.07	El
					9.5	258	4.8	1.36	1.30	El
					12.5	333	6.3	1.75	1.73	IB
					15.5	368	17.6	1.94	4.80	IB
					19.0	375	23	1.97	6.27	IB
350	6	207	3.5	El	6.35	229	3.7	1.10	1.07	El
					9.5	281	4.5	1.36	1.30	El
					12.5	362	6.0	1.75	1.72	IB
					15.5	397	15.5	1.91	4.45	IB
					19.0	404	20.2	1.95	5.80	IB
350	7.5	257	4.0	El	6.35	280	4.2	1.09	1.06	El
					9.5	338	5.0	1.32	1.26	El
					12.5	400	6.3	1.56	1.60	Y
					15.5	460	26.6	1.79	6.73	G
					19.0	476	34.4	1.85	8.71	IB

\* El = Elastic buckling, G = GFRP rupture, IB = Inelastic buckling, Y = Yielding of steel

## CURRICULUM VITAE

- Name:** Mohammad Al Amin Siddique
- Place of Birth:** Jamalpur, Bangladesh
- Year of Birth:** 1978
- Post-Secondary Education and Degrees:**
- M.Sc. 2002-2005  
Department of Civil Engineering,  
Bangladesh University of Engineering and Technology,  
Dhaka, Bangladesh
- B.Sc. 1996-2002  
Department of Civil Engineering,  
Bangladesh University of Engineering and Technology,  
Dhaka, Bangladesh
- Honours and Awards:**
- The University Award of Excellence in Undergraduate Studies (Dean's List), Bangladesh University of Engineering and Technology  
Dhaka, Bangladesh, 1997-2001
- Academic Appointments:**
- Teaching and Research Assistant  
Department of Civil and Environmental Engineering  
The University of Western Ontario, Canada, 2006-2011
- Assistant Professor  
Department of Civil Engineering,  
Bangladesh University of Engineering and Technology,  
Dhaka, Bangladesh, 2005-2006
- Lecturer  
Department of Civil Engineering,  
Bangladesh University of Engineering and Technology,  
Dhaka, Bangladesh, 2002-2005
- Publications:**
- M. Siddique and A. El Damatty, "Improvement of the Local Buckling Capacity of Steel Plates through bonding GFRP Plates", *Proceedings of the Fifth International Conference on Coupled Instabilities in Metal Structures (CIMS 2008)*, 23-25 June 2008, Sydney, Australia, pp 433-440.